

Faculty Excellence Award Application Form



Name: Dr. Arash Bodaghee

Rank: Assistant Professor of Physics and Astronomy

Department: Chemistry, Physics and Astronomy

Award applying for:
(Check one)

	Excellence in Teaching Award*
X	Excellence in Scholarship & Creative Endeavors Award*
	Excellence in University Service*
	Excellence in Scholarship of Teaching & Learning Award*
	Department/Program Excellence Award^
	Irene Rose Community Service Award^
	Laurie Hendrickson McMillian Faculty Award^

*college selection required before being forwarded to university

^university awards

College nominations are due by November 23, 2015 to the college Dean.

University nominations are due March 13, 2016 to the Director, Center for Faculty Development, Dr. Steve Jones

Please insert the required documentation in the pages below for the award category you have noted above. Detailed information associated with each award is available online at the Academic Affairs Intranet Forms Page – section titled “Awards”

<https://intranet.gcsu.edu/academic-affairs/policies-procedures-and-practices-manual-forms>

It is requested that all application materials be inserted into one document, saved, and submitted electronically for consideration.

To:
Dean Ken Proctor

Letter of Support for Dr. Arash Bodaghee

I am in strong support for Dr. Bodaghee's consideration for the Excellence in Scholarship Award in 2016.

Dr. Bodaghee has published two (2014-2015) important articles in the *Astrophysical Journal* as first author, highlighting his involvement with the NuStar team and his use of the Chandra x-ray telescope while at Georgia College. These papers investigate the x-ray emission from Milky Way Galactic objects in the effort to characterize them and identify Black-hole binary star systems. The class of object Dr. Bodaghee is studying is unique and an important step in the understanding of the stellar evolution. From these projects, Dr. Bodaghee has brought prestige from the acceptance of time and grant funds for the Chandra and Hubble space telescope. The Hubble telescope has never been used to study objects of this type. It is great that Georgia College can be part of this groundbreaking research. It is easy to say that Georgia College has significantly increased its x-ray astronomy community reputation and its presence in the premiere journals of the worldwide astronomical community through the work of Dr. Bodaghee.

Dr. Bodaghee has also co-authored 5 manuscripts in the *Astrophysical Journal*, *Monthly Notices of the Royal Astronomical Society* and *Astronomy & Astrophysics* journal with Georgia College as his affiliation.

The *Astrophysical Journal*, the *Monthly Notices of the Royal Astronomical Society* and the *Astronomy & Astrophysics* journal are the premiere journals in the area of astrophysics as published in the U.S., the UK and Europe respectively.

The journal and title of his recent work is listed below and should be considered for the Excellence in Scholarship Award.

2015 First Authored

- The *Astrophysical Journal*, Volume 801, Issue 1, article id. 49, 7 pp. (2015)
A First Look at the X-Ray Population of the Young Massive Cluster VVV CL077

2014 First Authored

- The *Astrophysical Journal*, Volume 791, Issue 1, article id. 68, 10 pp. (2014).
Initial Results from NuSTAR Observations of the Norma Arm

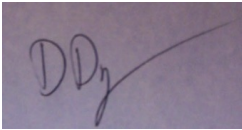
2015 co-authored

- The *Astrophysical Journal*, Volume 807, Issue 1, article id. 17, 11 pp. (2015).
Spectral State Dependence of the 0.4-2 MeV Polarized Emission in Cygnus X-1 Seen with INTEGRAL/IBIS, and Links with the AMI Radio Data
- *Monthly Notices of the Royal Astronomical Society*, Volume 449, Issue 1, p.597-604
Chandra identification of two AGN discovered by INTEGRAL

2014 co-authored

- The Astrophysical Journal, Volume 796, Issue 2, article id. 105, 26 pp. (2014).
The Norma Arm Region Chandra Survey Catalog: X-Ray Populations in the Spiral Arms
- The Astrophysical Journal Letters, Volume 795, Issue 2, article id. L27, 6 pp. (2014).
Discovery of X-Ray Pulsations from the INTEGRAL Source IGR J11014-6103
- Astronomy & Astrophysics, Volume 568, id.A54, 17
Near-infrared spectroscopy of 20 new Chandra sources in the Norma arm

Sincerely,

A handwritten signature in blue ink, appearing to read "DD", with a long horizontal stroke extending to the right.

Donovan Domingue
Professor of Physics
Georgia College
Dept. of Chemistry, Physics & Astronomy



Department of Chemistry, Physics and Astronomy

College of Arts and Sciences
Campus Box 82
Milledgeville, Georgia 31061-0490
Phone (478) 445-5769
Fax (478) 445-1092

February 5, 2016

To Whom This May Concern

It is my pleasure to write this letter of recommendation for Dr Arash Bodaghee. I have worked with Dr Bodaghee for over two years. He has proven to be an excellent teacher and academic. In the classroom Dr Bodaghee is always prepared with lectures that are clear, interesting and right on schedule with course objectives. Dr Bodaghee has eight publications in just the short time he has been with us. This quality and quantity of research is only realized in research universities. This would be fantastic for any professor, but in addition he has performed this cutting edge work with the involvement of undergraduates. His work has covered his summer salary, and provided a stipend for a summer research student.

His research group has grown at a fantastic rate for a faculty member with only a year of opportunity to raise student interest. At last count he has involved over 13 students in undergraduate research. He has made great use out of our departmental computing cluster. In addition, while performing this great research he has also found time for outreach. He has been actively involved in setting up public viewing opportunities at the Pohl Observatory. I highly recommend Dr Bodaghee for the Excellence in Scholarship and Creative Endeavors award. If you need any further information from me please contact me at your convenience.

Sincerely,

Dr K.C. McGill
Chair of GCSU Chemistry, Physics and Astronomy Department
ken.mcgill@gcsu.edu

Milledgeville • Macon • Warner Robins

*Georgia College & State University, established in 1889, is Georgia's Public Liberal Arts University.
University System of Georgia*



College of Arts and Sciences

Department of Chemistry, Physics and Astronomy

Campus Box 82
Milledgeville, Georgia 31061-0490
Phone 478-445-5769
Fax 478-445-1092

To: Excellence in Scholarship Committee

Letter of Support for Dr. Arash Bodaghee

Dr. Bodaghee has published two (2014-2015) important articles in the *Astrophysical Journal* as first author, highlighting his involvement with the NuStar team and his use of the Chandra x-ray telescope while at Georgia College. These papers investigate the x-ray emission from Milky Way or Galactic objects in the effort to characterize them and identify Black-hole binary star systems. The class of object Dr. Bodaghee is studying is unique and an important step in the understanding of the stellar evolution. From these projects, Dr. Bodaghee has brought prestige from the acceptance of time and grant funds for the Chandra and Hubble space telescope. The Hubble telescope has never been used to study objects of this type. It is great that Georgia College can be part of this groundbreaking research. It is easy to say that Georgia College has significantly increased its x-ray astronomy community reputation and its presence in the premiere journals of the worldwide astronomical community through the work of Dr. Bodaghee.

Dr. Bodaghee has also co-authored 6 additional manuscripts in the *Astrophysical Journal*, *Monthly Notices of the Royal Astronomical Society* and *Astronomy & Astrophysics* journal with Georgia College as his affiliation. This demonstrates the importance of his expertise to that research community and his ability to foster along successful results and insights into the universe with the use of the high energy telescopes.

Dr. Bodaghee has been very successful at involving students in his research group, a challenge I am familiar with. I am impressed that Georgia College has been the location of such fine research which has also provided new opportunities for our physics undergraduates.

I strongly recommend that this body of work be considered for the Excellence in Scholarship Award.

Sincerely,

Donovan Domingue
Professor of Physics and Astronomy
Georgia College
Dept. of Chemistry, Physics & Astronomy

Milledgeville • Macon • Warner Robins

Georgia College, the state's designated public liberal arts university, combines the educational experience



College of Arts and Sciences

Department of Chemistry, Physics and Astronomy

Campus Box 82
Milledgeville, Georgia 31061-0490
Phone 478-445-5769
Fax 478-445-1092

To:
Dean Ken Proctor

Letter of Support for the Excellence in Scholarship Award

I would like to submit a letter of support for **Arash Bodaghee**, Assistant Professor of physics in the Department of Chemistry, Physics and Astronomy.

Having served on the faculty research awards committee for the previous 5 years (from fall 2009 to spring 2014), I can honestly say that Dr. Bodaghee's work would have easily placed him among the winners, if not the top award, in each of those years.

His publications in 2014-2015 include two first author papers in the *Astrophysical Journal*, by far the top journal in astrophysics. This would be roughly equivalent to publication in Nature or Science in the biological sciences and would be sufficient for tenure at many R1 institutions. In addition, he is the co-author of three more papers published in the *Astrophysical Journal*, one in *Astronomy & Astrophysics* (another top international journal in the field), one in the *Astrophysical Journal Letters* (also a top international journal associated with the *Astrophysical Journal*), and one in *Monthly Notices of the Royal Astronomical Society* (the top astronomical journal from the UK). These journals are international in scope and read by all serious academic astronomers and astrophysicists world-wide.

Publication in these international peer-reviewed journals is very competitive and difficult. Doing so several times in a single year is quite unusual.

I am in strong support for Dr. Bodaghee's consideration for this Excellence in Scholarship Award in 2016.

Ralph H France III

Professor of Physics
Georgia College
Dept. of Chemistry, Physics & Astronomy

Excellence in Scholarship & Creative Endeavors Award ; Application Section 5

Dr. Arash Bodaghee, Assistant Professor of Physics & Astronomy

Chronological list of peer-reviewed publications with a Georgia College affiliation

1 "Chandra Observations of Eight Sources Discovered by INTEGRAL"

Tomsick, Krivonos, Wang, **Bodaghee**, Chaty, Rahoui, Rodriguez, Fornasini

The Astrophysical Journal, Vol. 816, Issue 1, id. 38, 14 pp. (Jan. 2016)

<http://adsabs.harvard.edu/abs/2016ApJ...816..38T>

Description: Using the Chandra space telescope, we provide firm classifications for 3 of 8 unidentified X-ray sources and we offer tentative classifications for the other 5 sources. This is part of an ongoing campaign to use Chandra to help classify sources discovered with the INTEGRAL space telescope.

2 "Spectral State Dependence of the 0.4-2 MeV Polarized Emission in Cygnus X-1 Seen with INTEGRAL/IBIS, and Links with the AMI Radio Data"

Rodriguez, Grinberg, Laurent, Cadolle Bel, Pottschmidt, Pooley, **Bodaghee**, Wilms, Gouiffès

The Astrophysical Journal, Vol. 807, Issue 1, id. 17, 11 pp. (Jul. 2015)

<http://adsabs.harvard.edu/abs/2015ApJ...807..17R>

Description: Measurements of polarization (i.e. the angle at which a light wave oscillates) from the accreting black hole Cygnus X-1 are made using data from the INTEGRAL space telescope. No significant polarization is detected except at high energies and only during a specific state. This study can help clarify the high-energy photons and jets of material emitted near black holes.

3 "Chandra Identification of Two AGN Discovered by INTEGRAL"

Tomsick, Krivonos, Rahoui, Ajello, Rodriguez, Barrière, **Bodaghee**, Chaty

Monthly Notices of the Royal Astronomical Society, Vol. 449, id 597, 7 pp. (May 2015)

<http://adsabs.harvard.edu/abs/2015MNRAS.449.597T>

Description: Chandra space telescope observations, paired with observations in the infrared taken with a large optical telescope in Chile, are used to classify 2 X-ray sources as active galactic nuclei (AGN). These are supermassive black holes (i.e. a single, infinitesimally small object with several tens of millions of times the mass of the Sun) that reside in the cores of other galaxies.

4 "A First Look at the X-Ray Population of the Young Massive Cluster VVV CL077"

Bodaghee, Tomsick, Fornasini, Rahoui, Bauer

The Astrophysical Journal, Vol. 801, Issue 1, id. 49, 7 pp. (Mar. 2015)

<http://adsabs.harvard.edu/abs/2015ApJ...801...49B>

Description: Young massive clusters (YMCs) are groups of of young (~10 million years) stars each around ten times as massive as the Sun. While hundreds of YMCs are known in the Milky Way, few of them have been detected in the X-rays. Our observations of one such YMC with Chandra revealed complex X-ray morphology which we compared to infrared and radio images.

5 "The Norma Arm Chandra Survey Catalog: X-Ray Populations in the Spiral Arms"

Fornasini, Tomsick, **Bodaghee**, Krivonos, An, Rahoui, Gotthelf, Bauer, Stern

The Astrophysical Journal, Vol. 796, Issue 2, id. 105, 26 pp. (Dec. 2014)

<http://adsabs.harvard.edu/abs/2014ApJ...796..105F>

Description: Results are presented for a large observing program consisting of mapping a 2-degree by 1-degree section of the Norma Arm of the Milky Way with the Chandra X-ray telescope. We discovered around 1100 new X-ray sources for which we provide, for the first time, their X-ray positions, photon count rates, spectral parameters, and tentative classifications.

6 "Discovery of X-Ray Pulsations from the INTEGRAL Source IGR J11014–6103"

Halpern, Tomsick, Gotthelf, Camilo, Ng, **Bodaghee**, Rodriguez, Chaty, Rahoui

The Astrophysical Journal Letters, Vol. 795, Issue 2, id. L27, 6 pp. (Nov. 2014)

<http://adsabs.harvard.edu/abs/2014ApJ...795L..27H>

Description: A few years ago, our group found that the X-ray source named IGR J11014–6103 is traveling through space at over 1000 km per second making it one of the fastest moving objects in our galaxy. In this paper, we announce that the object emits periodic X-ray pulses which indicates that the object is a neutron star spinning at the rate of 16 times per second (1000 rpm).

7 "Initial Results from NuSTAR Observations of the Norma Arm"

Bodaghee, Tomsick, Krivonos, Stern, Bauer, Fornasini, Barrière, Boggs, Christensen, Craig, Gotthelf, Hailey, Harrison, Hong, Mori, Zhang

The Astrophysical Journal, Vol. 791, Issue 1, id. 68, 10 pp. (Aug. 2014)

<http://adsabs.harvard.edu/abs/2014ApJ...791...68B>

Description: A section of the Norma Arm of the Milky Way was observed with the NuSTAR X-ray telescope. The raw images were affected by artifacts due to the telescope's optics. Nevertheless, we were able to remove most of these artifacts to obtain a clean map in which we detected a known black hole in outburst as well as 4 sources seen above 10 keV for the first time.

8 "Near-Infrared Spectroscopy of 20 New Chandra Sources in the Norma Arm"

Rahoui, Tomsick, Fornasini, **Bodaghee**, Bauer

Astronomy & Astrophysics, Vol. 568, id. A54, 17 pp. (Aug. 2014)

<http://adsabs.harvard.edu/abs/2014A%26A...568A..54R>

Description: Among the 1100 new unclassified X-ray sources discovered in our Chandra observations of the Norma Arm (see Fornasini et al., 2014, #5 above), twenty candidates were selected for targeted observations in the infrared band with the Cerro Tololo Inter-American Observatory in Chile. Their infrared positions and spectra are presented here for the first time.

NOTE 1: *The Astrophysical Journal* is the preeminent journal for peer-reviewed articles on astrophysics. It is published by IOP Sciences for the American Astronomical Society. The equivalent for the European Union is *Astronomy & Astrophysics* which is published by EDP Sciences for the European Southern Observatory. The equivalent for the United Kingdom is *Monthly Notices of the Royal Astronomical Society* which is published by Oxford University Press for the Royal Astronomical Society.

NOTE 2: In December 2015, an article titled “NuSTAR Discovery of a Cyclotron Line in the Accreting X-ray Pulsar IGR J16393–4643” by Bodaghee et al. (2016) was resubmitted to the *Astrophysical Journal*, after including suggestions from the peer-reviewer.

Excellence in Scholarship & Creative Endeavors Award; Application Section 6

Dr. Arash Bodaghee, Assistant Professor of Physics & Astronomy

Reflective Statement:

Once young scientists learn the theoretical framework as presented in class and in homework, they must be exposed to a laboratory setting in order to experience how these theories are applied to explain what we observe. Thankfully, as an astronomer, my laboratory is the Universe itself which means I never have a shortage of eager students looking to do research.

Since arriving at Georgia College in January 2014, I have engaged around 20 undergraduate students, mostly physics and engineering majors, to help with the analysis of X-ray and gamma-ray observations from the most advanced space telescopes ever built including Chandra, Fermi, INTEGRAL, NuSTAR, Swift, and XMM-Newton. Some of these students analyze gamma-ray data from the Fermi space telescope to look for emission from accreting black holes (currently, these students are Stephen Hood and Joshua O'Neill). A few students study X-ray data from INTEGRAL to look for new transient neutron stars and black holes (Kortni Hines, Michaella Morton, and Austin Waldron). While other students, including my research scholar (Ryan Agnew) and a talented programmer (Brenton Jackson), investigate the spatial distribution of neutron stars and black holes in nearby galaxies by combining Chandra and Hubble data.

What these students have done is remarkable. For example, they converted my clunky, but working, spatial analysis code into the more efficient MATLAB language which can run on the distributed computing cluster (consisting of 32 parallel processors) located in the basement of Herty Hall. A computing task that once took my high-end laptop one week to complete operating at full time, now takes a few minutes. This huge increase in computational efficiency enables us to easily and quickly apply our spatial analysis technique to any number of nearby galaxies including the Magellanic Clouds and Andromeda. In return, these students have learned to manipulate the computer cluster and have gained experience in programming and mathematical modeling that will help them succeed in their academic and professional careers. In April 2016, Mr. Agnew (and, it is hoped, Mr. Jackson) will accompany me to the 16th Meeting of the High-Energy Astrophysics Division (HEAD) of the American Astronomical Society (AAS) in Naples, FL, where we will present these results for the first time. When our analysis is complete, we will submit an article to the *Astrophysical Journal*. Other than Georgia College students and myself, the author list will include seasoned researchers from Harvard and UC Berkeley.

Another example of student development through research is the project I am working on with math senior Keri Spetzer. In August 2014, Ms. Spetzer and I attended the 15th HEAD Meeting in Chicago, IL, where she presented a poster describing our analysis of INTEGRAL observations of the Milky Way's spiral arms. Attending a major scientific conference was a huge eye-opener for her as an undergraduate. She was able to overcome her initial fears of being unprepared for such advanced topics, she formed new friendships and potential collaborations among the graduate students attending the conference, and she developed a career network that will help her get into a graduate program in applied mathematics when she leaves Georgia College.

Ms. Spetzer and I are part of a research collaboration that was awarded observing time on the Hubble space telescope, as well as funding to perform the analysis. We were featured on GCSU's Frontpage during November, 2014. We obtained around \$12,000 in funding from the Space Telescope Science Institute which operates Hubble (with the funds allocated to our group at GC through Caltech) to help cover the costs of research during Summer 2015 for her and for myself, and an additional \$30,000 from another source to finish the INTEGRAL project. Thus, Ms. Spetzer helped analyze proprietary Hubble data before anyone else (including the Principle Investigator!). Our results were handed over to our co-investigators at Caltech where they will be used to constrain models of massive stellar winds. The Principle Investigator of this program is currently writing the first draft of the article describing these results and Ms. Spetzer will be a co-author. These experiences are important for an undergraduate preparing for graduate school, and they will help pave the way to a career in science where women remain under-represented at all levels.

As for the future, there are a number of collaborations that should prove fruitful for research opportunities for students which will help them learn physics, engineering, and astronomy. I am excited about our plans (with help from physics faculty Mr. Johnson, Dr. France, Dr. Domingue, and Dr. McGill) to have students dismount and reassemble two large radio dishes that we inherited from Georgia Public Broadcasting. These dishes (each around 6 yards wide) will be converted to telescopes capable of performing high-quality radio astronomy. Another project for the next few years is the development of a balloon-borne X-ray polarimetry telescope called PolSTAR, a prototype of which has already flown.

The best part of teaching through research at Georgia College is the ability to interact with these very qualified and well-trained students; first in the classroom, then in the laboratory. Plus, I feel a tremendous amount of support from our department chair (Dr. Ken McGill), from my colleagues, and from the Dean of the College of Arts & Sciences (Dr. Ken Proctor), to continue doing research while teaching, and to maintain the collaborations that I developed in my previous stint as a postdoctoral scholar at UC Berkeley. There is the additional appeal in that I am really proud to see Georgia College listed in the author list among prestigious research laboratories such as Berkeley, Caltech, Columbia, Harvard, and NASA-Goddard. In the past two years, I have been invited to give talks at NASA and at the University of Rome, and each time the audience gets to see the Georgia College name and logo featured prominently on the title page, probably for the first time. While we are a public liberal arts university, it's clear that we are playing in the "big leagues." In a small way, this helps improve the reputation of Georgia College, and will hopefully make us more attractive to high school seniors and potential faculty from Georgia and beyond.

CHANDRA OBSERVATIONS OF EIGHT SOURCES DISCOVERED BY INTEGRAL

JOHN A. TOMSICK¹, ROMAN KRIVONOS², QINAN WANG¹, ARASH BODAGHEE³, SYLVAIN CHATY^{4,5}, FARID RAHOUI^{6,7}, JEROME RODRIGUEZ⁴, FRANCESCA M. FORNASINI^{1,8}

Accepted by ApJ

ABSTRACT

We report on 0.3–10 keV observations with the *Chandra X-ray Observatory* of eight hard X-ray sources discovered within 8° of the Galactic plane by the *INTEGRAL* satellite. The short (~5 ks) *Chandra* observations of the IGR source fields have yielded very likely identifications of X-ray counterparts for three of the IGR sources: IGR J14091–6108, IGR J18088–2741, and IGR J18381–0924. The first two have very hard spectra in the *Chandra* band that can be described by a power-law with photon indices of $\Gamma = 0.6 \pm 0.4$ and $-0.7^{+0.4}_{-0.3}$, respectively (90% confidence errors are given), and both have a unique near-IR counterpart consistent with the *Chandra* position. IGR J14091–6108 also displays a strong iron line and a relatively low X-ray luminosity, and we argue that the most likely source type is a Cataclysmic Variable (CV), although we do not completely rule out the possibility of a High Mass X-ray Binary. IGR J18088–2741 has an optical counterpart with a previously measured 6.84 hr periodicity, which may be the binary orbital period. We also detect five cycles of a possible 800–950 s period in the *Chandra* light curve, which may be the compact object spin period. We suggest that IGR J18088–2741 is also most likely a CV. For IGR J18381–0924, the spectrum is intrinsically softer with $\Gamma = 1.5^{+0.5}_{-0.4}$, and it is moderately absorbed, $N_{\text{H}} = (4 \pm 1) \times 10^{22} \text{ cm}^{-2}$. There are two near-IR sources consistent with the *Chandra* position, and they are both classified as galaxies, making it likely that IGR J18381–0924 is an Active Galactic Nucleus (AGN). For the other five IGR sources, we provide lists of nearby *Chandra* sources, which may be used along with further observations to identify the correct counterparts, and we discuss the implications of the low inferred *Chandra* count rates for these five sources.

Subject headings: galaxies: active — stars: white dwarfs — stars: neutron X-rays: galaxies — X-rays: stars — stars: individual (IGR J14091–6108, IGR J15335–5420, IGR J17164–3803, IGR J17174–2436, IGR J17306–2015, IGR J18088–2741, IGR J18381–0924, IGR J20107+4534)

1. INTRODUCTION

The *INTERNational Gamma-Ray Astrophysics Laboratory* (*INTEGRAL*) satellite (Winkler et al. 2003) has been surveying the sky in the hard X-ray/soft gamma-ray band since its launch in 2002. The Imager on-Board the *INTEGRAL* Satellite (IBIS; Ubertini et al. 2003) has detected large numbers of sources in the 20–100 keV band. The current version of the *INTEGRAL* General Reference Catalog⁹ includes 954 sources that have been detected by IBIS, and the majority of these are “IGR” sources, meaning that either they were discovered by *INTEGRAL*, or they were not known to produce hard X-ray emission prior to the *INTEGRAL* detection. The “*INTEGRAL* Sources” website¹⁰ lists over 550 IGR sources. The most recent published IBIS catalogs include Bird et al. (2010), which includes information on more than 700 sources (IGR and

non-IGR), and Krivonos et al. (2012), which lists 402 sources within 17.5° of the Galactic plane¹¹.

Thus, the IGR sources represent a large population of proven hard X-ray emitters, but, in most cases, more information is needed to determine their nature. The fact that these sources produce emission above 20 keV indicates that they are sites of particle acceleration or extreme heating, which leads to the production of non-thermal emission. Based on the source type identifications that have been obtained to date, Active Galactic Nuclei (AGN) are the most numerous group of IGR sources, but there are hundreds of Galactic sources as well, including Low Mass X-ray Binaries (LMXBs), High Mass X-ray Binaries (HMXBs), Cataclysmic Variables (CVs), and Pulsar Wind Nebulae (PWNe). *INTEGRAL* discoveries have increased the total number of known HMXBs from 65 to 96 and have multiplied the number of supergiant HMXBs almost threefold from 13 to 36 (Walter et al. 2015). Many of the IGR HMXBs belong to two new classes: the obscured HMXBs, where the compact object is enshrouded in the wind from the companion star (e.g., Matt & Guainazzi 2003; Filliatre & Chaty 2004; Walter et al. 2006); and the Supergiant Fast X-ray Transients (SFXTs; Negueruela et al. 2006; Smith et al. 2006; Pellizza et al. 2006; Sidoli et al. 2013; Romano et al. 2014). There are many other interesting individual Galactic objects such as the LMXB and transitional pulsar IGR J18245–2452 (Papitto et al. 2013), and the high velocity pulsar and PWN IGR J11014–6103 (Pavan et al. 2011; Tomsick et al. 2012b).

Observations with the *Chandra X-ray Observatory* are es-

¹ Space Sciences Laboratory, 7 Gauss Way, University of California, Berkeley, CA 94720-7450, USA

² Space Research Institute, Russian Academy of Sciences, Profsoyuznaya 84/32, 117997 Moscow, Russia

³ Georgia College & State University, CBX 82, Milledgeville, GA 31061, USA

⁴ Laboratoire AIM, UMR 7158 CEA/DSM-CNRS-Université Paris Diderot, IRFU/Sap, F-91191 Gif-sur-Yvette Cedex, France

⁵ Institut Universitaire de France, 103 Boulevard Saint-Michel, 75005 Paris, France

⁶ European Southern Observatory, Karl Schwarzschild-Strasse 2, 85748 Garching bei Munchen, Germany

⁷ Department of Astronomy, Harvard University, 60 Garden Street, Cambridge, MA 02138, USA

⁸ Astronomy Department, University of California, 601 Campbell Hall, Berkeley, CA 94720, USA

⁹ see <http://www.isdc.unige.ch/integral/catalog/39/catalog.html>

¹⁰ see <http://irfu.cea.fr/Sap/IGR-Sources/>

¹¹ see <http://hea.iki.rssi.ru/integral>

pecially useful for determining the nature of the IGR sources because *Chandra*'s superior angular resolution can improve the source localization from arcminutes (with *INTEGRAL*) to less than an arcsecond; thus, providing the opportunity to identify counterparts at other wavelengths, such as the optical or near-IR where all-sky images and catalogs are readily available. In addition, *Chandra*'s 0.3–10 keV coverage provides constraints on the soft X-ray spectrum, allowing for a determination of column densities, spectral slopes, and, in some cases, emission lines. We have been carrying out *Chandra* programs to follow up IGR sources in several previous *Chandra* observing cycles (Tomsick et al. 2006, 2008, 2009, 2012a; Bodaghee et al. 2012), and other groups also have similar programs (e.g., Fioocchi et al. 2010; Ratti et al. 2010; Paizis et al. 2011, 2012; Nowak et al. 2012; Karasev et al. 2012).

For the *Chandra* cycle 15 program, we selected IGR sources from the Krivonos et al. (2012) catalog. We excluded sources whose classification (e.g., AGN, HMXB, etc.) is known, leaving 34 unclassified sources of which 30 have an IGR designation. Next, we only considered sources situated within 8° of the Galactic Plane, which increases the probability of identifying new X-ray binaries, CVs, and PWNe. This selection also takes advantage of *Chandra*'s unparalleled X-ray positional accuracy, which we require to pinpoint an optical/IR counterpart in these crowded fields. After removing sources with existing soft X-ray coverage with *Chandra* and *XMM-Newton*, we were left with ten sources. We reported on the results of the cycle 15 *Chandra* observations for two of the sources (IGR J04059+5416 and IGR J08297–4250), concluding that they are AGN (Tomsick et al. 2015).

In this paper, we report on the results of the remaining eight observations. Section 2 provides a brief description of the *Chandra* observations and how the data were processed. In Section 3, we present results on *Chandra* source detection and photometry. For the three *Chandra* sources that we identify with IGR sources, we present *Chandra* and *INTEGRAL* energy spectra, *Chandra* light curves, and IR source identifications. A discussion of the nature of the three sources is included in Section 4, and conclusions are presented in Section 5. In addition, we include an Appendix with a full listing of the *Chandra* sources detected.

2. CHANDRA OBSERVATIONS AND DATA PROCESSING

Information about the eight *Chandra* observations, which occurred between late-2013 and early-2015, is given in Table 1. The integration time for each observation is ~ 5 ks, and we used the Advanced CCD Imaging Spectrometer (ACIS-I) instrument (Garmire et al. 2003). The pointing position was at the best known source position, and, in seven cases, this corresponds to the position measured by *INTEGRAL* (Krivonos et al. 2012). For IGR J14091–6108, a likely *Swift* counterpart has been reported (Landi et al. 2012), and we used the *Swift* position for the *Chandra* pointing. After obtaining the data from the *Chandra* X-ray Center, all of the *Chandra* data reduction in this work was done using the *Chandra* Interactive Analysis of Observations (CIAO) version 4.7 software and Calibration Data Base (CALDB) 4.6.7. We made new event lists using `chandra_repro` and used these event lists for the analysis described below.

3. ANALYSIS AND RESULTS

3.1. *Chandra* Source Detection and Photometry

For each of the eight observations, we inspected the full field of view (ACIS-I and ACIS-S) and used `wavdetect` (Freeman et al. 2002) to search for *Chandra* sources over ACIS-I, on which the *INTEGRAL* source position falls in each case. The accuracy of the *INTEGRAL* positions is $2'.1$ at 68% confidence (Krivonos et al. 2012), indicating that it is very likely that the true source position lies in the $16'.9$ -by- $16'.9$ ACIS-I field of view. In order to detect sources in both soft and hard bands, we divided events into a soft band with energy between 0.3 keV and 2 keV, and a hard band with energy between 2 keV and 10 keV. Before we ran `wavdetect`, we used `fluximage` and `mkpsfmap` to generate the exposure map and the point spread function (PSF) map in order to improve the accuracy of detection. A small number of sources with one or two counts was detected, and we discarded these. In total, we detected 115 sources in the ACIS-I fields of view, with the most and least crowded fields having 29 and 7 sources, respectively (see Table 1 for the totals in each field). Tables listing the basic information (position, counts detected, and hardness) for all 115 sources, as well as more details on how we obtained this information, are provided in the Appendix.

For all 115 sources, we performed photometry to determine the number of source counts in the 0.3–10 keV, 0.3–2 keV, and 2–10 keV bands. The size of the *Chandra* PSF changes significantly over the field of view, and we determined the off-axis angle for each source and then used the *Chandra* PSF Viewer¹² to determine the radius of the 90% encircled counts fraction at 3 keV for each source. For the photometry, we extracted counts from circular regions that were twice this radius, so that the extraction regions enclosed more than 99% of the counts. For each field, we identified a large source-free region, and used this region to estimate and then subtract the background contribution within each source extraction region. The results of the photometry are shown by plotting the hardness of each source, which is defined as $(C_2 - C_1)/(C_2 + C_1)$, where C_2 is the number of counts in the 2–10 keV band and C_1 is the number of counts in the 0.3–2 keV band, vs. the intensity, which is the number of counts in the 0.3–10 keV band (Figure 1).

Three sources stand out from the rest of the sources in the hardness-intensity diagram: CXOU J140846.0–610754 in the field of IGR J14091–6108; CXOU J180839.8–274131 in the field of IGR J18088–2741; and CXOU J183818.5–092552 in the field of IGR J18381–0924. CXOU J140846.0–610754 has 404.9 counts, a hardness of 0.56 ± 0.06 , and it is only $0'.45$ from the center of the error circle, which is well within the $1\text{-}\sigma$ *INTEGRAL* error circle. CXOU J180839.8–274131 has 229.9 counts and a hardness of 0.76 ± 0.09 . While it is $4'.5$ from the center of the *INTEGRAL* error circle, it is an order of magnitude brighter than any source that is closer to the *INTEGRAL* position, and it is harder than any other source in the field with more than 10 counts. CXOU J183818.5–092552 has 302.7 counts, a hardness of 0.73 ± 0.08 , and it is $2'.8$ from the best *INTEGRAL* position, which is within the $2\text{-}\sigma$ error circle. Thus, these three *Chandra* sources are very likely counterparts to their respective *INTEGRAL* sources, and in the following sections, we report on the details of these three sources, including their *Chandra* and *INTEGRAL* energy spectra, their *Chandra* light curves, and whether their *Chandra* positions allow us to identify counterparts at other wavelengths.

¹² see http://cxc.cfa.harvard.edu/cgi-bin/prop_viewer/build_viewer.cgi?psf

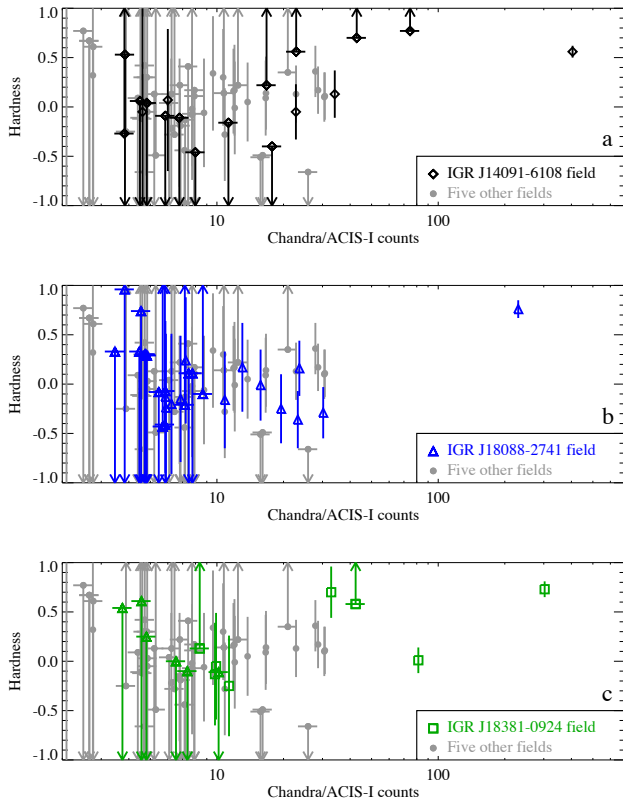


FIG. 1.— Hardness-intensity diagrams, where the intensity is given as the number of ACIS-I counts in the 0.3–10 keV energy band. The hardness is given by $(C_2 - C_1)/(C_2 + C_1)$, where C_2 is the number of counts in the 2–10 keV band and C_1 is the number of counts in the 0.3–2 keV band. The black diamonds in (a), blue triangles in (b), and green squares in (c) correspond to sources in the IGR J14091–6108, IGR J18088–2741, and IGR J18381–0924 fields, respectively. The points in the other fields are shown in grey.

For the other five IGR fields, some of the *Chandra* sources detected are potential counterparts. However, in those cases, there is a significant probability that the association is spurious. We first focus on CXOU J140846.0–610754, CXOU J180839.8–274131, and CXOU J183818.5–092552 and then consider the upper limits for the other five fields.

3.2. *Chandra* and *INTEGRAL* Energy Spectra

For all three sources, we produced *Chandra* and *INTEGRAL* energy spectra. For *Chandra*, we used circular source extraction regions with the same radii used for the photometry: $2.''5$ for CXOU J140846.0–610754 and CXOU J183818.5–092552; and $5.''0$ for CXOU J180839.8–274131. However, as CXOU J140846.0–610754 was on-axis with an ACIS count rate of 0.08 c/s, the spectrum can be distorted by photon pile-up. Using the Portable, Interactive Multi-Mission Simulator (PIMMS)¹³, we estimate the pile-up level at 10%. Thus, for CXOU J140846.0–610754, we used an annular source region with an inner radius of $0.''5$ and an outer radius of $2.''5$. In all three cases, a background spectrum was obtained from a source-free region close to the source. The source and background spectra and the response matrices were produced with the `specextract` script. We included the 0.3–10 keV energy range, and rebinned each spectrum with the criterion that the source be detected at a signal-to-noise (S/N) level of 3 or greater in each bin (except for the

highest energy bin).

The *INTEGRAL* energy spectra were produced using publicly available data from the IBIS/ISGRI instrument over a time period from 2003 to the end of 2014, yielding effective exposure times¹⁴ of 5.0, 23.6, and 8.0 Ms for IGR J14091–6108, IGR J18088–2741, and IGR J18381–0924, respectively. We reduced the IBIS/ISGRI data with the *INTEGRAL* data analysis package developed at IKI RAN¹⁵ (see, e.g., Churazov et al. 2005; Krivonos et al. 2010; Churazov et al. 2014, and references therein) using the most up-to-date gain calibration for ISGRI (Caballero et al. 2013) available through the Offline Scientific Analysis (OSA) version 10.1, provided by the ISDC¹⁶. To take the ongoing detector degradation and loss of sensitivity at low energies (Caballero et al. 2013) into account, we adjusted the flux scale in each IBIS sky image using the flux of the Crab nebula measured in the observation that is closest in time to when the data for the sky image was obtained. This results in a smooth recalibration of the ancillary response function over the span of the observations from 2003 to 2014. We previously used the same procedure for a subset of the data as described in Krivonos et al. (2012). The energy spectra were obtained from sky mosaic images in four energy bands: 17–26 keV, 26–38 keV, 38–57 keV, and 57–86 keV. The corresponding energy response matrices were produced using Crab nebula observations, assuming a spectral shape of $10(E/1\text{keV})^{-2.1}$ photons $\text{cm}^{-2} \text{s}^{-1} \text{keV}^{-1}$.

For each source, we initially fit the *Chandra* and *INTEGRAL* spectra separately. The S/N = 3 binning for *Chandra* results in about 10 counts per bin, which is close to the Poisson regime. Thus, for the *Chandra*-only fits, the fitting was done by minimizing the Cash statistic (Cash 1979). Due to the high *INTEGRAL* background, we performed the fits to the *INTEGRAL* spectra and the fits to the joint *Chandra*+*INTEGRAL* spectra by minimizing the χ^2 statistic. The fit parameters and χ^2 values are reported in Table 2, and the folded and unfolded spectra are shown in Figure 2. The errors on the spectral parameters in the table as well as values quoted in this section are at the 90% confidence level.

For CXOU J140846.0–610754, an absorbed power-law model to the *Chandra* spectrum leaves residuals in the iron line region, and we find that the addition of a Gaussian iron line at $E_{\text{line}} = 6.6 \pm 0.2$ keV with a width of $\sigma_{\text{line}} < 0.6$ keV leads to an improvement in the Cash statistic from 32.6 for 22 degrees of freedom (dof) to 19.4 for 19 dof. We used `simfittest` to produce 10,000 simulated *Chandra* spectra with the absorbed power-law model, fit the spectra with and without the addition of a Gaussian with E_{line} between 6.4 and 7.1 keV and $\sigma_{\text{line}} < 0.6$ keV, and recorded the Cash statistics for all the fits. Out of the 10,000 spectra, an improvement in the Cash statistic of 13.2 (=32.6–19.4) or more was seen eight times, corresponding to a detection significance of $3.35\text{-}\sigma$. Thus, we included this line, which has an equivalent width (EW) of $1.2^{+0.9}_{-0.7}$ keV, in our subsequent fits. Some weak residuals remain near 4.0 keV, but adding a Gaussian leads to only a small reduction in the Cash statistic to 15.0 for 16 dof. Using `simfittest`, there is a 15% probability of obtaining such an improvement by chance, indicating that the 4 keV feature is not statistically significant.

¹⁴ These correspond to dead-time corrected exposure times calculated for the fully coded field of view.

¹⁵ Space Research Institute of the Russian Academy of Sciences, Moscow, Russia

¹⁶ *INTEGRAL* Data Center for Astrophysics, <http://www.isdc.unige.ch/>

¹³ see <http://asc.harvard.edu/toolkit/pimms.jsp>

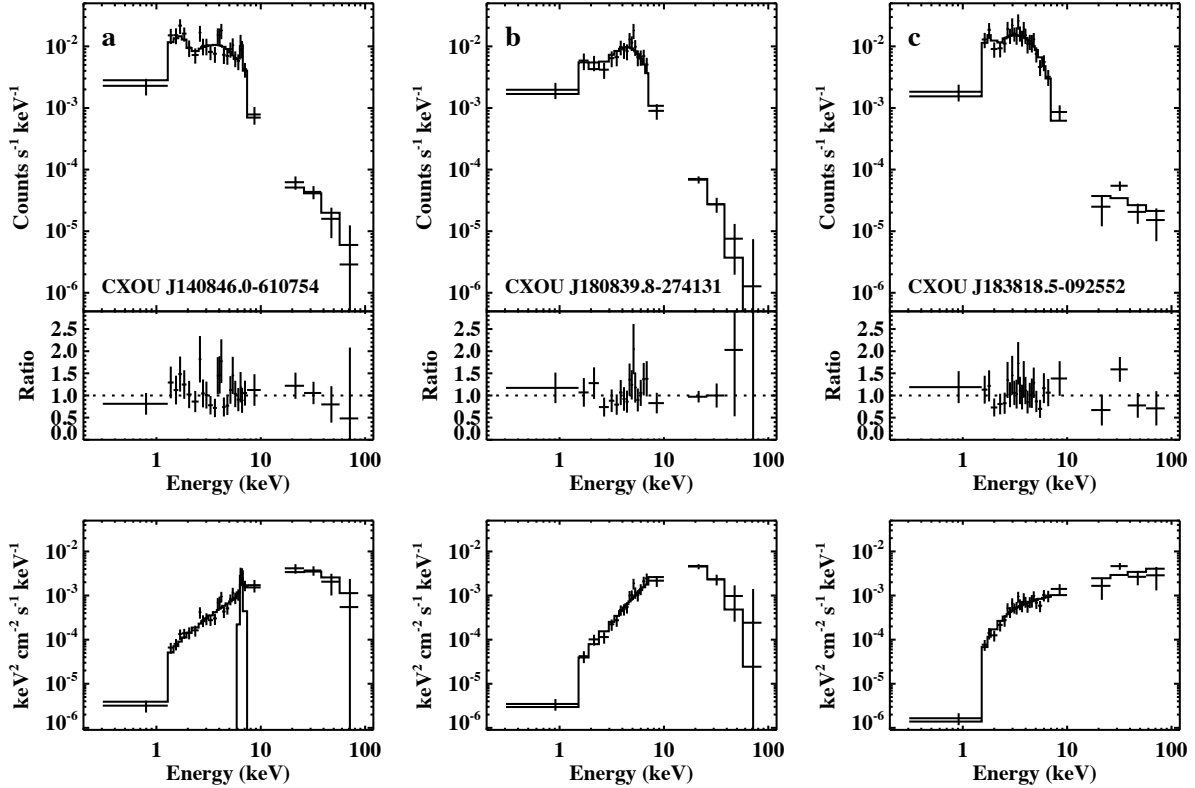


FIG. 2.— *Chandra* and *INTEGRAL* energy spectra for (a) CXOU J140846.0–610754/*IGR* J14091–6108, (b) CXOU J180839.8–274131/*IGR* J18088–2741, and (c) CXOU J183818.5–092552/*IGR* J18381–0924. For each source, the top panel is the counts “folded” spectrum, the middle panel is the data-to-model ratio, and the bottom panel is the “unfolded” spectrum in flux units. From left to right, the models are: `tbabs*(gaussian+cutoffpl)`, `tbabs*cutoffpl`, and `tbabs*powerlaw`.

As reported in Table 2, with *Chandra*, we measure a column density of $(1.0^{+0.7}_{-0.6}) \times 10^{22} \text{ cm}^{-2}$ and a power-law photon index of $\Gamma = 0.6 \pm 0.4$ for CXOU J140846.0–610754. This indicates that the spectrum in the 0.3–10 keV bandpass is even harder than the previously reported *Swift* value of $\Gamma \sim 1.3$ (Landi et al. 2012). While the photon index measured by *Chandra* is very hard, a power-law fit to the *INTEGRAL* spectrum yields a much softer photon index of $\Gamma = 2.9^{+1.0}_{-0.7}$, indicating that there must be a break or a cutoff between the *Chandra* and *INTEGRAL* spectra. To fit the *Chandra* and *INTEGRAL* spectra together, we used the model `cutoffpl`, which is a power-law multiplied by an exponential, $e^{-E/E_{\text{fold}}}$. As the *Chandra* and *INTEGRAL* observations were made at different times, and the source might be variable, we originally allowed for a normalization difference between the two spectra, obtaining $N_{\text{INTEGRAL}}/N_{\text{Chandra}} = 1.8^{+2.8}_{-1.1}$. Table 2 shows that the changes in the parameters are not significant when we fix the normalization ratio to 1.0. With the ratio fixed to 1.0, we find $\Gamma = 0.1^{+0.4}_{-0.5}$, and $E_{\text{fold}} = 14^{+11}_{-5} \text{ keV}$, and the folded and unfolded spectra are shown in Figure 2. For these fits, we restricted σ_{line} to be less than 0.6 keV.

We performed similar spectral fits for CXOU J180839.8–274131, and the results are reported in Table 2. While the *Chandra* power-law index is $\Gamma = -0.7^{+0.4}_{-0.3}$, fitting the *INTEGRAL* spectrum separately gives $\Gamma = 3.8^{+1.2}_{-0.8}$. As the *Chandra* source is 4.8′ off-axis, and the ACIS count rate is lower than for CXOU J140846.0–610754, 0.05 c/s, photon pile-up is not a concern, indicating that the spectrum is very hard in the 0.3–10 keV band and has a strong cutoff at higher

energies. Fitting the *Chandra* and *INTEGRAL* spectra with a `cutoffpl` model and the normalization ratio free gives $N_{\text{INTEGRAL}}/N_{\text{Chandra}} = 0.8^{+0.6}_{-0.4}$. With the normalization fixed to 1.0, we find $\Gamma = -1.5^{+0.4}_{-0.2}$ and $E_{\text{fold}} = 4.8^{+1.1}_{-0.8} \text{ keV}$. We also find that the spectrum is not highly absorbed with $N_{\text{H}} < 7 \times 10^{21} \text{ cm}^{-2}$.

The CXOU J183818.5–092552 spectrum is different from the previous two sources in that the power-law slopes measured by *Chandra* ($\Gamma = 1.5^{+0.5}_{-0.4}$) and *INTEGRAL* ($\Gamma = 1.8 \pm 0.6$) are consistent with each other. Fitting the *Chandra* and *INTEGRAL* spectra together gives a normalization ratio of $N_{\text{INTEGRAL}}/N_{\text{Chandra}} = 1.6^{+2.1}_{-0.9}$. With the normalization ratio fixed to 1.0, we find $\Gamma = 1.4 \pm 0.1$, and no cutoff is required (see Figure 2). This source also differs from the other two in that it is moderately absorbed with $N_{\text{H}} = (3.8^{+0.9}_{-0.7}) \times 10^{22} \text{ cm}^{-2}$.

3.3. *Chandra* Light Curves

For the three *Chandra* sources associated with *INTEGRAL* sources, we made 0.3–10 keV light curves with 200 s time bins (Figure 3). We performed two tests to check the sources for variability: a Kolmogorov-Smirnov (KS) test and a χ^2 test. The KS test is good for low count rates because it compares the event arrival times to a constant reference distribution and does not require the data to be binned. While the KS test is sensitive to random variations, like bursts, it is not as good at finding periodic variability. Thus, we also perform a χ^2 test by fitting a constant function to the binned light curves. Although this test is problematic in low count situations where the time bins follow a Poisson rather than a Gaussian distribu-

tion, in our case, we typically have 10–20 counts per bin, and χ^2 statistics are a good approximation.

For CXOU J140846.0–610754, the KS test measures only a 1.2% probability that the source is constant. The χ^2 test also indicates that the source is very likely to be variable as the reduced χ^2 is 2.1 for 25 dof. Although the light curve for CXOU J180839.8–274131 appears to be even more variable, the KS test probability is higher, 2.2%. However, the fit to the binned light curve with a constant gives a reduced χ^2 of 4.1 for 25 dof, confirming that there is a high level of variability. For the third source, CXOU J183818.5–092552, the KS test probability is 8.5%, which does not indicate significant variability. This is confirmed by the second test since we find a reduced χ^2 of 1.0 for 25 dof.

As CXOU J140846.0–610754 and CXOU J180839.8–274131 show evidence for variability, we performed light curve folding on many trial periods to determine if there is evidence for periodic variability. For each trial period, the χ^2 for a fit with a constant function is calculated, and a large value of χ^2 can indicate periodic variability. Although the former source did not show any candidate periods, CXOU J180839.8–274131 exhibits a broad and strong χ^2 peak between 800 s and 950 s (Figure 4). Although we note that the entire duration of our observation only covers five periods of the candidate oscillation, the folded light curve (Figure 4) shows that if the signal is real, it has a very large amplitude (defined as maximum minus minimum divided by maximum plus minimum) of $\approx 80\%$.

3.4. IR Identifications

The fields of CXOU J140846.0–610754 and CXOU J180839.8–274131 were covered by the VISTA Variables in the Via Lactea (VVV) survey (Minniti et al. 2010), and the field of CXOU J183818.5–092552 was covered by the UKIRT Infrared Deep Sky Survey (UKIDSS) survey (Lawrence et al. 2007). We used the images from these surveys to identify possible near-IR counterparts. Figure 5a shows the K_s -band images with the *Chandra* positions. For CXOU J140846.0–610754, we confirm the association with VISTA source 515845105705 (VVV J140845.99–610754.1) reported in Tomsick et al. (2014), and we provide the VISTA Z -, Y -, J -, H -, and K_s -magnitudes in Table 3. As reported in Tomsick et al. (2014), this source is also listed in the *Spitzer*/GLIMPSE catalog as G312.1289+00.3516.

CXOU J180839.8–274131 is within $0.''41$ of the VISTA source VVV J180839.77–274131.7, and the K_s -band image shown in Figure 5b indicates that this is the only possible counterpart in the VVV images. The VISTA magnitudes for this counterpart are given in Table 3. We also used the VizieR website to search for possible counterparts of this source in other catalogs, and we find a match with OGLE-BLG-RRLYR-14363, which is source number 14363 in the Optical Gravitational Lensing Experiment (OGLE-III) Catalog of Variable Stars (Soszyński et al. 2011). The OGLE-III catalog indicates that the star varies periodically in the I -band with a period of $0.28494563 \pm 0.00000062$ days. We obtained the I -band measurements folded on this period, and the folded light curve is shown in Figure 6. While Soszyński et al. (2011) classify this source as an RR Lyrae star, a remark in the catalog indicates that the classification is uncertain, and we discuss this further in Section 4.

The position of CXOU J183818.5–092552 is consistent with two near-IR sources from the UKIDSS Galactic Plane

Survey (UGPS): UGPS J183818.59–092551.8 at an angular distance of $0.''47$ and UGPS J183818.58–092552.9 at an angular distance of $0.''73$. Based on their spatial profiles in the near-IR, both sources are classified as galaxies in the UGPS catalog. The probability that the sources are stellar (i.e., not extended) is $<1\%$ for UGPS J183818.59–092551.8 and 5% for UGPS J183818.58–092552.9. In the UGPS catalog, the magnitudes listed for these sources do not appear to match the image shown in Figure 5c. Specifically, in the images, the source to the south (UGPS J183818.58–092552.9) is clearly the brighter of the two, but the catalog lists it as $K = 13.040 \pm 0.003$ (UKIDSS data release 10) compared to $K = 12.822 \pm 0.002$ for the northern source (UGPS J183818.59–092551.8). The UGPS survey has K -band images taken on 2005 September 28 and nearly three years later on 2008 May 31, and we examined both of the images to look for source variability; however, there are no discernible differences between the two images. The UKIDSS photometry is carried out using $2''$ radius extraction regions, and we suspect that this does not yield correct results for these two sources, which have a separation of $\approx 1''$. We note that UGPS J183818.59–092551.8 appears to be approximately the same brightness as the two sources to the south of the blended pair, and these are both listed as having $K = 14.2$ in the UKIDSS catalog. Thus, we conclude that the true brightnesses of UGPS J183818.59–092551.8 and UGPS J183818.58–092552.9 are likely $K \approx 14$ and $K \approx 13$, respectively (Table 3). The *Chandra* position is compatible with both sources, and both remain as candidate counterparts to CXOU J183818.5–092552.

3.5. Upper Limits for the Other Five IGR Sources

For IGR J15335–5420, IGR J17164–3803, IGR J17174–2436, IGR J17306–2015, and IGR J20107+4534, none of the *Chandra* sources listed in the table in the Appendix are clear counterparts, but these sources are possible counterparts. We identified the highest count rate source in each field and took this as the upper limit on the *Chandra* count rate. Then, extrapolating using a power-law model and the ACIS response matrix, we compared the *Chandra* count rate upper limit to the actual flux measurement for each of the five sources reported in Krivonos et al. (2012). There are at least three reasons why the sources might be relatively faint in the *Chandra* energy band: 1. the source may be intrinsically hard; 2. the source may be highly absorbed; or 3. the source may be variable (and any combination of these three is also possible). Table 4 lists the *Chandra* count rate upper limit and the 17–60 keV flux measured by *INTEGRAL* (Krivonos et al. 2012). Then, we performed calculations to consider the three effects mentioned above. In the first calculation, we determined the values of Γ required to produce the low *Chandra* count rate if the sources are unabsorbed. Second, we assumed a value of $\Gamma = 2.1$, which is used in Krivonos et al. (2012) to determine the *INTEGRAL* fluxes, and calculated the column densities that would lead to the *Chandra* count rate upper limits. Finally, we assumed $\Gamma = 1$ and $N_{\text{H}} = 5 \times 10^{22} \text{ cm}^{-2}$ and calculated the *Chandra* count rates that would be predicted for the *INTEGRAL* fluxes. In Table 4, we report the upper limits on Γ (first calculation), N_{H} (second calculation), and the variability factor, which is the ratio of the predicted count rate to the upper limit on the count rate.

4. DISCUSSION

The result of the *Chandra* observations is that we have identified X-ray counterparts to IGR J14091–6108, IGR J18088–

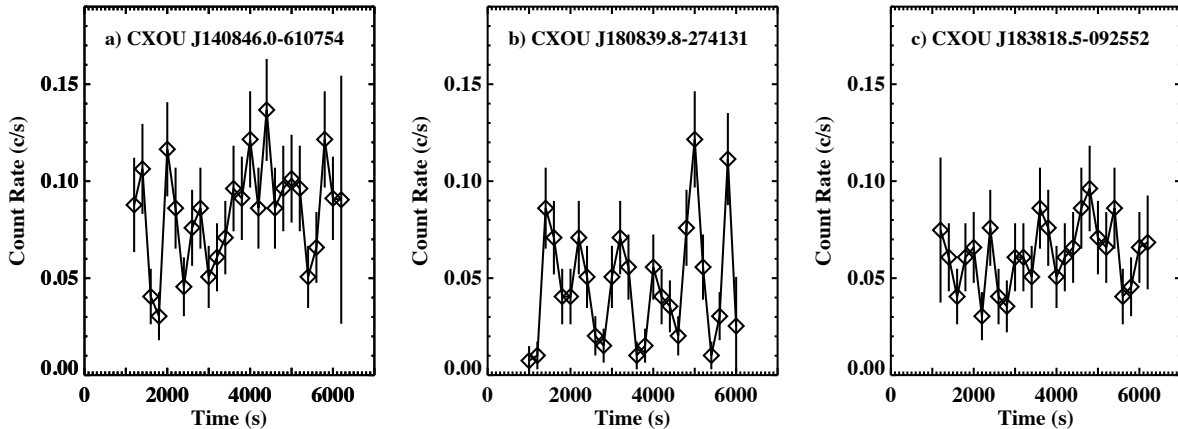


FIG. 3.— *Chandra* 0.3–10 keV light curves with 200 s time bins for (a) CXOU J140846.0–610754, (b) CXOU J180839.8–274131, and (c) CXOU J183818.5–092552.

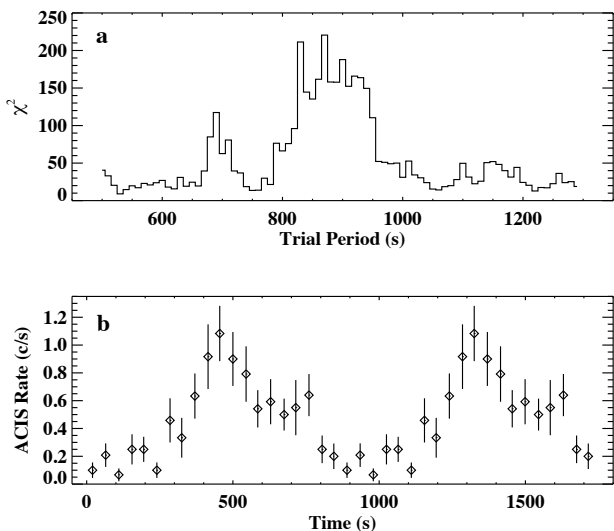


FIG. 4.— Results of folding the *Chandra* light curve for CXOU J180839.8–274131. (a) The resulting χ^2 value when fitting the light curve with a constant after folding on trial periods between 500 s and 1300 s. (b) The folded light curve for a period of 870 s, which is the trial period that gave the maximum χ^2 .

2741, and IGR J18381–0924, and henceforth, we will use the IGR names to refer to these *Chandra*/*INTEGRAL* sources. For IGR J14091–6108 and IGR J18088–2741, the *Chandra* positions provide unique near-IR identifications, and for IGR J18381–0924, there are two near-IR sources compatible with the *Chandra* position. Here, we discuss the nature of the three sources and then the implications of the parameter limits on the other five sources.

4.1. IGR J14091–6108

There is clear evidence that IGR J14091–6108 is in our Galaxy. The iron line detected in its spectrum is not redshifted, and the low measured column density indicates that it is relatively nearby: the Galactic column density along this line of sight ($l = 312.13^\circ$, $b = +0.35^\circ$) is $5.4 \times 10^{22} \text{ cm}^{-2}$, but we measure an upper limit of $<1.7 \times 10^{22} \text{ cm}^{-2}$. Although we do not know its intrinsic near-IR spectral shape, the fact that the VISTA magnitudes do not indicate strong reddening

is also consistent with a relatively small distance, probably less than a few kpc.

The hard X-ray spectrum ($\Gamma = 0.6 \pm 0.4$) favors the possibilities that either the compact object is a magnetic white dwarf in a CV (Revnivtsev et al. 2008) or that it is an accreting neutron star with a high, $\sim 10^{12}$ G, magnetic field (Coburn et al. 2002). Nearly all of the accreting black holes that we know of have photon indices softer than $\Gamma \approx 1.2$ – 1.4 , even in their hard state (McClintock & Remillard 2006), and neutron stars with weaker magnetic fields have even softer spectra. An isolated neutron star, such as a magnetar, could have a hard spectrum, but the brightness of IGR J14091–6108 in the near-IR requires a stellar companion. A CV with a spectrum as hard as we observe would almost certainly belong to the class of Intermediate Polars (IPs, Scaringi et al. 2010), where the white dwarf magnetic field is strong enough to truncate the accretion disk and funnel material onto the magnetic poles. In the neutron star case, nearly all high magnetic field neutron stars in binary systems are found in HMXBs. Thus, it is likely that IGR J14091–6108 is either a CV/IP or a neutron star HMXB.

The source’s X-ray luminosity could provide a way to distinguish between the different hypotheses because CV/IPs are not known to exceed values of $\sim 10^{35} \text{ erg s}^{-1}$. With the 0.3–10 keV unabsorbed flux being $(2.2_{-0.3}^{+0.4}) \times 10^{-12} \text{ erg cm}^{-2} \text{ s}^{-1}$, the luminosity is $3 \times 10^{32} d_1^2 \text{ erg s}^{-1}$, where d_1 is the distance in kpc, which leaves both possibilities open since neutron star HMXBs can have low luminosities. The CV hypothesis is somewhat favored by the fact that neutron star HMXBs typically have iron line equivalent widths of 200 eV or less (Giménez-García et al. 2015) while we measure $EW = 1.2_{-0.7}^{+0.9}$ keV. Although there are some HMXBs with unusually high iron line strengths (Barragán et al. 2009; Giménez-García et al. 2015), these only occur in cases where the continuum is absorbed by material intrinsic to the system (e.g., a stellar wind), but the low N_{H} for IGR J14091–6108 makes this possibility unlikely. While an EW of 1.2 keV is also somewhat high for a CV, values in excess of 400 eV (combining all iron ionization states) are not unusual (Hellier & Mukai 2004). An even higher equivalent width for the iron lines was reported for a combined spectrum consisting of *Chandra* sources in the Galactic Center region (Muno et al. 2004), and those spectra also show evidence for emission lines from argon and calcium in the 3–

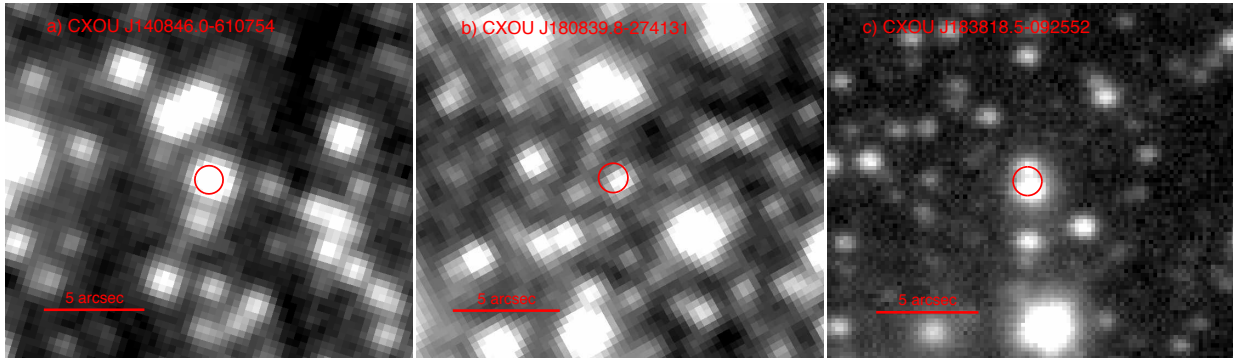


FIG. 5.— (a) K_s -band image of CXOU J140846.0–610754 from VISTA/VVV, (b) K_s -band image of CXOU J180839.8–274131 from VISTA/VVV, and (c) K -band image of CXOU J183818.5–092552 from UKIDSS. The *Chandra* error circle is shown.

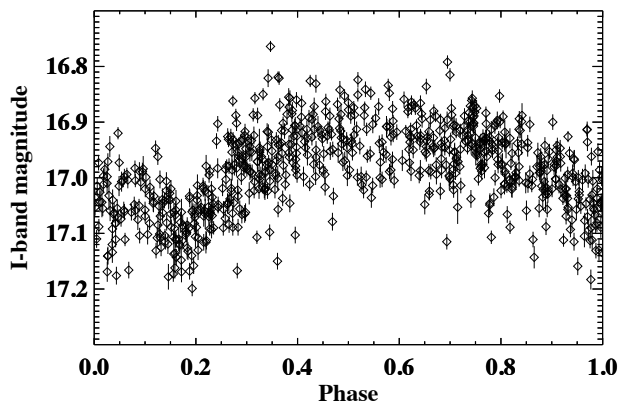


FIG. 6.— OGLE I -band light curve for VVV J180839.77–274131.7 after folding on the 0.28494563 day period listed in the OGLE-III Catalog of Variable Stars (Soszyński et al. 2011).

4 keV range. As discussed in section 3.2, the IGR J14091–6108 spectrum shows positive residuals at 4 keV, but they are not statistically significant. Munro et al. (2004) interpret the Galactic Center point source spectrum as being due to a thermal plasma model, and they suggest that the emission is from a population of CV/IPs.

4.2. IGR J18088–2741

A key piece of evidence that sheds light on the nature of IGR J18088–2741 is its identification with OGLE-BLG-RRLYR-14363, which has a 6.84 hr optical period. Although it is contained in a catalog of RR Lyrae stars (Soszyński et al. 2011), which produce periodic optical variations due to stellar pulsations, the fact that we detect this source with such a hard X-ray spectrum ($\Gamma = -0.7^{+0.4}_{-0.3}$) eliminates the possibility that the emission is coming from an isolated star. The combination of the hard spectrum and the optical periodicity strongly suggests that we are seeing a binary system with a compact object, but the origin of the periodicity and the type of compact object are uncertain. In many accreting systems, an optical modulation is seen at the orbital period of the system due to the heating of one side of the optical companion. However, such light curves are often approximately sinusoidal, and the fact that the IGR J18088–2741 optical light curve is more complex (see Figure 6) may indicate that we are also seeing light from the accretion disk. We also considered the possibility that we are seeing the superhump period, which is related to tidal stresses in the accretion disks of CVs, but these are

much more common for CVs with orbital periods less than a few hours (Patterson et al. 2005).

Similarly to IGR J14091–6108, the very hard X-ray spectrum of IGR J18088–2741 favors the possibilities that either the source is a CV/IP or that it is a highly magnetized neutron star in an X-ray binary. Although the 800–950 s X-ray period needs to be confirmed with a longer observation, by itself, such a period does not immediately distinguish between the CV/IP and X-ray binary possibilities. However, the X-ray binary hypothesis is challenged by the fact that such slow rotators are only common in HMXBs, while, if the 6.84 hr period is orbital, then this would be extremely short for an HMXB, where periods of days to weeks, or even months, are typical.

Given that its 0.3–10 keV unabsorbed flux is $3 \times 10^{-12} \text{ erg cm}^{-2} \text{ s}^{-1}$, this source would need to lie at a distance in excess of 15 kpc for its luminosity to challenge the CV/IP limit of $\sim 10^{35} \text{ erg s}^{-1}$. As the Galactic column density is $3 \times 10^{21} \text{ cm}^{-2}$ along this line of sight ($l = 3.65^\circ$, $b = -3.84^\circ$), the X-ray measured N_{H} (see Table 2) does not provide any indication of the distance. However, the fact that the optical extinction is low (see Table 3) favors a much smaller distance than 15 kpc, and with the luminosity being $4 \times 10^{32} d_1^2 \text{ erg s}^{-1}$, it is clear that this constraint does not rule out either possibility.

4.3. IGR J18381–0924

The X-ray spectrum of IGR J18381–0924 is significantly different from the other two sources. The power-law is consistent with being softer, $\Gamma = 1.5^{+0.5}_{-0.4}$ (for the *Chandra*-only fit), and there is no evidence for a cutoff up to 86 keV. Also, the spectrum is absorbed, and the measured $N_{\text{H}} = (4 \pm 1) \times 10^{22} \text{ cm}^{-2}$ is marginally higher than the Galactic column density along this line of sight ($l = 23.05^\circ$, $b = -1.36^\circ$) of $2.1 \times 10^{22} \text{ cm}^{-2}$. Based on just the X-ray spectrum, the source could be Galactic or extragalactic: if it is Galactic, then an accreting black hole in the hard state is a possibility; and, if it is extragalactic, then its properties are consistent with those of AGN. Both types of sources might have radio counterparts, but there is no radio counterpart listed in the NRAO VLA Sky Survey (NVSS, Condon et al. 1998) even though this area of the sky was covered. The interpretation of this source as being Galactic starts to become problematic when one considers the lack of X-ray variability on long and short time scales since most Galactic black holes are X-ray transients. Even stronger evidence in favor of an extragalactic nature comes from the fact that the two possible near-IR counterparts are identified as galaxies. Thus, we conclude that IGR J18381–0924 is proba-

bly an AGN.

4.4. Implications of the Upper Limits for the Other Five Fields

For the sources without clear *Chandra* counterparts (IGR J15335–5420, IGR J17164–3803, IGR J17174–2436, IGR J17306–2015, and IGR J20107+4534), Table 4 shows that the sources need to be extremely hard or highly variable in order to explain the *Chandra* upper limits. Values of $\Gamma = -1.2$ to -1.5 may be possible for some types of Galactic sources (e.g., IGR J18088–2741), but $\Gamma = -2.9$ is too hard to be realistic. Explaining the low *Chandra* count rates by high column densities requires value of N_{H} of $\sim 2 \times 10^{24} \text{ cm}^{-2}$. Such values occur very rarely in Galactic sources but have been seen for the most extreme obscured HMXB (Matt & Guainazzi 2003; Barragán et al. 2009). Such column densities occur relatively often for Seyfert 2 AGN (Brightman et al. 2015, and references therein), and we consider this a possibility for the nature of some of these sources. On the other hand, the low *Chandra* count rates can be explained by source variability with factors of > 11 –60. Such variability is possible for many types of Galactic sources. The observations are consistent with either long-term (years to decades) or short-term (hours) variability.

5. CONCLUSIONS AND FUTURE WORK

We conclude that IGR J14091–6108 and IGR J18088–2741 may be either CVs or HMXBs but that a CV is favored for the former source by the strong iron line, and a CV is strongly favored in the latter source if the 6.84 hr optical periodicity is the orbital period of the system. If the CV nature is confirmed by optical or near-IR spectroscopy, then these sources would join a group of 26 IGR CVs. An AGN nature is most likely for IGR J18381–0924. Follow-up optical or IR spectroscopy of the two candidate near-IR counterparts, which are both identified as galaxies in the UGPS catalog, is required to confirm that one or both of the counterparts are AGN. For the other

five IGR sources, the fact that we were not able to definitively determine a unique counterpart using the *Chandra* observations may indicate that these IGR sources are transient, highly variable, or that their spectra are extremely hard (either due to absorption or intrinsic spectral shape). Further observations of the sources listed in the Appendix may still provide a determination of the correct counterpart and the nature of these sources.

JAT and QW acknowledge partial support from the National Aeronautics and Space Administration (NASA) through *Chandra* Award Number GO4-15044X issued by the *Chandra* X-ray Observatory Center, which is operated by the Smithsonian Astrophysical Observatory under NASA contract NAS8-03060. RK acknowledges support from Russian Science Foundation (grant 14-22-00271). This work included observations with *INTEGRAL*, an ESA project with instruments and the science data center funded by ESA member states (especially the PI countries: Denmark, France, Germany, Italy, Switzerland, Spain), and Poland, and with the participation of Russia and the USA. This research has made use of the IGR Sources page maintained by J. Rodriguez and A. Bodaghee (<http://irfu.cea.fr/Sap/IGR-Sources>), the Vizier catalog access tool and the SIMBAD database, which are both operated at CDS, Strasbourg, France. This work is based in part on data obtained as part of the UKIRT Infrared Deep Sky Survey and also on data products from the VVV Survey observations made with the VISTA telescope at the ESO Paranal Observatory under program ID 179.B-2002. This publication makes use of data products from the Two Micron All Sky Survey, which is a joint project of the University of Massachusetts and the Infrared Processing and Analysis Center/California Institute of Technology, funded by NASA and the National Science Foundation. We acknowledge suggestions from an anonymous referee, which led to improvements in the manuscript.

APPENDIX

Section 3.1 describes how we used `wavdetect` to find 115 *Chandra* sources in the eight ACIS-I fields. A full source lists is provided in Table 5, and here we provide a more thorough explanation of how the values in those tables were derived. The sources are listed in order of how far they lie from the centers of each of the *INTEGRAL* error circles, and this angle (θ), in arcminutes, is given in the tables.

To determine the source positions, we started with the values provided by `wavdetect`. In order to reduce the systematic uncertainties due to the absolute *Chandra* pointing, we looked for matches to the *Chandra* sources in near-IR catalogs. We used the VISTA Variables in the Via Lactea (VVV) near-IR catalog (Minuti et al. 2010) for sources in the IGR J14091–6108, IGR J15335–5420, IGR J17164–3803, and IGR J18088–2741 fields. Due to the incomplete sky coverage of the VVV catalog, counterparts for other fields were not found in VVV. Thus, for IGR J17174–2436 and IGR J18381–0924, we searched the UKIRT Infrared Deep Sky Survey (UKIDSS) catalog (Lawrence et al. 2007), and for IGR J17306–2015 and IGR J20107+4534, we searched the 2 Micron All Sky Survey (2MASS) catalog (Cutri et al. 2003). For each field, we compiled a list of potential near-IR counterparts, and ran `wcs_match` to compare the *Chandra* and near-IR lists, determine likely matches, and calculate the astrometric correction. When we ran `wcs_match`, we used the “residlim” parameter to only include sources for which the *Chandra* and near-IR positions agree to better than $1''$ in order to discard unlikely matches as well as many of the *Chandra* sources with larger statistical position errors. We only found one match in the IGR J17174–2436, two matches in the IGR J17306–2015 field, and three matches in the IGR J18381–0924 field, which are not enough to calculate a reliable position shift. For the other five fields, we found between 5 and 15 matches, and the number of matches for each field is given in Table 6. Although `wcs_match` can consider both linear translations and coordinate rotations to optimize source matches, we restricted the shifts to linear translations since there are three fields where we only have five matches. The shifts determined by `wcs_match` are given in Table 6. We used `wcs_update` to apply these shifts to the positions reported in Table 5.

The position uncertainties have statistical and systematic contributions. Since the *Chandra* PSF becomes significantly larger for off-axis angles, the statistical uncertainty depends on the number of counts detected for each source as well as its off-axis angle. We used Equation 5 from Hong et al. (2005) to calculate the statistical uncertainty. Although this equation gives a 95% confidence error circle radius (2σ), we reduced the radius to 90% confidence (1.7σ) by multiplying by a factor of $1.7/2.0$. For the systematic contribution, we assumed a 90% confidence error of $0.''64$ (Weisskopf 2005). While this is an overestimate for the

fields where we shifted coordinates, we could not determine how much these shifts decrease the systematic position uncertainty due to the relatively small number of X-ray/near-IR matches. The total position uncertainty quoted in the tables is the value obtained by adding the statistical and systematic values in quadrature.

REFERENCES

- Barragán, L., Wilms, J., Pottschmidt, K., et al. 2009, *A&A*, 508, 1275
- Bird, A. J., Bazzano, A., Bassani, L., et al. 2010, *ApJS*, 186, 1
- Bodaghee, A., Rahoui, F., Tomsick, J. A., & Rodriguez, J. 2012, *ApJ*, 751, 113
- Brightman, M., Baloković, M., Stern, D., et al. 2015, *ApJ*, 805, 41
- Caballero, I., Zurita Heras, J. A., Mattana, F., et al. 2013, arXiv:1304.1349
- Cash, W., 1979, *ApJ*, 228, 939
- Churazov, E., Sunyaev, R., Isern, J., et al. 2014, *Nature*, 512, 406
- Churazov, E., Sunyaev, R., Sazonov, S., Revnivtsev, M., & Varshalovich, D. 2005, *MNRAS*, 357, 1377
- Coburn, W., Heindl, W. A., Rothschild, R. E., et al. 2002, *ApJ*, 580, 394
- Condon, J. J., Cotton, W. D., Greisen, E. W., et al. 1998, *AJ*, 115, 1693
- Cutri, R. M., Skrutskie, M. F., van Dyk, S., et al. 2003, *2MASS All Sky Catalog of Point Sources (NASA/IPAC Infrared Science Archive)*
- Dame, T. M., Hartmann, D., & Thaddeus, P. 2001, *ApJ*, 547, 792
- Filliatre, P., & Chaty, S. 2004, *ApJ*, 616, 469
- Fiocchi, M., Bassani, L., Bazzano, A., et al. 2010, *ApJ*, 720, 987
- Freeman, P. E., Kashyap, V., Rosner, R., & Lamb, D. Q. 2002, *ApJS*, 138, 185
- Garmire, G. P., Bautz, M. W., Ford, P. G., Nousek, J. A., & Ricker, G. R. 2003, *Proc. SPIE*, 4851, 28
- Gehrels, N., 1986, *ApJ*, 303, 336
- Giménez-García, A., Torrejón, J. M., Eikmann, W., et al. 2015, *A&A*, 576, A108
- Hellier, C., & Mukai, K. 2004, *MNRAS*, 352, 1037
- Hong, J., van den Berg, M., Schlegel, E. M., et al. 2005, *ApJ*, 635, 907
- Kalberla, P. M. W., Burton, W. B., Hartmann, D., et al. 2005, *A&A*, 440, 775
- Karasev, D. I., Lutovinov, A. A., Revnivtsev, M. G., & Krivonos, R. A. 2012, *Astronomy Letters*, 38, 629
- Krivonos, R., Revnivtsev, M., Tsygankov, S., et al. 2010, *A&A*, 519, A107
- Krivonos, R., Tsygankov, S., Lutovinov, A., et al. 2012, *A&A*, 545, A27
- Landi, R., Bassani, L., Masetti, N., et al. 2012, *The Astronomer's Telegram*, 4165
- Lawrence, A., Warren, S. J., Almaini, O., et al. 2007, *MNRAS*, 379, 1599
- Matt, G., & Guainazzi, M. 2003, *MNRAS*, 341, L13
- McClintock, J. E., & Remillard, R. A. 2006, *Black hole binaries, Compact Stellar X-ray Sources*, ed. W. Lewin & M. van der Klis (Cambridge: Cambridge Univ. Press), 157
- Minniti, D., Lucas, P. W., Emerson, J. P., et al. 2010, *New Astronomy*, 15, 433
- Muno, M. P., Arabadjis, J. S., Baganoff, F. K., et al. 2004, *ApJ*, 613, 1179
- Neguera, I., Smith, D. M., Reig, P., Chaty, S., & Torrejón, J. M. 2006, in *The X-ray Universe 2005*, ed. A. Wilson (ESA SP-604; Noordwijk: ESA), 165
- Nowak, M. A., Paizis, A., Rodriguez, J., et al. 2012, *ApJ*, 757, 143
- Paizis, A., Nowak, M. A., Rodriguez, J., et al. 2012, *ApJ*, 755, 52
- Paizis, A., Nowak, M. A., Wilms, J., et al. 2011, *ApJ*, 738, 183
- Papitto, A., Ferrigno, C., Bozzo, E., et al. 2013, *Nature*, 501, 517
- Patterson, J., Kemp, J., Harvey, D. A., et al. 2005, *PASP*, 117, 1204
- Pavan, L., Bozzo, E., Pühlhofer, G., et al. 2011, *A&A*, 533, A74
- Pellizza, L. J., Chaty, S., & Negueruela, I. 2006, *A&A*, 455, 653
- Ratti, E. M., Bassa, C. G., Torres, M. A. P., et al. 2010, *MNRAS*, 408, 1866
- Revnivtsev, M., Sazonov, S., Krivonos, R., Ritter, H., & Sunyaev, R. 2008, *A&A*, 489, 1121
- Romano, P., Krimm, H. A., Palmer, D. M., et al. 2014, *A&A*, 562, A2
- Scaringi, S., Bird, A. J., Norton, A. J., et al. 2010, *MNRAS*, 401, 2207
- Sidoli, L., Esposito, P., Sguera, V., et al. 2013, *MNRAS*, 429, 2763
- Smith, D. M., Heindl, W. A., Markwardt, C. B., et al. 2006, *ApJ*, 638, 974
- Soszyński, I., Dziembowski, W. A., Udalski, A., et al. 2011, *Acta Astron.*, 61, 1
- Tomsick, J. A., Bodaghee, A., Chaty, S., et al. 2012a, *ApJ*, 754, 145
- Tomsick, J. A., Bodaghee, A., Rodriguez, J., et al. 2012b, *ApJ*, 750, L39
- Tomsick, J. A., Chaty, S., Rodriguez, J., et al. 2006, *ApJ*, 647, 1309
- Tomsick, J. A., Chaty, S., Rodriguez, J., Walter, R., & Kaaret, P. 2009, *ApJ*, 701, 811
- Tomsick, J. A., Kalemci, E., Kaaret, P., et al. 2008, *ApJ*, 680, 593
- Tomsick, J. A., Krivonos, R., Rahoui, F., et al. 2015, *MNRAS*, 449, 597
- Tomsick, J. A., Rahoui, F., Krivonos, R., et al. 2014, *The Astronomer's Telegram*, 6793
- Ubertini, P., Lebrun, F., Di Cocco, G., et al. 2003, *A&A*, 411, L131
- Verner, D. A., Ferland, G. J., Korista, K. T., & Yakovlev, D. G. 1996, *ApJ*, 465, 487
- Walter, R., Lutovinov, A. A., Bozzo, E., & Tsygankov, S. S. 2015, *A&A Review*, 23, 2
- Walter, R., Zurita Heras, J., Bassani, L., et al. 2006, *A&A*, 453, 133
- Weisskopf, M. C., 2005, arXiv:astro-ph/0503091
- Wilms, J., Allen, A., & McCray, R. 2000, *ApJ*, 542, 914
- Winkler, C., Courvoisier, T. J.-L., Di Cocco, G., et al. 2003, *A&A*, 411, L1

TABLE 1
Chandra OBSERVATIONS

IGR Name	ObsID	l^a	b^b	Start Time	Exposure Time (s)	N_{sources}^c
J14091–6108	15789	312.13	+0.35	2013 Dec 7, 23.7 h UT	4912	18
J15335–5420	15790	325.18	+1.36	2014 Jun 4, 8.9 h UT	4912	8
J17164–3803	15788	349.07	+0.07	2014 Apr 15, 18.6 h UT	4912	12
J17174–2436	15797	0.19	+7.65	2014 Feb 27, 5.3 h UT	4902	14
J17306–2015	15796	5.52	+7.53	2015 Feb 8, 11.2 h UT	4906	7
J18088–2741	15794	3.65	–3.84	2014 Feb 16, 16.7 h UT	4915	29
J18381–0924	15791	23.05	–1.36	2014 Feb 15, 18.6 h UT	4912	14
J20107+4534	15795	81.39	+6.59	2013 Dec 21, 5.4 h UT	4912	13

^aGalactic longitude measured by *INTEGRAL* (degrees)

^bGalactic latitude measured by *INTEGRAL* (degrees)

^cNumber of *Chandra* sources detected in each field.

TABLE 2
 SPECTRAL PARAMETERS

Parameter ^a	Units	<i>Chandra</i> -only	<i>Chandra</i> + <i>INTEGRAL</i>	
CXOU J140846.0–610754				
N_{H}^b	10^{22} cm^{-2}	$1.0^{+0.7}_{-0.6}$	$0.8^{+0.7}_{-0.5}$	$0.6^{+0.6}_{-0.5}$
Γ	–	0.6 ± 0.4	0.3 ± 0.5	$0.1^{+0.4}_{-0.5}$
Unabsorbed Flux (0.3–10 keV)	$10^{-12} \text{ erg cm}^{-2} \text{ s}^{-1}$	$2.2^{+0.4}_{-0.3}$	2.3 ± 0.3	2.4 ± 0.3
E_{line}	keV	6.6 ± 0.2	$6.6^{+0.4}_{-0.2}$	$6.6^{+0.3}_{-0.2}$
σ_{line}	keV	$0.2^{+0.4}_{-0.2}$	<0.6	<0.6
N_{line}	$10^{-5} \text{ ph cm}^{-2} \text{ s}^{-1}$	$3.0^{+2.3}_{-1.8}$	$3.4^{+3.6}_{-2.0}$	$3.0^{+1.9}_{-1.8}$
E_{fold}	keV	–	13^{+10}_{-5}	14^{+11}_{-5}
$N_{\text{INTEGRAL}}/N_{\text{Chandra}}^c$	–	–	$1.8^{+2.8}_{-1.1}$	1.0^d
χ^2/dof	–	18.9/19	18.5/21	19.7/22
CXOU J180839.8–274131				
N_{H}^b	10^{22} cm^{-2}	$0.2^{+1.0}_{-0.2}$	<0.7	<0.7
Γ	–	$-0.7^{+0.4}_{-0.3}$	-1.5 ± 0.4	$-1.5^{+0.4}_{-0.2}$
Unabsorbed Flux (0.3–10 keV)	$10^{-12} \text{ erg cm}^{-2} \text{ s}^{-1}$	$3.5^{+0.7}_{-0.6}$	2.8 ± 0.5	2.8 ± 0.4
E_{fold}	keV	–	$5.1^{+1.6}_{-1.3}$	$4.8^{+1.1}_{-0.8}$
$N_{\text{INTEGRAL}}/N_{\text{Chandra}}^c$	–	–	$0.8^{+0.6}_{-0.4}$	1.0^d
χ^2/dof	–	13.6/15	12.0/17	12.3/18
CXOU J183818.5–092552				
N_{H}^b	10^{22} cm^{-2}	$4.0^{+1.3}_{-1.2}$	$4.3^{+1.4}_{-1.1}$	$3.8^{+0.9}_{-0.7}$
Γ	–	$1.5^{+0.5}_{-0.4}$	1.6 ± 0.4	1.4 ± 0.1
Unabsorbed Flux (0.3–10 keV)	$10^{-12} \text{ erg cm}^{-2} \text{ s}^{-1}$	$3.4^{+1.4}_{-0.6}$	$3.5^{+1.4}_{-0.7}$	3.2 ± 0.5
$N_{\text{INTEGRAL}}/N_{\text{Chandra}}^c$	–	–	$1.6^{+2.1}_{-0.9}$	1.0^d
χ^2/dof	–	14.4/22	20.4/25	21.2/26

^aThe errors on the parameters are 90% confidence.

^bThe column density is calculated assuming Wilms et al. (2000) abundances and Verner et al. (1996) cross sections. The Galactic column density (atomic and molecular Hydrogen) at the locations of CXOU J140846.0–610754, CXOU J180839.8–274131, and CXOU J183818.5–092552 are $5.4 \times 10^{22} \text{ cm}^{-2}$, $3.0 \times 10^{21} \text{ cm}^{-2}$, and $2.1 \times 10^{22} \text{ cm}^{-2}$, respectively (Kalberla et al. 2005; Dame et al. 2001).

^cThe *INTEGRAL* normalization relative to *Chandra*.

^dFixed.

TABLE 3
IR IDENTIFICATIONS

IR Source	Separation ^a	Magnitudes
CXOU J140846.0–610754		
VVV J140845.99–610754.1	0.''16	$Z = 16.165 \pm 0.005$
"	"	$Y = 15.806 \pm 0.005$
"	"	$J = 15.220 \pm 0.005$
"	"	$H = 14.833 \pm 0.007$
"	"	$K_s = 14.394 \pm 0.010$
CXOU J180839.8–274131		
VVV J180839.77–274131.7	0.''41	$Z = 16.77 \pm 0.06$
"	"	$Y = 16.65 \pm 0.07$
"	"	$J = 16.09 \pm 0.06$
"	"	$H = 15.82 \pm 0.08$
"	"	$K_s = 15.67 \pm 0.09$
CXOU J183818.5–092552		
UGPS J183818.59–092551.8	0.''47	$K \approx 14^b$
UGPS J183818.58–092552.9	0.''73	$K \approx 13$

^aThe angular separation between the *Chandra* position and the catalog position.

^bAs described in the text, the magnitudes listed in the UKIDSS catalog are not consistent with the images. Here, we provide estimates for the *K*-band magnitudes based on visual comparisons to other nearby sources.

TABLE 4
LIMITS ON PARAMETERS FOR THE IGR SOURCES WITHOUT CLEAR COUNTERPARTS

IGR Name	Limit on ACIS Rate (c/s)	<i>INTEGRAL</i> Flux ^a	Limit on Γ	Limit on N_H (cm ⁻²)	Limit on Variability ^b
J15335–5420	<0.0034	5.5×10^{-12}	<-1.5	$>1.80 \times 10^{24}$	>16
J17164–3803	<0.0057	8.7×10^{-12}	<-1.5	$>1.75 \times 10^{24}$	>15
J17174–2436	<0.0063	6.4×10^{-12}	<-1.2	$>1.50 \times 10^{24}$	>10
J17306–2015	<0.0025	1.6×10^{-11}	<-2.9	$>2.85 \times 10^{24}$	>60
J20107+4534	<0.0062	6.8×10^{-12}	<-1.2	$>1.55 \times 10^{24}$	>11

^aThe 17–60 keV flux in units of erg cm⁻² s⁻¹ from Krivonos et al. (2012).

^bThe ratio of the *Chandra* count rate assuming the *INTEGRAL* flux, $\Gamma = 1$, and $N_H = 5 \times 10^{22}$ cm⁻² to the measured upper limit on the count rate.

TABLE 5 *Chandra* Sources in IGR Source Fields

Source Number	θ^a (arcminutes)	<i>Chandra</i> R.A. (J2000)	<i>Chandra</i> Decl. (J2000)	Position Uncertainty ^b	ACIS Counts ^c	Hardness ^d
IGR J14091–6108						
1	0.45	14 ^h 08 ^m 46 ^s .02	-61°07'54.''2	0.''69	405 ⁺²¹ ₋₂₀	0.56 ± 0.06
2	1.13	14 ^h 08 ^m 36 ^s .70	-61°06'48.''1	0.''86	3.8 ^{+3.2} _{-1.9}	< 0.53
3	1.18	14 ^h 08 ^m 42 ^s .96	-61°08'47.''7	0.''80	5.8 ^{+3.6} _{-2.4}	< -0.09
4	1.58	14 ^h 08 ^m 31 ^s .37	-61°06'56.''1	0.''72	43 ⁺⁸ ₋₇	> 0.70
5	1.59	14 ^h 08 ^m 30 ^s .19	-61°07'52.''2	0.''90	3.8 ^{+3.2} _{-1.9}	> -0.27
6	2.08	14 ^h 08 ^m 27 ^s .89	-61°08'33.''5	0.''91	4.8 ^{+3.4} _{-2.2}	< 0.04
7	2.50	14 ^h 08 ^m 49 ^s .80	-61°05'14.''2	0.''76	23 ⁺⁶ ₋₅	-0.05 ± 0.28
8	2.66	14 ^h 08 ^m 34 ^s .99	-61°05'08.''6	0.''78	18 ⁺³ ₋₄	< -0.40
9	3.87	14 ^h 08 ^m 52 ^s .79	-61°11'18.''4	1.''41	4.5 ^{+3.4} _{-2.2}	< 0.06
10	4.35	14 ^h 08 ^m 40 ^s .33	-61°03'16.''8	1.''40	6.0 ^{+3.8} _{-2.8}	0.07 ± 0.72
11	5.10	14 ^h 08 ^m 32 ^s .36	-61°12'32.''2	1.''65	6.8 ^{+4.0} _{-2.8}	< -0.11
12	7.28	14 ^h 08 ^m 16 ^s .64	-61°01'04.''6	3.''04	8.0 ^{+4.6} _{-3.4}	< -0.46
13	7.64	14 ^h 09 ^m 42 ^s .67	-61°10'15.''2	2.''60	11 ⁺⁴ ₋₃	< -0.16
14	7.83	14 ^h 09 ^m 44 ^s .69	-61°05'08.''7	2.''08	17 ⁺⁶ ₋₅	> 0.22
15	8.32	14 ^h 08 ^m 13 ^s .99	-61°15'09.''3	7.''18	4.6 ^{+4.6} _{-3.5}	—
16	8.66	14 ^h 09 ^m 04 ^s .29	-61°15'53.''8	1.''23	75 ⁺¹⁰ ₋₉	> 0.77
17	8.80	14 ^h 08 ^m 18 ^s .16	-61°15'52.''5	2.''20	23 ⁺⁷ ₋₆	> 0.56
18	9.28	14 ^h 09 ^m 59 ^s .91	-61°08'13.''7	1.''94	34 ⁺⁸ ₋₇	0.13 ± 0.24
IGR J15335–5420						
1	0.65	15 ^h 33 ^m 34 ^s .98	-54°21'03.''2	0.''80	4.9 ^{+3.4} _{-2.2}	< 0.03
2	1.48	15 ^h 33 ^m 34 ^s .87	-54°23'03.''9	0.''85	4.8 ^{+3.4} _{-2.2}	> -0.05
3	3.22	15 ^h 33 ^m 30 ^s .98	-54°18'24.''5	1.''15	4.7 ^{+3.4} _{-2.2}	< 0.30
4	4.31	15 ^h 33 ^m 39 ^s .34	-54°17'24.''8	1.''35	6.2 ^{+3.8} _{-2.6}	> 0.13
5	5.12	15 ^h 32 ^m 57 ^s .89	-54°22'14.''6	1.''29	11 ⁺⁵ ₋₃	> 0.14
6	5.25	15 ^h 33 ^m 04 ^s .40	-54°18'23.''1	2.''22	4.7 ^{+3.6} _{-2.4}	< 0.42
7	8.19	15 ^h 32 ^m 47 ^s .81	-54°26'32.''7	2.''31	17 ⁺⁶ ₋₅	0.09 ± 0.38
8	8.38	15 ^h 33 ^m 21 ^s .52	-54°29'50.''1	4.''42	7.9 ^{+4.9} _{-3.7}	< 0.17
IGR J17164–3803						
1	0.17	17 ^h 16 ^m 29 ^s .26	-38°02'04.''9	0.''75	7.9 ^{+4.0} _{-2.8}	< 0.11
2	1.87	17 ^h 16 ^m 26 ^s .97	-38°00'07.''8	0.''73	28 ⁺⁶ ₋₅	0.36 ± 0.26
3	2.26	17 ^h 16 ^m 33 ^s .23	-37°59'46.''9	0.''93	4.8 ^{+3.4} _{-2.2}	< 0.30
4	2.89	17 ^h 16 ^m 19 ^s .94	-38°04'06.''1	1.''35	2.8 ^{+2.9} _{-1.7}	< 0.61
5	3.82	17 ^h 16 ^m 17 ^s .33	-37°58'58.''9	0.''94	12 ⁺⁵ ₋₄	> 0.22
6	4.01	17 ^h 16 ^m 09 ^s .39	-38°02'22.''6	1.''23	6.4 ^{+3.8} _{-2.6}	> -0.28
7	4.34	17 ^h 16 ^m 49 ^s .50	-38°03'48.''3	1.''67	4.4 ^{+3.4} _{-2.2}	< 0.09
8	5.83	17 ^h 16 ^m 02 ^s .06	-38°04'02.''9	1.''37	14 ⁺⁵ ₋₄	0.05 ± 0.40
9	6.57	17 ^h 17 ^m 00 ^s .25	-37°59'19.''0	2.''96	6.1 ^{+4.1} _{-3.0}	< 0.04
10	6.87	17 ^h 16 ^m 02 ^s .99	-38°06'22.''2	1.''97	12 ⁺⁵ ₋₄	0.17 ± 0.46
11	7.17	17 ^h 16 ^m 58 ^s .28	-37°57'30.''7	1.''54	21 ⁺⁶ ₋₅	> 0.35
12	7.29	17 ^h 16 ^m 56 ^s .86	-38°06'52.''0	1.''52	23 ⁺⁶ ₋₅	0.13 ± 0.29
IGR J17174–2436						
1	1.92	17 ^h 17 ^m 20 ^s .44	-24°33'58.''4	0.''83	6.8 ^{+3.8} _{-2.6}	< 0.22
2	2.75	17 ^h 17 ^m 10 ^s .65	-24°34'06.''6	0.''89	7.7 ^{+4.0} _{-2.8}	-0.02 ± 0.58
3	2.92	17 ^h 17 ^m 32 ^s .16	-24°35'03.''2	0.''76	29 ⁺⁶ ₋₅	0.17 ± 0.24
4	2.96	17 ^h 17 ^m 07 ^s .74	-24°34'49.''3	1.''41	2.6 ^{+2.9} _{-1.7}	< 0.67
5	2.97	17 ^h 17 ^m 12 ^s .49	-24°33'26.''6	1.''41	2.6 ^{+2.9} _{-1.7}	< 0.67
6	4.18	17 ^h 17 ^m 23 ^s .94	-24°31'49.''3	1.''43	5.2 ^{+3.6} _{-2.4}	< 0.13
7	4.95	17 ^h 16 ^m 58 ^s .26	-24°36'29.''2	0.''90	31 ⁺⁶ ₋₅	0.11 ± 0.24
8	5.24	17 ^h 17 ^m 42 ^s .86	-24°36'12.''6	1.''34	11 ⁺⁵ ₋₃	0.30 ± 0.49
9	5.41	17 ^h 17 ^m 39 ^s .59	-24°38'55.''5	2.''40	4.6 ^{+3.6} _{-2.4}	> -0.12
10	6.95	17 ^h 17 ^m 24 ^s .06	-24°42'46.''8	2.''79	7.7 ^{+4.0} _{-2.8}	> -0.07
11	7.01	17 ^h 17 ^m 40 ^s .13	-24°30'36.''2	2.''85	7.7 ^{+4.0} _{-2.8}	-0.08 ± 0.66
12	7.05	17 ^h 17 ^m 02 ^s .98	-24°29'58.''7	1.''70	17 ⁺⁶ ₋₅	0.14 ± 0.37
13	7.12	17 ^h 16 ^m 48 ^s .88	-24°34'51.''1	2.''49	10 ⁺⁵ ₋₄	0.34 ± 0.58
14	7.99	17 ^h 17 ^m 13 ^s .11	-24°43'44.''3	4.''11	7.4 ^{+4.7} _{-3.6}	< 0.41
IGR J17306–2015						
1	1.26	17 ^h 30 ^m 24 ^s .81	-20°17'03.''3	0.''75	12 ⁺⁵ ₋₃	0.16 ± 0.43
2	1.45	17 ^h 30 ^m 20 ^s .40	-20°14'36.''3	0.''88	3.9 ^{+3.2} _{-1.9}	> -0.25
3	2.91	17 ^h 30 ^m 30 ^s .27	-20°13'20.''0	0.''95	6.8 ^{+3.8} _{-2.6}	-0.16 ± 0.65
4	3.04	17 ^h 30 ^m 33 ^s .99	-20°13'55.''8	1.''42	2.8 ^{+2.9} _{-1.7}	—
5	6.66	17 ^h 29 ^m 58 ^s .31	-20°12'53.''0	2.''68	7.2 ^{+4.3} _{-3.1}	< -0.13
6	6.76	17 ^h 30 ^m 20 ^s .66	-20°22'32.''2	2.''78	7.1 ^{+4.3} _{-3.1}	< -0.44
7	7.96	17 ^h 30 ^m 50 ^s .39	-20°10'52.''1	2.''73	12 ⁺⁵ ₋₄	-0.01 ± 0.47
IGR J18088–2741						
1	0.38	18 ^h 08 ^m 58 ^s .55	-27°41'48.''9	0.''76	6.9 ^{+3.8} _{-2.6}	-0.15 ± 0.64
2	1.42	18 ^h 09 ^m 06 ^s .57	-27°42'00.''2	0.''88	3.8 ^{+3.6} _{-1.9}	< 0.96
3	1.65	18 ^h 08 ^m 53 ^s .76	-27°42'34.''8	0.''86	4.8 ^{+3.4} _{-2.2}	< 0.29

TABLE 5 Continued

Source Number	θ^a (arcminutes)	Chandra R.A. (J2000)	Chandra Decl. (J2000)	Position Uncertainty ^b	ACIS Counts ^c	Hardness ^d
4	1.68	18 ^h 09 ^m 03 ^s .59	-27° 40' 15.''6	0.''83	5.8 ^{+3.6} _{-2.4}	> -0.41
5	2.21	18 ^h 08 ^m 50 ^s .40	-27° 41' 26.''1	0.''84	7.8 ^{+4.0} _{-2.8}	< 0.11
6	2.21	18 ^h 08 ^m 58 ^s .14	-27° 39' 36.''6	0.''77	16 ^{+5.4} _{-4.4}	-0.01 ± 0.36
7	2.27	18 ^h 09 ^m 07 ^s .57	-27° 43' 21.''5	0.''94	4.8 ^{+3.4} _{-2.4}	< 0.30
8	2.29	18 ^h 08 ^m 58 ^s .24	-27° 44' 00.''9	0.''94	4.8 ^{+3.4} _{-2.4}	< 0.30
9	2.61	18 ^h 08 ^m 50 ^s .82	-27° 40' 12.''6	1.''00	4.7 ^{+3.4} _{-2.4}	< 0.30
10	2.79	18 ^h 08 ^m 48 ^s .86	-27° 40' 34.''6	0.''97	5.7 ^{+3.6} _{-2.4}	> -0.43
11	3.25	18 ^h 09 ^m 14 ^s .60	-27° 41' 03.''5	0.''79	24 ^{+6.5} _{-5.5}	0.16 ± 0.28
12	3.50	18 ^h 09 ^m 10 ^s .00	-27° 44' 19.''9	1.''15	5.5 ^{+3.6} _{-2.4}	< -0.08
13	3.52	18 ^h 08 ^m 47 ^s .45	-27° 43' 51.''1	1.''03	7.5 ^{+4.0} _{-2.8}	< 0.11
14	3.54	18 ^h 08 ^m 49 ^s .93	-27° 44' 28.''1	1.''28	4.5 ^{+3.4} _{-2.2}	< 0.33
15	3.61	18 ^h 09 ^m 14 ^s .30	-27° 43' 36.''4	1.''50	3.5 ^{+3.1} _{-2.2}	< 0.33
16	4.02	18 ^h 08 ^m 53 ^s .34	-27° 38' 03.''3	1.''25	6.2 ^{+3.8} _{-2.6}	-0.20 ± 0.71
17	4.05	18 ^h 08 ^m 57 ^s .42	-27° 37' 45.''8	1.''18	7.2 ^{+4.0} _{-2.8}	0.24 ± 0.64
18	4.24	18 ^h 08 ^m 45 ^s .39	-27° 44' 26.''2	0.''87	23 ^{+6.5} _{-5.5}	-0.36 ± 0.29
19	4.53	18 ^h 08 ^m 39 ^s .80	-27° 41' 31.''6	0.''74	230 ⁺¹⁶ ₋₁₅	0.76 ± 0.09
20	4.67	18 ^h 09 ^m 20 ^s .65	-27° 42' 57.''5	1.''56	5.9 ^{+3.8} _{-2.6}	-0.24 ± 0.75
21	6.24	18 ^h 09 ^m 28 ^s .33	-27° 41' 11.''9	2.''71	5.9 ^{+4.0} _{-2.8}	< -0.07
22	6.25	18 ^h 09 ^m 00 ^s .14	-27° 48' 00.''9	1.''75	11 ^{+3.5} _{-2.5}	-0.16 ± 0.49
23	6.30	18 ^h 08 ^m 56 ^s .93	-27° 48' 01.''5	2.''77	5.9 ^{+4.0} _{-2.8}	-0.13 ± 0.77
24	6.76	18 ^h 08 ^m 30 ^s .22	-27° 40' 33.''0	2.''40	8.6 ^{+4.0} _{-3.5}	> -0.10
25	7.40	18 ^h 09 ^m 00 ^s .16	-27° 49' 10.''3	1.''37	30 ^{+7.7} _{-6.6}	-0.29 ± 0.26
26	7.60	18 ^h 08 ^m 36 ^s .70	-27° 47' 17.''8	3.''71	7.2 ^{+4.6} _{-3.5}	> -0.21
27	7.72	18 ^h 08 ^m 30 ^s .25	-27° 45' 42.''7	2.''39	13 ^{+3.5} _{-2.4}	0.17 ± 0.45
28	7.87	18 ^h 08 ^m 54 ^s .52	-27° 49' 32.''1	1.''91	20 ^{+6.5} _{-5.5}	-0.25 ± 0.35
29	9.96	18 ^h 08 ^m 38 ^s .95	-27° 50' 32.''5	12.''77	4.5 ^{+5.5} _{-4.4}	< 0.74
IGR J18381-0924						
1	1.84	18 ^h 38 ^m 02 ^s .02	-09° 23' 43.''9	0.''73	33 ^{+7.6} _{-6.6}	0.70 ± 0.26
2	2.78	18 ^h 38 ^m 18 ^s .58	-09° 25' 52.''2	0.''70	303 ⁺¹⁸ ₋₁₂	0.73 ± 0.08
3	2.82	18 ^h 38 ^m 20 ^s .11	-09° 23' 55.''6	1.''14	3.7 ^{+3.2} _{-1.9}	< 0.54
4	3.63	18 ^h 38 ^m 15 ^s .91	-09° 27' 38.''9	1.''30	4.6 ^{+3.4} _{-2.2}	< 0.61
5	3.76	18 ^h 38 ^m 16 ^s .55	-09° 21' 12.''6	1.''14	6.5 ^{+3.8} _{-2.6}	< 0.00
6	4.14	18 ^h 38 ^m 22 ^s .64	-09° 22' 05.''8	0.''80	42 ^{+8.7} _{-7.7}	> 0.58
7	4.27	18 ^h 37 ^m 51 ^s .59	-09° 24' 09.''6	1.''24	7.4 ^{+4.0} _{-2.8}	< -0.10
8	5.72	18 ^h 37 ^m 59 ^s .66	-09° 29' 42.''5	1.''76	8.4 ^{+4.0} _{-3.8}	> 0.13
9	6.14	18 ^h 38 ^m 30 ^s .63	-09° 27' 26.''9	1.''77	10 ^{+5.5} _{-3.3}	< -0.11
10	6.46	18 ^h 38 ^m 07 ^s .59	-09° 18' 00.''3	3.''47	4.8 ^{+3.8} _{-2.6}	< 0.25
11	6.49	18 ^h 38 ^m 33 ^s .67	-09° 26' 38.''1	2.''02	10 ^{+5.5} _{-3.3}	-0.13 ± 0.52
12	7.51	18 ^h 38 ^m 17 ^s .63	-09° 31' 39.''2	2.''76	10 ^{+5.5} _{-3.3}	-0.05 ± 0.54
13	8.16	18 ^h 37 ^m 50 ^s .30	-09° 17' 41.''9	1.''11	81 ⁺¹⁰ ₋₉	0.01 ± 0.13
14	8.37	18 ^h 37 ^m 54 ^s .41	-09° 32' 01.''7	3.''24	11 ^{+5.5} _{-4.4}	-0.25 ± 0.51
IGR J20107+4534						
1	1.40	20 ^h 10 ^m 43 ^s .20	+45° 34' 49.''6	0.''76	11 ^{+4.4} _{-3.3}	-0.28 ± 0.47
2	1.44	20 ^h 10 ^m 30 ^s .05	+45° 34' 46.''7	0.''80	6.8 ^{+3.8} _{-2.6}	< -0.19
3	2.12	20 ^h 10 ^m 48 ^s .95	+45° 34' 06.''5	0.''74	26 ^{+6.5} _{-5.5}	< -0.66
4	2.87	20 ^h 10 ^m 20 ^s .61	+45° 33' 34.''7	1.''05	4.7 ^{+3.4} _{-2.2}	> -0.66
5	3.63	20 ^h 10 ^m 47 ^s .47	+45° 30' 51.''2	1.''31	4.5 ^{+3.4} _{-2.2}	> -0.11
6	3.69	20 ^h 10 ^m 34 ^s .82	+45° 37' 38.''3	1.''90	2.5 ^{+2.9} _{-1.7}	< 0.77
7	4.14	20 ^h 10 ^m 25 ^s .50	+45° 37' 36.''1	1.''40	5.3 ^{+3.6} _{-2.4}	> -0.49
8	4.30	20 ^h 10 ^m 12 ^s .27	+45° 33' 55.''6	1.''35	6.2 ^{+3.8} _{-2.6}	-0.22 ± 0.71
9	4.54	20 ^h 10 ^m 52 ^s .12	+45° 30' 17.''8	0.''99	16 ^{+5.5} _{-4.4}	< -0.49
10	4.74	20 ^h 10 ^m 26 ^s .36	+45° 38' 20.''4	3.''36	2.1 ^{+2.9} _{-1.7}	—
11	5.20	20 ^h 10 ^m 56 ^s .40	+45° 37' 53.''7	1.''47	8.7 ^{+4.3} _{-3.1}	-0.06 ± 0.55
12	5.63	20 ^h 10 ^m 27 ^s .57	+45° 28' 34.''4	1.''23	16 ^{+5.5} _{-4.4}	< -0.51
13	7.48	20 ^h 11 ^m 19 ^s .30	+45° 34' 51.''8	1.''38	31 ^{+7.7} _{-6.6}	0.10 ± 0.25

^aThe angular distance between the center of the *INTEGRAL* error circle and the source. In each case, the *INTEGRAL* error circle radius is 2.'1 at 1- σ (Krivonos et al. 2012) and 4.'2 at 2- σ .

^bThe 90% confidence uncertainty on the position, including statistical and systematic contributions.

^cThe number of ACIS-I counts detected (after background subtraction) in the 0.3–10 keV band. The errors are 68% confidence Poisson errors using the analytical approximations from Gehrels (1986).

^dThe hardness is given by $(C_2 - C_1)/(C_2 + C_1)$, where C_2 is the number of counts in the 2–10 keV band and C_1 is the number of counts in the 0.3–2 keV band.

TABLE 6
POSITION SHIFTS BASED ON *Chandra*/NEAR-IR MATCHES

IGR Name	Near-IR Catalog	$N_{\text{matches}}^{\text{a}}$	R.A. shift	Decl. shift
J14091–6108	VISTA/VVV	10	+0.''01	+0.''23
J15335–5420	VISTA/VVV	5	-0.''01	-0.''25
J17164–3803	VISTA/VVV	5	-0.''43	-0.''20
J17174–2436	UKIDSS	1	—	—
J17306–2015	2MASS	2	—	—
J18088–2741	VISTA/VVV	15	-0.''09	+0.''09
J18381–0924	UKIDSS	3	—	—
J20107+4534	2MASS	5	-0.''29	-0.''29

^aThe number of matches between *Chandra* sources and sources in the near-IR catalog after running `wcs_match`.

SPECTRAL STATE DEPENDENCE OF THE 0.4–2 MEV POLARIZED EMISSION IN
CYGNUS X-1 SEEN WITH INTEGRAL/IBIS, AND LINKS WITH THE AMI RADIO DATAJÉRÔME RODRIGUEZ¹, VICTORIA GRINBERG^{2,3}, PHILIPPE LAURENT⁴, MARION CADOLLE BEL⁵,
KATJA POTTSCHMIDT^{6,7}, GUY POOLEY⁸, ARASH BODAGHEE⁹, JÖRN WILMS²

AND

CHRISTIAN GOUIFFÈS¹*Draft version May 13, 2015*

ABSTRACT

Polarization of the $\gtrsim 400$ keV hard tail of the microquasar Cygnus X-1 has been independently reported by *INTEGRAL*/IBIS, and *INTEGRAL*/SPI and interpreted as emission from a compact jet. These conclusions were, however, based on the accumulation of all *INTEGRAL* data regardless of the spectral state. We utilize additional *INTEGRAL* exposure accumulated until December 2012, and include the AMI/Ryle (15 GHz) radio data in our study. We separate the observations into hard, soft, and intermediate/transitional states and detect radio emission from a compact jet in hard and intermediate states, but not in the soft. The 10–400 keV *INTEGRAL* (JEM-X and IBIS) state resolved spectra are well modeled with thermal Comptonization and reflection components. We detect a hard tail in the 0.4–2 MeV range for the hard state only. We extract the state dependent polarigrams of Cyg X-1, which all are compatible to no or undetectable level of polarization except in 400–2000 keV range in the hard state where the polarization fraction is $75 \pm 32\%$ and the polarization angle $40^\circ 0 \pm 14^\circ 3$. An upper limit on the 0.4–2 MeV soft state polarization fraction is 70%. Due to the short exposure, we obtain no meaningful constraint for the intermediate state. The likely detection of a > 400 keV polarized tail in the hard state, together with the simultaneous presence of a radio jet, reinforce the notion of a compact jet origin of the > 400 keV emission.

Subject headings: accretion, accretion disks — black hole physics — stars: individual (Cyg X-1) — X-rays: stars

1. INTRODUCTION

Black hole binaries (BHB) transit through different “spectral states” during their outbursts. The two canonical ones are the soft state (also known as “high” state, hereafter HSS) and the hard state (also known as “low” state, hereafter LHS).

In the HSS, the emission is dominated by a bright and warm (~ 1 keV) accretion disk, the level of variability is low, and the power density spectrum is power-law like. Little or no radio emission is detected in this state, which is interpreted as an evidence for an absence of jets.

In the LHS, the disk is colder (≤ 0.5 keV) and might be truncated at a large distance from the accretor (see however Reynolds & Miller 2013, for examples of results contradicting this picture). The X-ray spectrum shows a strong power-law like component extending up to hundreds of keV, usually with a roll-over at typically 50–200 keV. The level of rapid variability is higher than in the HSS and the power density spectrum shows a band lim-

ited noise component, sometimes with quasi-periodic oscillations (QPOs) with frequencies in the range ~ 0.1 –10 Hz. A so-called “compact-jet” is detected mainly through its emission in the radio to infrared domain (e.g., Corbel et al. 2013) where the spectrum can be modeled by $F_\nu \propto \nu^{-\alpha}$ where $\alpha \leq 0$ up to a break frequency ν_{break} that usually lies in the infrared domain (Corbel & Fender 2002; Rahoui et al. 2011). Above this break, the spectrum is a typical synchrotron spectrum with $\alpha \geq 0.5$.

Intermediate states (IS) exist between the HSS and LH (see, e.g., Remillard & McClintock 2006; Homan & Belloni 2005; Fender et al. 2009, for reviews and more detailed state classifications). Transitions between states indicate drastic changes in the properties of the flows and thus are crucial for the understanding of accretion-ejection connection. During a transition from the LHS to the HSS, the compact jet is quenched (e.g. Fender et al. 1999; Coriat et al. 2011); discrete, sometimes superluminal ejections occur, the level of X-ray variability drops abruptly, and QPOs, if present in the given source,

¹Laboratoire AIM, UMR 7158, CEA/DSM - CNRS - Université Paris Diderot, IRFU/SAP, F-91191 Gif-sur-Yvette, France. jrodriguez@cea.fr

²Dr. Karl Remeis-Sternwarte and Erlangen Centre for Astroparticle Physics, Friedrich Alexander Universität Erlangen-Nürnberg, Sternwartstr. 7, 96049 Bamberg, Germany

³Massachusetts Institute of Technology, Kavli Institute for Astrophysics, Cambridge, MA 02139, USA

⁴Laboratoire APC, UMR 7164, CEA/DSM CNRS – Université Paris Diderot, Paris, France

⁵LMU, Excellence Cluster “Universe”, Boltzmannstrasse 2, 85748 Garching, Germany

⁶CRESST, University of Maryland Baltimore County, 1000 Hilltop Circle, Baltimore, MD 21250, USA

⁷NASA Goddard Space Flight Center, Astrophysics Science Division, Code 661, Greenbelt, MD 20771, USA

⁸Astrophysics, Cavendish Laboratory, J J Thomson Avenue, Cambridge CB3 0HE, UK

⁹Georgia College & State University, Dept. of Chemistry, Physics, and Astronomy, CBX 82, Milledgeville, GA 31061, USA

change types before disappearing (see, e.g., Varnière et al. 2011, 2012, and references therein for both a description of the different types of QPOs and a possible theoretical interpretation of their origin and link to the spectral states).

The BHB Cygnus X-1 (Cyg X-1) was discovered in 1964 (Bowyer et al. 1965). It is the first Galactic source known to host a black hole (Bolton 1975) as the primary, and recent estimates led to a black hole mass of $M_{\text{BH}} = 14.8 \pm 1.0 M_{\odot}$ (Orosz et al. 2011). The donor star is the O9.7 Iab star HDE 226868 (Bolton 1972; Walborn 1973) with $M_{\text{HDE}} = 19.2 \pm 1.9 M_{\odot}$ (Orosz et al. 2011)¹⁰. The systems orbital period is 5.6 d (Webster & Murdin 1972; Brocksopp et al. 1999; Gies et al. 2003), it has an inclination $i = 27^{\circ}.1 \pm 0^{\circ}.8$ on the plane of the sky (Orosz et al. 2011), and is located at a distance of $d = 1.86 \pm 0.12$ kpc from Earth (Reid et al. 2011; Xiang et al. 2011).

Cyg X-1 can be found in both the LHS and the HSS; up to 2010, it was predominantly in the LHS. Since then, the behavior has changed and it spends most of its time in the HSS (Grinberg et al. 2013). It sometimes undergoes partial (“failed”) transitions from the LHS to the HSS, and can be found in a transitional or intermediate state (e.g., Pottschmidt et al. 2003b). The detection of compact relativistic jets in the LHS (Stirling et al. 2001) places Cyg X-1 in the family of microquasars. It is one of the few microquasars known to have a hard tail extending to (and beyond) the MeV range (e.g., McConnell et al. 2000).

The presence of the MeV tail has recently been confirmed with the two main instruments onboard the ESA’s *INTErnational Gamma-Ray Astrophysics Laboratory* (*INTEGRAL*): the Imager onBoard the *INTEGRAL* Satellite (IBIS; Ubertini et al. 2003) and the Spectrometer on *INTEGRAL* (SPI; Vedrenne et al. 2003). Cadolle Bel et al. (2006) and Laurent et al. (2011, ; LRW11) detect it with IBIS, and Jourdain et al. (2012, ; JRC12) with SPI. Utilizing photon that Compton scattered in the upper plane of IBIS, (ISGRI; Lebrun et al. 2003), and are absorbed in its lower plane PICsIT (Labanti et al. 2003, sensitive in the 200 keV–10 MeV energy band), we have shown that the ≥ 400 keV emission of Cyg X-1 was polarized at a level of about 70%. We obtained only a 20% upper limit on the degree of polarization at lower energies (LRW11). This result was independently confirmed by JRC12 using SPI data. Both studies obtained compatible results for the properties of the polarized emission, reinforcing the genuineness of this discovery. Both teams also suggested that the polarized emission was due to synchrotron emission coming from a compact jet.

The presence of polarized emission and the energy-dependency of the polarization have profound implication on our understanding of accretion and ejection processes. It can help to distinguish between the different proposed emitting media (Comptonization corona vs. synchrotron-self Compton jets) in microquasars and provide important clues to the composition, energetics and magnetic field of the jet.

A problem of both studies, however, is that they accumulated all *INTEGRAL* data available to them, regardless of the spectral state and radio (and thus jet) properties of the source. In this paper, we separate the whole *INTE-*

GRAL data set (accumulated up to December 2012) into different spectral states and study the properties of the state resolved broad band 10–2000 keV emission of Cyg X-1. We also utilize the Ryle/AMI radio data to determine the state dependent level of 15 GHz jet emission. In §2, we describe the data reduction and in particular the so-called “Compton mode” that allowed us to discover and measure the polarization in Cyg X-1 (LRW11). We carefully separate the data into spectral state following a procedure based based on the classification of Grinberg et al. (2013) that is described in §3. The results of both, the long term 15 GHz radio monitoring and *INTEGRAL* state resolved analysis, are presented in §4. We discuss the implications of our analysis in §5 and summarize our results in §6.

2. OBSERVATIONS AND DATA REDUCTION

2.1. Standard data reduction of the JEM-X and IBIS/ISGRI data

Cyg X-1 has been extensively observed by *INTEGRAL* since the launch of the satellite; preliminary results of the very first observations are described by Pottschmidt et al. (2003a). In LRW11, we first considered all uninterrupted *INTEGRAL* pointings, also called “science windows” (ScWs), where Cyg X-1 had an offset angle of less than 10° from the center of the field of view. We then removed all ScWs from the performance verification phase so that our analysis covered the period from 2003 March 24 (MJD 52722, satellite revolution [rev.] 54) to 2010 June 26 (MJD 55369, rev. 938). We further excluded ScWs with less than 1000 s of good ISGRI and PICsIT time. This resulted in a total of 2098 ScWs. Polarization was detected when stacking this sample (LRW11).

In the present work, we added to the LRW11 sample all observations belonging to our Cyg X-1 *INTEGRAL* monitoring program (PI J. Wilms) made until 2012 December 28 (MJD 56289.8, rev. 1246). We applied the same filtering criteria to select good ScWs. We consider both, the data of the low energy detector of IBIS, ISGRI (Lebrun et al. 2003) and of the X-ray monitors JEM-X (Lund et al. 2003). ISGRI is sensitive in the ~ 18 –1000 keV energy range, although its response falls off rapidly above a few hundred keV. The two JEM-X units cover the soft X-ray (3–30 keV) band. All data were reduced with the *Off Line Scientific Analysis* (OSA) v.10.0 software suite and the associated updated calibration (Caballero et al. 2012), following the methods outlined by (Rodriguez et al. 2008b).

The brightest and most active sources of the field, Cyg X-1, Cyg X-2, Cyg X-3, 3A 1954+319, and EXO 2032+375, were subsequently taken into account in the extraction of spectra and light curves. The Cyg X-1 spectra of each ScW were extracted with 67 spectral channels. All ScWs belonging to the same state were then averaged to produce one ISGRI spectrum for each spectral state. The spectral classification is described in §3 (see Grinberg et al. 2013, for the details of the method). A systematic error of 1% was applied for all spectral channels. Low significance channels were rebinned when necessary.

The JEM-X telescopes have a much smaller field of view than IBIS. The number of ScWs during which Cyg X-1 can be seen by these instruments is therefore smaller. Since

¹⁰See also Ziółkowski (2014) who obtain somewhat different values.

rev. 983 (MJD 55501) both units are on for all observations. Before rev. 983, both units were used alternately, so that the number of ScWs and time coverage is not the same. We derived images and spectra in the standard manner following the cookbook, separating the data into states following the same criteria as for the IBIS data. We applied systematic errors of 2% to all spectral channels of both units.

2.2. The Compton Mode

Thanks to its two position-sensitive detectors ISGRI and PICsIT, IBIS can be used as a Compton polarimeter (Lei et al. 1997). The concept behind a Compton polarimeter utilizes the polarization dependence of the differential cross section for Compton scattering,

$$\frac{d\sigma}{d\Omega} = \frac{r_0^2}{2} \left(\frac{E'}{E_0} \right)^2 \left(\frac{E'}{E_0} + \frac{E_0}{E'} - 2 \sin^2 \theta \cos^2 \phi \right) \quad (1)$$

where r_0 is the classical electron radius, E_0 the energy of the incident photon, E' the energy of the scattered photon, θ the scattering angle, and ϕ the azimuthal angle relative to the polarization direction. Linearly polarized photons scatter preferentially perpendicularly to the incident polarization vector. Hence by examining the scattering angle distribution of the detected photons (also referred to as polarigrams)

$$N(\phi) = S[1 + a_0 \cos(2(\phi - \phi_0))] \quad (2)$$

where S is the mean count rate, one can derive the polarization angle PA and polarization fraction Π . With $PA = \phi_0 - \pi/2 + n\pi$, equation 2 becomes $N(\phi) = S[1 - a_0 \cos(2(\phi - PA))][2\pi]$. The polarization angle therefore corresponds to the minimum of $N(\phi)$. The polarization fraction is $\Pi = a_0/a_{100}$, where a_{100} is the amplitude expected for a 100% polarized source, obtained from Monte-Carlo simulations of the instrument. Forot et al. (2008) obtained $a_{100} = 0.30 \pm 0.02$, hence a $\sim 6.7\%$ systematic uncertainty that should be taken into account in the derivation of Π . Recent simulations allowed us to reduce the uncertainty on a_{100} to $\sim 3\%$ which is small compared to the statistical errors on $N(\phi)$ (see below), and is therefore neglected.

To measure $N(\phi)$, we followed the procedure described by Forot et al. (2008) that led to the successful detection of the polarized signal from the Crab nebula. We consider events that interacted once in ISGRI and once in PICsIT. These events are automatically selected on board through a time coincidence algorithm. The maximum allowed time window was set to $3.8 \mu\text{s}$ during our observations. To derive the source flux as a function of ϕ , the Compton photons were accumulated in 6 angular bins, each with a width of 30° in azimuthal scattering angle. To improve the signal-to-noise ratio in each bin, we took advantage of the π -symmetry of the differential cross section (Eq. 2), i.e., the first bin contains the photons with $0^\circ \leq \phi < 30^\circ$ and $180^\circ \leq \phi < 210^\circ$, etc. Chance coincidences, i.e., photons interacting in both detectors, but not related to a Compton event, were subtracted from each detector image following the procedure described by Forot et al. (2008). The derived detector images were then deconvolved to obtain sky images. The flux of the source in each ϕ -bin was then measured by fitting the instrumental PSF to the source peak in the sky image.

The uncertainty of $N(\phi)$ is dominated by statistic fluctuations in our observations that are background dominated. Confidence intervals on a_0 and ϕ_0 are not derived by a $N(\phi)$ fit to the data, but through a Bayesian approach following Forot et al. (2008), based on the work presented in Vaillancourt (2006). The applicability of this method was recently thoroughly discussed in Maier et al. (2014). In this computation, we suppose that all real polarization angles and fractions have an uniform probability distribution (non-informative prior densities; Quinn 2012; Maier et al. 2014) and that the real polarization angle and fraction are ϕ_0 and a_0 . We then need the probability density distribution of measuring a and ϕ from N_{pt} independent data points in $N(\phi)$ over a period π , based on Gaussian distributions for the orthogonal Stokes components (Vaillancourt 2006; Forot et al. 2008; Maier et al. 2014):

$$dP(a, \phi) = \frac{N_{\text{pt}} S^2}{\pi \sigma_S^2} \times \exp \left[-\frac{N_{\text{pt}} S^2}{2\sigma_S^2} [a^2 + a_0^2 - 2aa_0 \cos(2\phi - 2\phi_0)] \right] a da d\phi \quad (3)$$

where σ_S is the uncertainty of S . Credibility intervals of a and ϕ correspond to the intervals comprised between the minimum and maximum values of the parameter considered in the two dimensional 1σ contour plot (not shown).

3. THE SPECTRAL STATES OF CYG X-1

We previously developed a method to classify the states of Cyg X-1 at any given time based on hardness and intensity measurements with the *RXTE*/ASM and MAXI and on the hard X-ray flux obtained with the *Swift*/BAT (Grinberg et al. 2013). The ASM and MAXI data can be used to separate all three states (LHS, IS, HSS), while using BAT we can only separate the HSS, but not the LHS and IS from each other.

In microquasars in general and Cyg X-1 in particular, spectral transitions can occur on short time scales (hours; e.g., Böck et al. 2011). We thus performed the spectral classification for each individual ScW. This is a sufficiently small exposure over which to consider the source to be spectrally stable in the majority of the data. The IBIS 18–25 keV light curve is shown in Fig. 1, where the different symbols and colors represent the three different spectral states.

Where available, we used simultaneous ASM data for the state classification. ScWs with two simultaneous ASM measurements that are classified into different states are presumed to have occurred during a state transition and excluded from the analysis. Most ScWs are, however, not strictly simultaneous with any ASM measurements. To classify ScWs without simultaneous ASM measurements, we therefore used the closest ASM measurement within 6 h before or after a given ScW. For the remaining pointings where no such ASM measurements exist, we used the same approach, first based on MAXI and then, if necessary, based on BAT. As shown by Grinberg et al. (2013), the probability that a state is wrongly assigned using this method is 5% within 6 h of an ASM pointing for both the LHS and HSS, and $\sim 25\%$ for the IS.

Out of the 3302 IBIS ScWs, 1739 ($\sim 52.7\%$) were taken during the LHS, 868 ($\sim 26.3\%$) during the HSS and 316 ($\sim 9.6\%$) during the IS. The remaining 379 (11.5%) have an uncertain classification and are thus not considered in our analysis: 351 lack a simultaneous or quasi-simultaneous all sky monitor measurements that would allow a classification and 28 were caught during a state transition.

From MJD 55700 until MJD 56000, Cyg X-1 was highly variable and underwent several transitions on short timescales (particularly striking in Fig. 1 of Grinberg et al. 2014). Inspection of some of the ScWs during this period shows that the source flux was very low in the ISGRI range. Since these ScWs were taken close to or in between state transitions, they were also removed from our analysis in order to limit the potential uncertainties they could introduce into the final data products. This filtering removed 32 additional ScWs.

The resulting IBIS exposure times are 2.05 Ms, 1.21 Ms, and 0.22 Ms for the LHS, HSS, and IS, respectively. The IBIS 18–25 keV and Ryle/AMI 15 GHz light curves are shown in Fig. 1.

4. RESULTS

4.1. Radio monitoring with the Ryle-AMI telescope

The 2002–2012 15 GHz light curve classified utilizing the same method as for the *INTEGRAL* data is shown in Fig. 1. As known from previous studies of microquasars, including Cyg X-1, the LHS and the IS show a high level of radio activity, while the radio flux is at a level compatible with or very close to zero during the soft state (e.g., Corbel et al. 2003; Gallo et al. 2003).

Cyg X-1 shows a high level of radio variability with a mean flux $\langle F_{15\text{ GHz}} \rangle \sim 12$ mJy and flares. The most prominent flare occurred on MJD 53055 (2004 February 20) and reached a flux of 114 mJy¹¹. Flares occur frequently (Fig. 1), and are connected with the X-ray behavior of the source (Fender et al. 2006; Wilms et al. 2007). The main flares seem to mostly coincide with the IS. The radio behavior in the LHS is usually steadier (although there is, e.g., a flare at MJD 53700, Fig. 1).

We obtained state resolved mean radio fluxes of $\langle F_{15\text{ GHz,LHS}} \rangle = 13.5$ mJy, $\langle F_{15\text{ GHz,IS}} \rangle = 15.4$ mJy, and $\langle F_{15\text{ GHz,HSS}} \rangle = 4.6$ mJy. Given the typical rms uncertainty of $\text{rms}(5\text{min}) = 3.0$ mJy (e.g. Pooley & Fender 1997; Rodriguez et al. 2008a), the mean radio flux in the HSS is not detected at the 3σ level. The few clear radio detections in this state (Fig. 1) do not correspond to a steady level of emission that would indicate a compact radio core (see also Fender et al. 1999). Such detections preferably occur after radio flares and thus likely represent the relic emission of previously ejected material (e.g. Corbel et al. 2004).

4.2. State resolved spectral analysis

We analyzed the state resolved energy spectra of each instrument using *XSPEC* v.12.8.0 (Arnaud 1996). For JEM-X we considered the 10–20 keV range.¹² and 20–

400 keV for the ISGRI data. We used Compton data between 300 keV and 1 or 2 MeV, depending on their statistical quality. We started by fitting the spectra in the 10–400 keV range since the contribution of the 1 MeV power-law tail is supposed to be negligible here (LRW11). When an appropriate model was found for this restricted range, we added the 0.3–2 MeV Compton spectra and repeated the spectral analysis.

In order to find the most appropriate models describing the 10–400 keV spectra for all three spectral states, we proceeded in an incremental way. We started with a simple power-law model and added spectral model components until an acceptable fit according to χ^2 -statistics was found. The phenomenological models were then replaced by more physical Comptonization models. Since the ≥ 10 keV data are not affected by the absorption column density of $N_{\text{H}} \sim$ a few 10^{22} cm^{-2} (e.g., Böck et al. 2011; Grinberg et al. 2015), no modeling of the foreground absorption is necessary. Cross-calibration uncertainties and source variability during different exposure times are taken into account by a normalization constant. The ISGRI constant was frozen to one and the others left free to vary independently. We required that the values of the free constants were in the range [0.85, 1.15]. The bestfit parameters obtained with the best phenomenological and with the Comptonization models are reported in Table 1 for all three spectral states.

4.2.1. Hard state

A power-law (Fig. 2a) gives a very poor representation of the 10–400 keV data with a reduced $\chi^2 = \chi^2_{\nu} \sim 70$ for 87 degrees of freedom (dof). The broad band spectrum clearly departs from a straight line, which indicates a curved spectrum. A power-law modified by a high energy cut-off (**highcut*power** in *XSPEC*) provides a highly significant improvement with $\chi^2_{\nu} = 0.89$ for 85 dof (Fig. 2b). We note, however, that the value of the high energy cut-off is unconstrained (Table 1), and deviations are seen at high energies.

As a cut-off power-law in this energy range is usually assumed to mimic the spectral shape produced by an inverse Compton process, we replaced the phenomenological model by a more physical model **comptt** (Titarchuk 1994; Titarchuk & Lyubarskij 1995; Titarchuk & Hua 1995). Due to our comparably high lower energy bound, the temperature of the seed photons could not be constrained. We fix it to a typical LHS value of 0.2 keV (Wilms et al. 2006). Although the high energy part is better represented, the fit is statistically unacceptable ($\chi^2_{\nu} = 2.9$ for 88 dof, Fig. 2c) and significant residuals are visible in 10–80 keV range. In this range, hard X-ray photons can undergo reflection on the accretion disk. This effect is usually seen as an extra curvature, or bump in the 10–100 keV range in the spectra of microquasars and AGNs (García et al. 2014, and references therein). We thus included a simple reflection model (**reflect**) convolved with the Comptonization spectrum and fixed the inclination angle to 30° . The residuals are much smaller, yielding an acceptable fit ($\chi^2_{\nu} = 1.67$ for 87

¹¹This flare was studied in detail by Fender et al. (2006), although the time axis of their Fig. 4 is wrongly associated with MJD 55049.2–55049.6

¹²Although the JEM-X units are well calibrated above ~ 5 keV, we chose to ignore the lower energy bins. Due to the possible influence of a disk and presence of iron fluorescence line at 6.4 keV they would add uncertainties and degeneracies to the models that the low energy resolution does not allow us to constrain.

dof)¹³. The normalization constants are 0.99, 1.06, and 0.98 for JEM X-1, JEM X-2, and the Compton mode respectively. The best fit results of this model are listed in Table 1, while the $\nu F\nu$ broad band 10–400 keV spectrum is shown in the rightmost panel of Fig 2.

Next, we added the ≥ 400 keV Compton mode spectrum (Fig. 3) to our data. These points are significant at the 8.2σ , 7.8σ , 6.9σ , and 6.5σ levels in the 451.4–551.9 keV, 551.9–706 keV, 706–1000.8 keV, and ~ 1 –2 MeV energy bands. A significant deviation from the previous best fit model is clearly visible above 400 keV. An additional power-law improves the fit significantly ($\chi_\nu^2 = 1.4$ for 90 dof). The photon index of this additional power-law is hard ($\Gamma = 1.1_{-0.4}^{+0.3}$) and marginally compatible with the values reported earlier (1.6 ± 0.2 , LRW11).

We model the reflection component using several distinct approaches, assuming 1) that the power-law component undergoes the same reflection as the Comptonization component (`reflect*(power+comptt)`), 2) that both components undergo reflection but with different solid angles $\Omega/2\pi$ (`reflect1*(power)+reflect2*(comptt)`), and 3) that the power-law is not reflected (`power+reflect*(comptt)`). In model 2, the value for the reflection of the power-law component is unconstrained. Model 3 results in a better χ_ν^2 , but the value of the power-law parameters are physically not acceptable. The normalization is too high and Γ too soft to reproduce the Compton data well. We therefore discard model 3, and consider model 1 as the most valid one. The value of the fit statistics is, however, still high with $\chi_\nu^2 = 1.8$ for 89 dof. The residuals show deviations in the ~ 50 –200 keV range that may be due to the accumulation of a large set of ScWs taken at different calibration epochs and at different off-axis and roll angles of Cyg X-1.

In the final fit to the 10 keV–2 MeV broad band spectrum the parameters of the Comptonized component are $kT_e = 53 \pm 2$ keV and $\tau = 1.15 \pm 0.04$, the reflection fraction is unchanged, and the photon index of the hard tail is $\Gamma = 1.4_{-0.3}^{+0.2}$, i.e., essentially compatible with the value reported in LRW11. The 0.4–1 MeV flux of the hard tail ($F_{\text{pow},0.4-1 \text{ MeV}} = 1.9 \times 10^{-9} \text{ erg cm}^{-2} \text{ s}^{-1}$) accounts for 86% of the total 0.4–1 MeV flux.

4.2.2. Intermediate state

A simple power-law gives a poor representation of the IS spectrum ($\chi_\nu^2 \sim 28$ for 82 dof). The inclusion of a high energy cut-off again greatly improves the fit ($\chi_\nu^2 = 1.35$, 80 dof), but the normalization constant of the Compton spectrum (C_{Compton}) is outside the range that is consistent with the flux calibration of the instrument. Replacing the phenomenological model by a `comptt` model, with the seed photon temperature fixed at 0.8 keV¹⁴ leads to a good fit ($\chi_\nu^2 = 1.1$ for 81 dof) and a physical value of C_{Compton} . Although the statistics are not as good as in the LHS due to the much shorter total exposure, and the residuals in the 10–100 keV region are rather acceptable, we included a

reflection component to be consistent with the LHS modeling. This approach improved the fit to $\chi_\nu^2 = 0.97$ for 79 dof, which indicates a chance improvement of $\sim 1.2\%$ according to an F-test (the reflection component has a significance lower than 3σ). The reflection fraction is very low and poorly constrained ($\Omega/2\pi = 0.04 \pm 0.03$). As the other parameters are not significantly affected, we still report the results obtained with the latter model in Table 1 despite this weak evidence for reflection.

We then added the ≥ 400 keV spectral points of the Compton mode spectrum (Fig. 3). The previous model (without reflection) leads to a good representation ($\chi_\nu^2 = 1.2$ for 83 dof), even if a deviation at high energies is present. Above 400 keV, however, only the 551.9–706 keV Compton mode spectral point is significant at $\geq 3\sigma$. Adding a power-law to the data leads to $\chi_\nu^2 = 1.04$ (81 dof), which corresponds to a chance improvement of 0.1%. Not surprisingly, the power-law photon index Γ is poorly constrained ($-0.4 \leq \Gamma \leq 1.8$) and the normalization constant for the Compton mode spectral points C_{Compton} tends to a very low value if not forced to be above 0.85. Fixing Γ at 1.6 (LRW11, JRC12) and setting C_{compton} to 0.90, the best value found in the LHS fits, allows us to estimate a 3σ upper limit for the 0.4–1 MeV flux of $1.5 \times 10^{-9} \text{ erg cm}^{-2} \text{ s}^{-1}$.

4.2.3. Soft State

In the soft state the soft X-ray spectrum below 10 keV is dominated by a ~ 1 keV accretion disk. This disk, however, does not influence the >10 keV spectrum studied here. A single power-law gives a poor representation of the broad band spectrum ($\chi_\nu^2 = 6.0$ for 77 dof). The JEM-X and IS-GRI spectra are particularly discrepant and a possible hint for a high energy roll-over is seen in the residuals. A cut-off power-law greatly improves the fit statistics ($\chi_\nu^2 = 1.68$ for 75 dof), but the modeling is still not satisfactory and the JEM-X normalization constants are inconsistent with the detector calibration uncertainty. Residuals in the 15–50 keV range suggest that reflection on the accretion disk may occur. Adding the `reflect` model improves the fit to $\chi_\nu^2 = 1.24$ (74 dof). The normalization constant for the JEM-X1 detector has to be forced to be above 0.85 as it would naturally converge to about 0.8. Alternatively describing the data with a simple reflected power-law without a cutoff results in $\chi_\nu^2 = 1.88$ (76 dof) and shows that the cut-off is genuinely present. The chance improvement from a reflected power-law spectrum to a reflected cut-off power-law spectrum is about 4×10^{-8} according to an F-test. Replacing the phenomenological model with a Comptonization continuum that is modified by reflection yields $\chi_\nu^2 = 1.69$ (75 dof, Table 1).

The >400 keV data were then added. Since the Compton mode spectrum has a very low statistical quality and in order not to increase the number of degeneracies, we fixed its constant to a value of one. The `reflect*comptt` model is still statistically acceptable, and only the highest spec-

¹³We have followed the recommendations of the IBIS user manual regarding the level of systematics added to the IBIS spectral points (http://isdc.unige.ch/integral/download/osa/doc/10.0/osa_um_ibis/node74.html). Systematic errors of 1% seem to underestimate the real uncertainties when dealing with (large) data sets that encompass several calibration periods. We have tested this notion by refitting the spectra with 1.5% and 2% systematics and, as expected, obtain χ_ν^2 much closer to 1. Since the values of the spectral parameters, and thus the conclusions presented here, do not change significantly, we decided to present the spectral fits using the recommended 1% for systematics.

¹⁴The choice of a higher seed photon temperature in the IS does not influence the > 10 keV spectrum and was only motivated by the desire to be consistent with the expectation of a hotter disk in the IS.

TABLE 1

SPECTRAL PARAMETERS OF FIT TO THE 10–400 keV SPECTRA. ERRORS AND LIMITS ON THE SPECTRAL PARAMETERS ARE GIVEN AT THE 90% CONFIDENCE LEVEL, WHILE THE ERRORS ON THE FLUXES ARE AT THE 68% LEVEL.

reflect*highcut(powerlaw)						
State	Γ	E_{cut} (keV)	E_{fold} (keV)	10–20 keV	Fluxes [†]	
					20–200 keV	200–400 keV
LHS	1.43 ± 0.01	≤ 12	155 ± 4	4.48 ± 0.02	22.30 ± 0.03	3.56 ± 0.03
IS	$1.87^{+0.02}_{-0.03}$	56^{+4}_{-6}	198 ± 8	5.10 ± 0.03	18.47 ± 0.04	2.52 ± 0.05
HSS [†]	2.447 ± 0.007	130^{+11}_{-16}	198^{+135}_{-59}	1.83 ± 0.01	3.33 ± 0.01	0.18 ± 0.03
reflect*comptt						
State	$\Omega/2\pi$	kT_e (keV)	τ	10–20 keV	Fluxes [†]	
					20–200 keV	200–400 keV
LHS	0.13 ± 0.02	$59.4^{+1.3}_{-1.2}$	1.06 ± 0.03	4.37 ± 0.03	22.60 ± 0.03	3.70 ± 0.03
IS	0.04 ± 0.03	$54.4^{+3.6}_{-2.8}$	0.82 ± 0.06	5.30 ± 0.03	18.42 ± 0.06	1.93 ± 0.07
HSS	0.36 ± 0.03	279 ± 15	< 0.013	1.84 ± 0.09	3.7 ± 0.6	0.36 ± 0.01

[†] A reflection component with $\Omega/2\pi=0.46\pm0.04$ was included for a good spectral fit to be obtained

[‡] In units of 10^{-9} erg cm⁻² s⁻¹

tral bin (550–2000 keV) indicates an excess of source photons compared to the model ($\chi^2_\nu = 1.76$, 77 dof). Adding a powerlaw component to the overall spectrum improves the modeling of the spectrum to $\chi^2_\nu = 1.69$ (75 dof), but if left free to vary Γ is completely unconstrained. We fix it at 1.6 ($\chi^2_\nu = 1.70$, 76 dof, 0.11 chance probability according to the F-test) and derive a 3σ upper limit of 0.93×10^{-9} erg cm⁻² s⁻¹ for the 0.4–1 MeV flux.

4.3. State resolved polarization analysis

Polarigrams were obtained for each of the three spectral states. The low statistics of the IS (the source significance in the Compton mode is 5.7σ) does not permit us to constrain the 250–3000 keV polarization fraction.

In the HSS, the detection significances of Cyg X-1 with the Compton mode are 4.2σ and 7.7σ in the 300–400 keV and 400–2000 keV bands respectively. A weighted least square fit procedure was used to fit the polarigrams. A constant represents the 400–2000 keV polarigram rather well ($\chi^2_\nu = 1.6$, 5 dof, not shown). The 1σ upper limit of the 400–2000 keV polarization fraction in the HSS is $\sim 70\%$.

Figure 4 shows the LHS polarigrams in two energy ranges: 300–400 keV and 400–2000 keV. Note that the data selection described in Sec. 3 is at the origin of the different count rates between the polarigrams shown here and those in Fig. 2 or LRW11. This effect is more obvious at the highest energies where the different spectral slopes have the largest impact (Fig. 3). In the lower energy range, the Compton mode detection significance of Cyg X-1 is 12.3σ . The polarigram can be described by a constant ($\chi^2_\nu = 0.87$, 5 dof). We estimate an upper limit for the polarization fraction of $\Pi_{300-400 \text{ keV, LHS}} = 22\%$ in this energy range. The 400–2000 keV energy range polarigram shows clear deviation from a constant and a constant poorly represents the data ($\chi^2_\nu = 3.5$, 5 dof). The pattern and fit indicate that the photons scattered in ISGRI are not evenly distributed in angle, but that the scattering has a preferential angle as is expected from a polarized signal

(§2.2). We describe the distribution of the polarigram with the expression of Eq. 2 and obtain the values of the parameters a_0 and ϕ_0 with a least square technique. The fit is better than that to a constant, although not formally good ($\chi^2_\nu = 2.0$, 3 dof) due to the low value of the periodogram at azimuthal angle 100° (Fig. 4). Assuming that the non constancy of the polarigram is an evidence for a real polarized signal (an assumption also consistent with the independent detections of polarized emission in Cygnus X-1 with SPI; Jourdain et al. 2012), we estimate that the polarization fraction is $\gtrsim 10\%$ at the 95% level, and greater than a few % at the 99.7% level. In other words we obtain a significance higher than 3σ for a polarized 400–2000 keV LHS emission. We determine a polarization fraction and a credibility interval of $\Pi_{400-2000 \text{ keV, LHS}} = 75 \pm 32\%$ at position angle $\text{PA}_{\text{CygX-1, LHS}} = 40.0^\circ \pm 14.3^\circ$. The values of the polarization fraction and angle are consistent with those found by JRC12. We note that an error of 180° in the angle convention in LRW11 led to $\text{PA} = 140^\circ$, which after correction becomes 40° , in agreement with our state resolved result (see also JRC12). Note that the good agreement of our results with those obtained with SPI in the case of Cyg X-1, but also the fact that IBIS also detected polarization in the high energy emission of the Crab nebula and pulsar (Forot et al. 2008) at values compatible with those obtained with SPI (Dean et al. 2008), increase the confidence in the reality and validity of our results.

5. DISCUSSION AND CONCLUSIONS

5.1. The ≥ 400 keV hard tail

Our analysis shows that the > 400 keV spectral properties of Cyg X-1 depend on the spectral state, as already suggested previously (e.g., McConnell et al. 2002). We detect a strong hard tail in the LHS, but obtain only upper limits in the IS and HSS. In Fig. 5 (left), we show a comparison of our LHS 0.75–1 MeV spectrum with those obtained with *CGRO/COMPTEL* during the June 1996 HSS and during an extended LHS observed with this instrument (McConnell et al. 2002, 2000). The IBIS hard tail is

compatible in terms of fluxes to within 2σ to those seen with COMPTEL and also with the *INTEGRAL*/SPI hard tail reported in JRC12 (see their Fig. 5). It is worth noting that Cyg X-1 is a notoriously highly variable source and flux evolution between different epochs is expected. To illustrate this behavior, we study data taken during two main periods, the covering March 2003 to December 2007 (MJD 52722–54460) and March 2008 to December 2009 (MJD 54530–55196), respectively. These intervals correspond to the analysis of LRW11. The two Compton spectra are shown in Fig. 5 (right). It is obvious that the flux of the hard tail varied between the two epochs and an evolution of the slope may also be visible. We note that these data are not separated by states, but as they cover the period before December 2009, they are dominated by the LHS (e.g., Fig. 1). We therefore conclude that, even in the same state, the hard tail shows luminosity variations.

A major difference to McConnell et al. (2002) is the non-detection of a hard tail in the HSS. McConnell et al. (2002) remark that between two epochs of HSS the hard tail either has a higher flux than in their averaged LHS or is not detected. Malyshev et al. (2013) also note that the 1996 HSS hard tail comes from a single occurrence of this state and may not reflect a typical behavior. While detection of a hard tail during the LHS, even if it shows variations, indicates an underlying process that is rather stable over long period of times, the apparent transience of the HSS hard tail may indicate a different origin for this feature. For example, in Cyg X-3 the very high energy (Fermi) flares are associated with transitions to the ultra soft state (Fermi LAT Collaboration et al. 2009). While this is similar to what is seen in Cyg X-1, all Fermi γ -ray flares of Cyg X-1 were reported during LHS (Bodaghee et al. 2013; Malyshev et al. 2013). While the lack of simultaneous very high energy GeV–TeV data, and/or polarimetric studies of the Comptel HSS hard tail prevent any further conclusion on the origin of this component, we conclude that the HSS hard tail and the LHS hard tail could be of different origin.

5.2. Polarization of the hard tail and its possible origin

A clear polarized signal is detected from Cyg X-1 with both IBIS and SPI while accumulating all data regardless of the spectral state of the source (LRW11, JRC12). Here we separated the data into different spectral states and studied the state dependent high energy polarization properties. The HSS and 300–400 keV polarigram can be described by a constant, indicating no or very little levels of polarization. The 400–2000 keV LHS polarigram shows a large deviation from a constant, which indicates that the Compton scattering from ISGRI is not an evenly circular distribution on PICSiT. We interpret this as evidence for the presence of polarization in this energy range, even if the polarigram shows some deviations from the theoretically expected curve (Fig. 4). In the 300–400 keV range, no evidence for polarization is found. This is consistent with the results obtained with SPI (JRC12) and shows that the polarization fraction is strongly energy dependent. Assuming a non-null level of polarization, a reasonable assumption given the above arguments, we estimate that the detection of polarized emission is significant at higher than 3σ . Given the larger amount of data and the separation into different spectral states, one could have

expected to obtain more robust results, and more constrained polarization parameters compared to LRW11 and JCR12, while the uncertainties we obtained are, at best, of the same order. The reason for this lies in the behavior of Cyg X-1. While the earlier studies did not perform a state dependent analysis, our state classification reveals that both studies were dominated by data taken during the LHS and the IS (see also Fig. 1). In fact, compared to LRW11 the number of ScWs measured during the LHS increased only by 13%, and 75% of the IS data comes from the period considered in these earlier studies, i.e., before \sim MJD 55200. On the other hand, about 94% of the HSS data are new. It is therefore not surprising that our hard state result is consistent with the earlier results, as these were fully dominated by the (polarized) hard state data. The exposure of the less polarized IS data was not large enough to significantly “dilute” the polarization. Our result clearly shows that larger amounts of data in each of the states are needed to refine the constrain on the polarization properties and their relation to the spectral states.

Our LHS spectral analysis shows that the 10–1000 keV spectrum can be decomposed into several spectral components. A (reflected) thermal Comptonization component in the range \sim 10–400 keV, and a power-law tail dominating above \sim 400 keV (§4.2.1). The origin of the seed photons for the Compton component may either be an accretion disk or synchrotron photons from a compact jet undergoing synchrotron self-Comptonization (SSC). As discussed elsewhere (e.g., Laurent et al. 2011), due to the large number of scatterings the Comptonization spectrum from a medium with an optical depth $\tau \geq 1$ is not expected to show intrinsic polarization, especially with such a high fraction as the one we detect here. Multiple Compton scattering, as expected in such a medium, will “wash out” the polarization of the incident photons even if the seed photons are polarized (e.g., jet photons). It is therefore not surprising that the LHS \lesssim 400 keV component has a very low (or zero) polarization fraction (see also Russell & Shahbaz 2013).

The origin of the hard-MeV tail is much less clear and is highly model-dependent. Two main families of models can explain the (co-)existence of cut-off power-law and/or pure power-law like emissions in the energy spectra of BHBs. The first is based on the presence of an hybrid thermal-non thermal population of electron in a “corona”, and hybrid Comptonization have been successfully applied to the spectra of, e.g., GRO J1655–40 or GX 339–4 (e.g., Caballero-García et al. 2009; Joinet et al. 2007), and even to \sim 1–10000 keV spectra of Cyg X-1, in both the HSS and LHS (McConnell et al. 2002). A double thermal component has been used to represent the 20–1000 keV SPI data of 1E 1740–2947 well (Bouchet et al. 2009).

The second family of models essentially contains the same radiation processes but is based on the presence of a jet emitting through direct synchrotron emission, thermal Comptonization of the soft disk photons on the base of the jet, and/or SSC of the synchrotron photons by the jet’s electrons (e.g., Markoff et al. 2005). Such models have been used with success to fit the data of some BH, and particularly GX 339–4 and XTE J1118+480 (Markoff et al. 2005; Maitra et al. 2009; Nowak et al. 2011). It should be noted, however, that they obviously rely on the presence

of a compact jet and therefore can only be valid when/if a compact jet is present.

The capacities of the current high energy missions, albeit excellent, do not permit today an easy discrimination between the different families of models. This has nicely been illustrated in the specific case of Cyg X-1 through the 0.8–300 keV spectral analysis of the Suzaku/RXTE observations (Nowak et al. 2011). Different and complementary approaches and arguments can, however, be used to try and identify the most likely origin for the hard power-law tail. The fundamental plane between radio luminosity and X-ray luminosity (e.g., Corbel et al. 2003) has originally been used as an argument for a (small) contribution of the jet to the X-ray domain. Our approach here was to first separate the radio data sets into different spectral states, based on a model-independent classification. It was only because of this separation that could we show that a hard polarized tail is present in the LHS, with a high polarization fraction, together with a radio jet. The very high level of polarization can only originate from optically thin synchrotron emission (see below), and implies a highly ordered magnetic field similar to that expected in jets. The synchrotron tail coincides with thermal Comptonization at lower energies and with a radio jet. The presence of all these features is qualitatively compatible with the multi-component emission processes predicted by compact jet models such as those of Markoff et al. (2005). While polarization of the (compact) jet emission has already been widely reported in the radio domain (Brocksopp et al. 2013, and references therein), a thorough study of the multi-wavelength polarization properties of Cyg X-1 has only recently been undertaken by Russell & Shahbaz (2013). These authors, in particular, showed that the multi-wavelength spectrum and polarization properties of Cyg X-1 are quantitatively compatible with the presence of a compact jet that dominates the radio to IR domain and is also responsible for the MeV tail. A similar conclusion was drawn by Malyshev et al. (2013) under the assumption that “the polarization measurements were robust” and that therefore the MeV tail could only originate from synchrotron emission. This prerequisite is reinforced by our refined and spectral-state dependent study of the polarized properties of Cyg X-1 at 0.3–1 MeV. A polarized signal is indeed suggested by the 400–2000 keV LHS data and the large degree of polarization measured in §4.3 implies a very ordered magnetic field. Assuming the magnetic field lines are anchored in the disk implies that the γ -ray polarized emission comes from close to the inner ridge of the disk where the magnetic energy density is highest. This constraint is difficult to reconcile with a spherically shaped corona medium, where the magnetic field lines are more likely to be tangled and where the polarized component necessarily comes from the outer shells of the corona where the optical depth is the lowest. We, therefore, conclude that **in the LHS** the 0.4–2 MeV tail detected with *INTEGRAL*/IBIS is very likely due to optically thin synchrotron emission, and that this emission comes from the detected compact jet.

5.3. Compatibility of the Cyg X-1 hard state parameters with synchrotron emission

The synchrotron spectrum of a population of electrons following a power-law distribution, $dN(E) \propto E^{-p}d(E)$, where p is the particle distribution index, can be approximated by a power-law function over a limited range of energy, i.e., $F_{E_1, E_2}(E) \propto E^{-\alpha}$ over $[E_1, E_2]$ (Rybicki & Lightman 1979). In the case of compact jets, two main domains are usually considered: the optically thick regime with $\alpha \lesssim 0$ and the optically thin regime with $\alpha > 0$. The break between the two regimes is typically in the infrared band (e.g., Corbel & Fender 2002; Rahoui et al. 2011; Russell & Shahbaz 2013; Corbel et al. 2013). The jet synchrotron spectrum is optically thin towards higher energies, and here $\alpha = (p - 1)/2$. The jet emission becomes negligible in the range from the optical to hard X-rays when compared to the contribution from other components such as the companion star, the accretion disk, or the corona. Our results indicate that it again dominates above a few hundred keV (see also Russell & Shahbaz 2013, for a multi-components modeling of the multi-wavelength Cyg X-1 spectrum).

The degree of polarized emission expected in the optically thin regime is $\Pi = \frac{p+1}{p+7/3}$ (Rybicki & Lightman 1979). Since the flux spectral index $\alpha = \Gamma - 1$, where Γ is the photon spectral index, it is possible to deduce p from the measured spectral shape. With $\Gamma = 1.4_{-0.3}^{+0.2}$ (§4.2.1) we obtain $p = 1.8_{-0.7}^{+0.4}$ and thus expect $\Pi_{\text{expected}} = 67.8_{-5.5}^{+2.7}\%$. This value is consistent with the value measured in the LHS ($\Pi = 75 \pm 32\%$).

We determine a polarization angle of $\sim 40^\circ$ compatible with the SPI results (JRC12). This angle, however, differs by about 60° from the polarization angles measured in the radio and optical (Russell & Shahbaz 2013, and references therein). Assuming that the γ -ray polarized component comes from the region of the jet that is closest to the launch site (i.e., the inner ridge of the disk and/or the BH), the change in polarization angle implies that the field lines in the γ -ray emitting region have a different orientation than further out in the jet. This could be indicative of a relatively large opening angle at the basis of the jet (as sketched in Fig. 3 of Russell & Shahbaz 2013). Alternatively the large offset could simply be due to strongly twisted magnetic field lines close to the accretion disk.

6. SUMMARY

We have presented a broad band 10 keV–2 MeV spectral analysis of the microquasar Cyg X-1 based on about 10 years of data collected with the JEM-X and IBIS telescopes onboard the *INTEGRAL* observatory. We have used the classification criteria of Grinberg et al. (2013) to separate the data into hard (LHS), intermediate (IS), and soft (HSS) states. We have studied the radio behavior of the source associated with these states as observed with the Ryle/AMI radio telescope at 15 GHz.

- The ≤ 400 keV emission is well represented by Comptonization spectra with further reflection off the accretion disk. In the LHS and IS, the Comptonization process is thermal and optically thick, i.e., the corona has an optical depth $\tau > 1$ and the electrons have a Maxwellian distribution. As a result, a clear high-energy cut-off is seen in the spectra. In the HSS the situation is not that

clear, although a cut-off is also necessary to give a good representation of the broad band spectrum.

- A clear hard tail is detected in the LHS when also considering the 0.4–2 MeV data. This high energy component is well represented by a hard power-law with no obvious cut-off. The detection of the hard tail is compatible with earlier claims of the presence of such a component in spectra of Cyg X-1. We show that this component is variable within same state, as is seen when considering *INTEGRAL* observations from two arbitrary epochs but the same state.
- In the radio domain, the 15 GHz data show a definite detection with averaged flux densities of respectively ~ 13 and ~ 15 mJy in the LHS and IS, compatible with the presence of a compact jet in those states. No persistent radio emission is detected in the HSS, implying the absence of a compact radio core.
- In the LHS, we measure a polarized signal above 400 keV with a large polarization fraction ($75 \pm 32\%$). This high degree of polarization and the polarization angle ($40^\circ 0 \pm 14^\circ 3$) are both compatible with previous studies by us and others. We obtain non-constraining upper limits on the polarization fraction in the IS and HSS, which have significantly lower exposure.
- The high degree of polarization of the hard tail can only originate from synchrotron emission in an highly ordered magnetic field. The demonstrated presence of radio emission in the LHS points towards the compact jet as the origin for the 0.4–2 MeV emission, corroborating earlier theoretical and multi-wavelengths studies (Malyshev et al. 2013; Russell & Shahbaz 2013). Our spectral state-resolved and multi-wavelength approach therefore further confirms the conclusion presented in the earlier, non state-resolved studies based

on *INTEGRAL* data only (Laurent et al. 2011; Jourdain et al. 2012).

- We increased the total *INTEGRAL* exposure time and, in particular, nearly doubled the amount of data taken in the HSS. We, however, still do not reach strong constraints on the polarization fraction in this state, even if we showed that the hard tail is much fainter. Provided the source does not change state, we have gotten *INTEGRAL* time approved to further increase the exposure time in the HSS, which will allow us to obtain tighter constraints on the polarization signal in this very state.

This paper is based on observations with *INTEGRAL*, an ESA project with instruments and science data centre funded by ESA member states (especially the PI countries: Denmark, France, Germany, Italy, Switzerland, Spain) and with the participation of Russia and the USA.

We acknowledge S. Corbel, R. Belmont, J. Chenevez, and J.A. Tomsick for very fruitful discussions about several aspects presented in this paper. J.R. acknowledges funding support from the French Research National Agency: CHAOS project ANR-12-BS05-0009 (<http://www.chaos-project.fr>), and from the UnivEarthS Labex program of Sorbonne Paris Cité (ANR-10-LABX-0023 and ANR-11-IDEX-0005-02). This work has been partially funded by the Bundesministerium für Wirtschaft und Technologie under Deutsches Zentrum für Luft- und Raumfahrt Grants 50 OR 1007 and 50 OR 1411. V.G. acknowledges support provided by NASA through the Smithsonian Astrophysical Observatory (SAO) contract SV3-73016 to MIT for Support of the Chandra X-Ray Center (CXC) and Science Instruments; CXC is operated by SAO for and on behalf of NASA under contract NAS8-03060. We acknowledge the support by the DFG Cluster of Excellence “Origin and Structure of the Universe”. We are grateful for the support of M. Cadolle Bel through the Computational Center for Particle and Astrophysics (C2PAP).

REFERENCES

- Arnaud, K. A. 1996, in *Astronomical Society of the Pacific Conference Series*, Vol. 101, *Astronomical Data Analysis Software and Systems V*, ed. G. H. Jacoby & J. Barnes, 17
- Böck, M., Grinberg, V., Pottschmidt, K., et al. 2011, *A&A*, 533, A8
- Bodaghee, A., Tomsick, J. A., Pottschmidt, K., et al. 2013, *ApJ*, 775, 98
- Bolton, C. T. 1972, *Nature*, 235, 271
- Bolton, C. T. 1975, *ApJ*, 200, 269
- Bouchet, L., del Santo, M., Jourdain, E., et al. 2009, *ApJ*, 693, 1871
- Bowyer, S., Byram, E. T., Chubb, T. A., & Friedman, H. 1965, *Science*, 147, 394
- Brocksopp, C., Corbel, S., Tzioumis, A., et al. 2013, *MNRAS*, 432, 931
- Brocksopp, C., Tarasov, A. E., Lyuty, V. M., & Roche, P. 1999, *A&A*, 343, 861
- Caballero, I., Zurita Heras, J. A., Mattana, F., et al. 2012, in *Proceedings of “An INTEGRAL view of the high-energy sky (the first 10 years)”* 15-19 October 2012, Paris, France.
- Caballero-García, M. D., Miller, J. M., Trigo, M. D., et al. 2009, *ApJ*, 692, 1339
- Cadolle Bel, M., Sizun, P., Goldwurm, A., et al. 2006, *A&A*, 446, 591
- Corbel, S., Aussel, H., Broderick, J. W., et al. 2013, *MNRAS*, 431, L107
- Corbel, S. & Fender, R. P. 2002, *ApJ*, 573, L35
- Corbel, S., Fender, R. P., Tomsick, J. A., Tzioumis, A. K., & Tingay, S. 2004, *ApJ*, 617, 1272
- Corbel, S., Nowak, M. A., Fender, R. P., Tzioumis, A. K., & Markoff, S. 2003, *A&A*, 400, 1007
- Coriat, M., Corbel, S., Prat, L., et al. 2011, *MNRAS*, 414, 677
- Dean, A. J., Clark, D. J., Stephen, J. B., et al. 2008, *Science*, 321, 1183
- Fender, R., Corbel, S., Tzioumis, T., et al. 1999, *ApJ*, 519, L165
- Fender, R. P., Homan, J., & Belloni, T. M. 2009, *MNRAS*, 396, 1370
- Fender, R. P., Stirling, A. M., Spencer, R. E., et al. 2006, *MNRAS*, 369, 603
- Fermi LAT Collaboration, Abdo, A. A., Ackermann, M., et al. 2009, *Science*, 326, 1512
- Forot, M., Laurent, P., Grenier, I. A., Gouiffès, C., & Lebrun, F. 2008, *ApJ*, 688, L29
- Gallo, E., Fender, R. P., & Pooley, G. G. 2003, *MNRAS*, 344, 60
- García, J., Dauser, T., Lohfink, A., et al. 2014, *ApJ*, 782, 76
- Gies, D. R., Bolton, C. T., Thomson, J. R., et al. 2003, *ApJ*, 583, 424
- Grinberg, V., Hell, N., Pottschmidt, K., et al. 2013, *A&A*, 554, A88
- Grinberg, V., Leutenegger, M. A., Hell, N., et al. 2015, *ã*
- Grinberg, V., Pottschmidt, K., Böck, M., et al. 2014, *A&A*, 565, A1

- Homan, J. & Belloni, T. 2005, *Ap&SS*, 300, 107
- Joinet, A., Jourdain, E., Malzac, J., et al. 2007, *ApJ*, 657, 400
- Jourdain, E., Roques, J. P., Chauvin, M., & Clark, D. J. 2012, *ApJ*, 761, 27
- Labanti, C., Di Cocco, G., Ferro, G., et al. 2003, *A&A*, 411, L149
- Laurent, P., Rodriguez, J., Wilms, J., et al. 2011, *Science*, 332, 438
- Lebrun, F., Leray, J. P., Lavocat, P., et al. 2003, *A&A*, 411, L141
- Lei, F., Dean, A. J., & Hills, G. L. 1997, *Space Sci. Rev.*, 82, 309
- Lund, N., Budtz-Jørgensen, C., Westergaard, N. J., et al. 2003, *A&A*, 411, L231
- Maier, D., Tenzer, C., & Santangelo, A. 2014, *PASP*, 126, 459
- Maitra, D., Markoff, S., Brocksopp, C., et al. 2009, *MNRAS*, 398, 1638
- Malyshev, D., Zdziarski, A. A., & Chernyakova, M. 2013, *MNRAS*, 434, 2380
- Markoff, S., Nowak, M. A., & Wilms, J. 2005, *ApJ*, 635, 1203
- McConnell, M. L., Ryan, J. M., Collmar, W., et al. 2000, *ApJ*, 543, 928
- McConnell, M. L., Zdziarski, A. A., Bennett, K., et al. 2002, *ApJ*, 572, 984
- Nowak, M. A., Hanke, M., Trowbridge, S. N., et al. 2011, *ApJ*, 728, 13
- Orosz, J. A., McClintock, J. E., Aufdenberg, J. P., et al. 2011, *ApJ*, 742, 84
- Pooley, G. G. & Fender, R. P. 1997, *MNRAS*, 292, 925
- Pottschmidt, K., Wilms, J., Chernyakova, M., et al. 2003a, *A&A*, 411, L383
- Pottschmidt, K., Wilms, J., Nowak, M. A., et al. 2003b, *A&A*, 407, 1039
- Quinn, J. L. 2012, *A&A*, 538, A65
- Rahoui, F., Lee, J. C., Heinz, S., et al. 2011, *ApJ*, 736, 63
- Reid, M. J., McClintock, J. E., Narayan, R., et al. 2011, *ApJ*, 742, 83
- Remillard, R. A. & McClintock, J. E. 2006, *ARA&A*, 44, 49
- Reynolds, M. T. & Miller, J. M. 2013, *ApJ*, 769, 16
- Rodriguez, J., Hannikainen, D. C., Shaw, S. E., et al. 2008a, *ApJ*, 675, 1436
- Rodriguez, J., Shaw, S. E., Hannikainen, D. C., et al. 2008b, *ApJ*, 675, 1449
- Russell, D. M. & Shahbaz, T. 2013, *MNRAS*, in press, arXiv, 1312.0942
- Rybicki, G. B. & Lightman, A. P. 1979, *Astronomy Quarterly*, 3, 199
- Stirling, A. M., Spencer, R. E., de la Force, C. J., et al. 2001, *MNRAS*, 327, 1273
- Titarchuk, L. 1994, *ApJ*, 434, 570
- Titarchuk, L. & Hua, X.-M. 1995, *ApJ*, 452, 226
- Titarchuk, L. & Lyubarskij, Y. 1995, *ApJ*, 450, 876
- Ubertini, P., Lebrun, F., Di Cocco, G., et al. 2003, *A&A*, 411, L131
- Vaillancourt, J. E. 2006, *PASP*, 118, 1340
- Varnière, P., Tagger, M., & Rodriguez, J. 2011, *A&A*, 525, A87+
- Varnière, P., Tagger, M., & Rodriguez, J. 2012, *A&A*, 545, A40
- Vedrenne, G., Roques, J.-P., Schönfelder, V., et al. 2003, *A&A*, 411, L63
- Walborn, N. R. 1973, *ApJ*, 179, L123
- Webster, B. L. & Murdin, P. 1972, *Nature*, 235, 37
- Wilms, J., Nowak, M. A., Pottschmidt, K., Pooley, G. G., & Fritz, S. 2006, *ã*, 447, 245
- Wilms, J., Pottschmidt, K., Pooley, G. G., et al. 2007, *ApJ*, 663, L97
- Xiang, J., Lee, J. C., Nowak, M. A., & Wilms, J. 2011, *ApJ*, 738, 78
- Ziólkowski, J. 2014, *MNRAS*, 440, L61

FIG. 1.— The two plots represent the long term radio (15 GHz, upper panels) *INTEGRAL*/IBIS hard X-ray (18-25 keV) light curves (lower panels) of Cyg X-1. The different symbols and colors (online version) indicate the different states of the source according to the classification presented by Grinberg et al. (2013). The upper plot covers the period MJD 52760–54250, when the radio monitoring was made with the older implementation of the radio telescope (known as the Ryle telescope). The lower one covers MJD 54500–56800 and shows the radio monitoring made after the upgrade (AMI telescope). Note the different vertical scales for the radio fluxes between the two plots.

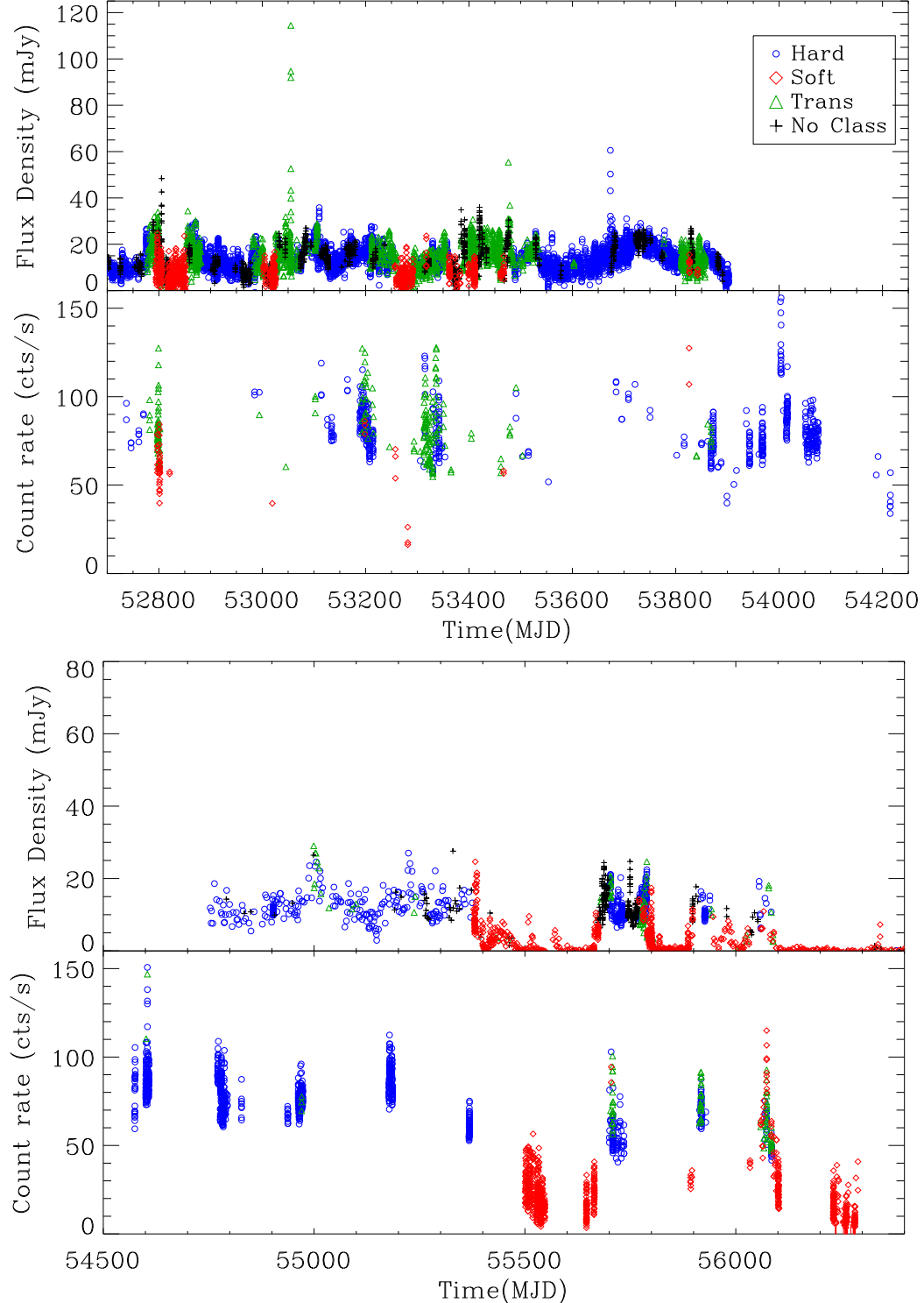


FIG. 2.— **Left:** χ^2 residuals to the hard state 10–400 keV spectra. From a) to d) simple power-law, power-law with exponential cut-off, Comptonization, Comptonization convolved by a reflection model. **Right:** 10–500 keV $\nu - F_\nu$ (JEM-X+ISGRI) spectrum with the best model (Comptonization convolved by a reflection model) superimposed as a continuous line. For the sake of clarity only one JEM X spectrum is represented.

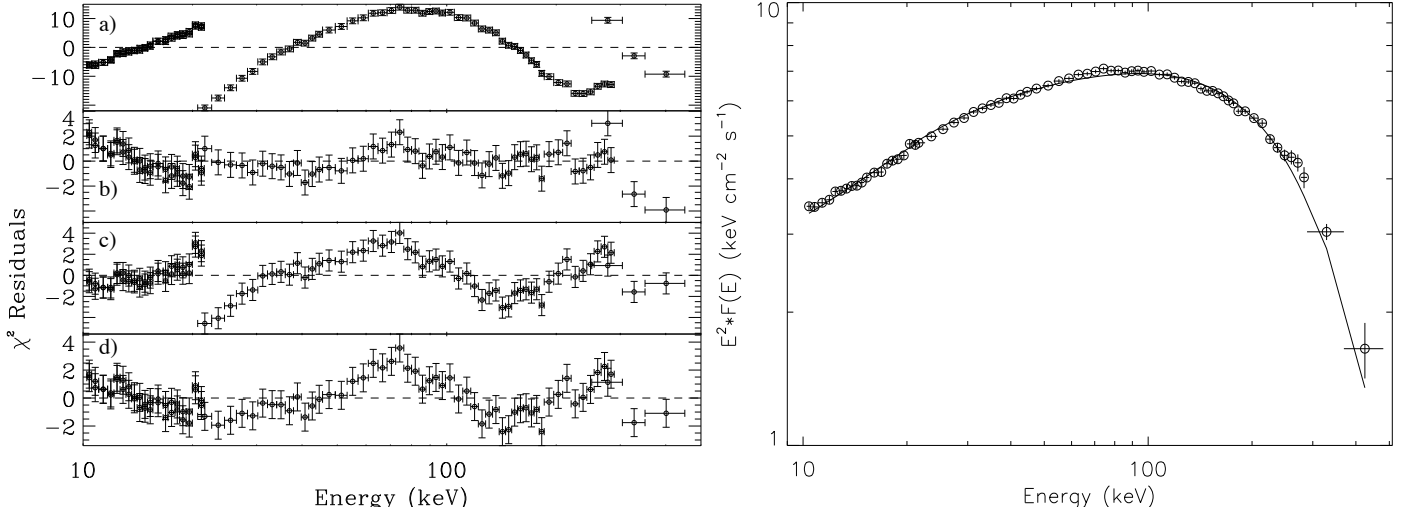


FIG. 3.— Unfolded 10 keV–2 MeV *INTEGRAL* spectra of Cyg X-1 in the three spectral states. The LHS spectrum is in blue circle, the IS in green diamonds and the HSS one in red triangles (colored points are available in the online version).

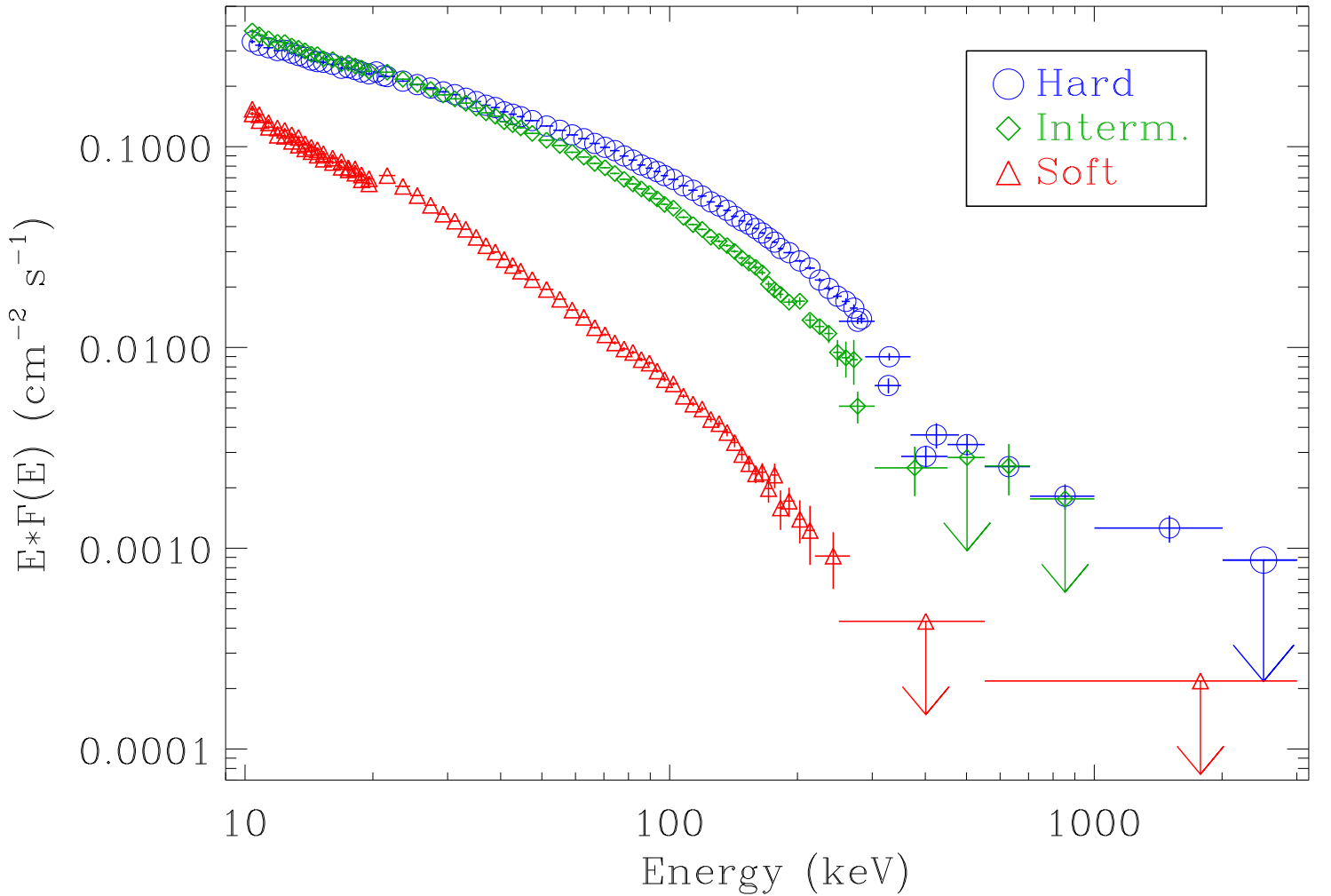


FIG. 4.— Polarigrams obtained in the LHS. **Left:** 300–400 keV. **Right:** 400–2000 keV.

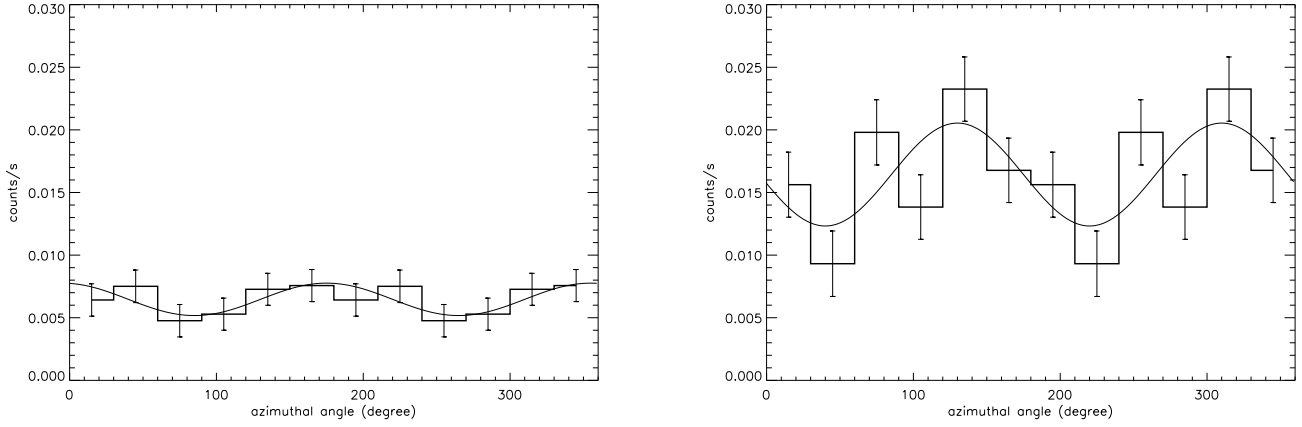
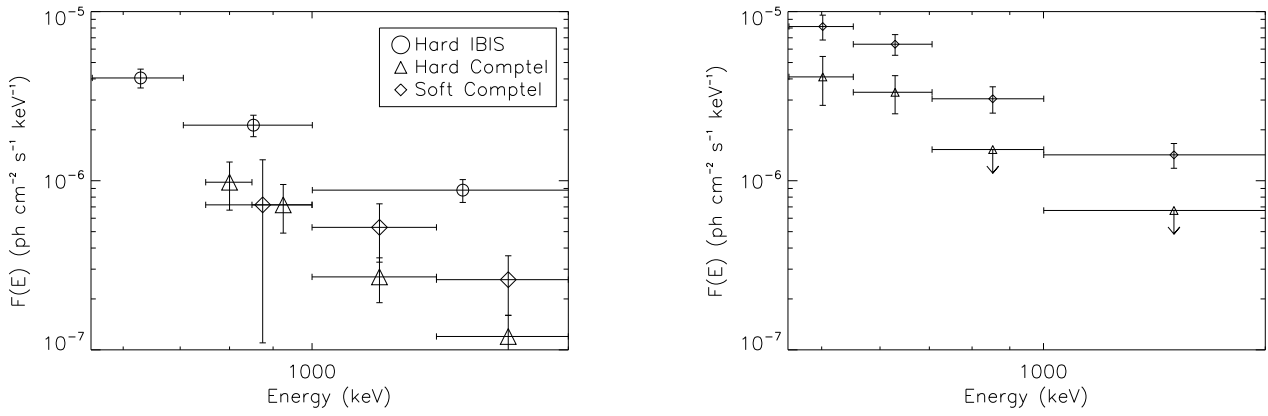


FIG. 5.— **Left:** Comparison of the *INTEGRAL*/IBIS and *CGRO*/Comptel high energy spectra. **Right:** Comparison of the *INTEGRAL*/Compton spectra accumulated over two different epochs.



Chandra Identification of Two AGN Discovered by *INTEGRAL*

John A. Tomsick^{1*}, Roman Krivonos^{1,2}, Farid Rahoui^{3,4}, Marco Ajello⁵, Jerome Rodriguez⁶,
Nicolas Barriere¹, Arash Bodaghee⁷, and Sylvain Chaty^{6,8}

¹*Space Sciences Laboratory, 7 Gauss Way, University of California, Berkeley, CA 94720-7450, USA*

²*Space Research Institute, Russian Academy of Sciences, Profsoyuznaya 84/32, 117997 Moscow, Russia*

³*European Southern Observatory, Karl Schwarzschild-Strasse 2, 85748 Garching bei Munchen, Germany*

⁴*Department of Astronomy, Harvard University, 60 Garden Street, Cambridge, MA 02138, USA*

⁵*Department of Physics and Astronomy, Clemson University, Clemson, SC 29634, USA*

⁶*Laboratoire AIM (UMR-E 9005 CEA/DSM-CNRS-Université Paris Diderot), Irfu/Service d'Astrophysique, CEA-Saclay, F-91191 Gif-sur-Yvette Cedex, France*

⁷*Georgia College & State University, CBX 82, Milledgeville, GA 31061, USA*

⁸*Institut Universitaire de France, 103 Boulevard Saint-Michel, 75005 Paris, France*

19 February 2015

ABSTRACT

Here, we report on observations of two hard X-ray sources that were originally discovered with the *INTEGRAL* satellite: IGR J04059+5416 and IGR J08297–4250. We use the *Chandra X-ray Observatory* to localize the sources and then archival near-IR images to identify the counterparts. Both sources have counterparts in the catalog of extended 2 Micron All-Sky Survey sources, and the counterpart to IGR J04059+5416 has been previously identified as a galaxy. Thus, we place IGR J04059+5416 in the class of Active Galactic Nuclei (AGN), and we suggest that IGR J08297–4250 is also an AGN. If this identification is correct, the near-IR images suggest that the host galaxy of IGR J08297–4250 may be merging with a smaller nearby galaxy. For IGR J04059+5416, the 0.3–86 keV spectrum from *Chandra* and *INTEGRAL* is consistent with an absorbed power-law with a column density of $N_{\text{H}} = (3.1^{+2.0}_{-1.5}) \times 10^{22} \text{ cm}^{-2}$ and a photon index of $\Gamma = 1.4 \pm 0.7$, and we suggest that it is a Seyfert galaxy. For IGR J08297–4250, the photon index is similar, $\Gamma = 1.5 \pm 0.8$, but the source is highly absorbed ($N_{\text{H}} = (6.1^{+10.1}_{-4.3}) \times 10^{23} \text{ cm}^{-2}$).

Key words: X-rays: general, X-rays: galaxies, galaxies: active, galaxies: Seyfert, stars: individual(IGR J04059+5416, IGR J08297–4250)

1 INTRODUCTION

The hard X-ray imaging by the *INTErnational Gamma-Ray Astrophysics Laboratory (INTEGRAL)* satellite (Winkler et al. 2003) has led to the discovery of a large number of new or previously poorly studied “IGR” sources. The most recent published catalogs of 20–100 keV sources detected by the Imager on-Board the *INTEGRAL* Satellite (IBIS; Ubertini et al. 2003) include more than 700 sources for the whole sky (Bird et al. 2010) and 402 sources within 17.5° of the Galactic plane¹ (Krivonos et al. 2012). The current *INTEGRAL* source catalog² includes 954 sources detected by IBIS. The nature of ≈ 200 of the IGR sources is still unknown according to the most up-to-date list³.

While *INTEGRAL* has found many new sources, it only localizes them to $1'–5'$, which is not nearly adequate for finding

optical/IR counterparts. Short exposures of IGR sources with the *Chandra X-ray Observatory* allow for a major advance in understanding the nature of these sources by providing sub-arcsecond positions, leading to unique optical/IR counterparts, as well as 0.3–10 keV spectra that can be used to measure column densities and continuum shapes (see Tomsick et al. 2006, 2008, 2009, 2012; Bodaghee et al. 2012, for examples of our previous work on *Chandra* follow-up of IGR sources). Other groups have been carrying out similar investigations (e.g., Fiocchi et al. 2010; Ratti et al. 2010; Paizis et al. 2011, 2012; Nowak et al. 2012; Karasev et al. 2012).

Prior to this study, little was known about IGR J04059+5416 and IGR J08297–4250. They were discovered in the Krivonos et al. (2012) hard X-ray survey, which includes 9-years of *INTEGRAL* data. They are listed as being unidentified in the Krivonos et al. (2012) catalog, and there have not been any more publications on these sources. A search of the SIMBAD database does not suggest any likely counterparts. The *Chandra* observations that we made to identify the sources are described in Section 2. Then, the results

* E-mail: jtomsick@ssl.berkeley.edu (JAT)

¹ see <http://hea.iki.rssi.ru/integral>

² see <http://isdc.unige.ch/integral/catalog/38/catalog.html>

³ see <http://irfu.cea.fr/Sap/IGR-Sources/>

are presented in Section 3, including *Chandra* localizations, near-IR identifications, and an analysis of the *Chandra* and *INTEGRAL* energy spectra. Section 4 includes a discussion of the results and the conclusions.

2 OBSERVATIONS AND DATA REDUCTION

IGR J04059+5416 and IGR J08297–4250 were both observed with *Chandra* for 4.9 ks in late-2013 (see Table 1). We used the Advanced CCD Imaging Spectrometer (ACIS, Garmire et al. 2003) instrument, which has a 0.3–10 keV bandpass, and includes two arrays of CCDs: ACIS-I and ACIS-S. Our observations used ACIS-I, giving a 16.9×16.9 arcmin² field-of-view (FOV), which easily covers the *INTEGRAL* error circles. We obtained the data from the *Chandra* X-ray Center and processed it using the *Chandra* Interactive Analysis of Observations (CIAO) v4.6 software and the Calibration Data Base (CALDB) v4.6.2. We used `chandra_repro` to produce event lists that were used for further analysis.

3 RESULTS

3.1 *Chandra* Counterpart Identifications

We searched for *Chandra* sources by running `wavdetect` (Freeman et al. 2002) on the ACIS-I images. We used the same method described in Tomsick et al. (2012), including binning the images to four different pixel sizes. In addition, we applied `wavdetect` to images in three different energy bands: 0.3–10 keV, 0.3–2 keV, and 2–10 keV. Considering the different binnings and different energy bands, we obtained 12 source lists, which we merged into a single list for each observation. We considered all sources detected at a significance level of $2\text{-}\sigma$ or greater.

For IGR J04059+5416, we detect 12 sources in the ACIS-I field, and they are listed in Table 2. The ACIS counts are determined using circular extraction regions with radii increasing with off-axis angle (θ) in the same manner as described in Tomsick et al. (2012). For the position uncertainties, we add the systematic and statistical errors in quadrature. For all sources, the systematic pointing error is $0.''64$ at 90% confidence and $1''$ at 99% confidence (Weisskopf 2005). The statistical uncertainty depends on the number of counts and the off-axis angle, and we use Equation 5 from Hong et al. (2005) to calculate this quantity. The Hong et al. (2005) equation gives a 95% confidence error, but we assume a normal distribution and convert it to a 90% confidence error before adding it in quadrature with the 90% confidence systematic error. Table 2 also includes an estimate of the hardness of each source. As detailed in Table 2 and Tomsick et al. (2012), it is defined so that the maximum hardness is 1.0 (all the counts in the 2–10 keV bin) and the minimum hardness is -1.0 (all the counts in the 0.3–2 keV bin).

Source #2 has the highest count rate, is only $2.2'$ from the *INTEGRAL* position of IGR J04056+5416, and has a hard spectrum. Source #1 is closer to the *INTEGRAL* position, but Source #2 is well within the $2\text{-}\sigma$ *INTEGRAL* error circle (see Figure 1). Considering that the count rate for Source #1 is an order of magnitude lower, we argue that Source #2 is a much more likely counterpart. The 2–10 keV image shown in Figure 1 also shows a relatively bright and hard source to the southwest of the *INTEGRAL* position. This is Source #7, and its count rate and hardness are only slightly lower than Source #2. Although Source #7 was not previously known to be an X-ray source, a catalog search shows that it is positionally coincident with a known radio source, 4C 54.04.

However, it is $6.2'$ away from the *INTEGRAL* position, which is well outside the $2\text{-}\sigma$ error circle and close to the $3\text{-}\sigma$ error circle. Overall, CXOU J040557.6+541845 (Source #2) is, by far, the most likely counterpart to IGR J04059+5416, and its *Chandra* position is given in Table 2. The 0.3–10 keV ACIS-I count rate for CXOU J040557.6+541845 is $1.89 \times 10^{-2} \text{ s}^{-1}$ (92.6 counts during the 4910 s observation).

We produced a source list for the IGR J08297–4250 field in the same manner as described above, and we find 18 sources detected by ACIS-I (see Table 3). Although Source #5 has the highest 0.3–10 keV count rate, it is a very soft source with a hardness of -0.72 ± 0.24 ($1\text{-}\sigma$ error). This is inconsistent with the hard spectrum required to explain the hard X-ray flux measured by *INTEGRAL*. Source #2 is closer to the center of the *INTEGRAL* error circle for IGR J08297–4250, and it is a much harder source with a hardness of >0.6 . In fact, of the 22.2 detected photons for Source #2, only one is in the 0.3–2 keV band. Other than Source #5, there are no sources with more than 20 counts, and the other sources with more than 5 counts listed in Table 3 are farther from the *INTEGRAL* position. The fact that CXOU J082941.0–425158 (Source #2) is the most likely counterpart for IGR J08297–4250 is illustrated in Figure 1 since it is clearly the brightest 2–10 keV source in the field. Its *Chandra* position is given in Table 3, and the 0.3–10 keV ACIS-I count rate for CXOU J082941.0–425158 is $4.52 \times 10^{-3} \text{ s}^{-1}$ (22.2 counts during the 4909 s observation). Below, we also discuss one of the fainter sources (Source #1 with 4.2 counts), CXOU J082940.7–425143, which is $16''$ from CXOU J082941.0–425158.

3.2 Near-IR identifications

We searched the VizieR database for counterparts to the *Chandra* sources at other wavelengths. Here, we only discuss the matches that led to conclusions about the nature of the sources. CXOU J040557.6+541845 (=IGR J04059+5416) is within $0.''46$ of 2MASX J04055765+5418446, which is from the catalog of extended sources found in the 2MASS survey (Skrutskie et al. 2006). The magnitudes are $J = 15.3 \pm 0.2$, $H = 14.2 \pm 0.2$, and $K_s = 13.6 \pm 0.2$. Figure 2 shows the UKIDSS *K*-band image for IGR J04059+5416, and the extended emission around 2MASX J04055765+5418446 is visible. The fact that this is an extended near-IR source provides evidence that it is an AGN. In addition, the source is present in the Sloan Digitized Sky Survey, SDSS J040557.62+541844.8, and is identified as a galaxy. A third identification is with WISE J040557.61+541844.9, which shows that the source is bright in the mid-IR with a $22.1 \mu\text{m}$ magnitude of 6.67 ± 0.06 . The WISE source has IR colors $[3.4 \mu\text{m}] - [4.6 \mu\text{m}] = 0.8$ and $[4.6 \mu\text{m}] - [12 \mu\text{m}] = 2.8$. These are typical colors of Flat Spectrum Radio Quasars (FSRQs) and Seyfert galaxies (see, e.g., Massaro et al. 2011). FSRQs have in general a bright radio emission. This source does not have any associated counterpart in the NRAO VLA Sky Survey (Condon et al. 1998). The lack of strong radio emission favors the Seyfert interpretation.

CXOU J082941.0–425158 (=IGR J08297–4250) is also present in the 2MASS catalog of extended sources being $0.''44$ from 2MASX J08294112–4251582. Its magnitudes are $J = 14.0 \pm 0.2$, $H = 12.5 \pm 0.1$, and $K_s = 12.3 \pm 0.1$. Figure 3 shows extended K_s -band emission out to $\approx 10''$. We also identify this source with WISE J082941.14–425157.8, which has a $22.1 \mu\text{m}$ magnitude of 6.37 ± 0.07 . The identification of IGR J08297–4250 with an extended near-IR source disfavors or rules out hard X-ray emitting Galactic populations. A High-Mass X-ray Binary (HMXB) might

be as bright in the near-IR as 2MASX J08294112–4251582, but HMXBs do not show extended near-IR emission. Another type of source to consider is the class of Pulsar Wind Nebulae (PWNe), which harbor rotation-powered pulsars. These sources have extended X-ray and radio emission, but they are extremely faint in the optical and near-IR. Out of 1800 rotation-powered pulsars, only 12 have UV, optical, or near-IR counterparts, and, with the exception of the Crab Nebula, they are all fainter than 22nd magnitude (Mignani 2011). Near-IR counterparts have also not been detected in observations of some of the brighter *INTEGRAL* PWNe (Curran et al. 2011). Thus, an AGN identification is very likely for IGR J08297–4250.

There is a second near-IR source about $16''$ to the North that also appears to be extended. It does not appear in the extended 2MASS catalog, but it is 2MASS J08294046–4251430 with magnitudes $H = 16.0 \pm 0.2$ and $K_s = 15.0 \pm 0.1$. We suggest a possible identification of this source with CXOU J082940.7–425143. The *Chandra* position falls within the extended emission, but it is $2.''6$ from the brightest part of the extended near-IR emission. The 2MASS astrometry is good to $\sim 0.''1$, indicating that the *Chandra* source position is clearly inconsistent with the brightest part of the near-IR emission. Whether the *Chandra*/2MASS association is valid or not, if 2MASS J08294046–4251430 is a galaxy, then it is possible that it is interacting with 2MASX J08294112–4251582. Thus, we consider these sources to potentially be a pair of merging galaxies.

3.3 Energy Spectra

We produced 0.3–10 keV *Chandra* source and background energy spectra and response files using the CIAO script `specextract`. We used a circular source extraction region with a radius of 5 pixels ($2.''5$) and obtained a background spectrum from a nearby source-free region. For part of our analysis, we also use 17–86 keV energy spectra from *INTEGRAL*/IBIS. The *INTEGRAL* spectra are data products obtained as part of the Krivonos et al. (2012) study, and they represent average spectra over a 9-year period. For IGR J04059+5416 and IGR J08297–4250, the *INTEGRAL* spectra include exposure times of 1.3 Ms and 5.6 Ms, respectively. In the following, we first perform spectral fitting for the two IGR sources with *Chandra* only, and then we jointly fit the *Chandra* and *INTEGRAL* spectra. Some caution is necessary regarding the joint fits since we are combining a single *Chandra* snapshot with *INTEGRAL*'s 9-year average. All spectral fitting is done with XSPEC v12.8.2.

3.3.1 IGR J04059+5416

Due to the low number of counts, we fit the *Chandra* spectra by minimizing the Cash statistic (Cash 1979). Although this statistic does not require binning of the data, we made a spectrum with a signal-to-noise ratio of at least 3 in each bin (except for the highest energy bin where the signal-to-noise ratio is 2.8) in order to look for any significant features in the residuals and to use the χ^2 value as a representative determination of the quality of the fit. A simple absorbed power-law model provides an acceptable fit with a Cash statistic of 2.0 and a reduced- χ^2 of 0.35 for 5 degrees of freedom (dof). As shown in Table 4, the column density, which is calculated using Wilms et al. (2000) abundances and Verner et al. (1996) cross sections, is $N_{\text{H}} = (3.5^{+2.4}_{-1.9}) \times 10^{22} \text{ cm}^{-2}$ (90% confidence errors are given here and throughout the paper). This is significantly

higher than the Galactic value along the IGR J04059+5416 line of sight, $N_{\text{H}} = 7 \times 10^{21} \text{ cm}^{-2}$ (Kalberla et al. 2005), indicating that some of the absorption is from the AGN's host galaxy. The photon index from the *Chandra*-only fit is $\Gamma = 1.5^{+0.9}_{-0.8}$.

We also performed spectral fits to the *Chandra*+*INTEGRAL* joint spectrum (see Table 4 and Figure 4). We used χ^2 minimization due to the high level of background for *INTEGRAL*. As before, we fit with an absorbed power-law model, and we also included a constant parameter, which allows for different overall normalizations for the two spectra (due to, e.g., possible source variability). For the joint fit, there is very little change to the N_{H} and Γ parameters. With a value of $2.9^{+8.9}_{-2.2}$, the *INTEGRAL* normalization relative to *Chandra* does not allow us to draw conclusions on the source variability (1.0 indicating no variability). The constant source case would imply a harder spectrum (see Table 4). For all the IGR J04059+5416 fits, we only included the three lowest energy *INTEGRAL* bins in the fit because the source was not detected in the highest energy bin. The $2\text{-}\sigma$ upper limit on the flux in the the 57–86 keV bin is somewhat lower than the power-law (see Figure 4), which could be the sign of a cutoff.

3.3.2 IGR J08297–4250

Here, we also began by fitting just the *Chandra* spectrum with an absorbed power-law model and minimizing the Cash statistic. This provides an acceptable fit with a Cash statistic of 6.4 and a reduced- χ^2 of 0.65 for 5 dof. For binning, we used a signal-to-noise ratio requirement of at least 1.25 per bin. The best fit spectral parameters are $N_{\text{H}} = 1.9 \times 10^{23} \text{ cm}^{-2}$ and $\Gamma = -0.8$, but they are both very poorly constrained since the spectrum only has 22 counts. We produced error contours for N_{H} and Γ , and these are shown in Figure 5. The two parameters are highly-degenerate, and it is unclear if the spectrum is intrinsically very hard or if the column density is very high.

As shown in Figure 4, the spectrum shows a high point at 6.0 ± 0.1 keV, and this could be interpreted as a noise fluctuation or a redshifted Fe K α emission line. When a narrow Gaussian is added, the Cash statistic drops from 6.4 to 0.4. To determine if the Gaussian is required by the data, we used `simfittest` to make 1000 simulated spectra with the absorbed power-law model as the parent distribution. For the significance test, we used a spectrum with 21 bins to lessen any bias due to binning. With the actual data, the Cash statistic decreases from 16.7 to 10.1 for 17 dof. When the simulated spectra are fit with and without a narrow Gaussian in the 5–7 keV range, they show improvements by at least as much as the actual data $\approx 5\%$ of the time, and we conclude that the significance of the line is $2.0\text{-}\sigma$. We consider this to be a marginal detection of a redshifted Fe K α line.

Fitting the *INTEGRAL* spectrum jointly with *Chandra* greatly improves the constraints on the spectral parameters (Table 5). A very large column density of $N_{\text{H}} = (6^{+10}_{-4}) \times 10^{23} \text{ cm}^{-2}$ is required, and while *Chandra* alone allowed for the possibility of a very hard power-law spectrum, we find $\Gamma = 1.5 \pm 0.8$, which is typical for AGN. The column density is very much in excess of the Galactic value along the line of sight. While the *INTEGRAL* normalization relative to *Chandra* allows for significant variability, the parameters do not change significantly for the constant source case, and the error contours for these parameters are shown in Figure 5. The addition of the *INTEGRAL* data allows us to rule out the low- N_{H} /hard- Γ solution that was a possibility with *Chandra* alone.

Figure 4 shows that the simple absorbed power-law fit results in a mismatch between the model and the lowest energy bin in the

Chandra spectrum. Although the discrepancy is only $1\text{-}\sigma$, the addition of absorption with partial covering provides a good explanation, and the ratio residual for this bin goes from being off-scale in Figure 4e (actually, the value of the ratio is 4.2 ± 3.2) to being very close to 1.0 (0.9 ± 0.7). While it is likely that there is partial covering absorption for this source, it does not provide a large enough improvement in the fit to be formally required, and the statistical quality of the spectrum is not sufficient to constrain the parameters.

4 DISCUSSION AND CONCLUSIONS

For our larger *Chandra* study in 2013–2014, we chose ten unidentified *INTEGRAL* sources from the Krivonos et al. (2012) catalog. While analysis of the data is still on-going (and one observation has not yet occurred), the observations that we report on here have yielded an identification of one AGN (IGR J04059+5416) and one likely AGN (IGR J08297–4250). Of the 402 sources in the Krivonos et al. (2012) catalog, 112 were identified as AGN or AGN candidates (with 104 being confirmed AGN). Although we selected sources within 8° of the Galactic plane (compared to the full catalog, which goes out to 17.5°), and IGR J04059+5416 and IGR J08297–4250 have Galactic latitudes of $b = 1.54^\circ$ and $b = -2.21^\circ$, respectively, it is still not extremely surprising for 20% of our sample to be composed of AGN. In our previous studies, we have identified several *INTEGRAL* sources near the Galactic Plane as AGN (Chaty et al. 2008; Zurita Heras et al. 2009; Tomsick et al. 2012).

The 112 AGN or AGN candidates in the Krivonos et al. (2012) catalog have 17–60 keV fluxes ranging from 0.37 mCrab to 12 mCrab with a median flux of 0.98 mCrab. In the Krivonos et al. (2012) catalog, the 17–60 keV fluxes of IGR J04059+5416 and IGR J08297–4250 are 0.86 and 0.35 mCrab, respectively. Thus, IGR J04059+5416 is close to the median flux, and IGR J08297–4250 is slightly fainter than the faintest source identified as an AGN in the catalog.

For IGR J04059+5416, the optical and near-IR information provides the strongest evidence that it is an AGN, but the type of AGN is not immediately clear. The *Chandra*+*INTEGRAL* spectral fit for the $N_{\text{INTEGRAL}}/N_{\text{Chandra}} = 1$ gives a very hard spectrum ($\Gamma = 0.9 \pm 0.2$), which might argue that the source is a blazar. However, the non-detection in the 57–86 keV band would require a sharp spectral cutoff, and this would not be expected for a blazar at this energy. It is more likely that the source is moderately variable and that it is a Seyfert galaxy. The 9-year 17–60 keV IBIS light curve⁴ does not show statistically significant variability, but the errors on individual flux measurements are large, and we calculate that the light curve allows for year-to-year flux changes by as much as a factor of two or three. Thus, it is possible that the *Chandra* observation occurred when the flux was relatively low.

For IGR J08297–4250, the *Chandra*+*INTEGRAL* fits indicate a power-law with an index consistent with what would be expected for a Seyfert galaxy, and the high absorption may indicate a Seyfert 2 classification. Although the 6.0 keV emission line is only significant at the $2\text{-}\sigma$ level, if its rest-frame energy is 6.4 keV (neutral iron $K\alpha$), then the redshift is $z = 0.07$. For an unabsorbed 0.3–10 keV flux of $2 \times 10^{-12} \text{ erg cm}^{-2} \text{ s}^{-1}$, the corresponding luminosity would be $\sim 10^{43} \text{ erg s}^{-1}$, which is typical for hard X-ray selected Seyfert 2 AGN (Ajello et al. 2012).

Koss et al. (2010) estimated that up to 25% of the AGN detected above 15 keV by *Swift*/BAT are found in hosts in an apparent state of merging with a nearby ($<30 \text{ kpc}$) galaxy. This, together with the fact that AGN luminosity increases for decreasing separation of the galaxy pair (Koss et al. 2012), highlights the role that merging has in triggering AGN activity. It is thus not unlikely to find an AGN hosted in a merging pair while following up on newly detected *INTEGRAL* sources. The majority of *INTEGRAL* Seyfert-like AGN are detected at $z \leq 0.1$, implying that the separation between CXOU J082941.0–425158 and CXOU J082940.7–425143 (assuming they are a merging pair of galaxies) is $<30 \text{ kpc}$. Koss et al. (2012) found that systems with a close companion (e.g. $<30 \text{ kpc}$) often display AGN activity in both hosts, similarly to what we find here. Moreover, some of the hosts of close merging pairs present a disrupted morphology (Koss et al. 2012), which might explain the offset of CXOU J082940.7–425143 from the brightest part of the extended near-IR emission. We thus believe that, on the basis of the evidence gathered so far, IGR J08297–4250 is an AGN that might possibly be hosted in a merging pair. However, final confirmation will have to await higher resolution near-IR imaging and optical spectroscopy.

ACKNOWLEDGMENTS

Support for this work was provided by the National Aeronautics and Space Administration (NASA) through *Chandra* Award Number GO4-15044X issued by the Chandra X-ray Observatory Center, which is operated by the Smithsonian Astrophysical Observatory for and on behalf of NASA under contract NAS8-03060. This publication makes use of data products from the Two Micron All Sky Survey, which is a joint project of the University of Massachusetts and the Infrared Processing and Analysis Center/California Institute of Technology, funded by the NASA and the National Science Foundation. This research has made use of the VizieR catalogue access tool, the SIMBAD database (CDS, Strasbourg, France), and the IGR Sources page maintained by J. Rodriguez & A. Bodaghee.

REFERENCES

- Ajello M., Alexander D. M., Greiner J., Madejski G. M., Gehrels N., Burlon D., 2012, *ApJ*, 749, 21
- Bird A. J. et al., 2010, *ApJS*, 186, 1
- Bodaghee A., Rahoui F., Tomsick J. A., Rodriguez J., 2012, *ApJ*, 751, 113
- Cash W., 1979, *ApJ*, 228, 939
- Chaty S., Rahoui F., Foellmi C., Tomsick J. A., Rodriguez J., Walter R., 2008, *A&A*, 484, 783
- Condon J. J., Cotton W. D., Greisen E. W., Yin Q. F., Perley R. A., Taylor G. B., Broderick J. J., 1998, *AJ*, 115, 1693
- Curran P. A., Chaty S., Zurita Heras J. A., Coleiro A., 2011, *A&A*, 534, A48
- Fiocchi M., Bassani L., Bazzano A., Ubertini P., Landi R., Capitanio F., Bird A. J., 2010, *ApJ*, 720, 987
- Freeman P. E., Kashyap V., Rosner R., Lamb D. Q., 2002, *ApJS*, 138, 185
- Garmire G. P., Bautz M. W., Ford P. G., Nousek J. A., Ricker G. R., 2003, in *X-Ray and Gamma-Ray Telescopes and Instruments for Astronomy*. Edited by Joachim E. Truemper, Harvey D. Tananbaum. Proceedings of the SPIE, 4851, 28

⁴ see <http://www.mpa-garching.mpg.de/integral/nine-years-galactic-survey/index.php>

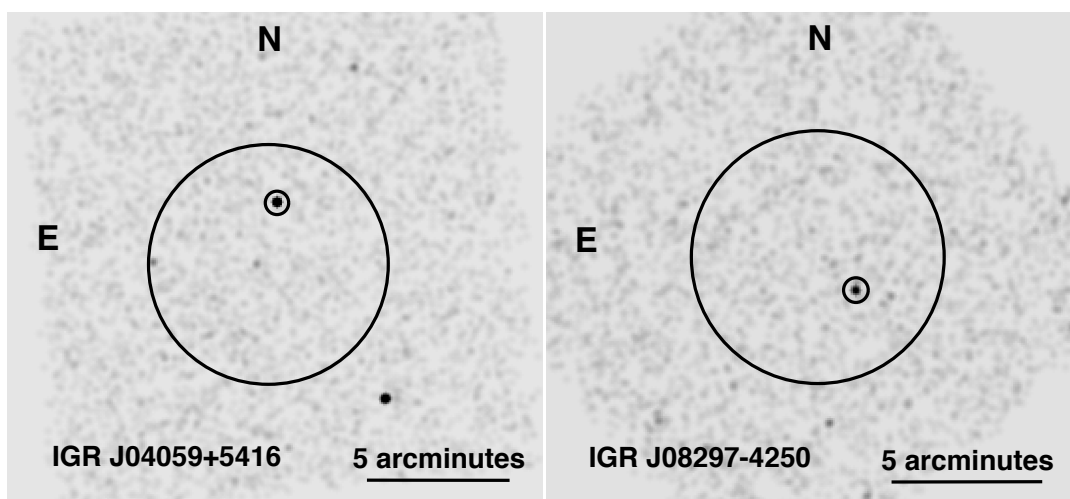


Figure 1. *Chandra*/ACIS-I images in the 2–10 keV band for IGR J04059+5416 (left) and IGR J08297–4250 (right). In each image, the larger circle has a $4'2$ radius and is the $2\text{-}\sigma$ *INTEGRAL* error circle. The smaller circles indicate the locations of the *Chandra* counterparts of the two IGR sources: CXOU J040557.6+541845 and CXOU J082941.0–425158. The images have been binned and smoothed.

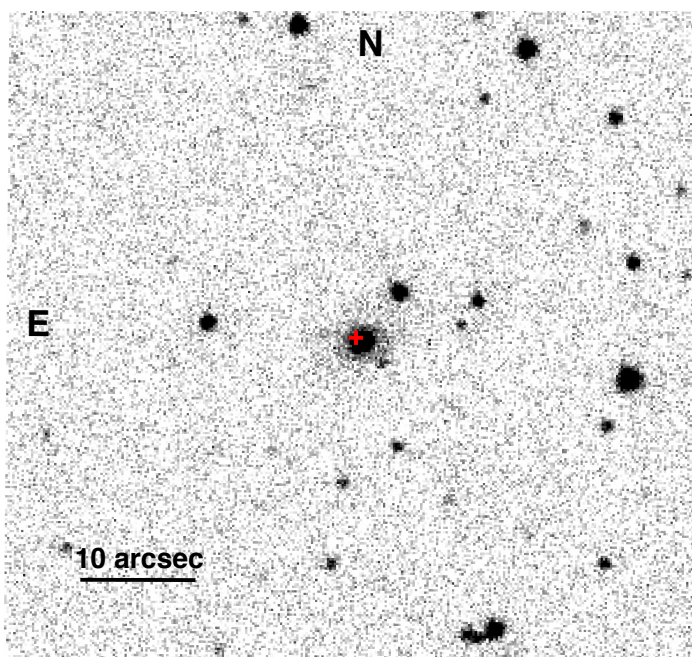


Figure 2. UKIDSS *K*-band image for IGR J04059+5416. The cross marks the *Chandra* position of CXOU J040557.6+541845, which we identify with 2MASX J04055765+5418446.

Table 1. *Chandra* Observation Log

Target	l (deg.)	b (deg.)	ObsID	Start Time (UT)	End Time (UT)	Exposure Time (s)
IGR J04059+5416	148.93	+1.54	15792	2013 Nov 22, 18.7 h	2013 Nov 22, 20.9 h	4910
IGR J08297–4250	261.08	–2.21	15793	2013 Dec 4, 20.3 h	2013 Dec 4, 22.1 h	4909

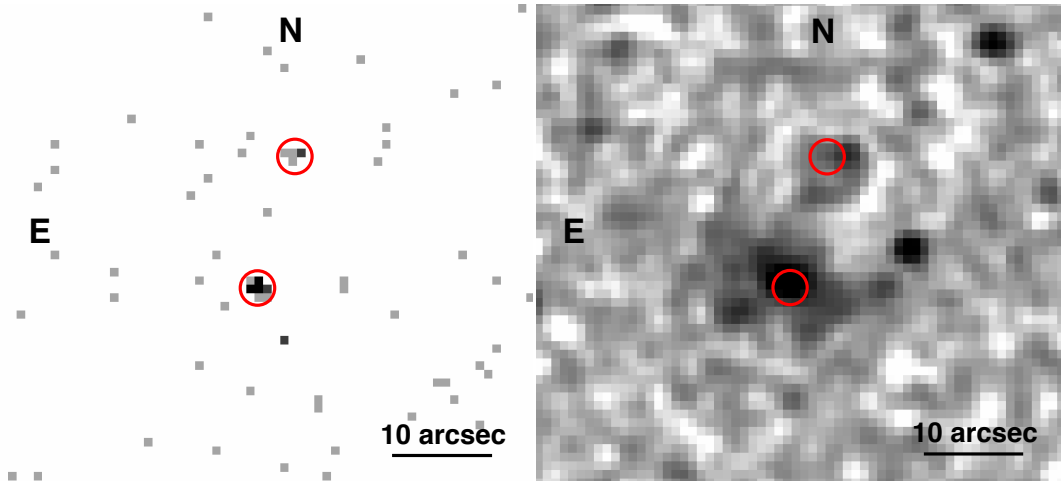


Figure 3. *Chandra* 0.3–10 keV (left) and 2MASS K_s -band (right) images for IGR J08297–4250. The southern source is CXOU J082941.0–425158 (=2MASX J08294112–4251582), which we identify as IGR J08297–4250. The northern source is CXOU J082940.7–425143. The centers of the red circles are coincident with the *Chandra* positions. The radii of these circles are $2''$, but the position uncertainties are significantly smaller ($0''.64$ at 90% confidence).

Table 2. *Chandra* Sources in IGR J04059+5416 Field

Source Number	θ^a (arcminutes)	<i>Chandra</i> R.A. (J2000)	<i>Chandra</i> Decl. (J2000)	ACIS Counts ^b	Position Uncertainty ^c	Hardness ^d
1	0.40	04 ^h 06 ^m 02 ^s .49	+54° 16' 34.''9	8.6	0.''75	>+0.1
2	2.21	04 ^h 05 ^m 57 ^s .69	+54° 18' 45.''1	92.6	0.''71	+0.59 ± 0.14
3	2.72	04 ^h 05 ^m 48 ^s .84	+54° 14' 21.''3	8.6	0.''86	<-0.2
4	3.64	04 ^h 06 ^m 14 ^s .57	+54° 19' 29.''7	6.6	1.''11	+0.1 ± 0.7
5	4.04	04 ^h 06 ^m 27 ^s .44	+54° 16' 38.''9	14.3	0.''94	+0.4 ± 0.4
6	5.60	04 ^h 05 ^m 26 ^s .99	+54° 13' 38.''6	7.3	1.''85	+0.0 ± 0.6
7	6.22	04 ^h 05 ^m 31 ^s .83	+54° 11' 51.''8	84.3	0.''87	+0.37 ± 0.14
8	6.44	04 ^h 05 ^m 54 ^s .96	+54° 10' 09.''7	6.3	2.''75	>-0.3
9	7.20	04 ^h 06 ^m 01 ^s .35	+54° 23' 45.''5	8.2	2.''90	>0.0
10	7.51	04 ^h 05 ^m 39 ^s .06	+54° 23' 26.''5	15.2	2.''03	+0.5 ± 0.4
11	7.64	04 ^h 05 ^m 44 ^s .57	+54° 23' 52.''1	7.2	3.''76	<+0.3
12	8.25	04 ^h 05 ^m 18 ^s .97	+54° 10' 51.''5	5.2	6.''28	<+0.2

^a The angular distance between the center of the *INTEGRAL* error circle, which is also the approximate *Chandra* aimpoint, and the source.

^b The number of ACIS-I counts detected (after background subtraction) in the 0.3–10 keV band.

^c The 90% confidence uncertainty on the position, including statistical and systematic contributions.

^d The hardness is given by $(C_2 - C_1)/(C_2 + C_1)$, where C_2 is the number of counts in the 2–10 keV band and C_1 is the number of counts in the 0.3–2 keV band.

Hong J., van den Berg M., Schlegel E. M., Grindlay J. E., Koenig X., Laycock S., Zhao P., 2005, *ApJ*, 635, 907
 Kalberla P. M. W., Burton W. B., Hartmann D., Arnal E. M., Bajaja E., Morras R., Pöppel W. G. L., 2005, *A&A*, 440, 775
 Karasev D. I., Lutovinov A. A., Revnivtsev M. G., Krivonos R. A., 2012, *Astronomy Letters*, 38, 629
 Koss M., Mushotzky R., Treister E., Veilleux S., Vasudevan R., Trippé M., 2012, *ApJ*, 746, L22
 Koss M., Mushotzky R., Veilleux S., Winter L., 2010, *ApJ*, 716, L125
 Krivonos R., Tsygankov S., Lutovinov A., Revnivtsev M., Churazov E., Sunyaev R., 2012, *A&A*, 545, A27
 Massaro F., D’Abrusco R., Ajello M., Grindlay J. E., Smith H. A., 2011, *ApJ*, 740, L48
 Mignani R. P., 2011, *Advances in Space Research*, 47, 1281

Nowak M. A. et al., 2012, *ApJ*, 757, 143
 Paizis A., Nowak M. A., Rodriguez J., Wilms J., Chaty S., Del Santo M., Ubertini P., 2012, *ApJ*, 755, 52
 Paizis A. et al., 2011, *ApJ*, 738, 183
 Ratti E. M., Bassa C. G., Torres M. A. P., Kuiper L., Miller-Jones J. C. A., Jonker P. G., 2010, *MNRAS*, 408, 1866
 Skrutskie M. F. et al., 2006, *AJ*, 131, 1163
 Tomsick J. A., Bodaghee A., Chaty S., Rodriguez J., Rahoui F., Halpern J., Kalemci E., Özbey Arabaci M., 2012, *ApJ*, 754, 145
 Tomsick J. A., Chaty S., Rodriguez J., Foschini L., Walter R., Kaaret P., 2006, *ApJ*, 647, 1309
 Tomsick J. A., Chaty S., Rodriguez J., Walter R., Kaaret P., 2009, *ApJ*, 701, 811
 Tomsick J. A. et al., 2008, *ApJ*, 680, 593
 Ubertini P. et al., 2003, *A&A*, 411, L131

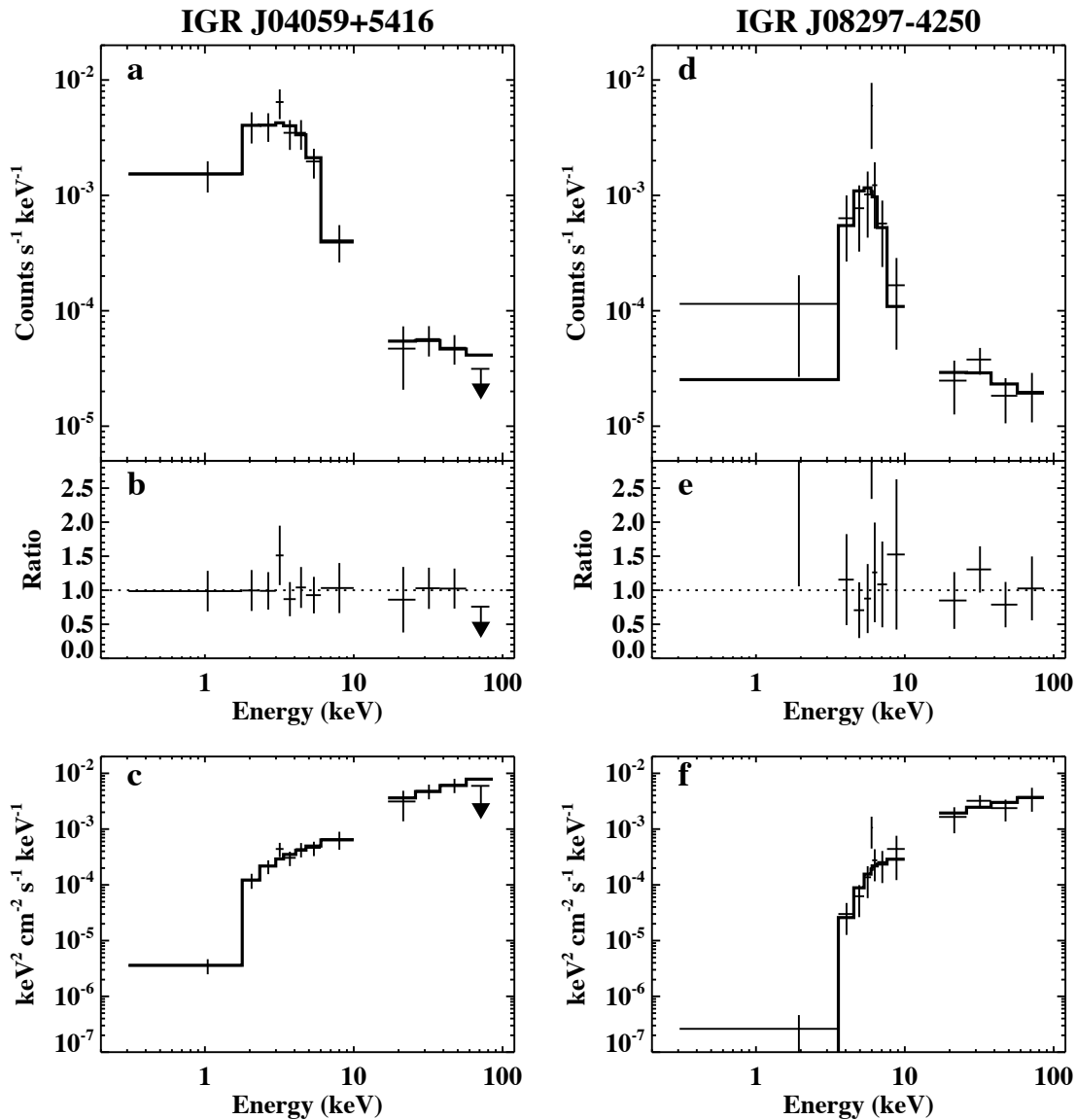


Figure 4. *Chandra* and *INTEGRAL* spectra for IGR J04059+5416 (3 left panels) and IGR J08297–4250 (3 right panels). (a) and (d): Counts spectra fitted with an absorbed power-law model. For IGR J04059+5416, the $2\text{-}\sigma$ upper limit is shown for the highest-energy *INTEGRAL* bin. (b) and (e): Data-to-model ratios. (c) and (f): Unfolded spectra.

- Verner D. A., Ferland G. J., Korista K. T., Yakovlev D. G., 1996, *ApJ*, 465, 487
 Weisskopf M. C., 2005, arXiv:astro-ph/0503091
 Wilms J., Allen A., McCray R., 2000, *ApJ*, 542, 914
 Winkler C. et al., 2003, *A&A*, 411, L1
 Zurita Heras J. A., Chaty S., Tomsick J. A., 2009, *A&A*, 502, 787

This paper has been typeset from a $\text{\TeX}/\text{\LaTeX}$ file prepared by the author.

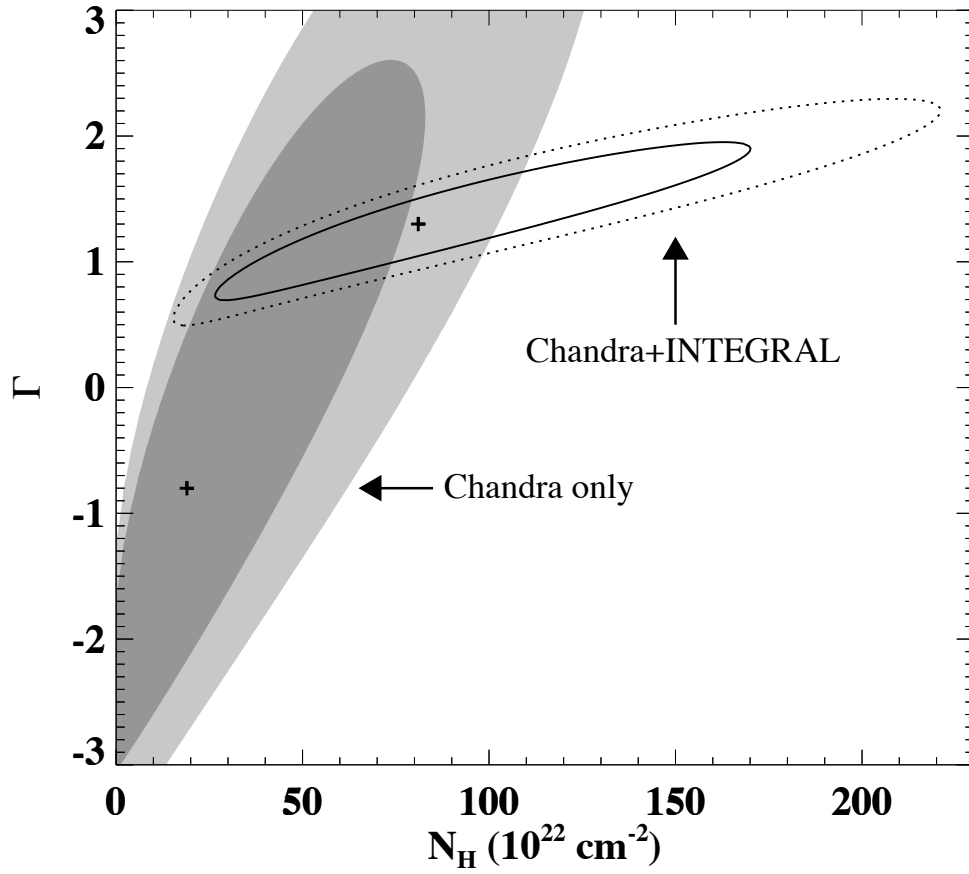


Figure 5. Contour plot for absorbed power-law fits to the IGR J08297–4250 spectra. The parameters are the column density (N_{H}) and the power-law index (Γ). For the fits to the *Chandra* spectrum, the dark shaded region corresponds to the 1- σ error range ($\Delta\chi^2 = 2.3$), and the light shaded region corresponds to the 90% confidence error range ($\Delta\chi^2 = 4.6$). For the joint fits to the *Chandra* and *INTEGRAL* spectrum, the solid line encloses the 1- σ error range, and the dotted line encloses the 90% confidence error range.

Table 3. *Chandra* Sources in IGR J08297–4250 Field

Source Number	θ^a (arcminutes)	<i>Chandra</i> R.A. (J2000)	<i>Chandra</i> Decl. (J2000)	ACIS Counts ^b	Position Uncertainty ^c	Hardness ^d
1	1.58	08 ^h 29 ^m 40 ^s .70	−42° 51′ 43.″3	4.2	0.″88	>−0.4
2	1.67	08 ^h 29 ^m 41 ^s .09	−42° 51′ 58.″5	22.2	0.″73	>+0.6
3	1.79	08 ^h 29 ^m 57 ^s .73	−42° 50′ 58.″4	3.2	0.″98	>−0.7
4	2.42	08 ^h 29 ^m 46 ^s .59	−42° 53′ 17.″0	3.2	1.″11	—
5	2.77	08 ^h 29 ^m 34 ^s .65	−42° 52′ 10.″6	40.2	0.″74	−0.7 ± 0.2
6	3.59	08 ^h 29 ^m 36 ^s .99	−42° 47′ 54.″8	8.2	1.″01	−0.4 ± 0.6
7	4.70	08 ^h 30 ^m 13 ^s .58	−42° 50′ 32.″1	5.8	1.″59	<−0.2
8	5.55	08 ^h 29 ^m 45 ^s .96	−42° 56′ 24.″8	13.8	1.″28	+0.4 ± 0.4
9	5.69	08 ^h 30 ^m 01 ^s .78	−42° 55′ 59.″0	5.8	2.″23	<+0.2
10	6.68	08 ^h 30 ^m 12 ^s .10	−42° 45′ 52.″3	10.8	2.″00	<−0.4
11	6.87	08 ^h 29 ^m 41 ^s .92	−42° 44′ 06.″2	2.8	6.″52	—
12	7.21	08 ^h 29 ^m 23 ^s .60	−42° 45′ 13.″3	2.9	7.″41	—
13	7.31	08 ^h 29 ^m 35 ^s .41	−42° 57′ 49.″0	4.9	4.″73	>−0.9
14	7.32	08 ^h 30 ^m 08 ^s .18	−42° 57′ 12.″0	7.9	3.″12	>+0.1
15	7.51	08 ^h 30 ^m 16 ^s .72	−42° 56′ 14.″5	16.9	1.″90	+0.5 ± 0.4
16	8.11	08 ^h 29 ^m 39 ^s .08	−42° 58′ 49.″2	4.9	6.″33	—
17	8.42	08 ^h 29 ^m 03 ^s .26	−42° 48′ 58.″3	11.9	3.″17	>+0.1
18	10.25	08 ^h 30 ^m 43 ^s .94	−42° 50′ 53.″8	4.9	13.″07	—

^a The angular distance between the center of the *INTEGRAL* error circle, which is also the approximate *Chandra* aimpoint, and the source.

^b The number of ACIS-I counts detected (after background subtraction) in the 0.3–10 keV band.

^c The 90% confidence uncertainty on the position, including statistical and systematic contributions.

^d The hardness is given by $(C_2 - C_1)/(C_2 + C_1)$, where C_2 is the number of counts in the 2–10 keV band and C_1 is the number of counts in the 0.3–2 keV band.

Table 4. IGR J04059+5416 Power-law Fit Parameters

Parameter ^a	Units	<i>Chandra</i> -only	<i>Chandra</i> + <i>INTEGRAL</i>	
N_{H}^b	10^{22} cm^{-2}	$3.5^{+2.4}_{-1.9}$	$3.1^{+2.0}_{-1.5}$	$2.1^{+1.2}_{-0.9}$
Γ	—	$1.5^{+0.9}_{-0.8}$	1.4 ± 0.7	0.9 ± 0.2
Unabs. Flux (0.3–10 keV)	$10^{-12} \text{ erg cm}^{-2} \text{ s}^{-1}$	$1.9^{+2.7}_{-0.6}$	$1.8^{+1.2}_{-0.5}$	$1.6^{+0.4}_{-0.3}$
Abs. Flux (0.3–10 keV)	$10^{-12} \text{ erg cm}^{-2} \text{ s}^{-1}$	$1.1^{+0.3}_{-0.4}$	$1.1^{+0.2}_{-0.4}$	$1.3^{+0.2}_{-0.3}$
$N_{\text{INTEGRAL}}/N_{\text{Chandra}}^c$	—	—	$2.9^{+8.9}_{-2.2}$	1.0^d

^a The errors on the parameters are 90% confidence.

^b The column density is calculated assuming Wilms et al. (2000) abundances and Verner et al. (1996) cross sections. Along this line of sight, the Galactic value is $N_{\text{H}} = 7 \times 10^{21} \text{ cm}^{-2}$ (Kalberla et al. 2005).

^c The *INTEGRAL* normalization relative to *Chandra*.

^d Fixed.

Table 5. IGR J08297–4250 Power-law Fit Parameters

Parameter ^a	Units	<i>Chandra+INTEGRAL</i>	
N_{H}^b	10^{22} cm^{-2}	61^{+101}_{-43}	81^{+100}_{-56}
Γ	–	1.5 ± 0.8	$1.3^{+0.7}_{-0.6}$
Unabs. Flux (0.3–10 keV)	$10^{-12} \text{ erg cm}^{-2} \text{ s}^{-1}$	$1.6^{+10.4}_{-1.2}$	$2.0^{+14.0}_{-1.6}$
Abs. Flux (0.3–10 keV)	$10^{-12} \text{ erg cm}^{-2} \text{ s}^{-1}$	$0.3^{+0.1}_{-0.2}$	0.3 ± 0.1
$N_{\text{INTEGRAL}}/N_{\text{Chandra}}^c$	–	$2.5^{+12.2}_{-2.0}$	1.0^d

^a The errors on the parameters are 90% confidence.

^b The column density is calculated assuming Wilms et al. (2000) abundances and Verner et al. (1996) cross sections. Along this line of sight, the Galactic value is $N_{\text{H}} = 9 \times 10^{21} \text{ cm}^{-2}$ (Kalberla et al. 2005).

^c The *INTEGRAL* normalization relative to *Chandra*.

^d Fixed.

A FIRST LOOK AT THE X-RAY POPULATION OF THE YOUNG MASSIVE CLUSTER VVV CL077

ARASH BODAGHEE^{1,2}, JOHN A. TOMSICK¹, FRANCESCA FORNASINI¹, FARID RAHOUI^{3,4}, AND FRANZ E. BAUER^{5,6,7}

Draft version January 6, 2015

ABSTRACT

Multi-wavelength analysis of the young massive cluster VVV CL077 is presented for the first time. Our *Chandra* survey of this region enabled the detection of three X-ray emitting stellar members of the cluster, as well as a possible diffuse X-ray component that extends a few arcseconds from the cluster core with an intrinsic flux of $(9\pm 3)\times 10^{-14}$ erg cm⁻² s⁻¹ in the 0.5–10 keV band. Infrared spectra we obtained for two of these X-ray point sources show absorption lines typical of the atmospheres of massive O stars. The X-ray spectrum from the visible extent of VVV CL077 i.e., a 15''-radius around the cluster, can be modeled with an absorbed power law with $N_{\text{H}} = (6^{+4}_{-3})\times 10^{22}$ cm⁻² and $\Gamma = 2\pm 1$. In addition, the X-ray core of VVV CL077 coincides with diffuse emission seen in the infrared band and with a local maximum in the radio continuum map. A possible association with a neighboring H II region would place VVV CL077 at a distance of around 11 kpc; on the far side of the Norma Arm. At this distance, the cluster is 0.8 pc wide with a mass density of $(1-4)\times 10^3 M_{\odot}$ pc⁻³.

Subject headings: X-rays: stars; infrared: stars; stars: early-type; open clusters and associations: individual (VVV CL077)

1. INTRODUCTION

Young Massive Clusters (YMCs) are loose collections of tens to thousands of stars more massive than the Sun (see Portegies Zwart et al. 2010, for a recent review). While they are a common feature of starburst galaxies, the Milky Way contains relatively few YMCs, only a small fraction of which are known X-ray emitters or have been (or can be) resolved into individual objects over several wavebands (e.g., Townsley et al. 2011b, and references therein). The most massive Galactic YMC is Westerlund 1 which is located 4 kpc away in the direction of the Norma Arm (e.g., Clark et al. 2005). Members of its stellar population have been resolved in several wavebands, including in the X-rays (by *Chandra*) where evidence was found for X-ray emission from massive, evolved (i.e., post-main-sequence) stars such as OB supergiants and Wolf-Rayet (WR) stars, from colliding wind binaries, and from an anomalous X-ray pulsar (Skinner et al. 2006; Munro et al. 2006b; Clark et al. 2008).

X-ray emitting YMCs with resolvable populations represent rare opportunities for observational tests of stellar evolution models including those involving the initial mass function and stellar and cluster dynamics, as well as for understanding the energetic feedback processes between massive stars and their environment. As the more massive stars tend to sink to the center of the cluster, they can pair up into massive binaries. Dynamical interactions between this core population can lead to the tightening of the binary (some of which can

evolve into an X-ray binary) or even to its ejection from the cluster (e.g., Portegies Zwart et al. 2007, 2010, and references therein). The distribution of the X-ray emitting point sources compared with the normal stellar content can be used to glean clues to the evolutionary history of the cluster.

We used *Chandra* to construct a high-resolution X-ray map of a section of the Norma Arm. Among the new objects discovered in the survey were multiple X-ray sources consistent with a YMC named VVV CL077 (Borissova et al. 2011) from the Vista Variables in the Via Lactae Survey (VVV: Minniti et al. 2010). In this paper, we describe the multi-wavelength properties of VVV CL077 by complementing the soft X-ray data with dedicated and archival observations gathered in the radio and infrared bands. The data and analytical methods are described in § 2, results are presented in § 3, and we discuss their implications in § 4. A summary of our key findings is given in § 5.

2. OBSERVATIONS & DATA ANALYSIS

2.1. X-ray Data

In 2011 June, the field of VVV CL077 was observed with *Chandra* during a survey of the Norma Arm (PI: Tomsick; observation IDs 12529 and 12530). An additional observation (ObsID 15625) was performed in early 2013 as part of *Chandra* Director's Discretionary Time in which VVV CL077 was serendipitously in the field. Table 1 contains the journal of these observations.

Reprocessing and reduction of the *Chandra* data relied on CIAO v4.5 and HEASoft 6.13. Detailed descriptions of the imaging analysis including background, exposure, and astrometric corrections, as well as the source-detection procedure are presented in Fornasini et al. (2014). These cleaned event files and their associated lists of detected sources were used as the inputs for this study. Source coordinates are given in the J2000.0 epoch with uncertainties quoted at 90% confidence.

Spectra were extracted from each event file in the 0.5–10 keV band for source regions (of variable sizes, see § 3) and from a source-free background region (a rectangle with dimensions: $200''\times 100'' = 400\text{ px}\times 200\text{ px}$) on the same detector chip. Parameters from absorbed power laws fit to the

¹ Space Sciences Laboratory, 7 Gauss Way, University of California, Berkeley, CA 94720, USA

² Dept. of Chemistry, Physics, and Astronomy, Georgia College and State University, CBX 082, Milledgeville, GA 31061, USA

³ European Southern Observatory, Karl-Schwarzschild-Strasse 2, 85748 Garching bei München, Germany

⁴ Dept. of Astronomy, Harvard University, 60 Garden Street, Cambridge, MA 02138, USA

⁵ Instituto de Astrofísica, Facultad de Física, Pontificia Universidad Católica de Chile, 306, Santiago 22, Chile

⁶ Millennium Institute of Astrophysics, Vicuña Mackenna 4860, 7820436 Macul, Santiago, Chile

⁷ Space Science Institute, 4750 Walnut Street, Suite 205, Boulder, CO 80301, USA

Table 1
Chandra observations

observation ID	start date	end date	exposure time (s)	off-axis angle of VVV CL077
12529	2011-06-16 06:58:05	2011-06-16 12:31:35	19014	3'6
12530	2011-06-16 12:31:35	2011-06-16 18:09:14	19260	8'5
15625	2013-03-23 08:17:49	2013-03-23 11:54:43	9839	6'3

individual spectra were statistically consistent with each other (i.e., there was no significant X-ray variability between 2011 and 2013). Therefore, the X-ray spectra described in the following sections are based on summing these individual spectra with `combine_spectra`.

2.2. Infrared Data

The infrared data consist of observations we gathered (PI: Rahoui) at the Cerro Tololo Inter-American Observatory (CTIO). Photometry was performed on 2011 July 19 with the NOAO/NEWFIRM instrument on the 4-m Blanco telescope. Simultaneous J , H , and K_s -band spectra ($R \sim 1200$) were collected on 2012 June 1–4 for five stars near the core of the VVV CL077 using the Ohio State Infrared Imager/Spectrometer (OSIRIS) mounted on the 4.1-m Southern Astrophysical Research (SOAR) Telescope.

A set of standard stars was observed in similar conditions in order to remove telluric absorption lines. The ABBA nodding technique was employed for background subtraction. Data reduction relied on the IRAF ECHELLE package which included bad-pixel correction, dark subtraction, linearity correction, flat-fielding, sky subtraction, and spectral extraction along the dispersion axis. The spectra were then wavelength-calibrated by comparing them to an argon lamp. Additional details regarding the observation and analysis procedures will be described in Rahoui et al. (2014).

Unfortunately, weather and atmospheric conditions were poor with thin clouds and a seeing higher than $1''.3$. Useful spectra were obtained for only 2 of the 5 targets, and only in the K -band. These data are supplemented by archival imaging observations from the VIRCAM instrument of the Vista Variables in the Via Lactae Survey (VVV: Minniti et al. 2010).

3. RESULTS

3.1. X-ray Data

In Fig. 1, we present images of the field of VVV CL077 in the X-rays (panels *a* and *b*: 0.5–10 keV from *Chandra*) and in the near infrared (K_s -band image from the VVV Survey (Minniti et al. 2010)). Detected X-ray sources are indicated by circles with radii equal to the position uncertainty at 90% confidence (see Table 2). The large circle (radius = $15''$) denotes the visual extent of the YMC in the infrared according to Borissova et al. (2011); it is centered at R.A. = $16^{\text{h}}34^{\text{m}}48^{\text{s}}$ and Decl. = $-47^{\circ}32'49''$.

This figure illustrates the complex morphology of the multi-wavelength emission from VVV CL077. In the infrared, the cluster contains 21 visually-identified members (Borissova et al. 2011), plus an extended component from unresolved stars and diffuse emission. In the X-rays, there are 3 detected sources not including extended emission. The size and shape of the extended emission in X-rays and infrared are similar and both have positions that are consistent with a local maximum in the radio continuum map from the Molonglo Galactic Plane Survey 2nd Epoch (MGPS-2: Murphy et al. 2007).

Two candidate X-ray sources are detected near the core of VVV CL077 (Table 2). The first source (in R.A.) is CXOU J163447.8–473243, is detected at a significance of 5.8σ at R.A. = $16^{\text{h}}34^{\text{m}}47^{\text{s}}.88$ and Decl. = $-47^{\circ}32'43''.8$ with an error radius of $1''.1$. The other, CXOU J163448.0–473246, is detected at 6.9σ at R.A. = $16^{\text{h}}34^{\text{m}}48^{\text{s}}.02$ and Decl. = $-47^{\circ}32'46''.3$ with an error radius of $1''.6$.

An angular distance of $2''.9$ separates the two X-ray objects, which is somewhat larger than the 90% encircled energy radius (i.e., $2''.4$ at 2.3 keV) of the Chandra point-spread function (PSF). Their X-ray positions are statistically incompatible at 90% confidence, and they are consistent with two bright nodes (stars belonging to VVV CL077) at opposite ends of a clump of unresolved emission in the infrared images. Given the positional coincidence with stars seen in the infrared, we conclude that these are likely to be two distinct X-ray sources rather than a single extended source.

To confirm whether any of the X-ray emission emanating from the VVV CL077 is extended or simply arises from two point sources, we used ray-tracing simulation data from ChaRT (part of the CIAO package) to generate reprojected PSFs for the observation in which the source had the smallest off-axis angle (ObsID 12529). For this simulation, we adopted an exposure time of 19 ks, and an absorbed power law spectrum with $\Gamma = 2.2$ and N_{H} fixed at $6 \times 10^{22} \text{ cm}^{-2}$ (see below, and in Table 3). The CIAO tool `srcextent` returns an intrinsic source size of $(7''.0 \pm 2''.5)$ for this emission, assuming the object is placed on-axis. Using an observation with a larger off-axis angle (ObsID 12530) leads to a larger intrinsic source size ($\sim 15''$), as expected.

After subtracting off 95% of the photons from the two X-ray point sources in the core via aperture restriction (see below), we find that there is still some residual emission with as many net counts outside the core (44) as from the two point sources combined (40). Along with the large intrinsic size of the X-ray emitting region, this indicates the presence of an extended and diffuse X-ray component, in addition to the emission from the two point sources.

Just outside the YMC is CXOU J163448.5–473229 which coincides spatially with a star that is likely associated with the YMC given the similar infrared colors to those of other cluster members. The best-fitting X-ray position (6.2σ detection significance) is R.A. = $16^{\text{h}}34^{\text{m}}48^{\text{s}}.53$ and Decl. = $-47^{\circ}32'29''.8$ with an error radius of $0''.9$. Its intrinsic size, estimated via ChaRT, is consistent with $0''$ in ObsID 12529.

Note that in ObsID 12530, a second candidate X-ray source is detected outside the YMC, CXOU J163448.6–473234, located at R.A. = $16^{\text{h}}34^{\text{m}}48^{\text{s}}.62$ and Decl. = $-47^{\circ}32'34''.1$ with an error radius of $2''.5$ (significance = 5.1σ). The large estimate of the source extent from `wavdetect` ($= 10''$), the fact that it was only detected in this ObsID when the YMC was $8''.5$ off axis, and the lack of a clear infrared counterpart suggest that this is the same source as CXOU J163448.5–473229 ($4''.4$ away), and so it will not be discussed further.

Spectral data were fit with power law, `apec`, and

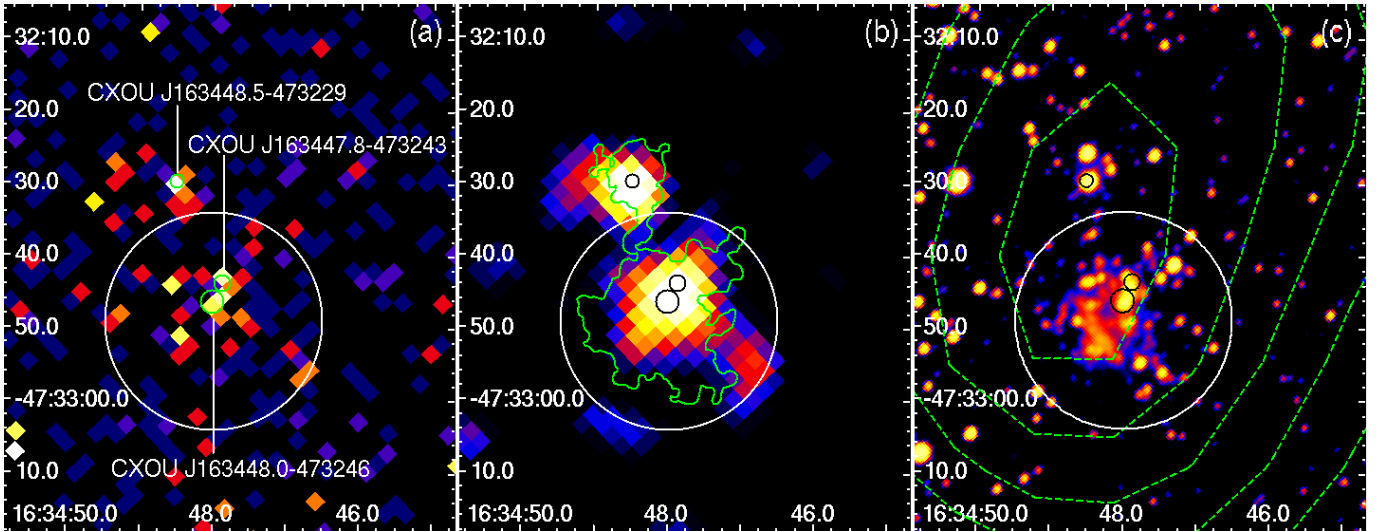


Figure 1. Images of the young massive cluster VVV CL077 in X-rays (0.5–10 keV) from *Chandra*-ACIS-I (panels *a* and *b*) and in the infrared (K_s) band from the VVV Survey (panel *c*: Minniti et al. 2010). Each image covers the same region of the sky presented in equatorial (J2000.0) coordinates where North is up and East is left. The X-ray mosaic images combine ObsIDs 12529 and 12530, they are astrometrically corrected, background subtracted, rebinned with $2''$ -wide pixels, and logarithmically scaled. The X-ray image in panel *b* has been smoothed with a Gaussian ($\sigma = 3$ px) while the infrared image is scaled with a histogram equalization. Detected X-ray sources are shown with their CXOU designations and circle sizes representing the position uncertainty (at 90% confidence, see Table 2). The large circle (radius = $15''$) represents the visual extent of the YMC according to Borissova et al. (2011). Contours overlaid on the smoothed X-ray image denote the outline of diffuse infrared emission from the cluster (and bright point sources), while the contours on the K_s -band image signify radio intensities at 843 MHz from the MGPS-2 Survey (Murphy et al. 2007).

Table 2
X-ray sources detected in the vicinity of VVV CL077

name	R.A. (deg)	decl. (deg)	90% conf. radius	det. sig. (σ)
CXOU J163447.8-473243	248.69950	-47.54550	$1''.1$	5.8
CXOU J163448.0-473246	248.70008	-47.54619	$1''.6$	6.9
CXOU J163448.5-473229	248.70221	-47.54161	$0''.9$	6.2

bremsstrahlung models. However, the observed photon counts within the source extraction regions are low (i.e., $\lesssim 100$ counts), and so we caution that any derived spectral parameters are merely estimates, and may not be indicative of the true values. Given the low source counts and very low background counts, spectral fitting relied on Cash (1979) statistics and Pearson (1900) χ^2 test statistics. All fits assumed Wilms et al. (2000) abundances and photoionization cross sections from Balucinska-Church & McCammon (1992). The hardness ratio is defined as $(H - S)/(H + S)$ where H is the count rate in 3–10 keV and S is the count rate in 0.5–3 keV.

The X-ray spectrum extracted from a $15''$ radius (30 pixels) around the infrared position of VVV CL077 is presented in Fig. 2. This spectrum includes the two X-ray point sources in the core of the YMC, plus diffuse X-ray emission. There are 107 net counts in this region for a hardness ratio of 0.10 ± 0.11 . A power law fit to the data yields $N_H = (6.4^{+3.7}_{-2.9}) \times 10^{22} \text{ cm}^{-2}$ and $\Gamma = 2.2^{+1.2}_{-1.0}$, while an apec model yields $N_H = (5.6^{+3.2}_{-2.1}) \times 10^{22} \text{ cm}^{-2}$ and $kT = 4^{+8}_{-2} \text{ keV}$.

To compare the properties of the X-ray emission in the core of the YMC with that of the diffuse emission, we extracted a spectrum from a circle of $6''$ radius (12 pixels) that encompasses the 95% encircled energy radius (EER) of both point sources in the core (CXOU J163447.8-473243 and CXOU J163448.0-473246) giving 40 net source counts, as well as a spectrum from an annulus (centered at the same position) with

inner and outer radii of $6''$ and $12''.5$, respectively, that represents the diffuse emission (44 net counts). The results of models fit to these spectra are tabulated in Table 3. There are hints that the diffuse component has a slightly higher plasma temperature (with apec models) and a harder photon index (with power law models) than the stellar sources in the core region, but the low photon counts results in large uncertainties, which leads to some overlap in the range of possible temperatures and photon indices at the 90% confidence level. We attempted to extract spectra for each X-ray point source in the core by using non-overlapping regions but the sources ended up with too few counts (9 net counts each) to permit reliable fitting.

A source spectrum was made for CXOU J163448.5-473229 by using an extraction radius of $6''$ (12 pixels) centered on its X-ray position. While the spectral parameters of CXOU J163448.5-473229 are compatible with those of the other source regions (within the statistical uncertainties), it is clearly softer than the others given its hardness ratio of -0.43 ± 0.25 . This is illustrated in Fig. 3 which compares the 68%, 90%, and 99% confidence contours of spectral parameters from the power law model fit to the data of CXOU J163448.5-473229 (dashed lines), and for the YMC (solid lines). There is some overlap between the parameter spaces at the 99% confidence level, but the X-ray emission from the cluster tends to be harder and more absorbed than that of a point source situated in the cluster's outskirts.

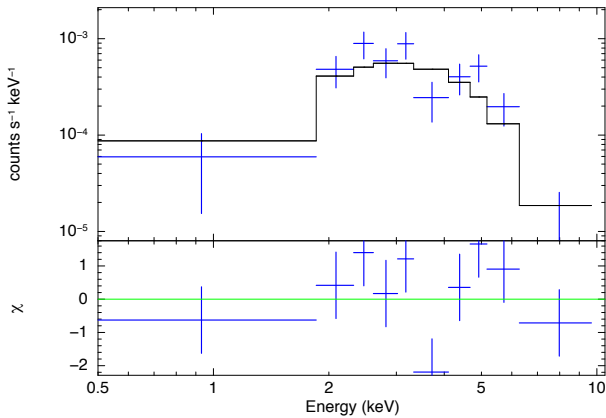


Figure 2. X-ray spectrum extracted from a $15''$ radius (30 pixels) around the infrared position of VVV CL077. The lower panel shows residuals from fitting an absorbed power law (solid curve) to the spectral data. For visual clarity, each spectral bin contains a minimum of 15 counts. Spectral parameters from the unbinned analysis are listed in Table 3.

3.2. Infrared Data

Figure 4 shows the K_s -band image of the region gathered with NAOJ/NEWFIRM. Infrared spectra for Source #2 and Source #3 are presented in Fig. 5. In the K_s -band spectra of Source #2, we detect a Br- γ line in absorption at 21660 \AA . The equivalent width is 11.5 \AA with a typical error of ~ 1 – 1.5 \AA . There is a marginal detection of the He I line in absorption at 20600 \AA . Source #3 also presents a Br- γ line in absorption with an equivalent width of 6.5 \AA . With standard deviations being less than 0.06, this leads to $S/N > 10$ in both sources. Comparing these spectra to those of a sample of high-mass stars provided by Hanson et al. (1996) indicates that Sources #2 and #3 are probably late-O giants.

In addition to these spectra, we searched the ViZier archives for multi-wavelength counterparts consistent with the X-ray error circles of the sources detected by *Chandra*. Table 4 lists the reported magnitudes of these counterpart candidates. The derived $J - H$ and $H - K_s$ colors are compatible with the colors observed in O stars (e.g., Ramírez Alegría et al. 2012). Comparing CXOU J163448.0–473246 and CXOU J163448.5–473229, we find consistent values (within the uncertainties) for their $J - H$ (1.8 ± 0.2 vs. $2.0^{+0.1}_{-0.2}$) and $J - K_s$ ($3.3^{+0.1}_{-0.2}$ vs. $3.0^{+0.1}_{-0.2}$) colors, but the $H - K_s$ color is $\sim 50\%$ higher for CXOU J163448.0–473246 (1.5 ± 0.2 vs. $1.0^{+0.2}_{-0.1}$) which suggests it has a slight near-to-mid-infrared excess, although the source is blended in the 2MASS K_s -band image. We point out the presence of a mid-infrared source located $2''.9$ away from CXOU J163448.0–473246 (i.e., $1''.4$ from the IR position of the cluster): WISE J163448.13–473248.9 has reported magnitudes of 5.563 ± 0.110 (at $3.35 \mu\text{m}$), 4.756 ± 0.055 ($4.6 \mu\text{m}$), -0.896 ± 0.121 ($11.6 \mu\text{m}$), and -3.190 ± 0.020 ($22.1 \mu\text{m}$).

4. DISCUSSION

At least 21 stars belonging to VVV CL077 were visually identified in the infrared (Borissova et al. 2011), and this young massive cluster is now detected for the first time in the X-rays with *Chandra*. A complete census of the X-ray emitting sources in VVV CL077 can not be achieved with the current data. Nevertheless, recent X-ray observations of this region reveal a number of intriguing results.

Imaging data from *Chandra* suggest that there are three X-

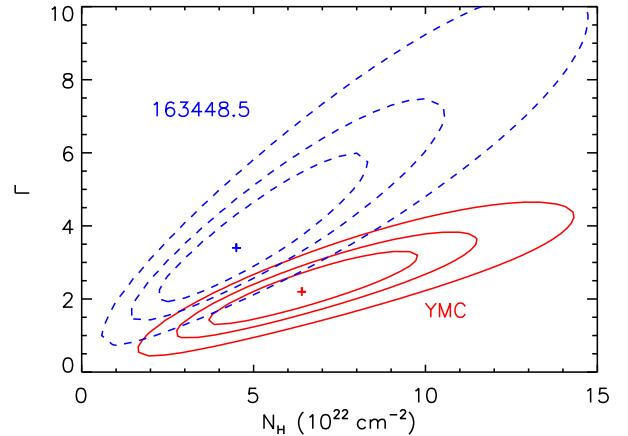


Figure 3. Parameter space of N_H and Γ resulting from absorbed power-law fits to the X-ray spectra (0.5–10 keV) of selected extraction regions. Two extraction regions are considered: a $15''$ -radius circle centered on the IR position of VVV CL077 (solid lines), and a $6''$ -radius circle centered on the X-ray position of CXOU J163448.5–473229 (dashed lines). The best-fitting parameters are represented by crosses and the contours denote confidence levels of 68%, 90%, and 99%.

ray point sources associated with infrared stellar counterparts that belong to the cluster. Two of these sources are located near the cluster core, and the third is located in the cluster’s outskirts. In addition to these point sources, there is extended and diffuse X-ray emission: the estimated intrinsic (on-axis) size of the X-ray emitting core of the YMC is larger than expected for the combined 95% energy-containment circles of the two closely-spaced point sources in the core; and this component, which contains as many net counts as the core X-ray point sources combined, can not be directly associated with any resolved sources.

The presence of diffuse emission, with X-ray spectral properties statistically consistent with that of the resolved stellar X-ray sources, would suggest a population of unresolved X-ray sources in the YMC whose emission lies below the sensitivity limit of the survey ($\sim 10^{-15} \text{ erg cm}^{-2} \text{ s}^{-1}$ Fornasini et al. 2014).

Diffuse X-ray emission has been observed in other YMCs including in Wd 1 and in active star-forming regions like the Carina Nebula (Muno et al. 2006a; Townsley et al. 2011a,c). In addition to the combined emission from unresolved stars, the diffuse component could originate from putative collisions between the winds of massive stars, although the temperature and absorption in VVV CL077 are higher than expected for such processes (e.g., Stevens & Hartwell 2003).

Two of the stars VVV CL077 display infrared spectral signatures typical of late-type O stars (Hanson et al. 1996). There is good overall agreement between the outlines of the emission as seen in the X-rays and infrared, and this multi-wavelength consistency continues into the radio band where the X-ray and infrared emission coincide spatially with a local maximum in the 843 MHz continuum map from MGPS-2 (Murphy et al. 2007). The coincidence of the multi-wavelength emission from VVV CL077 could indicate a common physical origin, however, the observed X-ray flux of the diffuse component is larger than expected from an extrapolation of the infrared flux density (see below).

The nearest catalogued ultra-compact HII region is IRAS 16311–4726 (Helou & Walker 1988; Bronfman et al.

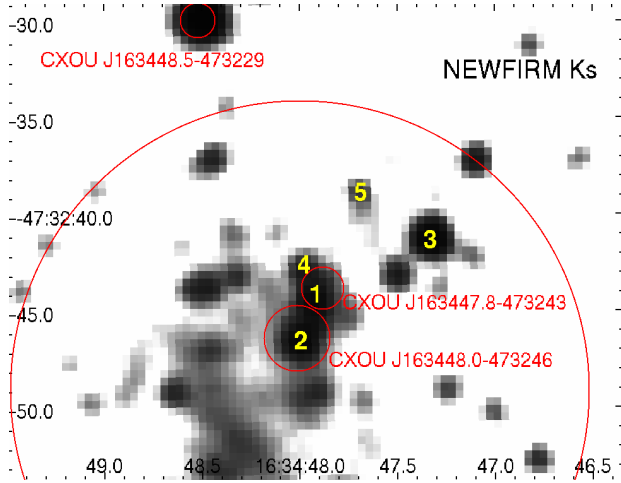


Figure 4. Image of VVV CL077 in the infrared K_s -band from NOAO/NEWFIRM. Circles denote the positional uncertainty of the X-ray point sources described in this work (Table 2), and the visual extent of the YMC according to Borissova et al. (2011). Infrared objects targeted for follow-up spectroscopy are numbered 1–5.

1996) which is $6''$ from the infrared position of VVV CL077. It has a velocity of 121 km s^{-1} with respect to the local standard of rest, which translates to a source distance of approximately 11 kpc (e.g., Brand & Blitz 1993). There is also a catalogued H II region $7'$ away from VVV CL077 with a listed distance of $10.9 \pm 0.2 \text{ kpc}$ (Russeil 2003). If these regions are related, then we can assign a distance of around 11 kpc to VVV CL077. This would make it one of the most distant Galactic YMCs known, comparable to Mercer 81 (Davies et al. 2012), at a location consistent with the far Norma Arm.

Taking the visual extent of the bulk of the stellar population in the infrared as the angular scale ($15''$: Borissova et al. 2011) gives a cluster diameter of 0.8 pc for an assumed distance of 11 kpc. This value is consistent with the intrinsic sizes of other Galactic YMCs (Figer 2008, and references therein).

Corrected for absorption, the diffuse emission from VVV CL077 has an intrinsic flux of $(9 \pm 3) \times 10^{-14} \text{ erg cm}^{-2} \text{ s}^{-1}$ (0.5–10-keV). This is more than an order of magnitude above the flux expected from the Galactic Ridge diffuse emission (Ebisawa et al. 2001, 2005). If we assume, nevertheless, that the Ridge emission accounts for 20% of the flux from VVV CL077, as it does for Wd 1 (Muno et al. 2006a), then the residual flux of $\sim 7 \times 10^{-14} \text{ erg cm}^{-2} \text{ s}^{-1}$ can be attributed to the diffuse cluster emission. For a distance of 11 kpc (assumed), this translates to an X-ray luminosity of $10^{34} \text{ erg s}^{-1}$. Flux densities reported for IRAS 16311–4726 are $20.1 \pm 0.6 \text{ Jy}$ at $12 \mu\text{m}$ and $153 \pm 5 \text{ Jy}$ at $25 \mu\text{m}$ (Helou & Walker 1988). Extrapolating a power law with a photon index of $\Gamma = 2.8 \pm 0.1$ leads to an X-ray flux density of $1.3 \times 10^{-10} \text{ Jy}$ at 1 keV ($3.0 \times 10^{-15} \text{ erg cm}^{-2} \text{ s}^{-1}$ over 0.5–10 keV). This is an order of magnitude smaller than the lower 90%-confidence boundary of the intrinsic flux density ($3 \times 10^{-9} \text{ Jy}$ at 1 keV). In order to match the X-ray flux, the photon index should be no steeper than 2.5, which is consistent with what we found in Section 3.1.

A simple estimation of the cluster mass density yields $\rho \sim (1\text{--}4) \times 10^3 M_{\odot} \text{ pc}^{-3}$. This assumes that all 21 visually-identified members of the cluster are similar to the sources we identified as O type stars with masses in the range of 10– $50 M_{\odot}$. While the mass density is consistent with those of

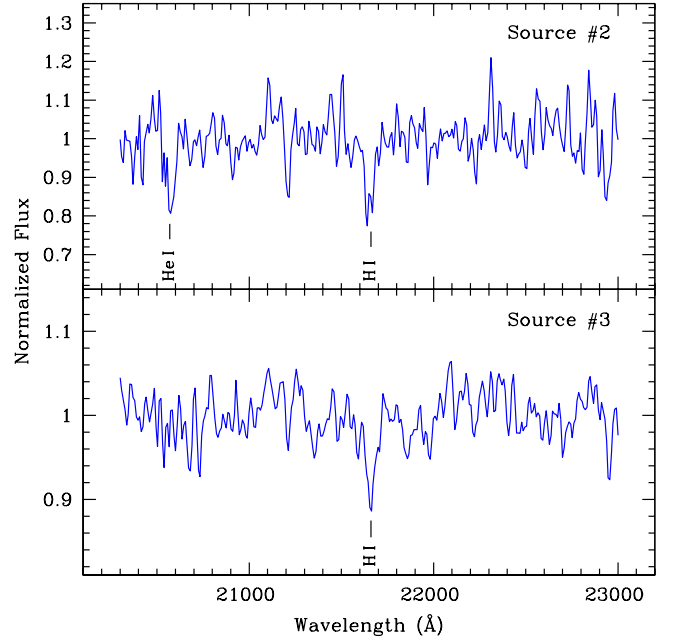


Figure 5. Infrared K_s -band spectra of two stars (labeled “2” and “3” in Fig. 4) in the YMC VVV CL077 from observations gathered with NOAO/OSIRIS.

other YMCs, the cluster mass implied by this first-order approximation ($\sim 10^3 M_{\odot}$) is an order of magnitude below the inferred masses of other YMCs (Figer 2008). This indicates a large population of unresolved stars hiding in and around the cluster which is not surprising given the extinction in this direction.

From the observed infrared excess $E(H - K_s) = 1.5 \pm 0.2$, we estimate the extinction in the optical band as $A_V = 15 \pm 2$ assuming a near-infrared extinction law with $\alpha = -2.1$ (Stead & Hoare 2009). Applying the relation of Güver & Özel (2009) yields a column density of $N_{\text{H}} = (3.3^{+1.1}_{-1.0}) \times 10^{22} \text{ cm}^{-2}$. When the contribution from molecular hydrogen is included, the total column density of the interstellar medium towards the Norma region ranges from $4.9 \times 10^{22} \text{ cm}^{-2}$ to $9.4 \times 10^{22} \text{ cm}^{-2}$ (Rahoui et al. 2014). This is consistent with our X-ray-derived value of $(6.4^{+3.7}_{-2.9}) \times 10^{22} \text{ cm}^{-2}$.

Plasma temperatures of around 1–2 keV are found for the X-ray emitting point sources in the cluster which is higher than average for massive stars (e.g., Rauw et al. 2014). The X-ray source located in the outskirts of the cluster (CXOU J163448.5–473229) has a temperature that is statistically compatible (at 90% confidence) with 0.7 keV which is a more typical value. As we move towards the center of the cluster, we find that the X-ray derived temperatures of these stars are higher, possibly due to increasing column density (which preferentially absorbs low-temperature photons). With its proximity to IRAS 16311–4726, this could indicate that the stars in the core of VVV CL077 are still embedded within their dusty natal cocoons; similar to the hot, young stars of W49A (Conti & Blum 2002), a cluster that resides within an ultra-compact H II region. However, we can not exclude that the unusual spectral values are the result of poor photon statistics.

Based on the IR spectra, we narrowed the range of spectral types to O5–O9 giants for two of the stars in the cluster. We

derived the distance modulus $m-M = 5 \log(d) + A - 5$ using the observed J -band magnitude of CXOU J163448.0-473246 in Table 4, the absolute J -band magnitude of -4.6 for an O giant (Martins & Plez 2006), and $A_J = 0.28A_V$. This gives a distance to the object of 10 ± 3 kpc, consistent with the distance assumed based on its possible link with IRAS 16311-4726.

In massive stars, the ratio between the X-ray and bolometric luminosities is $\sim 10^{-7}$ (e.g., Berghoefer et al. 1997; Rauw et al. 2014). Such stars have bolometric luminosities of $\log(L/L_\odot) \sim 5.2-5.7$ (Martins et al. 2005). To test whether the objects we classify as massive stars obey this rule, we began with the observed X-ray flux of the “inner core” region and corrected this for the interstellar absorption alone ($N_{\text{H}} = 3 \times 10^{22} \text{ cm}^{-2}$), then halved this value to obtain the absorption-corrected flux of one of the stars of the pair. For an assumed distance of 10 ± 3 kpc, this yields an X-ray luminosity of $3.5 \times 10^{32} \text{ erg s}^{-1}$. A ratio L_X/L_{bol} of 10^{-7} is obtained for either the high end of the bolometric luminosity range ($\log(L/L_\odot) \sim 5.7$), or for distances at the lower end of the estimate (~ 7 kpc). Fixing the temperature to a more reasonable value of 0.6 keV raises the column density to unlikely values ($N_{\text{H}} = (22^{+7}_{-5}) \times 10^{22} \text{ cm}^{-2}$), which, once corrected for interstellar absorption, results in $L_X \sim 2.5 \times 10^{32} \text{ erg s}^{-1}$, and so it remains consistent (within the uncertainties) with the expected L_X/L_{bol} value for massive stars.

Finally, we consider the question of whether there are supernova remnants and accreting compact objects in VVV CL077. There are no obvious shell-like features in the infrared and X-ray data that would indicate recent supernova activity, although the low level of soft X-ray emission and lack of hard X-ray or gamma-ray detections appear to rule out such scenarios. Luminous ($L_X \gtrsim 10^{38} \text{ erg s}^{-1}$) X-ray point sources are missing from VVV CL077 which excludes high-mass X-ray binaries (HMXBs) where the accretion proceeds through Roche-lobe overflow. Wind-fed HMXBs could be present but they would have to be weakly-accreting or quiescent ($L_X \sim 10^{33} \text{ erg s}^{-1}$), such as is the case for Supergiant Fast X-ray Transients (SFXTs) outside of outbursts. However, the photon indices measured in the core and for the external X-ray sources are too soft to support the weakly-accreting SFXT scenario (e.g., Romano et al. 2011). An additional point to consider is that the supernova that leads to the formation of the compact object in such systems can impart a velocity to the nascent X-ray binary that is several times larger than the cluster escape velocity (van den Heuvel et al. 2000; Clark et al. 2005). The apparent lack of supernova remnants or accreting compact objects would tend to favor a relatively young age for the YMC, i.e., a few Myr at most.

5. SUMMARY & CONCLUSIONS

We presented results from recent *Chandra* observations of VVV CL077, a Young Massive Cluster (YMC) located towards the Norma Arm. Three X-ray point sources were detected that correspond to visually-identified stellar members of the cluster. Infrared spectra we obtained for two members of the cluster show absorption lines typical of the atmospheres of massive stars. Plus, the infrared colors and L_X/L_{bol} relation also indicate massive stars. However, X-ray spectral fits of these stars yield temperatures that are higher than average for massive stars.

In addition to these point sources, there are hints that an extended region of diffuse X-ray emission permeates the cluster core. The X-ray column density and optical extinction, as well as an estimate of the cluster mass, suggests a popula-

tion of unresolved stars that contribute to the diffuse emission. The X-ray spectrum of the $15''$ -radius visible extent of the VVV CL077 is best modeled with an absorbed $[N_{\text{H}} = (3 - 10) \times 10^{22} \text{ cm}^{-2}]$ power law ($\Gamma = 2 \pm 1$).

The X-ray core of the cluster coincides with diffuse emission seen in the infrared band and with a local maximum in the radio continuum map. A tentative link with a neighboring H II region would place VVV CL077 at a distance of around 11 kpc; on the far side of the Norma Arm. At this distance, the cluster is 0.8 pc wide with a mass density of $(1-4) \times 10^3 M_\odot \text{ pc}^{-3}$, i.e., within the range of values seen for other YMCs.

A complete picture of the X-ray population and diffuse emission from VVV CL077 is not possible at this time, but continued X-ray observations of YMCs are important for the study of massive stars, the formation and evolution of compact objects, and the recent star formation history of the Galaxy.

The authors thank the anonymous referee whose careful, patient, and constructive review led to significant improvements in the manuscript. This work was supported in part through *Chandra* Award Number GO1-12068A issued by the *Chandra* X-ray Observatory Center, which is operated by the Smithsonian Astrophysical Observatory for and on behalf of the National Aeronautics Space Administration under contract NAS8-03060. FEB acknowledges support from Basal-CATA (PFB-06/2007) and CONICYT-Chile (under grant FONDECYT 1141218 and Anillo ACT1101). The scientific results reported in this article are based on observations made by the *Chandra* X-ray Observatory. This research has made use of: software provided by the *Chandra* X-ray Center (CXC) in the application packages CIAO, ChIPS, and Sherpa; data obtained from the High Energy Astrophysics Science Archive Research Center (HEASARC) provided by NASA’s Goddard Space Flight Center; NASA’s Astrophysics Data System Bibliographic Services; the SIMBAD database operated at CDS, Strasbourg, France; data products from the Two Micron All Sky Survey, which is a joint project of the University of Massachusetts and the Infrared Processing and Analysis Center/California Institute of Technology, funded by NASA and the NSF; data products from the Wide-field Infrared Survey Explorer, which is a joint project of the University of California, Los Angeles, and the Jet Propulsion Laboratory/California Institute of Technology, funded by NASA and the NSF.

Facilities: CXO, Blanco (NEWFIRM), SOAR (OSIRIS)

REFERENCES

- Balucinska-Church, M., & McCammon, D. 1992, *ApJ*, 400, 699
 Berghoefer, T. W., Schmitt, J. H. M. M., Danner, R., & Cassinelli, J. P. 1997, *A&A*, 322, 167
 Borissova, J., et al. 2011, *A&A*, 532, A131
 Brand, J., & Blitz, L. 1993, *A&A*, 275, 67
 Bronfman, L., Nyman, L.-A., & May, J. 1996, *A&AS*, 115, 81
 Cash, W. 1979, *ApJ*, 228, 939
 Clark, J. S., Muno, M. P., Negueruela, I., Dougherty, S. M., Crowther, P. A., Goodwin, S. P., & de Grijs, R. 2008, *A&A*, 477, 147
 Clark, J. S., Negueruela, I., Crowther, P. A., & Goodwin, S. P. 2005, *A&A*, 434, 949
 Conti, P. S., & Blum, R. D. 2002, *ApJ*, 564, 827
 Davies, B., de La Fuente, D., Najarro, F., Hinton, J. A., Trombly, C., Figer, D. F., & Puga, E. 2012, *MNRAS*, 419, 1860
 DENIS Consortium. 2005, *VizieR Online Data Catalog*, 2263, 0

- Ebisawa, K., Maeda, Y., Kaneda, H., & Yamauchi, S. 2001, *Science*, 293, 1633
- Ebisawa, K., et al. 2005, *ApJ*, 635, 214
- Figer, D. F. 2008, in *IAU Symposium*, Vol. 250, IAU Symposium, ed. F. Bresolin, P. A. Crowther, & J. Puls, 247–256
- Fornasini, F. M., et al. 2014, *ApJ*, 796, 105
- Güver, T., & Özel, F. 2009, *MNRAS*, 400, 2050
- Hanson, M. M., Conti, P. S., & Rieke, M. J. 1996, *ApJS*, 107, 281
- Helou, G., & Walker, D. W., eds. 1988, *Infrared astronomical satellite (IRAS) catalogs and atlases. Volume 7: The small scale structure catalog*, Vol. 7
- Martins, F., & Plez, B. 2006, *A&A*, 457, 637
- Martins, F., Schaerer, D., & Hillier, D. J. 2005, *A&A*, 436, 1049
- Minniti, D., et al. 2010, *New Astronomy*, 15, 433
- Muno, M. P., Law, C., Clark, J. S., Dougherty, S. M., de Grijs, R., Portegies Zwart, S., & Yusef-Zadeh, F. 2006a, *ApJ*, 650, 203
- Muno, M. P., et al. 2006b, *ApJ*, 636, L41
- Murphy, T., Mauch, T., Green, A., Hunstead, R. W., Piestrzynska, B., Kels, A. P., & Sztajer, P. 2007, *MNRAS*, 382, 382
- Pearson, K. 1900, *Philosophical Magazine Series 5*, 50, 157
- Portegies Zwart, S. F., McMillan, S. L. W., & Gieles, M. 2010, *ARA&A*, 48, 431
- Portegies Zwart, S. F., McMillan, S. L. W., & Makino, J. 2007, *MNRAS*, 374, 95
- Rahoui, F., Tomsick, J. A., Fornasini, F. M., Bodaghee, A., & Bauer, F. E. 2014, *A&A*, 568, A54
- Ramírez Alegría, S., Marín-Franch, A., & Herrero, A. 2012, *A&A*, 541, A75
- Rauw, G., et al. 2014, *ArXiv e-prints*: 1401.8098
- Romano, P., et al. 2011, *MNRAS*, 410, 1825
- Russeil, D. 2003, *A&A*, 397, 133
- Skinner, S. L., Simmons, A. E., Zhekov, S. A., Teodoro, M., Daminieli, A., & Palla, F. 2006, *ApJ*, 639, L35
- Skrutskie, M. F., et al. 2006, *AJ*, 131, 1163
- Spitzer Science, C. 2009, *VizieR Online Data Catalog*, 2293, 0
- Stead, J. J., & Hoare, M. G. 2009, *MNRAS*, 400, 731
- Stevens, I. R., & Hartwell, J. M. 2003, *MNRAS*, 339, 280
- Townsley, L. K., Broos, P. S., Chu, Y.-H., Gruendl, R. A., Oey, M. S., & Pittard, J. M. 2011a, *ApJS*, 194, 16
- Townsley, L. K., et al. 2011b, *ApJS*, 194, 1
- . 2011c, *ApJS*, 194, 15
- van den Heuvel, E. P. J., Portegies Zwart, S. F., Bhattacharya, D., & Kaper, L. 2000, *A&A*, 364, 563
- Wilms, J., Allen, A., & McCray, R. 2000, *ApJ*, 542, 914

Table 3
Parameters from absorbed power law and appec models fit to the unbinned X-ray spectra of selected regions

N_H^a	Γ^b	kT^c	norm. ^d	C-stat./goodness ^e	S^f	H^g	HR ^h	obs. flux ⁱ	unabs. flux ^j
VVV CL077: 15'' extraction radius centered on IR position of Borissova et al. (2011)									
$6.4^{+3.7}_{-2.9}$	$2.2^{+1.2}_{-1.0}$	—	5.4	73%	48 ± 6	59 ± 10	0.10 ± 0.11	$6.8^{+2.4}_{-1.8}$	$21.6^{+10.9}_{-5.9}$
$5.6^{+3.2}_{-2.1}$	—	4^{+8}_{-2}	9.9	78%	—	—	—	$6.6^{+2.3}_{-1.7}$	$15.0^{+16.1}_{-4.5}$
VVV CL077 diffuse emission: annulus with 6''–12'' radii centered between CXOU J163447.8–473243 and CXOU J163448.0–473246									
$5.4^{+5.0}_{-3.5}$	$1.7^{+1.6}_{-1.3}$	—	1.4	73%	16 ± 5	28 ± 7	0.27 ± 0.20	$4.6^{+2.8}_{-1.7}$	$8.9^{+3.1}_{-2.5}$
$5.9^{+3.7}_{-2.4}$	—	5^{+26}_{-3}	5.4	82%	—	—	—	$4.1^{+1.7}_{-1.3}$	$8.9^{+8.8}_{-3.2}$
VVV CL077 inner core: circle with 6'' radius centered between CXOU J163447.8–473243 and CXOU J163448.0–473246									
$8.0^{+8.9}_{-4.6}$	$3.1^{+2.4}_{-1.6}$	—	9.2	61%	18 ± 5	22 ± 5	0.10 ± 0.18	$2.8^{+1.5}_{-0.9}$	$27.7^{+8.1}_{-6.9}$
$9.0^{+8.5}_{-6.3}$	—	$1.6^{+1.0}_{-0.4}$	16.8	70%	—	—	—	$2.4^{+1.3}_{-0.7}$	$19.6^{+21.1}_{-14.8}$
CXOU J163448.5–473229: circle with 6'' radius									
$4.5^{+4.3}_{-2.5}$	$3.4^{+2.9}_{-1.6}$	—	4.5	3%	20 ± 5	8 ± 4	-0.43 ± 0.25	$1.3^{+0.9}_{-0.5}$	$13.1^{+22.3}_{-6.9}$
$4.9^{+2.2}_{-2.0}$	—	$1.2^{+1.2}_{-0.5}$	8.2	2%	—	—	—	$1.1^{+0.6}_{-0.4}$	$12.0^{+36.6}_{-8.6}$

^a Column density in units of 10^{22} cm^{-2} .

^b Photon index of the power law model.

^c Plasma temperature (keV) for the appec model.

^d Model normalization ($\times 10^{-5}$).

^e Goodness of fit defined as the percentage of simulated spectra (of 10,000 trials) which return a statistic smaller than the observed value.

^f Net source counts in the soft (S) band: 0.5–3 keV.

^g Net source counts in the hard (H) band: 3–10 keV.

^h Hardness ratio defined as $(H - S)/(H + S)$.

ⁱ Observed flux (i.e., not corrected for absorption) in units of $10^{-14} \text{ erg cm}^{-2} \text{ s}^{-1}$ in the 0.5–10 keV band.

^j Absorption-corrected flux in units of $10^{-14} \text{ erg cm}^{-2} \text{ s}^{-1}$ in the 0.5–10 keV band.

Table 4
Infrared counterpart candidates to X-ray sources near VVV CL077

name	counterpart	offset (")	J	H	K_s	$3.6\ \mu\text{m}$	$4.5\ \mu\text{m}$	$5.8\ \mu\text{m}$
CXOU J163447.8–473243	— [†]	—	—	—	—	—	—	—
CXOU J163448.0–473246	2MASS J16344796–4732452	1.2	14.485±0.087	12.700±0.137	11.230±0.081	—	—	—
	DENIS J163447.9–473245	0.8	14.10±0.11	—	11.12±0.07	—	—	—
	VVV 515726976188	0.2	14.731±0.005	13.466±0.005	—	—	—	—
CXOU J163448.5–473229	2MASS J16344850–4732297	0.3	13.729±0.075	11.772±0.075	10.730±0.043	—	—	—
	VVV 515726978416	0.6	13.647±0.002	11.898±0.001	—	—	—	—
	GLIMPSE G336.8914+00.0524	0.4	—	—	—	10.052±0.048	9.844±0.053	9.818±0.103

Note. — Infrared magnitudes of counterpart candidates in: the J , H , and K_s bands from 2MASS (Skrutskie et al. 2006), DENIS (DENIS Consortium 2005), and VVV (Minniti et al. 2010); and at $3.6\ \mu\text{m}$, $4.5\ \mu\text{m}$, and $5.8\ \mu\text{m}$ from *Spitzer*-GLIMPSE (*Spitzer* Science 2009).

[†] The nearest IR source with catalogued magnitudes, 2MASS J16344796–4732452, is 1"7 away and is likely associated with CXOU J163448.0–473246.

THE NORMA ARM REGION *CHANDRA* SURVEY CATALOG: X-RAY POPULATIONS IN THE SPIRAL ARMS

FRANCESCA M. FORNASINI^{1,2}, JOHN A. TOMSICK², ARASH BODAGHEE^{2,3}, ROMAN A. KRIVONOS^{2,4}, HONGJUN AN⁵,
FARID RAHOUT^{6,7}, ERIC V. GOTTHELF⁸, FRANZ E. BAUER^{9,10,11}, AND DANIEL STERN¹²

¹ Astronomy Department, University of California, 601 Campbell Hall, Berkeley, CA 94720, USA; f.fornasini@berkeley.edu

² Space Sciences Laboratory, 7 Gauss Way, University of California, Berkeley, CA 94720, USA

³ Georgia College and State University, CBX 082, Milledgeville, GA 31061, USA

⁴ Space Research Institute, Russian Academy of Sciences, Profsoyuznaya 84/32, 117997 Moscow, Russia

⁵ Department of Physics, McGill University, Rutherford Physics Building, 3600 University Street, Montreal, QC H3A 2T8, Canada

⁶ European Southern Observatory, Karl Schwarzschild-Strasse 2, D-85748 Garching bei München, Germany

⁷ Department of Astronomy, Harvard University, 60 Garden Street, Cambridge, MA 02138, USA

⁸ Columbia Astrophysics Laboratory, Columbia University, 550 West 120th Street, New York, NY 10027, USA

⁹ Instituto de Astrofísica, Facultad de Física, Pontificia Universidad Católica de Chile, 306, Santiago 22, Chile

¹⁰ Millennium Institute of Astrophysics, Vicuña Mackenna 4860, 7820436 Macul, Santiago, Chile

¹¹ Space Science Institute, 4750 Walnut Street, Suite 205, Boulder, CO 80301, USA

¹² Jet Propulsion Laboratory, California Institute of Technology, 4800 Oak Grove Drive, MS 169-506, Pasadena, CA 91109, USA

Received 2013 October 30; accepted 2014 September 4; published 2014 November 12

ABSTRACT

We present a catalog of 1415 X-ray sources identified in the Norma Arm Region *Chandra* Survey (NARCS), which covers a $2^\circ \times 0.8$ region in the direction of the Norma spiral arm to a depth of ≈ 20 ks. Of these sources, 1130 are point-like sources detected with $\geq 3\sigma$ confidence in at least one of three energy bands (0.5–10, 0.5–2, and 2–10 keV), five have extended emission, and the remainder are detected at low significance. Since most sources have too few counts to permit individual classification, they are divided into five spectral groups defined by their quantile properties. We analyze stacked spectra of X-ray sources within each group, in conjunction with their fluxes, variability, and infrared counterparts, to identify the dominant populations in our survey. We find that $\sim 50\%$ of our sources are foreground sources located within 1–2 kpc, which is consistent with expectations from previous surveys. Approximately 20% of sources are likely located in the proximity of the Scutum-Crux and near Norma arm, while 30% are more distant, in the proximity of the far Norma arm or beyond. We argue that a mixture of magnetic and nonmagnetic cataclysmic variables dominates the Scutum-Crux and near Norma arms, while intermediate polars and high-mass stars (isolated or in binaries) dominate the far Norma arm. We also present the cumulative number count distribution for sources in our survey that are detected in the hard energy band. A population of very hard sources in the vicinity of the far Norma arm and active galactic nuclei dominate the hard X-ray emission down to $f_X \approx 10^{-14}$ erg cm⁻² s⁻¹, but the distribution curve flattens at fainter fluxes. We find good agreement between the observed distribution and predictions based on other surveys.

Key words: binaries: general – catalogs – Galaxy: disk – novae, cataclysmic variables – X-rays: binaries – X-rays: stars

Online-only material: color figures, machine-readable tables

1. INTRODUCTION

X-ray observations of the Galactic stellar population provide an important probe of several stages of stellar evolution. The brightest stellar X-ray sources are associated with compact stellar remnants. Neutron stars (NS), black holes, and white dwarfs (WD) that are accreting matter from a binary companion are bright X-ray emitters. Isolated NS are also bright X-ray sources when they are young and hot, or if they accelerate particles in strong magnetic fields ($10^{12} \lesssim B \lesssim 10^{14}$ G). We can learn about earlier stages of stellar evolution from X-ray observations as well. Massive OB and Wolf–Rayet stars can produce X-rays through shocks in their stellar winds, and are sometimes more luminous than X-ray sources associated with compact stellar remnants. Low-mass main sequence stars can produce low levels of X-ray emission in their magnetic coronae, and young stellar objects can produce X-rays due to their strong magnetic fields.

Over the past decade, studies of X-ray source populations in several Galactic regions have been carried out using observations from the *Chandra X-Ray Observatory*. These surveys have targeted the Galactic center (Wang et al. 2002; Munro et al.

2009), the Galactic bulge (Hong et al. 2009), the Orion region (Grosso et al. 2005), the Carina arm (Townsend et al. 2011), and a “typical” region of the Galactic plane without point sources brighter than 2×10^{-13} erg cm⁻² s⁻¹ (Ebisawa et al. 2005). Although some young, X-ray emitting massive stars have been discovered in the Galactic center (Mauerhan et al. 2010), the Galactic center and bulge are dominated by old X-ray stellar populations. In contrast, the Orion region is a well-known star-forming region, and it has been argued that the Carina region is also a very young star-forming region since there is no evidence of a supernova explosion having occurred there yet (Smith & Brooks 2007).

We have conducted a *Chandra* survey of the Norma spiral arm, which complements the aforementioned surveys since Norma’s stellar population is likely more evolved than that of the Orion and Carina regions, but less evolved than that of the Galactic center and bulge. The line-of-sight tangent to the Norma spiral arm contains the highest number of massive star-forming complexes in the Galaxy (Russeil 2003), demonstrating that there is a significant population of young stars in this arm. Further evidence that this is a region of recent star formation is the presence of warm dust emission in *Spitzer* 8 μ m images and

Table 1
Observations of the Norma Region

ObsID	R.A.	Decl.	Roll	Start Time	Exposure
(1)	(deg) (2)	(deg) (3)	(deg) (4)	(UT) (5)	(ks) (6)
12507	250.373201	-46.662951	342.217237	2011 Jun 6 10:15:53	18.8
12508	250.155011	-46.530604	342.217232	2011 Jun 6 15:57:13	18.5
12509	249.937805	-46.397816	342.217176	2011 Jun 6 21:22:23	19.4
12510	250.180190	-46.812896	342.217230	2011 Jun 9 12:29:02	19.9
12511	249.961646	-46.681456	333.217149	2011 Jun 17 11:15:19	19.3
12512	249.743370	-46.550407	317.716418	2011 Jun 27 04:52:55	20.5
12513	249.984947	-46.965904	317.716539	2011 Jun 27 11:00:21	20.2
12514	249.767582	-46.829470	342.217317	2011 Jun 10 16:07:39	19.8
12515	249.550110	-46.695978	342.217265	2011 Jun 10 22:04:48	19.5
12516	249.790838	-47.111874	342.217386	2011 Jun 11 03:46:38	19.5
12517	249.572205	-46.978413	342.217342	2011 Jun 11 09:28:28	19.5
12518	249.354673	-46.844540	342.217308	2011 Jun 11 15:10:18	19.5
12519	249.594334	-47.262081	333.217286	2011 Jun 13 04:25:13	19.3
12520	249.375577	-47.128273	333.217242	2011 Jun 13 10:13:08	19.0
12521	249.157932	-46.994022	333.217206	2011 Jun 13 15:46:38	19.0
12522	249.396933	-47.410725	333.217339	2011 Jun 13 21:20:08	19.0
12523	249.178061	-47.276529	333.217293	2011 Jun 14 02:53:38	19.0
12524	248.960334	-47.141940	333.217275	2011 Jun 14 08:27:08	19.5
12525	249.198427	-47.559064	333.217397	2011 Jun 14 14:08:58	19.5
12526	248.979417	-47.424468	333.217332	2011 Jun 14 19:50:48	19.0
12527	248.761625	-47.289491	333.217351	2011 Jun 15 19:36:46	19.3
12528	248.998831	-47.707016	333.217482	2011 Jun 16 01:24:35	19.0
12529	248.779750	-47.572056	333.217441	2011 Jun 16 06:58:05	19.0
12530	248.561776	-47.436667	333.217382	2011 Jun 16 12:31:35	19.3
12531	248.798050	-47.854617	333.217515	2011 Jun 16 18:09:14	19.5
12532	248.578823	-47.719259	333.217450	2011 Jun 16 23:51:04	19.5
12533	248.360823	-47.583518	333.217451	2011 Jun 17 05:32:54	19.5

Notes. (1) Observation ID number. (2) Right ascension (J2000.0) of observation pointing. (3) Declination (J2000.0) of observation pointing. (4) Roll angle of observation. (5) Start time of observation. (6) Exposure time of observation.

several H II regions mapped by 1420 MHz continuum emission from the Southern Galactic Plane Survey (Georgelin et al. 1996). However, the supernova remnants (SNRs) discovered in this region (Green 2004, 2009; Funk et al. 2007; Combi et al. 2005) suggest that the Norma stellar population is older than the populations in the Orion and Carina regions observed with *Chandra*. Thus, the relative fractions of X-ray populations in the Norma arm may differ from those in other regions of the Galactic plane; in particular, the fraction of X-ray sources associated with evolved massive stars may be enhanced in Norma.

The Norma Arm Region *Chandra* Survey (NARCS) consists of a 1.3 deg^2 region in the direction of the Norma spiral arm observed to a depth of 20 ks. We present a catalog of all sources detected in NARCS (Section 2). We divide the sources into groups based on their quantile properties (Section 3) and analyze the photometric and spectral properties of each group to attempt to identify the dominant X-ray populations in this survey (Section 4). We calculate the NARCS number-flux distribution, correcting for the Eddington bias, the incompleteness of our detection procedure, and the variations in sensitivity across the surveyed area (Section 5). We compare the resulting number-flux distribution to predictions based on previous surveys of Galactic X-ray sources (Section 6).

2. OBSERVATIONS AND SOURCE CATALOG

We performed *Chandra* ACIS-I observations in faint mode of a $2^\circ \times 0.8^\circ$ region of the Norma spiral arm in 2011 June. The primary goal of this survey was to discover faint high-mass X-ray binaries (HMXBs) that may have been missed in previous

surveys performed with instruments with less sensitivity and angular resolution than *Chandra*. The Norma spiral arm was chosen as the target for this search because, likely due to its evolutionary state, it hosts the largest number of known HMXBs of any line-of-sight through the Galaxy (Bodaghee et al. 2012c). Even though HMXBs are more common in the Norma arm than elsewhere, they are rare sources compared to other X-ray populations; thus, our ongoing efforts to identify new HMXBs will be discussed in future papers while here we will focus on studying the dominant classes of X-ray sources in this survey.

Our field was subdivided into 27 pointings; Table 1 reports their coordinates and exposure times and Figure 1 is a mosaic image of the survey. Our observing strategy was to cover a wide area with relatively uniform flux sensitivity and good spatial resolution; therefore, we chose field centers spaced by $12'$, which provided roughly 70 arcmin^2 of overlap on the outskirts of adjacent observations such that the additional exposure time in these overlapping regions partly made up for the worsening point-spread function (PSF) at large off-axis angles. There are only four archival *Chandra* imaging observations of $>20 \text{ ks}$ which fall within the area of our survey region. We chose not to incorporate these data into our survey because they do not add much value compared to the modifications we would have to make to our analysis strategy, and because they might bias our study of faint X-ray populations in the Norma region since they only provide deeper coverage of a fourth of the surveyed area, which may not be representative of the region as a whole.

The ACIS-I consists of four 1024×1024 pixel CCDs, covering a $17' \times 17'$ field of view (Garmire et al. 2003).

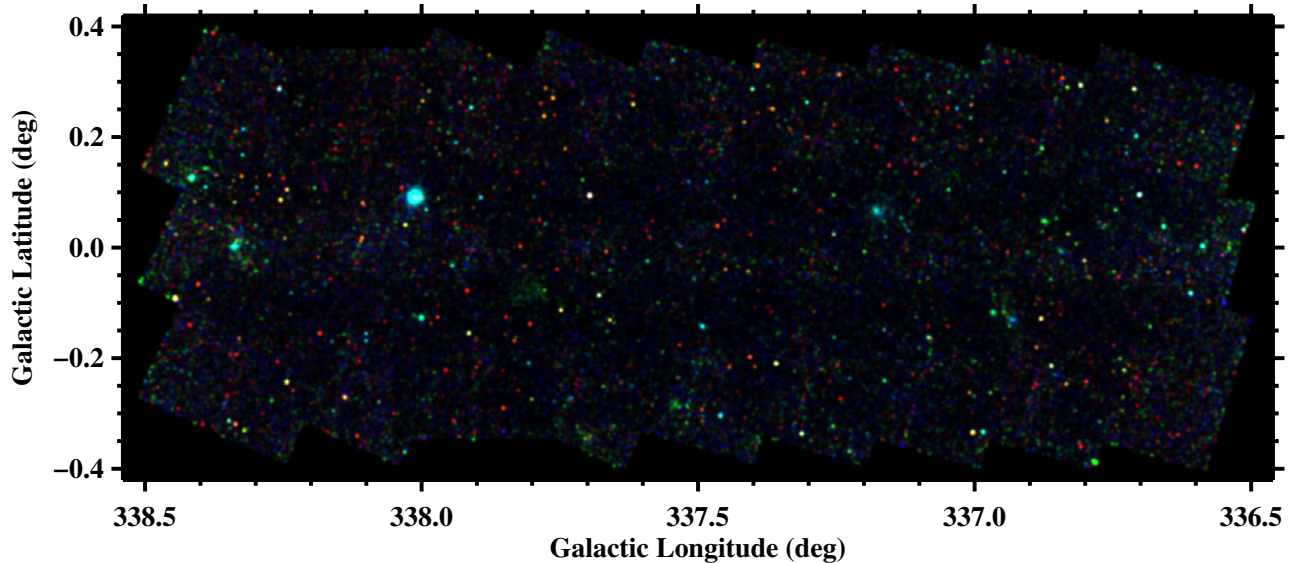


Figure 1. Three-color image of the Norma survey area. Red is 0.5–2 keV, green is 2–4.5 keV, and blue is 4.5–10 keV. Each energy band was smoothed using `aconvolve`. Some artifacts are present at the chip edges.

(A color version of this figure is available in the online journal.)

The on-axis spatial resolution of the ACIS-I is fully sampled by the $0'.492 \times 0'.492$ CCD pixel but it increases greatly off-axis. The PSF increases in size and becomes more elliptical at large off-axis angles, such that at an off-axis angle of $10'$, the PSF has ellipticity ≈ 0.3 and semi-major axis $\approx 15'$ for an enclosed-count fraction (ECF) of 90% for 4.5 keV photons (Allen et al. 2004). The CCDs are sensitive to incident photons with energies in the 0.3–10.0 keV range, and have a resolution of about 50–300 eV. The time resolution of the CCDs, which is determined by the read-out time, is 3.2 s.

We analyzed the data using standard tools from the CIAO package, version 4.4.¹³ We used `chandra_repro` to reprocess the level 1 event lists provided by the Chandra X-Ray Center (CXC). This tool calls on `acis_process_events` to clean the cosmic ray background for very faint mode observations and also applies the sub-pixel event repositioning algorithm EDSEER. Background flares accounted for $<1\%$ of the exposure time and were all relatively weak so, for simplicity, they were not removed.

2.1. Source Detection and Localization

We searched for X-ray sources in each observation separately using the wavelet detection algorithm `wavdetect`. For each observation, we generated images in three energy bands and four spatial resolutions. The three energy bands were the full 0.5–10 keV band (FB), the soft 0.5–2 keV band (SB), and the hard 2–10 keV band (HB); these three bands were chosen to make our source search sensitive to spectrally different sources. For each energy band, we made one image with the full resolution ($0'.5$), one binned by a factor of two ($1''$), one binned by a factor of four ($2''$), and another binned by a factor of eight ($4''$). Exposure maps for each of the three energy bands and four spatial resolutions were also generated applying the spectral weights for a power-law model with $\Gamma = 2.0$ and $N_{\text{H}} = 5.0 \times 10^{22} \text{ cm}^{-2}$, a column density appropriate for sources in the far Norma arm at 10–12 kpc distances¹⁴; the `wavdetect` exposure threshold was set to 0.1 to minimize

spurious detections at detector locations with low exposure times. PSF maps of the 39.3% ECF¹⁵ at 4.5 keV (for the FB and HB) and at 1.5 keV (for the SB), computed using `mkpsfmap`, were also supplied to `wavdetect`. We used wavelet scales that increased by a factor of $\sqrt{2}$ from 1 to 16; this range of wavelet scales and four different spatial resolutions were chosen because the ACIS-I PSF varies significantly with offset from the aim point. We selected the Mexican Hat wavelet, and a sensitivity threshold equal to one over the number of pixels in the image, which corresponds to the chance of detecting approximately one spurious source per image assuming a spatially uniform background. Therefore, we expect `wavdetect` to identify 324 spurious sources ($27 \text{ observations} \times 3 \text{ energy bands} \times 4 \text{ resolutions}$); we find 315 sources are detected at $<3\sigma$, which is in rough agreement with the expected number of spurious sources, so the sample of sources detected at $\geq 3\sigma$ in at least one energy band is probably mostly free of spurious sources.

We combined the source lists from the four images with different spatial resolutions for each observation and energy band. Sources were identified as matches if the separation between them was smaller than the 50% encircled energy contour for the PSF of 4.5 keV photons at the detector position of the source plus the uncertainty in position due to the pixel size in the lower resolution image (e.g., when comparing sources in the full resolution image and the image binned by a factor of two, this uncertainty is $2 \text{ pixels} \times \sqrt{2} \times 0'.492/\text{pixel} = 1'.39$). When duplicate sources were identified, we only retained the position of the source detected in the highest resolution image.

Then we made background maps for each of the observations and energy bands by removing the counts of sources detected in that particular observation and energy band and filling these regions in with a number of counts determined from the average local background. The source regions we removed were defined as circles centered on the source position, with a radius ($r_{96\%}$) equal to the 96% ECF PSF for 4.5 keV photons (for the full and high energy bands) or for 1.5 keV (for the low energy band). In addition, we manually defined regions for the extended sources present in observations ObsID 12508, 12516, 12523,

¹³ Available at <http://cxc.harvard.edu/ciao4.4/>.

¹⁴ See Section 3 for details on the calculation of N_{H} to a given distance.

¹⁵ As recommended by Freeman et al. (2002).

12525, 12526, and 12528. The background regions were defined as annuli with an inner radius equal to the radius of the punched-out region, and an outer radius twice as large; if an annulus overlapped a punched-out region, that overlapping segment was removed from the annulus. The number of background counts to be randomly distributed within the punched-out region was calculated by multiplying the counts in the background region by the ratio of the region areas and the ratio of the region mean effective areas, as determined from the exposure maps. After the punched-out regions had been filled in with the appropriate number of background counts, the background maps were smoothed using *csmooth* with Gaussian kernels of sizes ranging from 20 to 50 pixels. For the observations containing extended sources, first, a smoothed background map was made with both the extended and point sources removed. This map was passed to *csmooth* as a background map, and a smoothed background map was made with only the point sources removed.

We then employed *wavdetect* again to search for X-ray sources in each observation, but this time we used the smoothed background maps we made instead of defaulting to the background maps automatically generated by *wavdetect*. We found that when the background maps we made were used, a larger fraction of sources was detected in higher resolution images than with the automatically generated maps. As before, for each observation, we combined the source lists from the four images with different spatial resolutions. Then we combined the source lists from the three energy bands. When two sources were identified as a match, only one source entry was retained; preference was given to sources detected in the full energy band and then the SB, because the PSF size is smaller at low energies, allowing better source localization.

In order to refine the astrometry of our observations, we searched the VISTA Variables in the Via Lactea (VVV) Survey catalog (Minniti et al. 2010) for infrared counterparts to the X-ray sources we detected.¹⁶ For each *Chandra* observation, we made a list of VVV sources within 12' of the observation aim point with less than a 0.137% probability of being a noise fluctuation. We then determined the reliability of each IR counterpart based on the positional uncertainties of the X-ray and IR sources, the distance between the X-ray and IR source, and the density of IR sources following the treatment of Sutherland & Saunders (1992) but without making any assumptions about the probability distribution function in magnitude of the true IR counterparts.¹⁷ The 1σ positional uncertainty of sources in the VVV catalog is typically 0''.07. We determined the positional uncertainty of the *Chandra* sources using the parameterization of the statistical error as a function of offset angle and net counts¹⁸ in Equation (5) of Hong et al. (2005). These statistical errors were combined in quadrature with a systematic error of 0''.7 (95% error¹⁹) due to *Chandra* guide star alignment uncertainties. We used VVV matches with a reliability greater than 0.9 and *reproject_aspect* to derive a linear and rotational astrometric correction for each *Chandra* observation,

Table 2
Refined Astrometry

ObsID	R.A. (deg)	Decl. (deg)	Roll (deg)	Unc.	Number Counterparts
(1)	(2)	(3)	(4)	(5)	(6)
12507	250.373197	-46.666299	342.207886	0''.38	14
12508	250.155064	-46.530768	342.256256	0''.16	6
12509	249.937691	-46.397888	342.258575	0''.42	26
12510	250.180484	-46.812861	342.220398	0''.32	21
12511	249.961539	-46.681483	333.150848	0''.39	7
12512	249.743528	-46.550463	317.725342	0''.38	14
12513	249.985150	-46.965931	317.737030	0''.35	24
12514	249.767578	-46.829508	342.200439	0''.39	9
12515	249.550029	-46.696055	342.115234	0''.35	22
12516	249.790920	-47.111803	342.203583	0''.35	10
12517	249.572277	-46.978334	342.136200	0''.54	5
12518	249.354557	-46.844589	342.191071	0''.35	23
12519	249.594337	-47.262048	333.187683	0''.36	19
12520	249.375668	-47.128341	333.142365	0''.35	3
12521	249.157996	-46.994096	333.227539	0''.32	24
12522	249.396838	-47.410790	333.249512	0''.34	18
12523	249.178005	-47.276545	333.162964	0''.31	6
12524	248.960241	-47.141987	333.209045	0''.34	24
12525	249.198264	-47.559033	333.258545	0''.29	15
12526	248.979187	-47.424375	333.234863	0''.28	5
12527	248.761554	-47.289507	333.188904	0''.37	19
12528	248.998873	-47.707003	333.211639	0''.39	19
12529	248.779969	-47.572088	333.210205	0''.30	9
12530	248.561714	-47.436723	333.186920	0''.39	15
12531	248.797988	-47.854470	333.221191	0''.31	17
12532	248.578674	-47.719259	333.231171	0''.34	9
12533	248.360765	-47.583555	333.165527	0''.32	18

Notes. (1) Observation ID number. (2) Right ascension (J2000.0) after astrometric correction. (3) Declination (J2000.0) after astrometric correction. (4) Roll angle after astrometric correction. (5) Average systematic uncertainty between IR and X-ray positions after astrometric refinement. (6) Number of VVV counterparts used to refine astrometry.

reducing the systematic astrometric errors to $\leq 0''.54$. We applied the same corrections to the source positions in our source lists. We replaced the 0''.7 systematic errors with the average residuals from the astrometric transformation derived from the VVV counterparts to the X-ray sources. Table 2 presents the refined astrometry for each observation.

We detected a total of 1658 sources, but since each of the 27 observations partially overlaps with at least 3 other survey observations, we checked for duplicate sources between the different observations in order to only have 1 entry per source in our final catalog (see Tables 3–5 for a sample). A source was considered a true duplicate if the distance between the two sources was smaller than the quadrature sum of the positional uncertainties of the two sources. If the distance between two sources was larger than the quadrature sum of the positional uncertainties but smaller than the regular sum of the uncertainties, then the sources were flagged for manual inspection. Some sources that met the true duplicate criterion but were unusual in some respect (e.g., one source was flagged as extended while the other was not) were also flagged by the algorithm for manual inspection. Whether or not the sources flagged for manual inspection were determined to be duplicates, they were flagged with “id” for “inspected duplicate” in the catalog.²⁰ In total, 38 sets of sources were flagged for manual

¹⁶ See http://www.eso.org/sci/observing/phase3/data_releases/vvv_dr1.html for the first data release used in this paper.

¹⁷ Our calculation takes into account the probability that the NIR counterpart of an X-ray source is undetected in the VVV survey. In Sutherland & Saunders (1992) this null probability is the quantity $(1-Q)$. Since we do not know Q a priori, we guess its value and then refine our guess iteratively until the Q value meets the criterion in Equation (7) of Sutherland & Saunders (1992). In this way, we find $Q = 0.85$.

¹⁸ These are the net counts reported by *wavdetect*, not those determined by aperture photometry.

¹⁹ See <http://cxc.harvard.edu/cal/ASPECT/celmon>.

²⁰ Flags for each source are provided in Column 13 of Table 3. Descriptions of all flags are provided in Appendix A.1.

Table 3
Catalog of Point and Extended Sources: Detection and Localization

No.	Source (CXOU J)	ObsID (125**)	R.A. (deg)	Decl. (deg)	Unc. (arcsec)	Offset (arcmin)	Sig. FB	Sig. SB	Sig. HB	Radius (arcsec)	PSF (arcsec)	Flags
(1)	(2)	(3)	(4)	(5)	(6)	(7)	(8)	(9)	(10)	(11)	(12)	(13)
1	163228.2–473755	33	248.117829	–47.632173	4.03	10.3	3.6	2.3	2.5	13.8	13.8	...
2	163241.5–474039	33	248.172944	–47.677522	1.79	9.5	9.0	10.4	2.5	11.9	11.9	...
3	163244.6–474133	33	248.186065	–47.692513	3.63	9.6	2.4	0.0	2.8	12.2	12.2	...
4	163248.7–473017	33	248.203151	–47.504857	1.41	7.9	8.4	1.2	8.5	9.2	9.2	...
5	163251.0–474135	33	248.212798	–47.693198	3.16	8.9	3.0	5.0	0.0	10.7	10.7	...
6	163253.0–474201	33	248.221111	–47.700286	2.26	9.0	5.2	1.8	4.8	10.9	10.9	...
7	163259.0–473819	33	248.246176	–47.638806	1.13	5.7	7.5	7.2	4.1	5.2	5.2	...
8	163259.4–472804	33	248.247582	–47.467941	3.39	8.3	2.3	3.4	0.4	10.1	10.1	...
9	163303.2–472547	33	248.263337	–47.429724	13.98	10.0	0.0	0.8	0.0	14.0	14.0	...
10	163306.2–473239	33	248.276159	–47.544291	1.55	4.2	3.3	0.7	3.1	3.5	3.5	...

Notes. See Appendix A.1 for detailed column descriptions.

(This table is available in its entirety in a machine-readable form in the online journal. A portion is shown here for guidance regarding its form and content.)

Table 4
Catalog of Point and Extended Sources: Photometry

No.	C_{net} FB	C_{net} SB	C_{net} HB	f_{ph} FB ($10^{-6} \text{ cm}^{-2} \text{ s}^{-1}$)	f_{ph} SB ($10^{-6} \text{ cm}^{-2} \text{ s}^{-1}$)	f_{ph} HB ($10^{-6} \text{ cm}^{-2} \text{ s}^{-1}$)	E_{50} (keV)	E_{25} (keV)	E_{75} (keV)	f_X FB ($10^{-14} \text{ erg cm}^{-2} \text{ s}^{-1}$)	Phot. Flag	Quantile Group
(1)	(2–4)	(5–7)	(8–10)	(11–13)	(14–16)	(17–19)	(20–21)	(22–23)	(24–25)	(26–28)	(29)	(30)
1	16_{-6}^{+7}	6_{-3}^{+4}	10_{-5}^{+6}	$3.76_{-1.32}^{+1.57}$	$0.76_{-0.40}^{+0.55}$	$2.47_{-1.13}^{+1.39}$	2.9 ± 1.8	1.6 ± 0.8	5.6 ± 2.4	$1.75_{-1.25}^{+1.31}$...	C
2	47_{-8}^{+9}	37_{-6}^{+7}	10_{-5}^{+6}	$10.55_{-1.76}^{+1.99}$	$4.68_{-0.80}^{+0.93}$	$2.28_{-1.07}^{+1.31}$	1.4 ± 0.1	1.0 ± 0.1	1.8 ± 0.5	$2.35_{-0.44}^{+0.49}$...	A
3	9_{-4}^{+5}	3	9_{-4}^{+5}	$3.48_{-1.71}^{+2.15}$	0.69	$3.88_{-1.69}^{+2.14}$	5.4 ± 0.9	4.5 ± 1.3	6.1 ± 0.9	$3.03_{-1.56}^{+1.93}$	- S -	D
4	36_{-7}^{+8}	2_{-2}^{+3}	34_{-6}^{+7}	$7.95_{-1.46}^{+1.69}$	$0.28_{-0.24}^{+0.40}$	$7.60_{-1.42}^{+1.66}$	4.6 ± 0.3	3.7 ± 0.3	5.2 ± 0.5	$5.90_{-1.17}^{+1.33}$...	D
5	13_{-5}^{+6}	13_{-4}^{+5}	6	$2.85_{-1.12}^{+1.36}$	$1.70_{-0.51}^{+0.65}$	1.32	1.0 ± 0.1	0.9 ± 0.2	1.1 ± 0.1	$0.44_{-0.18}^{+0.21}$	-- H	A
6	22_{-6}^{+7}	4_{-2}^{+4}	19_{-5}^{+6}	$6.00_{-1.53}^{+1.82}$	$0.59_{-0.36}^{+0.55}$	$5.07_{-1.41}^{+1.71}$	3.0 ± 0.7	2.2 ± 0.4	5.7 ± 1.2	$2.90_{-0.99}^{+1.10}$...	C
7	20_{-5}^{+6}	12_{-3}^{+5}	9_{-3}^{+4}	$4.70_{-1.10}^{+1.35}$	$1.53_{-0.46}^{+0.60}$	$2.08_{-0.78}^{+1.04}$	1.8 ± 0.6	1.5 ± 0.1	3.5 ± 0.5	$1.37_{-0.53}^{+0.57}$...	B
8	8_{-4}^{+5}	7_{-3}^{+4}	1_{-1}^{+4}	$1.82_{-0.92}^{+1.17}$	$0.85_{-0.37}^{+0.51}$	$0.33_{-0.33}^{+0.93}$	1.6 ± 0.9	1.4 ± 0.3	1.8 ± 3.8	$0.47_{-0.35}^{+0.40}$...	A
9	7	2_{-2}^{+3}	5	1.74	$0.27_{-0.27}^{+0.48}$	1.23	5.2 ± 4.8	2.9 ± 7.1	7.6 ± 7.1	1.46	F - H	C
10	6_{-3}^{+4}	1_{-1}^{+2}	5_{-2}^{+4}	$1.11_{-0.50}^{+0.74}$	$0.08_{-0.08}^{+0.26}$	$0.98_{-0.47}^{+0.72}$	5.1 ± 0.8	4.4 ± 1.4	5.4 ± 0.3	$0.91_{-0.44}^{+0.62}$...	E

Notes. See Appendix A.2 for detailed column descriptions of the electronic version.

(This table is available in its entirety in a machine-readable form in the online journal. A portion is shown here for guidance regarding its form and content.)

Table 5
Catalog of Point and Extended Sources: Infrared Counterparts

No.	VVV Source Name	R.A. (deg)	Decl. (deg)	Δ_{X-IR} (arcsec)	p_{noise}	Reliability
(1)	(2)	(3)	(4)	(5)	(6)	(7)
1	515727792649	248.117752	–47.631649	1.89	3.07e^{-03}	0.3216
2	515726841264	248.172806	–47.677017	1.84	5.29e^{-07}	0.8660
3	515726837733	248.185730	–47.693638	4.13	5.29e^{-07}	0.3508
4	515727238897	248.203003	–47.505127	1.05	1.71e^{-04}	0.7804
5	515726847521	248.212341	–47.693485	1.52	1.71e^{-04}	0.9482
6	515727540494	248.220947	–47.700108	0.76	1.71e^{-04}	0.9142
7	515726868309	248.246140	–47.638630	0.64	5.29e^{-07}	0.9777
8	515726918176	248.247345	–47.468082	0.78	9.52e^{-06}	0.4607
9	515726930863	248.262817	–47.429794	1.29	5.29e^{-07}	0.0657
10	515727577185	248.276459	–47.544682	1.59	2.81e^{-04}	0.8825

Notes. See Appendix A.3 for detailed column descriptions of the electronic version.

(This table is available in its entirety in a machine-readable form in the online journal. A portion is shown here for guidance regarding its form and content.)

inspection and we determined 28 of them were true duplicates. The catalog entries for duplicates were combined so that exposure times and net counts were summed, source positions were weight-averaged, and the ObsIDs, offsets from the aim

point, source region radii, 90% PSF sizes, and flags of the duplicate sources were all listed. If a source was determined to be variable on long timescales (see Section 2.3), its derived photometric properties were averaged, but if it was determined

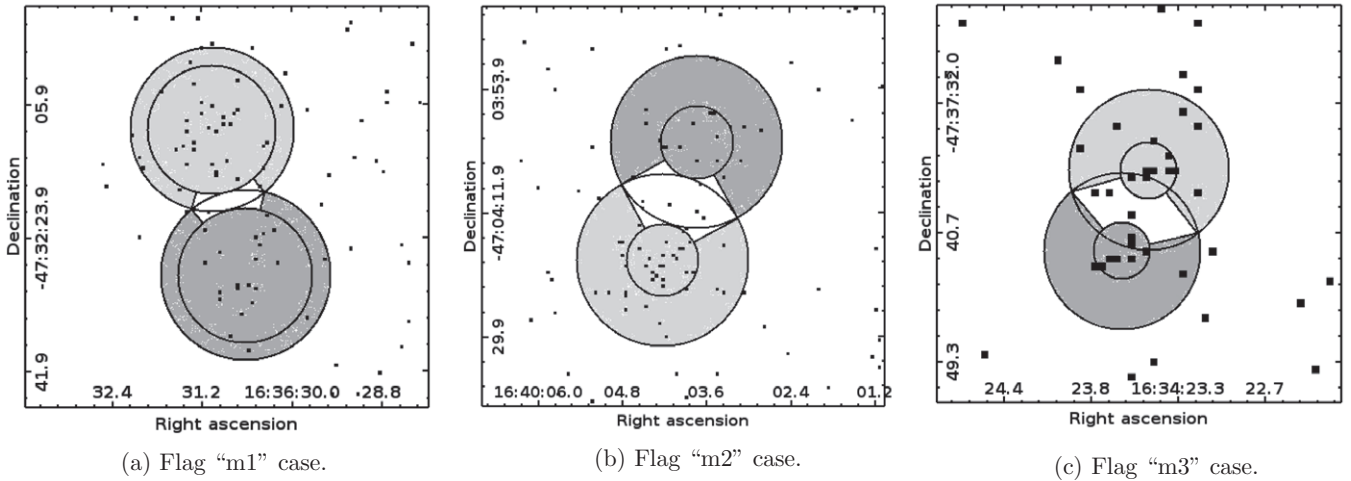


Figure 2. Examples of modified overlapping regions.

Table 6
Aperture Region Definitions

Source Region Overlap	Condition	Core Radius r_c	Refined Source Region	Background Region	Flag
No...	$\Delta \geq r_{90\%} + r'_{90\%}$	$r_{90\%}$	$r \leq r_c = r_{90\%}$	$r_{96\%} < r < 2r_{96\%}$ and $r'' > r''_{96\%}$ for all neighbors	...
Yes...	$\Delta \geq 1.5r'_{90\%}$, $\Delta < r_{90\%} + r'_{90\%}$	$\Delta - r'_{90\%}$	$r \leq r_c$ and pie sector with $r_c < r \leq r_{90\%}$	Same as above	m1
Yes...	$\Delta < 1.5r'_{90\%}$, $\Delta \geq r_{68\%} + r'_{90\%}$	$\Delta - r'_{90\%}$	Same as above	Same as above	m2
Yes...	$\Delta < r_{68\%} + r'_{90\%}$	$\Delta/3$	Same as above	Same as above	m3

Notes. Parameter Δ is the distance between the source and its nearest neighbor, and $r'_{90\%}$ is the 90% PSF radius of the nearest neighbor. r refers to the distance from the source and r'' refers to the distance from neighbors. The PSF radii are calculated for 4.5 keV photons. For sources flagged as potentially extended ("e"), these criteria remain the same, except that instead of using $r_{90\%}$ and $r_{96\%}$, the radii listed in the catalog are used.

to be constant, they were weight-averaged. After combining the entries of duplicate sources, our catalog contains 1415 sources.

2.2. Photometry

We used `dmextract` to compute photometric quantities for each of the X-ray sources in our catalog. In most cases, we defined an aperture region for each source as a circle with radius ($r_{90\%}$) equal to the 90% ECF PSF for 4.5 keV photons. Given the relatively low source counts for the vast majority of sources, this radius is well optimized to obtain the highest signal-to-noise ratio. However, if the semi-major axis of the source region provided by `wavdetect` was more than twice as large as $r_{90\%}$ in all images in which the source was detected, then the semi-major axis was used as the radius of the aperture region and the source was flagged with "e" for "extended," to denote that it may be an extended source. In some cases, these "e" source regions surrounded another source region; these sources were additionally flagged with an "s" for "surrounding." We nonetheless included these sources in our analysis of point-like sources, but they only constitute 3% of sources detected at $\geq 3\sigma$. We also modified the aperture regions of overlapping sources; following the method of Hong et al. (2005), we defined a source region as the sum of a circular core and a pie sector of an annular shell that excludes the common sector with the neighbor's source region. The core size was determined empirically to maximize the source photons included and to minimize contamination from neighbors, as described in Table 6, which also lists the flags

associated with each type of source region modification from the standard one. As was implemented in Hong et al. (2005), if the source region overlapped with more than one neighbor, the core size was determined by the nearest neighbor and the pie sector excluded all common sectors with the neighbors' aperture regions. Figure 2 shows some examples of these modified overlapping source regions. We manually modified 12 aperture regions of sources with multiple nearby neighbors. Finally, we manually created source and background regions for the extended sources in observations ObsID 12508, 12516, 12523, 12525, 12526, and 12528 that were not detected by `wavdetect` and flagged these sources with a "c" for "created."

The background region for each source was defined as an annulus with an inner radius equal to $r_{96\%}$ and an outer radius equal to $2r_{96\%}$. In the few instances when a source flagged as "e" had a source radius larger than $r_{96\%}$, then the inner radius of the annulus was set equal to the source radius, and the outer radius was twice as large as this inner radius. As we did when making the background maps, we generated images with punched-out $r_{96\%}$ source regions, which were again defined as circles with radii equal to $r_{96\%}$. When extracting photometric information from the background regions, we used these punched-out images so that contamination from neighboring sources was avoided. When calculating the background region area, we corrected the annular area for any segments that were excluded due to overlap with punched-out source regions.

Having defined source and background regions, we used `dmextract` to calculate the source core, source shell, and

background region counts (C_{core} , C_{pie} , and C_{bkg}) in the full, hard, and soft energy bands, their areas (A_{core} , A_{pie} , and A_{bkg}), and their mean effective areas (E_{core} , E_{pie} , and E_{bkg}) by including exposure maps in the call to `dmextract`. We calculated the 1σ Gaussian errors in the measured counts (both in the source and background regions) using the recommended approximations for upper and lower limits in Gehrels (1986). For sources with apertures consisting of a circular core and a pie sector of an annular shell, the total source region counts, area, and effective area were calculated in the following manner, assuming azimuthal symmetry of the PSF:

$$C_{\text{src}} = C_{\text{core}} + \frac{A_{\text{ann}}}{A_{\text{pie}}} C_{\text{pie}} \quad (1)$$

$$A_{\text{src}} = A_{\text{core}} + A_{\text{ann}} \quad (2)$$

$$E_{\text{src}} = E_{\text{core}} + \frac{A_{\text{ann}}}{A_{\text{pie}}} E_{\text{pie}}, \quad (3)$$

where $A_{\text{ann}} = \pi(r_{\text{outer}}^2 - r_{\text{inner}}^2)$ is the total area of the annular shell. For all other sources, the source region simply consists of the circular core region, and thus $C_{\text{src}} = C_{\text{core}}$, $A_{\text{src}} = A_{\text{core}}$, and $E_{\text{src}} = E_{\text{core}}$. The total observed source region counts include contributions from the source and from the background. The background counts within the source region were estimated and subtracted as shown below to estimate the true source counts:

$$C_{\text{net}} = C_{\text{src}} - f C_{\text{bkg}}, \quad f = \frac{A_{\text{src}} E_{\text{src}}}{A_{\text{bkg}} E_{\text{bkg}}}. \quad (4)$$

If the estimated background counts were equal to or greater than the source region counts, then we calculated the 90% upper confidence limit to the net source counts based on the method described in Kraft et al. (1991). The photon flux for each energy band was calculated by dividing the net source counts by the mean source region effective area and the exposure time. Since the mean effective area was determined from the exposure maps, these photon fluxes will not be accurate for all sources because in making the exposure maps we assumed a source spectral model with $\Gamma = 2.0$ and $N_{\text{H}} = 5.0 \times 10^{22} \text{ cm}^{-2}$. To determine the extent to which we may be under or overestimating the fluxes of sources with different spectral properties, we made exposure maps for one observation using different spectral models spanning the range of Γ and N_{H} covered by our sources. We find that the mean effective areas vary by $\lesssim 20\%$ in the FB and $\lesssim 5\%$ in the SB and HB, making our derived photon fluxes uncertain by the same percentages.

We also computed the probability that the sources in our catalog could be noise fluctuations of the local background using the following formula derived in Appendix A of Weisskopf et al. (2007):

$$P(\geq C_{\text{src}} | C_{\text{bkg}}; C_{\text{net}} = 0) = \sum_{c=C_{\text{src}}}^{C_{\text{bkg}}+C_{\text{src}}} \frac{(C_{\text{bkg}} + C_{\text{src}})!}{c!(C_{\text{bkg}} + C_{\text{src}} - c)!} \times \left(\frac{f}{1+f}\right)^c \left(1 - \frac{f}{1+f}\right)^{C_{\text{bkg}}+C_{\text{src}}-c}. \quad (5)$$

We determine the significance of a source based on this probability and the Gaussian cumulative distribution function. For sources detected in multiple observations, these probability

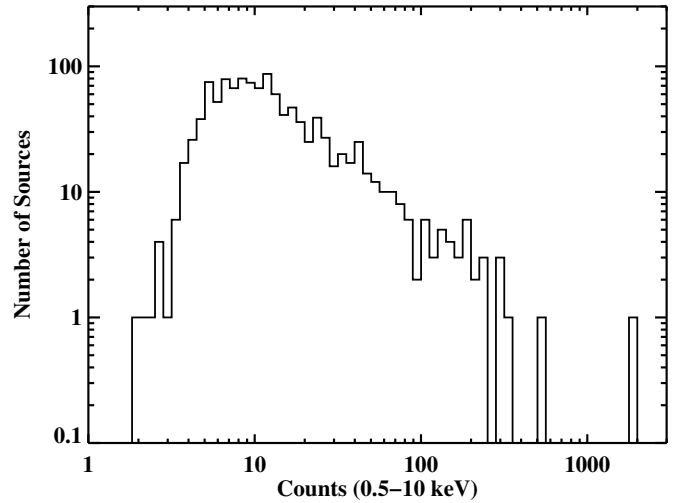


Figure 3. Histogram of 0.5–10 keV net counts for $\geq 3\sigma$ sources. The brightest source with 14,716 counts is not shown.

values from individual observations were multiplied together, and the source significance was determined from this combined probability. The photometric values used in our data analysis are included in our catalog, a sample of which can be seen in Table 4. Although in our catalog we include all detected sources, in our analysis we only use sources detected at $\geq 3\sigma$ in the full, soft, or hard energy band and refer to these sources as the full sample. Figure 3 shows the histogram distribution of the total 0.5–10 keV counts detected for these sources; as can be seen, most of these sources have fewer than 100 counts, which is roughly the number of photons required to determine their spectral and variability properties accurately enough to determine the nature of the X-ray source. Our catalog contains 1130 point-like sources detected at $\geq 3\sigma$ in at least 1 of the 3 energy bands and 5 extended sources which we identified by eye and are shown in Figure 4. Three of these extended sources are confirmed SNRs (G337.2+0.1, G337.8–0.1, and HESS J1640–465), another is a possible SNR based on its morphology (CXOU J163942.3–471257), and one has a jet-like morphology and is probably a pulsar wind nebula (CXOU J163802.6–471345). New results about these extended sources are discussed in Jakobsen (2013) and Jakobsen et al. (2014).

2.3. Source Variability

X-ray sources can be variable on timescales from milliseconds to years, so we tried to characterize the variability of the sources in our catalog to help classify them. We determined whether a source was variable on short timescales (seconds to hour) by comparing the arrival times of events with a constant event rate using the K-S test. Sources that have $\geq 99.73\%$ chance of not being constant are flagged with “vs” (short variability), while those that have $\geq 95\%$ chance of not being constant are flagged with “vp” (probable short variability). The K-S test is more reliable for sources with more counts; we only consider the K-S test to be reliable for sources with at least 40 counts. Of the 80 sources with more than 40 counts (in a single observation), 27 (16) show short-timescale variability with $\geq 95\%$ (99.73%) confidence.

We also checked whether sources detected in multiple observations demonstrated long-term variability (hours–days) by determining whether the source photon flux in two observations differed by more than 3σ in the full, soft, or hard energy band;

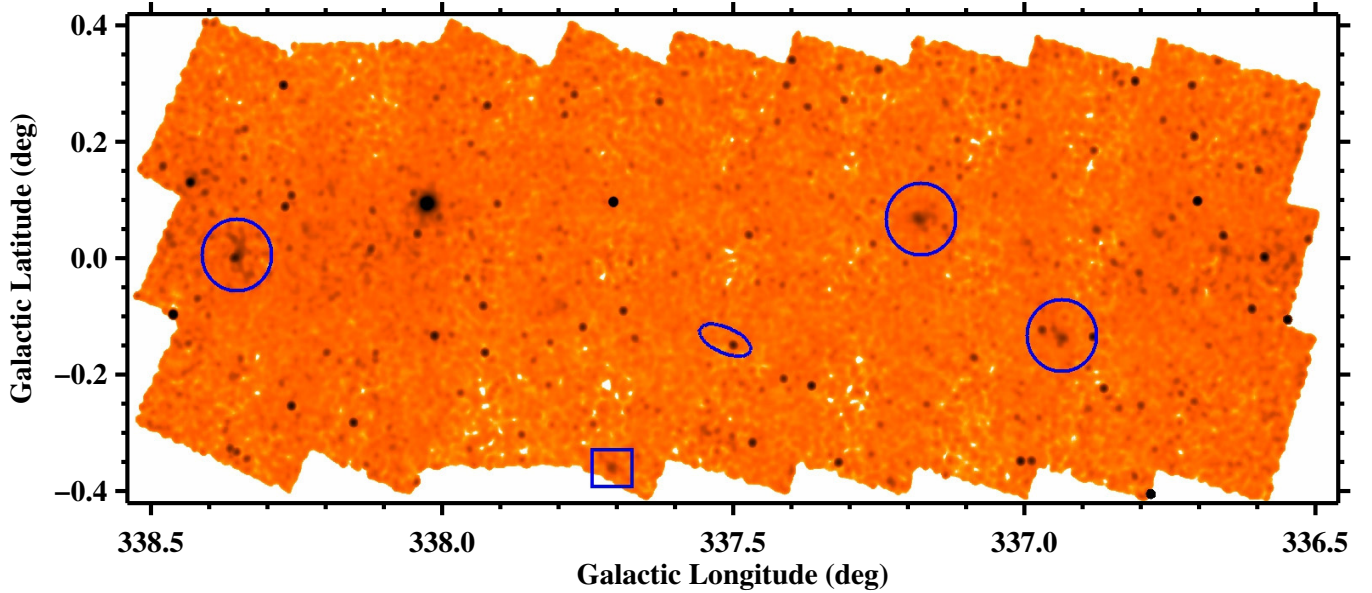


Figure 4. Mosaic image of the 0.5–10 keV band showing locations of extended sources identified by eye. Circles indicate confirmed SNRs, while the square indicates a candidate SNR, and the ellipse indicates a PWN candidate.

(A color version of this figure is available in the online journal.)

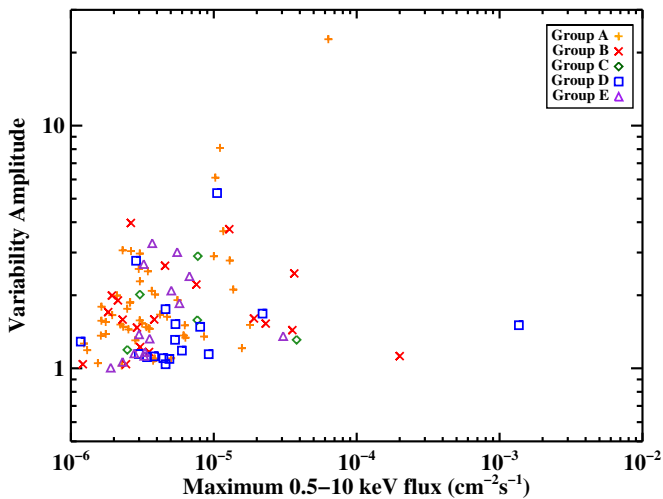


Figure 5. Variability amplitudes in the 0.5–10 keV band (maximum photon flux divided by the minimum photon flux) vs. maximum photon flux for sources that are detected in multiple observations and found to vary between observations at $\geq 3\sigma$ confidence. The median 1σ fractional errors are $+0.36/-0.29$ for the maximum flux and $+0.58/-0.23$ for the variability amplitude. Different symbols represent different quantile groups.

(A color version of this figure is available in the online journal.)

these sources were flagged with “vl” (long variability). In cases in which a source’s flux is measured in one observation but only an upper limit can be obtained in another, we consider the source to be variable on long timescales if the measured flux and upper limit are inconsistent at $>3\sigma$ confidence. We found 219 sets of sources detected in 2 or more observations with a combined significance $\geq 3\sigma$, 105 (48%) of which show long-term variability. Of the 758 sources with $\geq 3\sigma$ confidence located in regions where multiple observations overlap, 373 are not detected in multiple observations. This is not surprising because the fluxes of all but 7 of these 373 sources are lower than the flux to which 100% of our survey area is sensitive (see Section 5.1). We calculated the variability amplitude of each source

Table 7
Sources Showing Periodic Variability

No.	Source (CXOU J)	C_{net} FB	Period (s)	Z_2^2	Variability Flags
(1)	(2)	(3)	(4)	(5)	(6)
750	163750.8–465545	1790 ± 40	7150 ± 50	95	vs, vl
961	163855.1–470145	160 ± 10	5660 ± 20	213	vp, vl
999	163905.6–464212	14720 ± 120	906 ± 1	368	vs, vl

Notes. (1) Catalog source number. (2) *Chandra* source name. (3) Net source counts in the full 0.5–10 keV band. (4) Most probable period determined by the Z_n^2 -test. (5) Result of Z_2^2 -test. (6) “vl”—variability on long timescales (hours–days), “vp”—variability on short timescales (second–hours) at $\geq 95\%$ confidence, “vs”—variability on short timescales at $\geq 99.73\%$ confidence.

displaying long-term variability, which we defined as the ratio of the maximum photon flux to the minimum photon flux in the 0.5–10 keV band. The variability amplitude does not seem to correlate with the photon flux of these variable sources, as shown in Figure 5.

Finally, we searched for a coherent signal with period $6.8 \text{ s} < P < 10 \text{ ks}$ in sources with more than 50 counts in at least one observation using the Z_n^2 -test (Buccheri et al. 1983), which depends on the sum of the Fourier powers of the first n harmonics. Since it is not feasible to try an infinite number of n values, Buccheri et al. (1983) suggested using $n = 2$ as a general test; we decided to use both $n = 2$ and $n = 1$ since the latter is equivalent to the traditional Rayleigh test. For each source, photon arrival times were corrected to the solar system barycenter using the JPL DE405 ephemeris and our catalog coordinates, and for sources detected in multiple observations, photon arrival times from different observations were combined. We found three sources with significant Z_2^2 values; these sources have significant Z_1^2 values as well. Table 7 provides the periods and Z_2^2 values of these sources; the uncertainties in the periods were calculated using the method described in Ransom et al. (2002). In Figure 6 we present the phase-folded light curve of each periodic source. Source 999 is a previously discovered

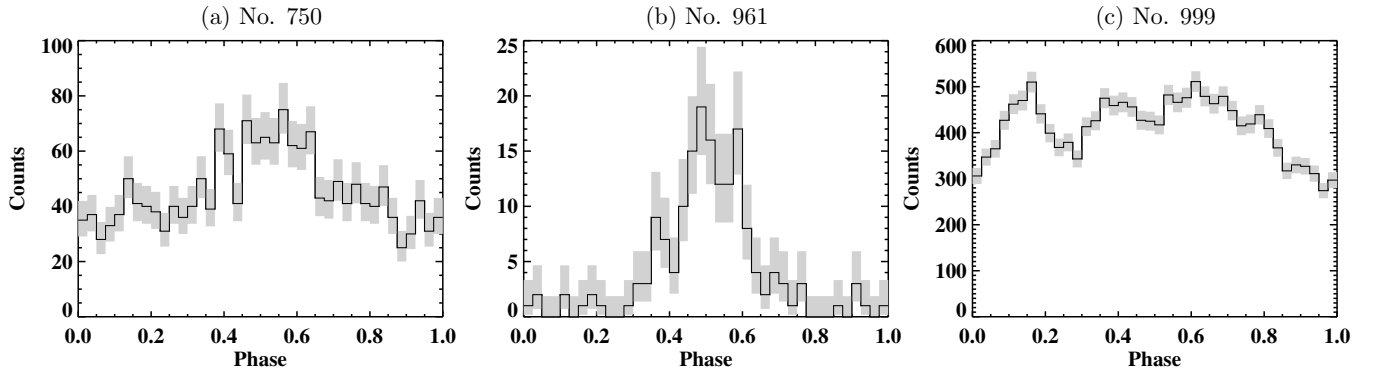


Figure 6. Phase-folded light curves of periodic sources labeled with source catalog number. Periods are presented in Table 7. Gray bars show 1σ errors.

HMXB; the period we measure is consistent with the period found by Bodaghee et al. (2006). The other two sources are most likely magnetic cataclysmic variables (CVs), as discussed in Section 4.2.

2.4. Infrared Counterparts

We searched for infrared counterparts to our X-ray sources in the VVV catalog. First, we created a list of non-duplicate VVV sources lying within our surveyed area; we considered an entry in the VVV catalog to be duplicate if the angular difference between the source positions was less than the 3σ positional uncertainty of the sources (approximately $0''.21$). Then, we determined the reliability of each counterpart as described in Section 2.1, and consider a match good if its reliability is $\geq 90\%$ and the noise probability of the VVV source is $\leq 0.31\%$. The latter constraint excludes low-significance detections and very bright sources, which saturate the array and have less accurate positions and magnitudes. Table 5 provides information about the closest VVV source to each *Chandra* source and its reliability as a counterpart.

We have found reliable counterparts for 52% of X-ray sources detected at $\geq 3\sigma$. X-ray sources without reliable counterparts may have IR counterparts below the sensitivity limits of the VVV survey, have large positional uncertainties, and/or be in a particularly crowded region in which multiple IR sources are equally likely counterparts. Figure 7 shows the ($J-H$) versus H magnitude of the reliable counterparts (the K_s magnitudes have not yet been made publicly available). In this color-magnitude diagram, the distribution of reliable counterparts does not match that of all the VVV sources located within our field-of-view, indicating that the majority of these counterparts are not random associations.

2.5. Quantile Properties

Robust identifications of X-ray sources typically require multiwavelength information, but the X-ray data itself can provide clues to the nature of a source. First, we tried to classify the sources using a hardness ratio and a soft and hard X-ray color. However, we found that this method was ineffective for distinguishing between sources with intrinsically hard spectra and very absorbed sources. This distinction is important since the H II regions near which we expect to find younger populations of X-ray sources, the primary target of this survey, are at a distance of ~ 11 kpc and thus the X-ray emission from such sources would be attenuated by large amounts of intervening gas.

Therefore, we instead employed quantile analysis to classify the X-ray sources. Quantile analysis, first introduced by Hong et al. (2004), uses the median energy and other quantile energies of a source as proxies for its spectral hardness and spectral shape. Its main advantage is that it does not require subdivision of the full energy range into different bands, making it free of the selection effects inherent in the hardness ratio and colors methods and yielding meaningful results even for low-count sources. The fundamental quantities required in quantile analysis are E_x , the energy below which $x\%$ of the source counts reside. We made event files for each source and background region and passed them to `quantile.pro`, an IDL program developed by J. Hong.²¹ The other input to this code is the ratio of source and background areas and effective areas:

$$\text{ratio} = \frac{(A_{\text{core}} + A_{\text{pie}})(E_{\text{core}} + E_{\text{pie}})}{A_{\text{bkg}} E_{\text{bkg}}}. \quad (6)$$

With this code, we computed E_{25} , E_{50} , and E_{75} , which are included in our catalog and can be seen in Table 4. These parameters were then combined into two quantities, $Q_x = \log(E_{50}/E_{\text{min}})/\log(E_{\text{max}}/E_{\text{min}})$ and $Q_y = 3(E_{25} - E_{\text{min}})/(E_{75} - E_{\text{min}})$, where E_{min} and E_{max} are 0.5 and 10 keV, respectively. Q_x measures the hardness of the spectrum, while Q_y indicates how broad or narrow the spectrum is. Figure 8 shows diagrams of Q_x and Q_y for all sources in our catalog detected at $\geq 3\sigma$ in the full energy band. To facilitate interpretation of this diagram, we have overlaid grids for a power-law model and a thermal bremsstrahlung model, both attenuated by interstellar absorption (see Figures 9 and 10).

3. SPECTRAL ANALYSIS

One of the goals of our survey is to understand the nature of the X-ray sources in our field. Analyzing the X-ray spectrum of a source can provide important clues about its physical nature, but most of our sources have too few counts to permit meaningful spectral analysis. Therefore, to identify the dominant populations of X-ray sources in our survey, we divided them into spectral groups based on their quantile properties (see Section 2.5) and analyzed the stacked spectrum of each quantile group. Our goals in making group divisions were to combine enough sources together to reduce the errors caused by poor statistics in spectral fitting, but also to maintain the maximum spectral diversity in our sample.

As can be seen in Figure 8, the sources are loosely confined to a U-shaped region in the Q_x - Q_y diagram, with overdensities

²¹ Available at <http://hea-www.harvard.edu/ChaMPlane/quantile>.

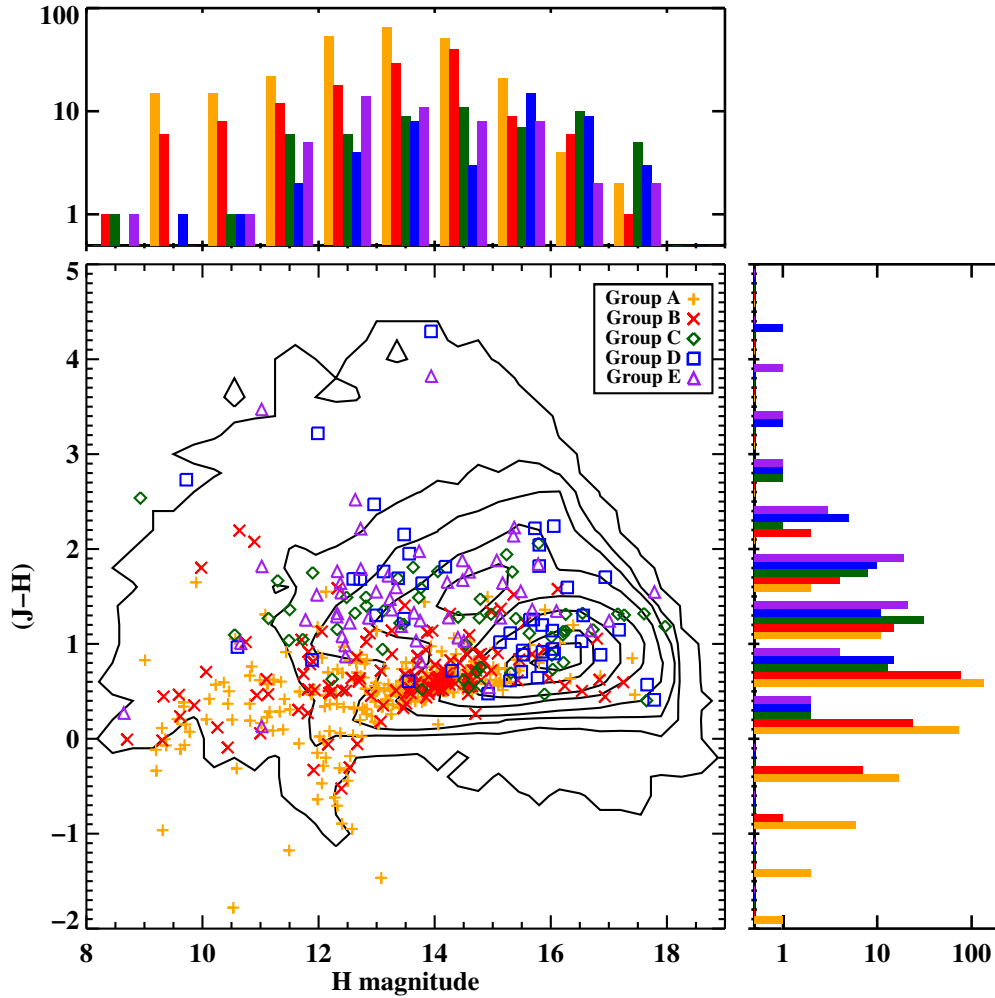


Figure 7. Near-IR color–magnitude diagram showing the distribution of all VVV sources in our surveyed area (black contours) and the reliable counterparts to X-ray sources in our survey (symbols). The black contours, from outside inward, encircle 99%, 95%, 90%, 80%, 60%, 40%, 20%, and 10% of the VVV sources. For the counterparts represented with symbols, the median 1σ error is 0.005 mag for the H magnitude and 0.007 mag for the $(J - H)$ color.

(A color version of this figure is available in the online journal.)

toward the upper right and middle left. However, apart from these slight overdensities, the sources do not split up into visibly discernible groups, so we decided to split up the sources into groups with physically motivated dividing lines roughly following the $N_{\text{H}} \approx 2 \times 10^{22} \text{ cm}^{-2}$ and $\Gamma \approx 3$ grid lines, as shown in Figure 9. The dividing N_{H} line corresponds to the average N_{H} out to a distance of ~ 6 kpc in our survey region, as determined from the sum of $N_{\text{H}1}$ estimated from the Leiden/Argentine/Bonn (LAB) Survey (Kalberla et al. 2005) and $N_{\text{H}2}$ estimated from the MWA CO survey (Bronfman et al. 1989)²²; this line roughly divides sources in the foreground and in the Scutum-Crux and near Norma spiral arms from sources in the far Norma arm. The dividing Γ line instead splits thermal and nonthermal sources. We further subdivided sources along $Q_x = 0.5$, because, as shown in Figure 11, this Q_x value roughly separates sources detected in the SB from sources detected in

the HB. The equations of the dividing lines, in counterclockwise order from the top left of the diagram, are

$$\begin{aligned} Q_y &= Q_x + 0.8 \\ Q_x &= 0.5 \\ Q_y &= 0.5Q_x + 1.05 \\ Q_y &= 3.9Q_x - 0.84. \end{aligned} \quad (7)$$

Varying the quantile divisions by ~ 0.1 dex leads to no significant change in the best-fitting spectral parameters of the stacked spectrum of each quantile group (Section 4), and the maximum likelihood (ML) slopes of the number-flux distributions of the sources in each quantile group remain consistent at the 2σ level or better (Section 6). Thus, our results are robust to ~ 0.1 dex variations in the quantile group definitions.

For each source, we used `specextract` to extract source and background spectra and build associated ARFs and RMFs. Then the spectra of sources within each quantile group were combined with `combine_spectra`. Sources with more than 500 net counts were excluded from the stacked spectra to prevent individual sources from excessively influencing the combined spectrum. The spectra of these three individual sources are

²² To estimate $N_{\text{H}1}$ ($N_{\text{H}2}$) to a distance of 6 kpc, we calculated the line-of-sight velocity of an object at this distance in circular motion around the Galaxy, integrated the brightness temperature measured in the LAB (MWA) survey from 0 km s^{-1} to this velocity, and multiplied the total brightness by $N_{\text{H}1}/I_{\text{H}} = 1.8 \times 10^{18} \text{ cm}^{-2} \text{ K}^{-1} \text{ km}^{-1} \text{ s}$ ($N_{\text{H}2}/I_{\text{CO}} = 2 \times 10^{20} \text{ cm}^{-2} \text{ K}^{-1} \text{ km}^{-1} \text{ s}$ derived in Dame et al. (2001)). The sum of $N_{\text{H}1}$ and $N_{\text{H}2}$ will actually be a lower limit of N_{H} since this calculation assumes the emission lines are optically thin.

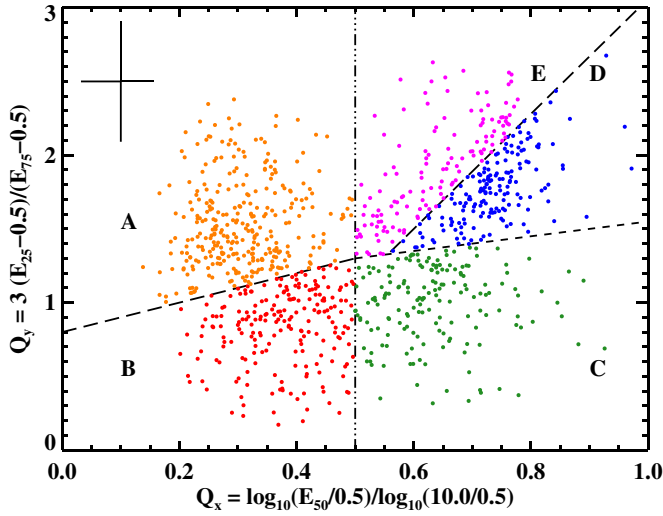


Figure 8. Quantile diagram for sources detected at $\geq 3\sigma$ in the 0.5–10 keV band. Sources were split into five spectral groups defined by the black lines. Short dashes at $N_{\text{H}} \approx 2 \times 10^{22} \text{ cm}^{-2}$ roughly divide nearby ($\lesssim 6$ kpc) and distant ($\gtrsim 6$ kpc) sources. Long dashes roughly separate thermal and nonthermal sources. The dash-dotted line at $Q_x = 0.5$ subdivides sources detected in the soft energy band from those detected in the hard energy band. Median 1σ errors are shown in the upper left.

(A color version of this figure is available in the online journal.)

shown in Figure 12 and their best-fit spectral parameters are provided in Table 8. Sources 78 and 999 fall in quantile group D while source 750 falls in quantile group B, and they are best fit by absorbed power-laws.

Each of the stacked spectra was fit with an interstellar absorption model (tbabs, Wilms et al. 2000; with cross-section from Verner et al. 1996) convolved with a power-law model (pegpwr1w) and an optically thin thermal plasma model (vpec, Smith et al. 2001; with abundances frozen to values from Güdel et al. 2007 relative to Anders & Grevesse 1989; scaled to Wilms et al. 2000). If an Fe line was visible between 6 and 7 keV, we added a Gaussian component to the power-law model. If neither the power-law nor thermal model produced a fit with reduced χ^2 less than 1.2, then a second component was added to the model; both power-law and thermal second components were tried in all such cases and the best fit was determined by the minimum reduced χ^2 . For each quantile group, we made and fit a stacked spectrum first only using sources detected at $\geq 3\sigma$ confidence in the 0.5–10 keV band and then only using sources detected at $\geq 3\sigma$ confidence in the 2–10 keV band. The stacked spectra and their best fits are shown in Figure 13 and Table 9.

Following the example of Ebisawa et al. (2005), we studied how the spectral parameters of sources with or without IR counterparts differ. We split up the sources detected at $\geq 3\sigma$ in the FB in each quantile group into two groups, based on whether

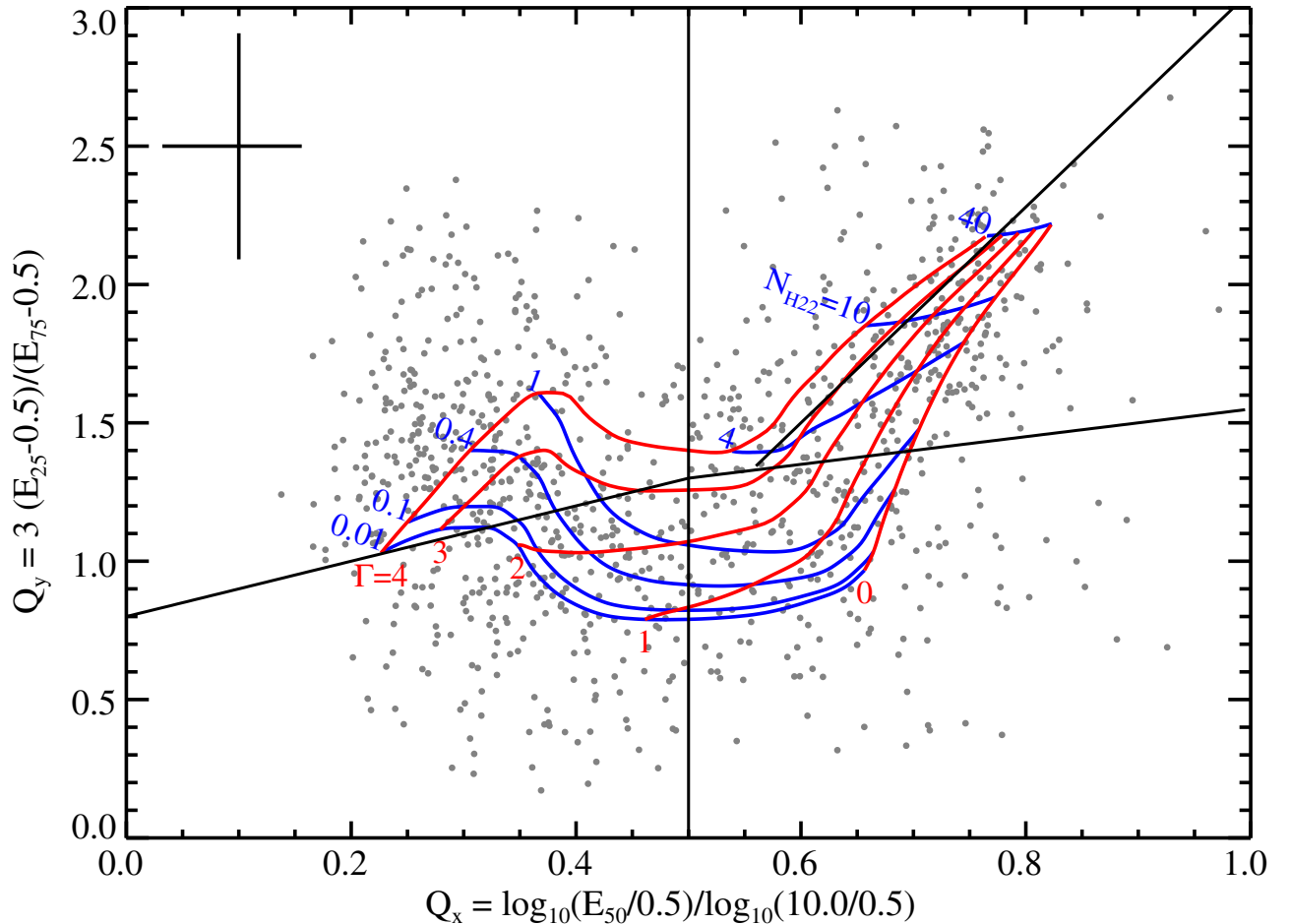


Figure 9. Quantile diagram of sources detected at $\geq 3\sigma$ in the 0.5–10 keV band. A grid of power-law spectra attenuated by interstellar absorption is overlaid. Red (primarily vertical) lines represent values of the photon index $\Gamma = 0, 1, 2, 3,$ and 4 from right to left. Blue (primarily horizontal) lines represent values of the hydrogen column density $N_{\text{H}} = 10^{20}, 10^{21}, 10^{21.6}, 10^{22}, 10^{22.6}, 10^{23},$ and $10^{23.6} \text{ cm}^{-2}$ from bottom to top. Black solid lines separate the five spectral groups defined in Section 3.

(A color version of this figure is available in the online journal.)

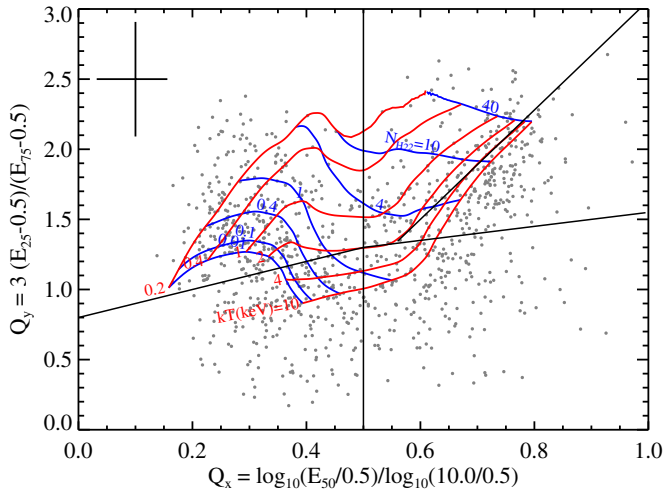


Figure 10. Quantile diagram of sources detected at $\geq 3\sigma$ in the 0.5–10 keV band. A grid of thin thermal plasma spectra attenuated by interstellar absorption is overlaid. Red (primarily vertical) lines represent values of the photon index $kT = 0.2, 0.4, 1, 2, 4,$ and 10 keV from left to right. Blue (primarily horizontal) lines represent values of the hydrogen column density $N_H = 10^{20}, 10^{21}, 10^{21.6}, 10^{22}, 10^{22.6}, 10^{23},$ and $10^{23.6}$ cm^{-2} from bottom to top. Black solid lines are the same as in Figure 9.

(A color version of this figure is available in the online journal.)

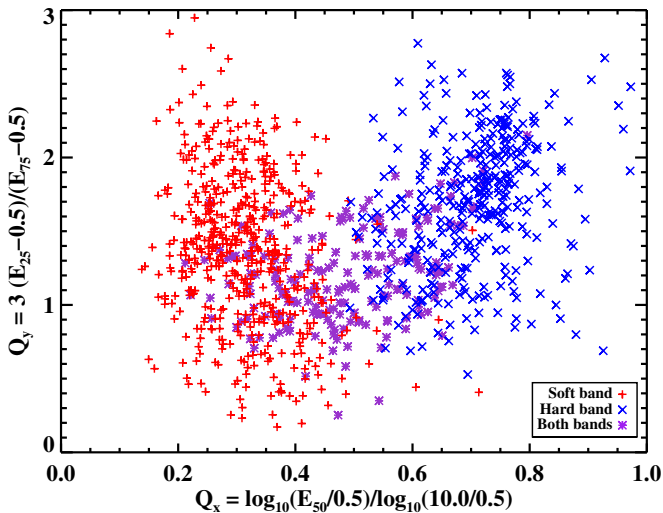


Figure 11. Quantile diagram showing soft sources in red crosses (detected at $\geq 3\sigma$ in SB but not HB), hard sources in blue X's (detected at $\geq 3\sigma$ in HB but not SB), and bright sources in purple asterisks (detected at $\geq 3\sigma$ in both SB and HB).

(A color version of this figure is available in the online journal.)

or not they have a VVV counterpart with $\geq 90\%$ reliability. A stacked spectrum for each of these subgroups was made and fit with the best-fitting model for its parent quantile group. For the case of a power-law model (with or without a Gaussian component), the power-law index, column density, and the normalization of the power-law and Gaussian components were left free, while for two-temperature thermal models, only the normalizations of the two components were allowed to vary. In addition, since the strength of the Fe emission line for group E sources with and without IR counterparts appeared different, we decided to measure the equivalent width of the Fe line in the group E stacked spectra by fitting the 5–9 keV band of these stacked spectra with a power-law plus Gaussian line model. The results of this spectral analysis are shown in Table 10. Finally,

we also studied how the spectral parameters of a given quantile group vary with source brightness. The sources within each quantile group were organized by photon flux and combined into subgroups containing 800–1000 total source counts. The analysis of the stacked spectra for these subgroups was done in the same way as for the subgroups based on the presence/absence of IR counterparts. All the brightness trends that we found can be explained by changes in the relative fraction of sources with and without IR counterparts as a function of flux. Thus, we only discuss the dependence of the spectral fitting results on the presence/absence of an IR counterpart.

4. DISCUSSION OF X-RAY POPULATIONS

Although it is difficult to determine the nature of individual sources in our survey, it is possible to make reasonable inferences about the classes of X-ray sources that dominate each quantile group defined in Section 2.5. The stacked spectra, variability, and IR counterparts of the sources in each group provide important clues to the nature of the sources. In order to facilitate our understanding of the reliable counterparts, we estimated the J and H magnitudes of main sequence and supergiant high-mass (O,B) and low-mass (G,K,M) stars at distances of 100 pc, 1 kpc, 4 kpc, 10 kpc, and 12 kpc with corresponding N_H values²³ of 0.0, 0.3, 1.0, 3.0, and 5.0×10^{22} cm^{-2} . These J and H magnitude estimates were based on the absolute V magnitudes from Wegner (2007), the intrinsic colors from Ducati et al. (2001), the $N_H - A(V)$ relationship derived by Güver & Özel (2009), and the $A(\lambda)/A(V)$ relations from Cardelli et al. (1989). Unless explicitly stated otherwise, we refer readers to Munro et al. (2004) and references therein for an overview of the spectral and timing properties of Galactic X-ray sources.

4.1. Group A

The group A stacked spectrum is best fit by a two-temperature thermal plasma model. The column density associated with each temperature component is low ($\lesssim 10^{21}$ cm^{-2}), suggesting most sources in this group are foreground sources, located at a distance $\lesssim 1$ kpc. Both components have low temperatures ($kT \lesssim 2$ keV), and the sources in this group have 0.5–10 keV luminosities²⁴ between $L_X = 10^{27}$ – 10^{31} erg s^{-1} , assuming they are located at a distance between 100 pc and 1 kpc. The very soft component ($kT = 0.75$ keV) most likely originates from the magnetic coronae of low-mass stars, which are the faintest sources of X-ray emission. X-ray active low-mass stars typically have $kT < 1$ keV and $L_X < 10^{29}$ erg s^{-1} . The higher kT component is more consistent with X-ray emission from coronally active binaries (ABs) such as RS CVn systems. These binaries usually have $kT \approx 0.1$ – 2 keV and $L_X = 10^{29}$ – 10^{32} erg s^{-1} . Other types of sources which could contribute to the group A X-ray emission are symbiotic binaries and massive stars. Symbiotic binaries, which consist of a mass-losing cool supergiant and WD companion, are often considered a subtype of CVs and tend to have $kT = 0.3$ – 1.3 keV and $L_X = 10^{30}$ – 10^{33} erg s^{-1} (Muerseet et al. 1997). X-rays can be produced in the shocks in the winds of high-mass stars, either in isolation or in a colliding-wind binary (CWB), and typically have $kT = 0.1$ – 6 keV; in fact, three group A sources (#622, 469, and 298) are coincident with previously identified O and B stars, HD149452, HD149358, and ALS 3666, respectively.

²³ For each distance listed, the corresponding N_H value was calculated as described in Section 3.

²⁴ In the remainder of this section, L_X refers to 0.5–10 keV luminosity.

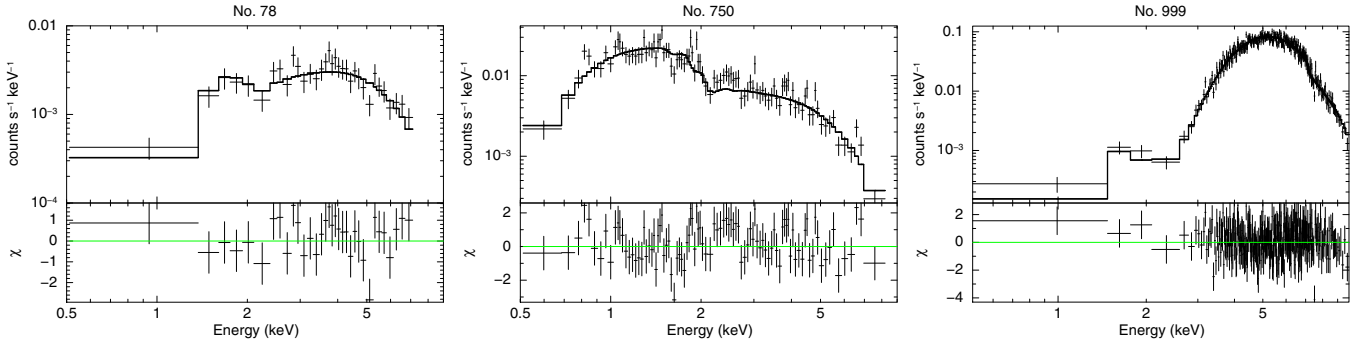


Figure 12. X-ray spectra of sources with more than 500 net counts in the 0.5–10 keV band. Title labels provide source catalog number. Grouped data and best-fit model convolved with the instrumental response are shown in the upper panels. Lower panels show the data residuals. Table 8 provides the best-fit parameters.

(A color version of this figure is available in the online journal.)

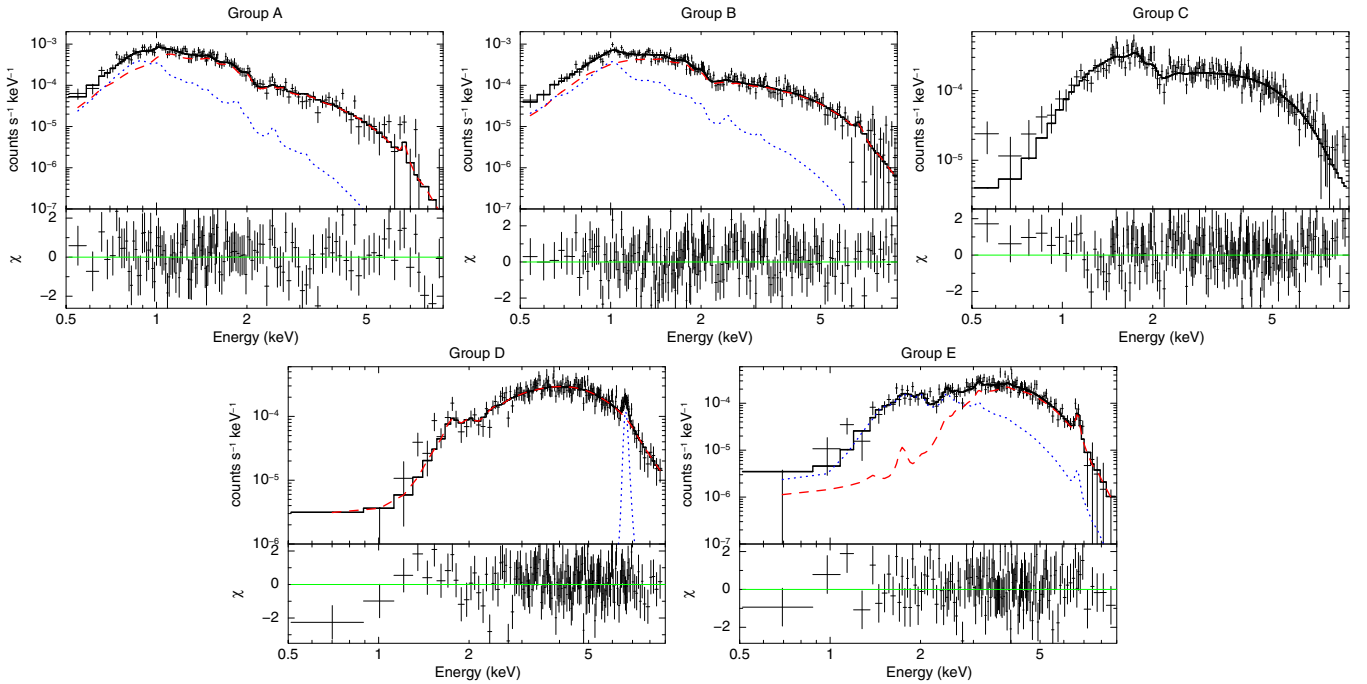


Figure 13. Stacked spectra and the best-fit models for each quantile group. Best-fit parameters can be found in Table 9.

(A color version of this figure is available in the online journal.)

Table 8
Spectral Fit Results for Individual Bright Sources

No.	Source CXOU J	C_{net} FB	N_{H} (10^{22} cm^{-2})	Γ	$f_{\text{X FB}}$ ($10^{-13} \text{ erg cm}^{-2} \text{ s}^{-1}$)	χ^2/dof	Galactic N_{H} (10^{22} cm^{-2})	Unabsorbed $f_{\text{X FB}}$ ($10^{-13} \text{ erg cm}^{-2} \text{ s}^{-1}$)
(1)	(2)	(3)	(4)	(5)	(6)	(7)	(8)	(9)
78	163355.1–473804	530 ± 20	$2.4^{+1.1}_{-0.9}$	0.5 ± 0.4	$8.8^{+0.8}_{-0.9}$	31/31	7.0	$10.0^{+0.9}_{-1.0}$
750	163750.8–465545	1790 ± 40	$0.12^{+0.09}_{-0.08}$	1.2 ± 0.1	9.9 ± 0.4	124/95	9.4	10.3 ± 0.5
999	163905.4–464212	14720 ± 120	49 ± 2	0.9 ± 0.1	268^{+5}_{-4}	347/314	8.1	301^{+6}_{-5}

Notes. Quoted errors are 1σ unless specified in notes. (1) Catalog source number. (2) *Chandra* source name. (3) Net source counts in the full 0.5–10 keV band. (4) Hydrogen column density from spectral fit with 90% uncertainties. (5) Power-law photon index from spectral fit with 90% uncertainties. (6) 0.5–10 keV flux determined from spectral model. (7) Chi-square of best-fit model over degrees of freedom. (8) Estimated line-of-sight N_{H} through the Galaxy based on $N(\text{H})$ from the LAB survey and $N(\text{H}_2)$ from the MWA CO survey (see Section 3). (9) 0.5–10 keV flux corrected for line-of-sight N_{H} .

Based on the optical band spectral and photometric information available on these sources, we estimate they are located at a distance of approximately 1–4 kpc, farther than the majority of sources in this group appear to be based on the column density of the group A stacked spectrum.

Group A contains an enhanced fraction of variable sources compared to other quantile groups. Of 26 group A sources with ≥ 40 counts, 10 (38%) show variability on \sim hour timescales (see Section 2.3) at $\geq 95\%$ confidence. Of the 83 group A sources detected in multiple observations, 50 (60%) are found

Table 9
Spectral Fit Results for Stacked Sources

Power-law Fit Parameters									
Quantile Group	Energy Band	Number of Sources	N_{H} (10^{22} cm $^{-2}$)	Γ	Line E (keV)	Eq. Width (eV)	f_X 2–10 keV (10^{-14} erg cm $^{-2}$ s $^{-1}$)	χ^2_{ν}/dof	ϵ^{-1} (10^{-9} erg per photon)
(1)	(2)	(3)	(4)	(5)	(6)	(7)	(8)	(9)	(10)
C	Full	170	$1.4^{+0.3}_{-0.2}$	1.1 ± 0.1	$2.94^{+0.08}_{-0.13}$	1.02/180	8.66
	Hard	136	1.8 ± 0.3	1.2 ± 0.1	$3.2^{+0.10}_{-0.2}$	0.99/158	8.60
D	Full	164	7 ± 1	0.7 ± 0.2	$6.65^{+0.04}_{-0.05}$	300^{+60}_{-50}	$7.1^{+0.1}_{-0.4}$	1.06/153	11.47
	Hard	168	$6.6^{+0.9}_{-0.8}$	0.6 ± 0.2	6.60 ± 0.04	300^{+50}_{-40}	$6.83^{+0.09}_{-0.31}$	1.16/186	11.13
Thermal Fit Parameters									
Quantile Group	Energy Band	Number of Sources	N_{H} (10^{22} cm $^{-2}$)	kT_1 (keV)	N_{H} (10^{22} cm $^{-2}$)	kT_2 (keV)	$f_{X,\text{low}}/f_{X,\text{high}}$	χ^2_{ν}/dof	ϵ^{-1} (10^{-9} erg per photon)
(1)	(2)	(3)	(4)	(11)	(4)	(11)	(12)	(9)	(10)
A	Full	312	<0.43	$2.4^{+1.5}_{-0.4}$	<0.58	$0.75^{+0.05}_{-0.12}$	$0.04^{+0.05}_{-0.01}$	0.95/124	2.60
	Hard	41	0.7 ± 0.4	$2.4^{+0.6}_{-0.4}$	0.3 ± 0.2	0.39 ± 0.06	0.0092 ± 0.0006	1.01/106	5.78
B	Full	210	$0.3^{+0.4}_{-0.1}$	7 ± 3	<0.14	$1.2^{+0.1}_{-0.2}$	0.04 ± 0.02	1.08/186	3.83
	Hard	70	5^{+9}_{-3}	4^{+3}_{-2}	0.29 ± 0.08	$2.1^{+0.9}_{-0.3}$	0.74 ± 0.05	1.09/134	7.33
E	Full	131	25^{+7}_{-5}	$1.8^{+0.5}_{-0.3}$	5.4 ± 0.9	$1.4^{+0.8}_{-0.4}$	$0.25^{+0.10}_{-0.07}$	1.01/125	16.5
	Hard	128	24^{+7}_{-6}	$1.8^{+0.5}_{-0.3}$	6 ± 1	$1.2^{+0.9}_{-0.4}$	0.20 ± 0.01	0.99/122	9.51

Notes. All quoted errors are 90% unless otherwise indicated. (1) Quantile groups defined in Section 2.5. (2) Stacked spectrum contains all sources that are detected at $\geq 3\sigma$ in given energy band with fewer than 500 counts. (3) Number of sources in stacked spectrum. (4) Hydrogen column density associated with model component in next column. (5) Power-law photon index. (6) Energy of Gaussian line component. (7) Equivalent width of Gaussian line component (1σ errors). (8) 2–10 keV absorbed flux (1σ errors). (9) Chi-square of best-fit model over degrees of freedom. (10) Photon flux to unabsorbed energy flux conversion factor. (11) Temperature of thin thermal plasma component. (12) Flux ratio in 2–10 keV band of low kT component over high kT component (1σ errors).

Table 10
Spectral Comparison of Sources with and without IR Counterparts

Power-law Stacked Spectra								
Quantile Group	With/Without IR Counterparts	Number of Sources	N_{H} (10^{22} cm $^{-2}$)	Γ	Line Eq. Width (eV)	f_X 2–10 keV (10^{-14} erg cm $^{-2}$ s $^{-1}$)	χ^2_{ν}/dof	
(1)	(2)	(3)	(4)	(5)	(6)	(7)	(8)	
C	IR	62	1.6 ± 0.3	1.3 ± 0.2	...	2.8 ± 0.2	0.93/72	
	No IR	108	1.4 ± 0.4	0.9 ± 0.2	...	3.0 ± 0.2	1.08/120	
D	IR	49	6^{+2}_{-1}	$0.8^{+0.4}_{-0.3}$	330^{+150}_{-100}	$5.1^{+0.1}_{-0.7}$	0.89/55	
	No IR	115	7 ± 1	0.6 ± 0.3	270^{+80}_{-50}	$8.6^{+0.2}_{-0.6}$	1.12/115	
Thermal Stacked Spectra								
Quantile Group	With/Without IR Counterparts	Number of Sources	f_X 2–10 keV (10^{-14} erg cm $^{-2}$ s $^{-1}$)	$f_{X,\text{low}}/f_{X,\text{high}}$	χ^2_{ν}/dof	Γ	Line Eq. Width (eV)	χ^2_{ν}/dof
(1)	(2)	(3)	(7)	(9)	(8)	(10)	(11)	(12)
A	IR	246	0.49 ± 0.02	0.034 ± 0.004	0.99/97
	No IR	66	0.26 ± 0.02	0.036 ± 0.006	1.71/49
B	IR	135	1.37 ± 0.03	0.034 ± 0.003	1.22/157
	No IR	75	0.55 ± 0.04	0.07 ± 0.01	1.33/57
E	IR	64	2.50 ± 0.10	0.29 ± 0.02	1.08/73	5 ± 2	1700^{+1000}_{-100}	0.20/11
	No IR	67	2.14 ± 0.09	0.21 ± 0.02	1.06/64	2^{+2}_{-1}	<316	1.25/11

Notes. All quoted uncertainties are 90% unless stated otherwise. (1) Quantile groups defined in Section 2.5. (2) Stacked spectrum of sources with or without IR counterparts. (3) Number of sources in stacked spectrum. (4) Hydrogen column density associated with model component in next column. (5) Power-law photon index. (6) Equivalent width of Gaussian line component at energy 6.65 keV, line center determined from stacked spectrum of all FB, group D sources (1σ errors). (7) 2–10 keV absorbed flux (1σ errors). (8) Reduced chi-square of best-fit model over degrees of freedom. (9) Flux ratio in 2–10 keV band of low kT component over high kT component (1σ errors). (10) Power-law photon index of 5–9 keV band when fitting with power-law plus Gaussian line model. (11) Equivalent width of Gaussian line component at 6.65 keV, line center determined from stacked spectrum of all FB group E sources (1σ errors). (12) Reduced chi-square of best-fit model for 5–9 keV band over degrees of freedom.

to be variable between observations, a higher percentage than is found for sources in the full sample detected in multiple observations. The significant variability seen in this group of sources is consistent with the flaring behavior of low-mass active stars and interacting binaries. As can be seen in

Figure 5, the fluxes of some group A sources vary by large factors (>5) in between observations; hour-long flares with amplitudes as large as a factor of 10 have been observed in RS CVns and could be the origin of these large variability amplitudes.

In the VVV catalog, we found reliable infrared counterparts to 67% of the group A sources. The only significant difference between the X-ray properties of group A sources with and without IR counterparts is that those without counterparts tend to have lower X-ray fluxes; thus sources without IR counterparts may be intrinsically dimmer in both the X-ray and NIR bands or they may be located at larger distances. As can be seen in Figure 7, these counterparts have blue ($J - H$) colors, in agreement with our inference that group A sources are mostly foreground sources. In this color–magnitude diagram, there is a tight cluster of counterparts with H magnitudes between 13 and 15, and a looser cluster of counterparts with H magnitudes between 8 and 13. The former is consistent with the colors and magnitudes of low-mass main sequence stars at a distance of ≈ 1 kpc, while the latter is likely a mixture of low-mass main sequence stars at ≈ 100 pc and cool giants at ≈ 1 kpc; the small number of counterparts with negative ($J - H$) are more likely to be high mass stars at ≈ 1 kpc. The fact that the majority of counterparts are most likely to be low-mass stars, either on the main sequence or in a giant/supergiant phase, is consistent with the suggestion that the dominant X-ray populations in group A are X-ray active low-mass stars and interacting binaries.

4.2. Group B

Similar to group A, the group B stacked spectrum is also best-fit by a two-temperature thermal model with low hydrogen column densities. However, the temperature of the hotter component is significantly higher ($kT \approx 7$ keV) for the B sources than for the A sources. The origin of the low-temperature component may be low-mass X-ray active stars, ABs, and symbiotic binaries, the dominant sources in group A, while the high-temperature component is more typical of CVs. The majority of CVs are close binary systems with a WD accreting matter from a low-mass main-sequence stellar companion, although some have been found to have giant donors (Kuulkers et al. 2006). CVs are typically subdivided into three main categories based on the magnetic field strength of the WD they host. The majority of CVs have weak magnetic fields ($B \lesssim 10^4$ G) that do not significantly affect the accretion flow from the Roche lobe-filling donor and are called nonmagnetic CVs. About 20% of CVs are polars, exhibiting strong magnetic fields ($B \gtrsim 10^{6.5}$ G) which prevent the formation of an accretion disk; about 5% are intermediate polars (IPs), having intermediate strength magnetic fields which channel material from the inner accretion disk onto the magnetic poles. Nonmagnetic CVs and polars have $\Gamma \approx 1-2$ or $kT \approx 1-25$ keV and $L_X = 10^{29}-10^{32}$ erg s $^{-1}$. IPs tend to be more luminous ($L_X = 10^{31}-10^{33}$) and display harder emission ($\Gamma < 1$) than other CVs. Assuming that the group B sources lie at a distance between 100 pc and 1 kpc based on their low N_H , they span the luminosity range $10^{27.4}-10^{31.5}$ erg s $^{-1}$, consistent with the luminosities of low-mass stars at the faint end and with the luminosities of ABs and CVs at the bright end.

Further evidence that a CV population exists in group B is provided by one of the brightest sources in our survey, source 750, which is coincident with ASCA source AX J1637.8–4656 (Sugizaki et al. 2001). This source has $\Gamma = 1.15$ (see Table 8), and, assuming a distance of 1 kpc from its low N_H , $L_X \approx 8 \times 10^{31}$ erg s $^{-1}$. In addition to having a luminosity and photon index consistent with that of a CV, this source is variable on both short and long timescales. As can be seen in Table 7, this source was determined to be periodic by the Z_n^2 test (Buccheri et al. 1983), with a best period of roughly 7100 s. Periodic X-ray emission has been observed from magnetic CVs and is

believed to be associated with the spin period of the WD, which can range from 10^2 to 10^4 s (Scaringi et al. 2010). Finally, the near-IR spectrum obtained of the IR counterpart of this source exhibits strong emission lines suggestive of an accretion disk (Rahoui et al. 2014). Thus source 750 is likely a CV with an intermediate strength magnetic field that is not fully disrupting the accretion disk.

As mentioned in Section 2.3, source 961, another group B source, is also likely to be a magnetic CV. Its ≈ 5700 s period is consistent with the spin and orbital periods of CVs. As can be seen in Figure 6(b), its pulse profile shows large brightness variations from approximately 0 to 20 counts; such variations could either result from pulsations due to emission from accretion spots at the WD magnetic poles as the WD rotates or from eclipsing of the WD by its companion. Its location in the quantile diagram indicates it has $\Gamma \approx 1.5$, which is more typical of polars and nonmagnetic CVs than IPs. Although it is likely a nearby source based on its low N_H (estimated to be $\sim 10^{21}$ cm $^{-2}$ from its quantile parameters), it has no stellar IR counterpart in the VVV survey; we do find an infrared counterpart to this source in the VVV survey, but it is morphologically classified as a galaxy, and therefore it cannot be the true counterpart since the X-ray spectrum of the *Chandra* source shows very little absorption. Since the source is likely located $\lesssim 1$ kpc, the stellar IR counterpart must be very faint to avoid detection, thus making it unlikely that this source has a significant accretion disk which indicates that, of all CV types, this source is most likely a polar. Thus, there is evidence that both sources 750 and 961 are magnetic CVs, and their location in the quantile diagram supports the hypothesis that group B may contain a significant CV population.

Group B has a comparable percentage of variable sources to group A. Eight of the 17 (47%) group B sources with ≥ 40 counts are variable on short timescales, and 19 of the 52 (37%) group B sources detected in multiple observations are variable on long timescales. The fact that this latter percentage is lower than that of group A sources may be partly explained by the significant number of CVs, probably present in group B but not group A, which undergo flaring episodes less frequently than flare stars and thus tend to be fairly constant on day–week timescales.

We found reliable IR counterparts for 61% of group B sources, which largely overlap in the color–magnitude diagram with the group A counterparts, indicating that they have similar stellar types and are located at similar distances. This similarity is not surprising since the X-ray properties of the group B sources indicate that they are dominated by the same X-ray populations as group A plus a population of CVs, which tend to have near-IR properties similar to low-mass main sequence or evolved stars (Hoard et al. 2002). As can be seen in Table 10, group B sources without IR counterparts have a lower average flux and a more significant contribution from the low kT component compared to group B sources with IR counterparts. These trends suggest that X-ray active low-mass stars make up a relatively larger fraction of group B sources without counterparts than of B sources with counterparts.

4.3. Group C

The group C stacked spectrum is best-fit by an absorbed power-law with $\Gamma \approx 1.1$ and $N_H = 1.4 \times 10^{22}$ cm $^{-2}$, which suggests that these sources are located at a distance of 3–5 kpc, in the Scutum-Crux and near Norma spiral arms. The luminosities spanned by group C sources are $L_X = 10^{31}-10^{32.7}$ erg s $^{-1}$, assuming a distance of 4 kpc. Possible

classes of X-ray sources present in this group are magnetic and nonmagnetic CVs, hard-spectrum symbiotic binaries, low-mass X-ray binaries (LMXBs), and HMXBs. IPs and HMXBs tend to have $\Gamma < 1$ while nonmagnetic CVs, polars, symbiotic binaries, and LMXBs tend to have $\Gamma > 1$. CVs are the most numerous accreting sources, so they are most likely the dominant population.

Group C sources show the lowest levels of variability of any group. Only 2 of 12 (17%) sources with ≥ 40 counts exhibit short-timescale variability and only 5 of 26 (19%) sources detected in multiple observations are variable on long timescales. These results are consistent with magnetic CVs and LMXBs dominating group C, since although they show periodic variations and occasional outbursts, they generally have stable emission.

Reliable IR counterparts were found for 35% of group C sources. They have redder ($J - H$) colors than the counterparts of group A and B sources, confirming that they are more distant than the group A or B counterparts. Their H magnitudes are consistent with high-mass stars and evolved low-mass stars located at ~ 4 kpc. Considering the extinction resulting from the N_H measured for these sources and their likely distances, most main-sequence, low-mass counterparts of group C sources would be undetectable in the VVV survey. The stacked spectrum of group C sources with IR counterparts has a softer power-law index ($\Gamma \approx 1.3$) than that of sources lacking IR counterparts ($\Gamma \approx 0.9$). Thus, the majority of group C sources with counterparts may be symbiotic binaries and CVs with subgiant and giant companions, while those without counterparts may primarily be CVs with main-sequence companions, especially IPs given the lower photon index of these sources. The presence of some type II active galactic nuclei (AGNs) among the group C sources lacking IR counterparts could also help explain their lower photon index, but, as discussed in Section 4.6, very few AGNs are likely to be found in group C.

4.4. Group D

The group D stacked spectrum has a very hard photon index ($\Gamma \approx 0.7$), a prominent Fe line, and a high N_H , indicating that these sources typically lie on the far side of the Galaxy, near, in, or beyond the far Norma arm. The Fe emission is well-modeled by a Gaussian centered at 6.65 keV with an equivalent width of approximately 300 eV; this emission likely results from the blending of lines at 6.4 keV and 6.7 keV, arising from low-ionization Fe and He-like Fe, respectively. The presence of this strong, non-redshifted Fe line suggests that many of the sources in this group must be Galactic; otherwise, if this group were dominated by AGNs, their spread in redshift would result in a smearing out of the Fe line.

Two classes of X-ray sources that are frequently observed having spectra with $\Gamma < 1$ are IPs and HMXBs. Fe line emission has been observed from both of these types of sources. Although the luminosity range spanned by group D ($L_X = 10^{32} - 10^{33.7}$ erg s $^{-1}$ assuming $d = 10$ kpc) extends to higher luminosities than are typically observed for IPs, roughly 80% of group D sources have $L_X \lesssim 10^{33}$ erg s $^{-1}$ for $d = 10$ kpc, a reasonable luminosity range for IPs. Thus, IPs could be the dominant population among faint group D sources. In contrast, HMXBs can have X-ray luminosities as high as $L_X \sim 10^{34}$ erg s $^{-1}$ during quiescence and $L_X \sim 10^{38}$ erg s $^{-1}$ during outburst. In fact, one of the group D sources, source 999, is a previously discovered HMXB (Sugizaki et al. 2001; Bird et al. 2004; Bodaghee et al. 2006) and has $\Gamma \approx 0.9$ and

$L_X \approx 10^{35.3}$ erg s $^{-1}$. Nonetheless, as discussed in Section 6, we only expect a few HMXBs in our survey, so they are a likely contributing but not dominating class of sources in group D.

Five of 14 (36%) group D sources exhibit short-timescale variability, and although 17 of 35 (49%) group D sources detected in multiple observations display long-timescale variability, they have the lowest mean and median variability amplitude of any group. These modest levels of variability are consistent with, although not necessarily proof of, group D being dominated by a population of IPs, which tend to have fairly stable emission.

Only 29% of group D sources have reliable IR counterparts. The ($J - H$) color and H magnitudes of these counterparts are consistent with being high-mass and evolved low-mass stars at distances between 8–12 kpc. The low fraction of detected counterparts is more easily explained by a dominant population of IPs rather than HMXBs, since a large fraction of the low-mass companions of the WDs in IPs would have J and H magnitudes greater than the VVV sensitivity limit when located at distances of 8–12 kpc. However, while most massive stellar counterparts of HMXBs in group D should be above the VVV sensitivity limit, they can occasionally be so obscured by circumbinary gas and dust that they are much fainter than otherwise expected (Bodaghee et al. 2012b); in fact, our counterpart-matching algorithm does not find the faint massive counterpart of HMXB IGR J16393–4643 (Bodaghee et al. 2012a) in the VVV catalog.

The X-ray spectral differences between group D sources with and without IR counterparts are not statistically significant. Nonetheless, if the lower photon index and lower Fe equivalent width of the sources without IR counterparts is a real trend, it could be explained if the sources without counterparts are primarily IPs and type II AGNs (see Section 4.6), while those with counterparts include some hard-spectrum symbiotic binaries (Luna et al. 2013), whose spectra are a bit softer and whose red giant companions should be detectable by the VVV survey.

4.5. Group E

The group E stacked spectrum is best-fit by a two-temperature thermal model, making it significantly different from the group D power-law spectrum, even though some of the same classes of X-ray sources must be present in both groups D and E since they are not sharply separated in the quantile diagram. Both temperature components have $kT = 1 - 2$ keV but very different hydrogen column densities, the lower of which is similar to that of group D, and the higher of which is $N_H \approx 2.4 \times 10^{23}$ cm $^{-2}$. This N_H value is roughly three times higher than the maximum N_H value measured through the Galaxy along a line of sight within our surveyed area, indicating that some E sources are obscured by large amounts of local absorption and/or may be imbedded in the molecular clouds of the far Norma arm. Assuming the same typical distance of 10 kpc as we did for group D, these sources span the luminosity range $L_X = 10^{32} - 10^{33.7}$ erg s $^{-1}$. A significant fraction of these sources may be associated with the shocks produced in the winds of high-mass stars; these sources typically have $kT = 0.1 - 6$ keV, $L_X \sim 10^{33} - 10^{35}$ erg s $^{-1}$, and their emission can be significantly absorbed by circumstellar material. The photometric and spectral properties of group E are also consistent with symbiotic binaries. In addition, a small number of magnetars could be present in this group. In fact, one of the group E sources is a previously discovered magnetar, SGR 1627-41, and data from this survey was used in an in-depth study of this magnetar by An et al. (2012).

Only two of the nine (22%) group E sources with ≥ 40 counts exhibits variability on short timescales. However, 14 of the 24 (58%) group E sources detected in multiple observations are found to vary between observations. If group E is indeed dominated by high-mass stellar populations, these trends in X-ray variability are similar to those found for high-mass stars in the Galactic center survey (Mauerhan et al. 2010).

Although group E sources are roughly located at the same distance as group D sources based on the N_H measured in their stacked spectra, a higher fraction of group E sources (48%) have reliable IR counterparts. At distances of ≈ 10 kpc, only high-mass stars and cool giants have J and H magnitudes above the sensitivity limit of the VVV survey. The higher percentage of IR counterparts is consistent with group E having a larger fraction of high-mass stellar X-ray sources and symbiotic binaries than group D, since the high-mass and giant counterparts of these sources are brighter than the primarily main-sequence low-mass counterparts of IPs. A significant fraction of group E sources without IR counterparts are also likely to be type I AGNs, as discussed in the following section.

4.6. AGN Contribution

In addition to the Galactic classes of sources described in the previous sections, we expect a significant population of AGNs to be present in our catalog. Using the AGN count distribution from the COSMOS survey (Cappelluti et al. 2009) and taking into account the sensitivity variations across the survey area (see Section 5.1) and the incompleteness of our detection method (see Section 5.2), we estimate that roughly 150 AGNs could be present in our catalog. X-ray emission from AGNs is attenuated by the integrated column density through the whole galaxy and typically has $\Gamma \approx 1.7$ (Molina et al. 2009) for type I AGNs or $\Gamma \lesssim 1$ for type II AGNs with a reflection component. Thus, AGNs are most likely to be found in groups D and E based on the regions of quantile space they occupy. Due to the spread in N_H values across our field of view and the large median error bars on Q_x and Q_y , some group C sources may also be AGNs.

We expect to find most of the AGNs in our sample among the sources without NIR counterparts. Only 2% of AGNs in the *Chandra* COSMOS Survey (Civano et al. 2012) with $f_X > 1 \times 10^{-15}$ erg cm $^{-2}$ s $^{-1}$ have H magnitudes ≤ 18 —the sensitivity limit of the VVV survey—and we would expect an even smaller percentage of the AGNs in NARCS to be detected in the VVV survey due to the higher extinction in the Galactic plane compared to the COSMOS field; the integrated N_H through the galaxy in the NARCS region varies between $3\text{--}8 \times 10^{22}$ cm $^{-2}$, which corresponds to extinction values of $A(J) \approx 4\text{--}10$ mag and $A(H) \approx 3\text{--}7$ mag.

Based on the spectral properties of group E sources without IR counterparts, it seems likely that many of them are AGNs. Their stacked spectrum shows a more prominent high-column density component compared to the spectrum of group E sources with counterparts; this enhancement could be due to a large number of AGNs, which suffer from extinction by their local environment and host galaxy as well as the Milky Way ISM. In addition, fitting the 5–9 keV stacked spectra of group E sources with and without counterparts with a power law plus Fe line model shows that the sources lacking IR counterparts have a harder spectrum with $\Gamma \approx 2$ and a lower Fe line equivalent width. This photon index is typical of type I AGNs and the lower Fe equivalent width is expected for a group of extragalactic sources whose Fe line would be smeared out due to their redshift distribution. Thus, a large number of type I AGNs among the group E sources lacking

IR counterparts can explain the difference between the stacked spectra of group E sources with and without IR counterparts.

There is weaker evidence for the presence of AGNs among the group C and group D sources lacking IR counterparts. The stacked spectrum of group D sources without counterparts is harder ($\Gamma \approx 0.6$) and has a lower Fe line equivalent width than the spectrum of sources with counterparts; however, while these trends are consistent with the presence of type II AGNs with a reflection component among the sources lacking counterparts, these differences are not statistically significant. Thus, these trends may be real and indicative of an AGN population, or they may be statistical fluctuations, in which case the group D sources lacking counterparts are probably just faint and/or distant versions of the group D sources with counterparts. The stacked spectrum of group C sources without counterparts is harder ($\Gamma \approx 0.9$) than that of the sources with counterparts; this difference could be driven by a population of type II AGNs among the sources lacking counterparts. However, it is unlikely that many AGNs would be found in group C, since the average column density of sources in this group is $N_H \approx 10^{22}$ cm $^{-2}$, which is low for an AGN whose light would be shining through the entire Galaxy. Thus, it appears more likely that the differences between the group C sources with and without counterparts are due to different populations of Galactic sources (as discussed in Section 4.3), although a small AGN contribution cannot be ruled out.

In order for our survey to contain the expected number of AGNs, the majority of group E sources lacking IR counterparts and 30%–50% of group C and D sources without counterparts must be AGNs. Given that there is good evidence for the former and that the latter cannot be ruled out, it is possible that about 150 AGNs are present in our catalog, as expected from other surveys.

5. COMPUTING THE NUMBER-FLUX DISTRIBUTION

Having determined the X-ray populations that likely dominate each of the quantile groups, we sought to compare the populations in our survey to predictions based on surveys of other regions of the Galaxy. A useful tool in comparing the populations of different surveys is the number count distribution. In addition, for a particular population of sources located at similar distances, the number-flux distribution is closely related to the luminosity function of the sources and thus can also shed light on the physics which determines the brightness of these sources.

At faint fluxes, this calculation is complicated by the nonuniform sensitivity across the *Chandra* image, the incompleteness of the source-detection algorithm, and the Eddington bias, which is caused by fluctuations in the source and/or background making a faint source appear brighter. To help correct for these effects, we used a method similar to that developed by Georgakakis et al. (2008) and adapted by Lehmer et al. (2012), which uses a Bayesian approach with ML optimizations. We decided to compute the number count distribution in the 2–10 keV band, because (1) most foreground, thermal sources are not detected in this band, allowing us to concentrate on the populations in the spiral arms, (2) photons in this energy band are less likely to be absorbed by dust along the line-of-sight, resulting in more robust conversion factors between the net counts of a source and its unabsorbed energy flux, and (3) it will enable comparisons to published number count distributions from previous surveys of Galactic X-ray populations, which are primarily in the 2–10 or 2–8 keV band. In the remainder of this section, whenever we

refer to catalog sources, we only mean sources detected at $\geq 3\sigma$ in the 2–10 keV band.

5.1. Sensitivity Curves

Near the flux limit of a survey, a source of a given flux can only be detected over a limited fraction of the total solid angle covered by the survey due to the inhomogeneous background and nonuniform PSF across the *Chandra* image. In order to account for this varying sensitivity in our number count distribution, we calculate the effective solid angle as a function of source flux, which we refer to as the sensitivity curve. This sensitivity curve depends on the significance threshold we choose to select our sources. In computing the number count distribution of sources in our survey, we select point-like sources that have been detected by *wavdetect* in any energy band as described in Section 2.1 and have $P(\geq C_{\text{src}}) \leq 0.00137 = P_{\text{thresh}}$ in the 2–10 keV band as determined by Equation (5), which is the probability required for a 3σ detection. This selection procedure will not include all real sources with $P(\geq C_{\text{src}}) \leq P_{\text{thresh}}$ because of *wavdetect*'s complex source detection criteria (see Freeman et al. 2002). Correcting for this detection incompleteness is discussed in Section 5.2.

To compute the sensitivity curve, we follow the method described in Georgakakis et al. (2008), which should allow us to extrapolate the number-flux distribution to fluxes roughly an order-of-magnitude fainter than the formal survey flux limit—the flux to which $\gtrsim 90\%$ of the image is sensitive. First, we determine the minimum number of counts, C_{lim} , required for a detection, such that $P(\geq C_{\text{lim}}) = P_{\text{thresh}}$, at each location in the image. We use the background maps (see Section 2.1) to determine the mean expected background counts, $\langle C_{\text{bkg}} \rangle$, within circular regions with radii equal to the local 90% ECF radius. The cumulative probability that the observed counts will exceed C_{lim} within a particular region is

$$P(\geq C_{\text{lim}}) = \gamma(C_{\text{lim}}, \langle C_{\text{bkg}} \rangle), \quad (8)$$

where $\gamma(a, x)$ is the lower incomplete gamma function, defined as

$$\gamma(a, x) = \frac{1}{\Gamma(a)} \int_0^x e^{-t} t^{a-1} dt. \quad (9)$$

Equation (8) is a simplification of Equation (5) for situations in which the mean background within an aperture region is well determined. Setting $P(\geq C_{\text{lim}}) = P_{\text{thresh}} = 0.00137$, we invert Equation (8) numerically to find C_{lim} for a region with mean expected background $\langle C_{\text{bkg}} \rangle$. For each observation, we perform this procedure for different regions, which combined cover the full image area, thus obtaining a 2D image of C_{lim} known as a sensitivity map.

Then we can compute the probability of detecting a source of a given flux f_x and spectral shape within each region of the sensitivity map. The total observed counts in the region are the sum of the source and background contributions, which can be expressed as

$$C_{\text{src}} = C_{\text{net}} + \langle C_{\text{bkg}} \rangle = f_x t_{\text{exp}} E_{\text{src}} \eta \epsilon + \langle C_{\text{bkg}} \rangle, \quad (10)$$

where t_{exp} , E_{src} , η , and ϵ are the exposure time, mean effective area, ECF, and unabsorbed energy flux to observed photon flux conversion factor, respectively. ϵ includes a correction factor for extinction along the line-of-sight due to the amount of N_{H} determined by the spectral fits of each quantile group, but not exceeding $5.5 \times 10^{22} \text{ cm}^{-2}$, the average N_{H} integrated through

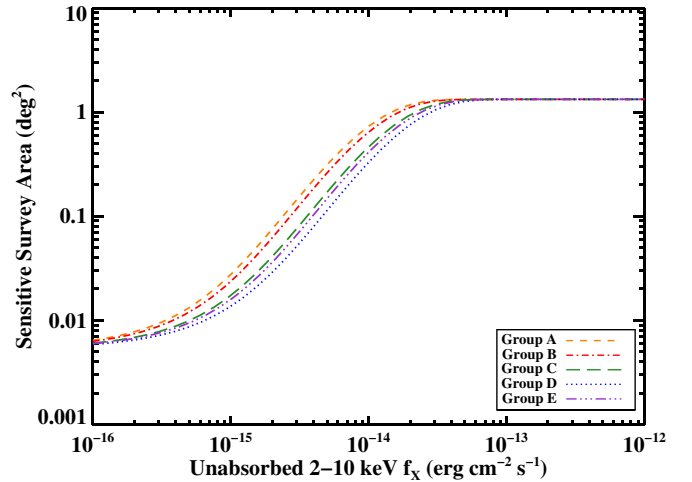


Figure 14. Angular area of our survey that is sensitive to a given source flux. (A color version of this figure is available in the online journal.)

the entire Galaxy in our surveyed area; we assume that larger values of N_{H} are likely due to both interstellar and intrinsic absorption, and we do not wish to correct for absorption that may be intrinsic or very local to the source. The energy flux to photon flux conversion factor depends on the source spectrum, and we used the same ϵ for all sources in the same quantile group; the conversion factors are listed in Table 9. For a region with particular values of $\langle C_{\text{bkg}} \rangle$ and C_{lim} , the probability of detecting a source of flux f_x is given by

$$P_{f_x}(\geq C_{\text{lim}}) = \gamma(C_{\text{lim}}, C_{\text{src}}). \quad (11)$$

We calculate the sensitivity curve for each observation by summing the $P_{f_x}(\geq C_{\text{lim}})$ distributions of individual regions, each weighted by the solid angle (in degrees) of each region. Then we added together the sensitivity curves of all the individual observations, and divided the combined sensitivity curve by a factor of 1.54 so that the maximum value of the sensitivity curve was equal to the total survey area (1.3268 deg²); this division was necessary because the observations partially overlap. This combined sensitivity curve, $A(f_x, \epsilon)$ (shown in Figure 14), is an approximation which overweights the overlapping regions, which generally have worse sensitivity since they are at large off-axis angles. We estimate errors in the sensitivity curve to be 0.1 dex, which are satisfactory for our purposes. We choose to only compute number counts to a flux limit of $1 \times 10^{-15} \text{ erg cm}^{-2} \text{ s}^{-1}$, to which 1%–3% of the total solid angle is sensitive; below this flux, too few sources are detected by *wavdetect* to make reliable predictions. Note that the sensitivity curve as a function of source counts is the same for all spectral groups, but since different spectral groups have different count-to-flux conversions, they have different sensitivity curves as a function of flux.

5.2. Recovery Fraction Correction

The sensitivity curve will only successfully correct for the incompleteness of our catalog if all sources are detected above a specific selection probability. However, due to the complex criteria of *wavdetect*, some faint sources that would meet the probability criterion are not detected. Employing an approach similar to that of Lehmer et al. (2012) to compute and correct for detection incompleteness, we generated 200 mock images in the full, soft, and hard energy bands of ObsID 12519, which

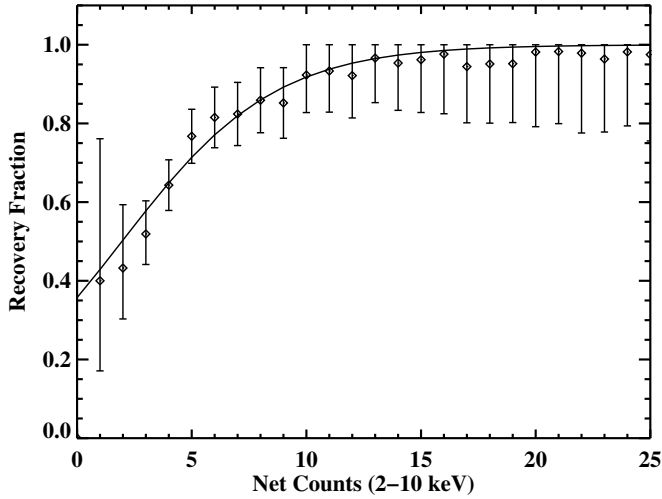


Figure 15. Fraction of simulated sources that are detected at $\geq 3\sigma$ in the 2–10 keV band and are also detected by our detection procedure as a function of net 2–10 keV counts. The solid line shows our best-fit model for this recovery fraction, which we use in Section 5.4 to correct for incompleteness in our number-count computation.

we took to be representative of all observations since they have very similar exposure and background maps. To make each set of mock observations, we added 60 sources to the full, soft, and hard unsmoothed background images (see Section 2.1), since this was the average number of sources detected in an individual observation. Each source was assigned a random position on the sky and a random number of total counts between 3 and 50, taken from a power-law count distribution with an index of -1.6 (a compromise between approximating the count distribution we measure and having a statistically significant sample of sources within each count bin). The total counts were then randomly divided between the SB and HB. We approximated the PSF at the location of each source as an azimuthally symmetric Rayleigh distribution in the radial direction, the normalization parameters of which were determined from the size of the PSF for 4.5 keV photons (for the full and high energy band mock images) or 1.5 keV (for the low energy band mock images) and a range of ECFs. The counts for each source were then distributed according to this approximation of the local PSF.

We determined the photometric properties of the 60 sources in each set of mock observations as described in Section 2.2. We also produced a sourcelist including photometric properties for each set of mock observations using our standard pipeline beginning with the second round of `wavdetect` using the background and exposure maps for ObsID 12519. Then we calculated, as a function of the input source counts in a particular energy band, what fraction of input sources that satisfy our 3σ threshold in that energy band were detected by `wavdetect`. This recovery fraction is shown in Figure 15 for the 2–10 keV band, and it is well fitted by the analytic form $F_{\text{rec}}(C) = 1/(1 + \exp[-\delta\{C - \xi\}])$, where C are the input source counts in a given band, and δ and ξ are fitting constants that vary with energy band. For the 2–10 keV band, $\delta = 0.30 \pm 0.07$, and $\xi = 1.96 \pm 0.79$.

5.3. Flux Probability Distributions

In addition to correcting for incompleteness in our catalog, we take into account the fact that the observed counts in a given source aperture can be attributed to a source with a range of possible fluxes, rather than assigning a single flux value to each source. For C_{src} total counts in the source aperture

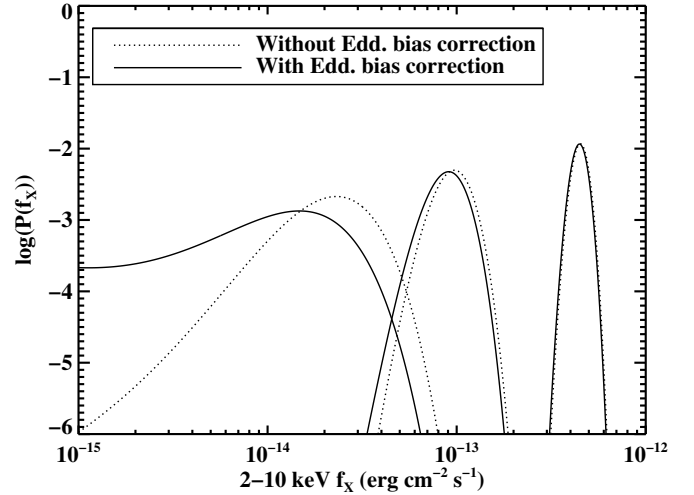


Figure 16. Example flux probability density distributions, before and after implementing the Eddington bias correction based on the best-fit power-law index β reported in Table 11. From left to right, these sources are detected at confidence levels of 3.2σ , 8.5σ , and 29.8σ , respectively, in the 2–10 keV band.

and C_{bkg} counts in the background aperture, the probability distribution of source counts, C_{net} within the source aperture is given by (derived from Weisskopf et al. (2007) with $\psi_T \rightarrow 1$ and $\psi_R \rightarrow 0$)

$$P(C_{\text{net}} | C_{\text{src}}, C_{\text{bkg}}) = \frac{1}{Z} \sum_{i=0}^{C_{\text{src}}} \frac{(C_{\text{src}} + C_{\text{bkg}} - i)!}{C_{\text{bkg}}! (C_{\text{src}} - i)!} \times \omega_B^{C_{\text{bkg}}} \omega_S^{C_{\text{src}} - i} \frac{C_{\text{net}}^i e^{-C_{\text{net}}}}{i!}, \quad (12)$$

where the partition function, Z , is

$$Z = \sum_{i=0}^{C_{\text{src}}} \frac{(C_{\text{bkg}} + i)!}{C_{\text{bkg}}! i!} \omega_B^{C_{\text{bkg}}} \omega_S^i \quad (13)$$

and ω_B or ω_S is the probability that a background event occurs in the background or source aperture, respectively:

$$\omega_B = \frac{A_{\text{bkg}} E_{\text{bkg}}}{A_{\text{bkg}} E_{\text{bkg}} + A_{\text{src}} E_{\text{src}}}, \quad \omega_S = \frac{A_{\text{src}} E_{\text{src}}}{A_{\text{bkg}} E_{\text{bkg}} + A_{\text{src}} E_{\text{src}}}. \quad (14)$$

$P(C_{\text{net}})$ is normalized and converted into $P(f_X)$, using the relationship included in Equation (10). Finally, assuming that the differential counts of sources within each quantile group obey a power law of the form $dN/df_X \propto f_X^\beta$, we corrected for the Eddington bias by multiplying each source flux distribution, $P(f_X)$, by f_X^β . Examples of the resulting flux distributions are shown in Figure 16.

5.4. Cumulative Number-flux Computation

The number count distribution is equal to the sum of the flux probability distributions of individual sources, divided by the sensitivity curve calculated in Section 5.1 and the recovery fraction function determined in Section 5.2:

$$N(> f_X) = \int_{f_X}^{\infty} \left[\sum_{i=1}^{N_{\text{src}}} \frac{P_i(f_X)}{A(f_X, \epsilon_i) F_{\text{rec},i}} \right] df_X. \quad (15)$$

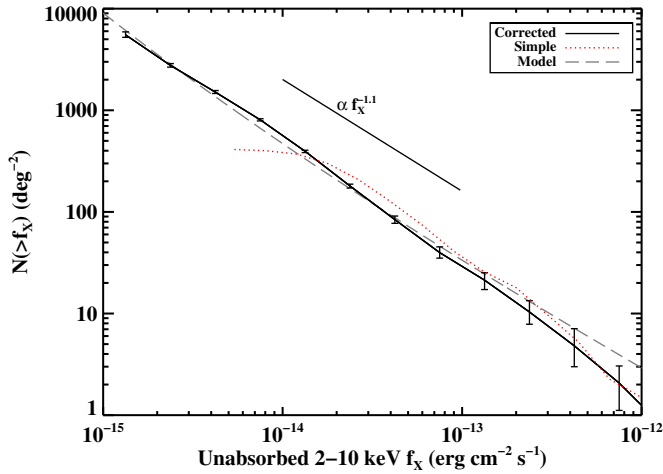


Figure 17. Cumulative number-flux distribution for all sources detected at $\geq 3\sigma$ in the 2–10 keV band. The red dotted line is calculated by assigning a single flux value to each detected source and not correcting for any systematic errors. The bars represent 1σ uncertainties. The gray dashed line represents the sum of the maximum-likelihood models for each quantile group computed as described in Section 5. The black solid line is the result of using a flux probability distribution for each source and correcting for the Eddington bias, the variations in sensitivity across the surveyed area, and the incompleteness of our detection procedure. A line with a power-law index equal to -1.1 is shown as a visual aid.

(A color version of this figure is available in the online journal.)

However, the number count distribution depends on the power-law index β through $P(f_X)$. We estimate β using a ML method with power-law differential number-flux Bayesian priors. The probability of source i being present in our catalog is

$$p_i = \frac{\int P_i(f_X) df_X}{\int dN/df_X|_{\epsilon_i} A(f_X, \epsilon_i) F_{\text{rec},i} df_X}. \quad (16)$$

Therefore, the total likelihood of obtaining the sources in our catalog is $\prod_i p_i$. We find the best-fit power-law index for each quantile group by maximizing the total likelihood for each quantile group model separately. The normalization, K , of each group model was found by computing the differential number counts in 20 flux bins,

$$\frac{dN}{df_X} = \left(\int_{f_{X,\min}}^{f_{X,\max}} \left[\sum_{i=1}^{N_{\text{src}}} \frac{P_i(f_X)}{A(f_X, \epsilon_i) F_{\text{rec},i}} \right] df_X \right) / (f_{X,\max} - f_{X,\min}) \quad (17)$$

calculating 20 corresponding normalizations, and then weight-averaging these normalization values. We calculate the statistical errors of the number counts using the bootstrap method; we resample our list of catalog sources, determine new best-fit β and K parameters, and recompute the number count distribution.

6. THE NUMBER COUNT ($\log N$ – $\log S$) DISTRIBUTION

Figure 17 compares the number-flux distribution calculated using the methodology described in Section 5 with the “simple” distribution constructed using a single flux value for each detected source and without corrections for the Eddington bias, sensitivity curve, or recovery fraction. As can be seen in the figure, we can compute the number-flux distribution down to a flux limit roughly an order-of-magnitude below the nominal flux limit of the survey, the point at which the “simple” distribution turns over ($f_X \approx 2 \times 10^{-14}$ erg cm $^{-2}$ s $^{-1}$). The power-law parameters describing the differential count distribution for each quantile group in the 2–10 keV band that are found to have ML

Table 11

Maximum Likelihood Parameters for dN/df_X Distributions in the 2–10 keV Band

Quantile Group (1)	β (2)	K_{norm} (10^{14} deg $^{-2}$ (erg cm $^{-2}$ s $^{-1}$) $^{-1}$) (3)
A	-3.1 ± 0.3	20_{-8}^{+4}
B	-2.5 ± 0.1	52_{-11}^{+8}
C	$-2.37_{-0.08}^{+0.05}$	150_{-20}^{+10}
D	-1.97 ± 0.05	200_{-30}^{+10}
E	-2.31 ± 0.05	140_{-50}^{+20}

Notes. All quoted errors are 1σ statistical. (1) Quantile groups defined in Section 2.5. (2) Power-law index of dN/df_X distribution. (3) Normalization of dN/df_X distribution.

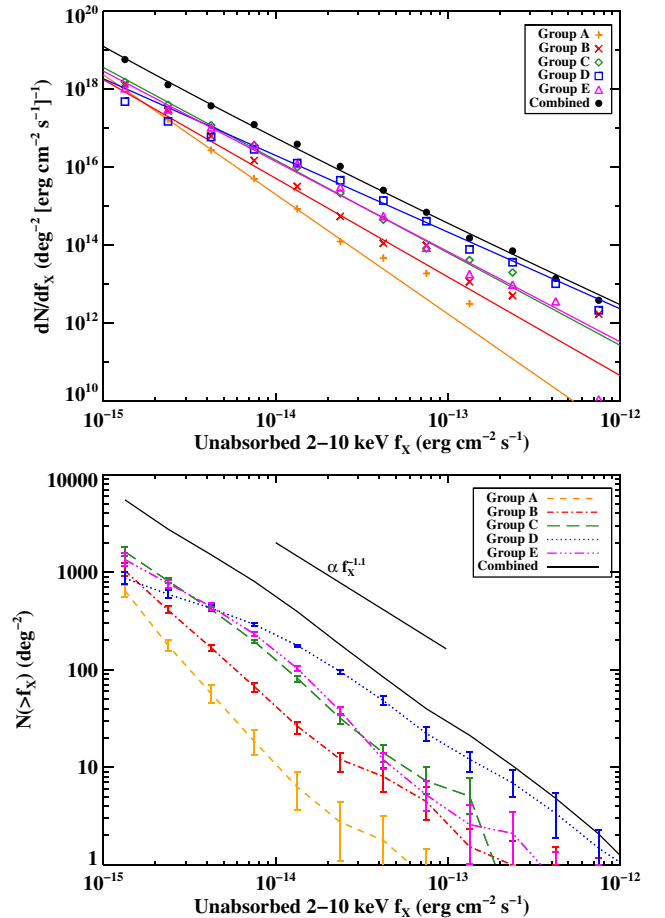


Figure 18. Upper panel shows the differential number counts vs. 2–10 keV flux calculated as described in Section 5. The solid lines represent the maximum-likelihood simple power-law models while the points represent the corrected data with 1σ errors. Lower panel shows the cumulative number counts vs. 2–10 keV flux. Lines represent the corrected data with 1σ errors. Both dN/dS and $\log N$ – $\log S$ are shown for the five quantile groups and for all groups combined. (A color version of this figure is available in the online journal.)

are provided in Table 11, and the differential and cumulative count distributions are shown in Figure 18. The combined cumulative distribution for all groups has a power-law index of roughly -1.1 . This index is similar to those found for the cumulative distributions of sources in other surveys, which vary from -1.0 to -1.5 (Muno et al. 2009; Hong et al. 2009; Ebisawa et al. 2005). The group D sources dominate in the 2–10 keV band down to a flux limit of $\approx 5 \times 10^{-14}$ erg cm $^{-2}$ s $^{-1}$, below which

group C and E sources dominate. We modified the quantile group divisions by ~ 0.1 dex and re-calculated the number-flux distributions; the power-law indices of the differential count distributions of the modified quantile groups vary by $< 2\sigma$, and the $\log N$ – $\log S$ distributions also remain consistent at the 2σ level or better.

Groups B, C, and E have differential count distributions with power-law indices that are consistent with each other at $\lesssim 1\sigma$ confidence, with $\beta \approx -2.4$. The similarity between the group B and C slopes was expected since the majority of hard sources in these groups are likely to be a mixture of different types of CVs. However, it is somewhat surprising that the group E slope is so similar to those of groups B and C since we expect group E to contain a significant fraction of high-mass stars and AGNs in addition to WD binary systems. Perhaps group E does not contain quite as many high-mass stellar X-ray sources as we expect based on the spectral properties of this group, or perhaps the flux distribution of X-ray sources associated with high-mass stars is similar to that CVs.

The group A power-law index is significantly steeper than $\beta \approx -2.4$, which may be because this group is made up of very different X-ray populations, such as low-mass X-ray active stars, coronally ABs, and high-mass stars. However, this very steep power-law index may be a result of poor statistics, since only a small number of group A sources are detected in the 2–10 keV band. In addition, since only about five group A sources have fluxes higher than fluxes at which the sensitivity curve and recovery fraction corrections become important, its differential count distribution parameters will be more severely impacted than any other group by any systematic imperfections in these corrections. However, even if the ML results for this group are not reliable, the results for all other groups are independent and since group A only contributes $\lesssim 10\%$ of sources at all fluxes, it also has little impact on the combined group distribution.

The other power-law index that significantly differs from those of groups B, C, and E is that of group D, which is significantly flatter. It is not too surprising that the group D slope is different since this group appears to be dominated by a single class of CVs, IPs, rather than a mixture of magnetic and nonmagnetic CVs. As can be seen in Figure 18, only the group D differential-count distribution deviates at $> 3\sigma$ confidence from a simple power-law model at fluxes $< 10^{-13}$ erg cm $^{-2}$ s $^{-1}$; while other group distributions deviate significantly from a simple power-law model above this flux, there are simply not enough bright sources in each group to constitute a statistically significant sample. The group D distribution deviates from the simple power-law model at fluxes $\lesssim 10^{-14}$ erg cm $^{-2}$ s $^{-1}$ by as much as 8σ at the faintest fluxes. The turnover in the group D distribution remains significant even when we modify the quantile divisions by ~ 0.1 dex. Although our sensitivity curve, recovery fraction, and Eddington bias corrections may still not perfectly correct for all these systematic errors, it is unlikely that this group D deviation is simply due to a systematic error since it is the only group displaying this turnover at faint fluxes.

Thus, the turnover at faint fluxes in the group D number-count distribution is likely indicative of a real break in the power-law distribution. Such a break could result if the sources in group D have a break in their luminosity function, a minimum luminosity, or a high enough luminosity to be seen through the entire galaxy. As discussed in Section 4.6, 30%–50% of group D sources without IR counterparts may be AGNs, which have a number-count distribution that is shallower at fluxes $< 10^{-14}$ erg cm $^{-2}$ s $^{-1}$ (Cappelluti et al. 2009), and therefore,

the break in the AGN distribution could at least partly explain the break in the group D distribution. However, if the turnover in the group D distribution is primarily due to AGNs, it is surprising that a significant turnover is not also seen in the group E distribution, since there is stronger evidence for AGNs being present in group E than group D. Since group D appears to be dominated by IPs, this break in the number-count distribution could be an indication of a break in the luminosity function of IPs, although we emphasize that this is a possibility but it cannot be confirmed with this data alone. A break in the IP luminosity function could be due to the propeller effect, a centrifugal barrier to accretion at low mass accretion rates that results when the magnetosphere of a compact object has a higher angular velocity than the accretion flow at the Alfvén radius (Illarionov & Sunyaev 1975). The propeller effect has been invoked to explain the turnover of the HMXB luminosity function at the faint end (Shtykovskiy & Gilfanov 2005), the variability of supergiant fast X-ray transients (Grebenev & Sunyaev 2007; Bozzo et al. 2008), and the state transitions in some LMXBs (Zhang et al. 1998). Although this effect has primarily been used to explain the behavior of low-luminosity accreting NS, similar physical mechanisms may be important in accreting WD systems, even in CVs with weak magnetic fields (Matthews et al. 2006). We only present this interpretation of the break in the group D number-count distribution as a speculative hypothesis; a theoretical study of the propeller effect in IPs is beyond the scope of this paper, and multiwavelength follow-up of group D sources that will help to confirm whether they indeed are primarily IPs is ongoing.

6.1. Comparison to Expectations Based on Previous Surveys

Having calculated the number-count distribution of the NARCS X-ray sources, we want to compare it to the expected distribution based on other Galactic surveys since any significant discrepancies would indicate that the X-ray populations in this region might be unusual in some way. Thus, we estimated the expected contributions of ABs, CVs, LMXBs, HMXBs, and AGNs to the observed number-count distribution.

In the hard X-ray band, CVs are the most numerous Galactic X-ray sources and they are thought to be the main contributors to the observed Galactic Ridge X-Ray Emission, the large-scale background emission of the Galaxy. CVs are low-luminosity sources ($L_X \lesssim 10^{33}$ erg s $^{-1}$) and trace the old stellar population of the Milky Way. Another significant population of low-luminosity sources that follow the stellar mass distribution are ABs. Thus, to calculate the expected flux distribution of ABs and CVs in NARCS, both their luminosity functions and a model of the Galactic stellar mass distribution are required. Sazonov et al. (2006) measured the combined luminosity function of ABs and CVs in the local vicinity of the Sun over the luminosity range $L_X = 10^{27}$ – 10^{34} erg s $^{-1}$. Since the local AB/CV cumulative emissivity per unit stellar mass was found to be consistent with that measured elsewhere in the Galaxy (Revnitsev et al. 2006, 2008; Revnitsev & Sazonov 2007; Krivonos et al. 2007), we used the AB/CV luminosity function per unit stellar mass from Sazonov et al. (2006) to estimate the AB/CV flux distribution in NARCS. We utilize a stellar mass model similar to that used by Sazonov et al. (2006), which is an exponential disk with a central hole:

$$\rho \propto \exp \left[- \left(\frac{R_m}{R} \right)^3 - \frac{R}{R_{\text{scale}}} - \frac{z}{z_{\text{scale}}} \right], \quad (18)$$

where R is the radial distance from the Galactic center, z is the height above the plane, R_m is the radius of the hole in the Galactic disk, R_{scale} is the disk scale length, and z_{scale} is the scale height of CVs. We assume $R_m = 3$ kpc (Binney et al. 1997; Freudenreich 1998), but adopt a range of values for parameters that are not well constrained: 2.5–3.5 kpc for R_{scale} (Binney et al. 1997; Freudenreich 1998; Hammersley et al. 1999) and 80–220 pc for z_{scale} (Revnivtsev et al. 2008). For our stellar mass model we further adopt a disk-to-bulge mass ratio of 2:1 and a range of values for the Galactic bulge mass of $1.3 \pm 0.5 \times 10^{10} M_\odot$ (Dwek et al. 1995). Using this model, the projected stellar mass contained in NARCS is roughly $1.4 \times 10^8 M_\odot$.

To compute the number of ABs/CVs expected above a given flux, f_{lim} , in our survey, we first consider a small volume element dV within the surveyed volume, and integrate the luminosity function per stellar mass from $L_{\text{lim}} = f_{\text{lim}} \times 4\pi d^2$, where d is the distance to dV , to L_{max} . Multiplying by the stellar mass contained in dV as determined from our stellar mass model distribution then gives the number of ABs/CVs with $f_X > f_{\text{lim}}$ in dV . Integrating the number per volume over all distances d and all lines of sight through our survey, and then simply repeating this procedure for the range $10^{-15} < f_{\text{lim}} < 10^{-11}$, we obtain the expected $\log N$ – $\log S$ for ABs/CVs. We repeat this calculation many times, choosing values randomly for each of the uncertain stellar mass model parameters.

LMXBs are more luminous and far rarer than CVs, but they too scale with the old stellar mass. Thus, to estimate the number of LMXBs expected in NARCS, we take the LMXB luminosity function from Sazonov et al. (2006) and apply the same method as for ABs/CVs, except that we use a scale height of $z_{\text{scale}} = 410$ pc (Grimm et al. 2002). We find that $\lesssim 1$ LMXB is expected in our survey region.

Unlike CVs and LMXBs, the number of HMXBs is not correlated with the old stellar mass, and thus our estimate of the HMXBs in NARCS is independent of the Galactic stellar mass model. Our predictions for the HMXB contribution to the number-count distribution is based on the luminosity function from Lutovinov et al. (2013), which is derived from the number of Galactic HMXBs observed by *International Gamma-Ray Astrophysics Laboratory (INTEGRAL)* (Winkler et al. 2003). Since our *INTEGRAL* luminosity function was calculated in the 17–60 keV band, we converted it to the 2–10 keV band by assuming a typical spectral model for accreting pulsars that includes a power-law with a high-energy cutoff (White et al. 1983):

$$f(E) \propto E^{-\Gamma} \times \begin{cases} 1, & (E \leq E_{\text{cut}}) \\ e^{-(E-E_{\text{cut}})/E_{\text{fold}}}, & (E > E_{\text{cut}}). \end{cases} \quad (19)$$

Using $\Gamma = 1$, $E_{\text{cut}} = 20$ keV, $E_{\text{fold}} = 10$ keV, and intrinsic $N_{\text{H}} = 5 \times 10^{22} \text{ cm}^{-2}$ (Filippova et al. 2005), the conversion factor $f_{2-10 \text{ keV}}/f_{17-60 \text{ keV}} \simeq 0.5$. Since our HMXB prediction is based on a survey of the HMXB population throughout the whole Galaxy, it does not take into account that, as discussed in Section 1, the Norma region appears to have an enhanced number of HMXBs due to its star formation activity. Therefore, we may be underestimating the number of HMXBs in this region, but probably by no more than a factor of two based on the comparison of predictions and observations presented in Lutovinov et al. (2013) for the brightest HMXBs in the whole Norma arm.

One population of sources whose contribution is difficult to predict are isolated high-mass stars and CWBs because they are not evenly distributed throughout the Galaxy and their

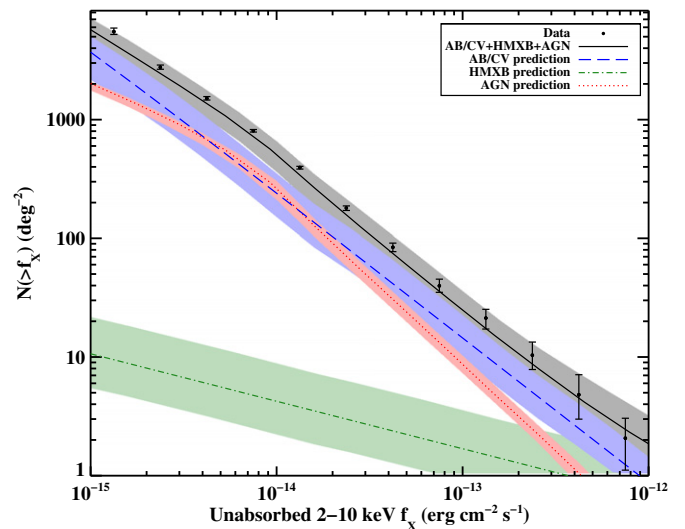


Figure 19. Observed number-flux distribution compared to the combined estimates of the expected AB/CV, HMXB, and AGN flux distributions based on the luminosity functions of these populations from other surveys. Estimated uncertainties for the predictions are shown as shaded regions. The AB/CV line shown is the average distribution of the ones we calculated by varying the parameters of the Galactic stellar mass model.

(A color version of this figure is available in the online journal.)

X-ray luminosity functions have yet to be determined. However, we do expect high-mass stellar X-ray sources to be present in our survey due to the presence of massive-star forming complexes and H II regions along this line-of-sight, and we have already identified a small number of these sources. As discussed in Section 4.1, three group A sources with known massive counterparts are likely isolated high-mass stars. In addition, Rahoui et al. (2014) find that 5 of 20 NARCS counterparts for which they obtained infrared spectra are high-mass stars; their X-ray properties favor the interpretation that three of these sources (#239, 1168, and 1326) are quiescent HMXBs and two (#1278 and 1279) are CWBs. Ongoing spectroscopic follow-up of IR counterparts and improved constraints on the X-ray properties of NARCS sources with *Nuclear Spectroscopic Telescope Array (NuSTAR)* (Harrison et al. 2013) observations will help to determine their total number and their flux distribution. Given the rarity of high-mass stars even in regions of recent star formation like the Norma arm, we do not expect these sources to constitute a large fraction of the NARCS population; however, identifying even a small sample (~ 10) of such sources would be a significant contribution to the number of known high-mass X-ray sources (e.g., Mauerhan et al. 2010; Gagné et al. 2011) and our understanding of their X-ray properties.

Figure 19 shows our estimates for the expected flux distributions of ABs/CVs and HMXBs in our survey region (there are too few expected LMXBs to be shown), while Table 12 provides their power-law indices and normalizations. The observed AGN distribution from the COSMOS survey (Cappelluti et al. 2009) is also included, attenuated by the average column density from the outer Norma arm to the outer edge of the Galaxy ($N_{\text{H}} \approx 3 \times 10^{22} \text{ cm}^{-2}$). Uncertainties in the predicted AGN distribution are determined by considering N_{H} values from zero to $8 \times 10^{22} \text{ cm}^{-2}$, the maximum measured along any line-of-sight in our surveyed area.

As can be seen, the sum of the predicted distributions of ABs/CVs, AGNs, and HMXBs matches the calculated flux distribution of hard sources in NARCS. The fact that the slope of the expected distribution matches the observed one so well,

Table 12
Normalizations and Indices of $\log(N)$ – $\log(S)$ Distributions

Population (1)	Normalization (2)	Power-law Index (3)
Observed	630	$\begin{cases} -1.14, f_X < 10^{-14} \text{ erg cm}^{-2} \text{ s}^{-1} \\ -1.24, f_X > 10^{-14} \text{ erg cm}^{-2} \text{ s}^{-1} \end{cases}$
AB/CV predicted	250 ± 100	-1.21
HMXB predicted	4_{-2}^{+4}	-0.40
AGN predicted	260_{-50}^{+40}	$\begin{cases} -0.90, f_X < 10^{-14} \text{ erg cm}^{-2} \text{ s}^{-1} \\ -1.46, f_X > 10^{-14} \text{ erg cm}^{-2} \text{ s}^{-1} \end{cases}$

Notes. (1) Population of sources, observed or predicted. (2) Number of sources with $f_X > 10^{-14} \text{ erg cm}^{-2} \text{ s}^{-1}$. (3) Power-law index of distribution.

including some of the kinks in the slope, suggests that ABs, CVs, and AGNs are the dominant populations in our survey and that their relative numbers are similar to the proportions predicted from other observations.

7. SUMMARY AND FUTURE WORK

We have presented a catalog of $1129 \geq 3\sigma$ point-like sources and 5 extended sources detected in a *Chandra* survey of a $2^\circ \times 8^\circ$ region in the direction of the Norma spiral arm. These sources span the luminosity range $L_X = 10^{27}$ – $10^{35} \text{ erg s}^{-1}$. The systematic positional errors were reduced by matching X-ray sources to infrared VVV counterparts, so that the median positional error for sources in our catalog is $1''.26$ (95% statistical plus systematic uncertainty). The median number of counts for sources in our survey is 11, making most of them too faint to enable accurate determination of their spectral properties. Therefore, to help classify the sources, we split them into five spectral groups based on their quantile properties. The stacked spectra, photometric variability, and IR counterparts of the sources within each spectral group allowed us to identify the classes of X-ray sources that populate the foreground, the Scutum-Crux and near Norma arm, and the far Norma arm. Foreground sources, which make up roughly 50% of cataloged sources, are a heterogeneous group, probably containing X-ray active low-mass stars, interacting binaries, symbiotic binaries, and CVs. The X-ray populations of the Scutum-Crux and near Norma arms are most likely dominated by a mixture of magnetic and nonmagnetic CVs. The far Norma arm hard X-ray population is likely dominated by IPs, while the softer X-ray population probably includes high-mass stars (both isolated and in CWBs) and symbiotic binaries.

We also calculated the number-count distribution for sources in our survey down to a flux limit of $10^{-15} \text{ erg cm}^{-2} \text{ s}^{-1}$, correcting for the Eddington bias, the variations in sensitivity across the surveyed area, and the incompleteness of our detection procedure. The observed distribution matches predictions based on AB, CV, AGN, and HMXB luminosity functions very well, lending further support to our conclusions that CVs are the dominant population in NARCS. Furthermore, the fact that the observed number-count distribution shows the same changes in slope as the predicted distribution, suggests that roughly a third of the NARCS sources detected in the hard energy band probably are AGNs as predicted; we see some evidence for the presence of AGNs in the stacked spectrum of group C, D, and E sources lacking NIR counterparts. However, it is unclear whether AGNs can fully account for the flattening at faint fluxes that is seen in the number-count distribution of group D sources; additional X-ray observations would help to disentangle the rel-

ative fractions of AGNs and IPs in this group and help determine which population is responsible for the break in the $\log N$ – $\log S$ distribution.

The analysis we have presented is primarily statistical in nature, but multiwavelength data could permit the classification and deepened understanding of individual sources. Our ongoing follow-up campaigns are focused on but not limited to group D X-ray sources, since any HMXBs in this survey are most likely to belong to this group. Near-IR spectroscopic follow-up of counterparts to these X-ray sources is ongoing and will help us to determine which of these X-ray sources have high-mass versus low-mass counterparts. A *NuSTAR* survey of this region will help to constrain the hard X-ray emission from these sources. The combination of this multiwavelength data should enable us to distinguish HMXBs, which have high-mass stellar counterparts and significant hard X-ray emission, from X-ray emission from shocks in the winds of high-mass stars, which have softer spectra, and IPs, which should have low-mass stellar or accretion disk signatures in the near-IR and significant hard X-ray emission. This multiwavelength data set will help us to constrain the faint end of the HMXB luminosity function and be useful in advancing our understanding of other Galactic X-ray sources.

We thank the referee and the editor for their suggestions, which helped us improve the scientific quality of these results. We thank G. K. Keating and C. Heiles for helpful discussions about various components of the statistical analysis carried out for this work. We are also grateful to B. Lehmer for clarifications regarding the maximum likelihood number-flux computation, to J. Hong for providing his quantile analysis tools, and to L. Blitz and M. Ajello for valuable conversations. The scientific results reported in this article are based on observations made by the *Chandra X-Ray Observatory*. Our analysis of IR counterparts was based on data products from observations made with ESO Telescopes at the La Silla or Paranal Observatories under ESO programme ID 179.B-2002. This research has made use of software provided by the Chandra X-Ray Center (CXC) in the application packages CIAO and Sherpa. This work was supported in part by NASA through *Chandra* Award Number G01-12068A issued by the *Chandra X-Ray Observatory Center*, which is operated by the Smithsonian Astrophysical Observatory for and on behalf of NASA under contract NAS8-03060. In addition, FMF received support from the National Science Foundation Graduate Research Fellowship and the Berkeley Fellowship. F.E.B. acknowledges support from Basal-CATA PFB-06/2007, CONICYT-Chile FONDECYT 1141218 and “EMBIGGEN” Anillo ACT1101, and Project IC120009 “Millennium Institute of Astrophysics (MAS)” of Iniciativa Científica Milenio del Ministerio de Economía, Fomento y Turismo.

APPENDIX

COLUMN DESCRIPTIONS OF CATALOG TABLES

Below are detailed descriptions of the information provided in the catalog, published in its entirety in the electronic edition. In these tables, when a value is presented along with its errors, the first column listed in the column range contains the value. In the case of symmetric errors, the second column contains the error. In the case of asymmetric errors, the second column contains the upper error and the third column contains the lower error.

A.1. Detection and Localization Table

- (1) NARCS catalog source number.
- (2) *Chandra* source name.
- (3) Observation(s) in which `wavdetect` detects the source. The format of ObsID numbers is 125XX, where the last two digits are those provided in the catalog. See Section 2.1 for details about `wavdetect` usage.
- (4)–(5) Right ascension and declination (J2000.0) of the source. If the source is detected in multiple observations, the position reported is the weighted average of its positions in different observations.
- (6) Positional uncertainty of the source. For a source detected in a given observation, this uncertainty is equal to the quadrature sum of the 95% statistical uncertainty based on Equation (5) of Hong et al. (2005) and the average systematic uncertainty of positions in that observation after astrometric refinement (see Column 5 in Table 2). For sources detected in multiple observations, the uncertainties associated with the source position in different observations were combined to provide the uncertainty of the weighted average of the source positions.
- (7) Offset angular separation of the source from the center of the observation aim point. For sources detected in multiple observations, a semicolon-separated list of the offset angle of the source from each observation aim point is provided; the order of offsets matches the order of ObsIDs reported in Column 3.
- (8)–(10) Significance of source in the full 0.5–10 keV band, the soft 0.5–2 keV band, and the hard 2–10 keV band. It is calculated by finding the probability that the source is a noise fluctuation using Equation (5) and using the Gaussian cumulative distribution function to determine the corresponding source significance. If the source is detected in multiple observations, the reported significance is the sum in quadrature of the source significance in individual observations.
- (11) Radius of the aperture source region. For most sources, the aperture source region is defined as a circle with radius equal to the 90% ECF for 4.5 keV photons (see Column 12). For potentially extended sources, flagged with “e” (see Column 13), the radius is instead equal to the semi-major axis of the aperture region defined by `wavdetect`. In cases where two or more sources have overlapping circular regions, the regions are redefined as a circular core plus an annular pie sector following the guidelines in Table 6; in such cases, the radius provided in the catalog represents the outer radius of the pie sector. For sources detected in multiple observations, a semicolon-separated list of the aperture region radius used in different observations is provided; the order of radii matches the order of ObsIDs reported in Column 3.
- (12) PSF radius for 90% ECF for 4.5 keV photons at the detector location of the source. The PSF radius varies with detector position, generally increasing with increasing offset angle from the observation aim point. For sources detected in multiple observations, a semicolon-separated list of the PSF radius at the source detector position in different observations is provided; the order of PSF radii matches the order of ObsIDs reported in Column 3.
- (13) An alphabetical list of the possible flags:
 - “b”–“blended”: blended source that is unblended in another observation.
 - “c”–“created”: source noticed by eye but not detected by `wavdetect`. The source aperture region was created manually based on the visible position and extent of the source. The positional uncertainties calculated for such sources underestimate

the true uncertainties, since the source is found by eye and not by `wavdetect`.

“e”–“extended”: possibly extended source. The semi-major axis of the smallest aperture region defined by `wavdetect` for such sources is larger than twice the PSF radius reported in Column 12. These sources are typically detected in images that have been binned by 4×4 or 8×8 pixels.

“id”–“inspected duplicate”: possible duplicate source flagged for manual inspection. A “duplicate” source refers to a single source detected in multiple overlapping observations; sources were considered to be duplicates of one another if the distance between them was smaller than the quadrature sum of their positional uncertainties. Sources were flagged for manual inspection if (1) they were separated by a distance greater than the quadrature sum of their positional uncertainties but smaller than the simple sum of their positional uncertainties, or (2) they were separated by a distance smaller than the quadrature sum of their positional uncertainties but differed in a substantial way (e.g., one is flagged as possibly extended while another is not, one is found to have two duplicates by the distance criterion but these two duplicates of the first source are not found to be duplicates of one another by the distance criterion). Generally, if sources flagged with “id” showed consistent photon fluxes and quantile parameters, they were determined to be true duplicates.

“m1,” “m2,” or “m3”–“modified”: in cases where the circular source aperture region overlaps with the aperture region of another source, the source region is modified to reduce overlapping. See Table 6 for details.

“nb”–“near bright”: source near a very bright source which may be a spurious detection.

“nd”–“not detected”: source is located where at least two observations overlap but it is only detected in one observation.

“s”–“surrounding”: a possibly extended source that completely surrounds one or more point sources. The aperture regions of the surrounded sources are excluded from the aperture region of the source flagged with “s.”

“vl”–“variable long”: source determined to be variable on long (hours–days) timescales. The photon flux in at least one energy band (full, soft, or hard) varies by $\geq 3\sigma$ between different observations.

“vp”–“variable probable”: source is probably variable on short (second–hour) timescales. The K-S test finds the source light curve within a single observation to be inconsistent with a constant light curve at $\geq 95\%$ confidence.

“vs”–“variable short”: source is variable on short (second–hour) timescales. The K-S test finds the source light curve within a single observation to be inconsistent with a constant light curve at $\geq 3\sigma$ confidence.

For sources detected in multiple observations, a semicolon-separated list of the flags relevant for the source region in each observation is provided; the order of flags matches the order of ObsIDs reported in Column 3.

A.2. Photometry Table

- (1) NARCS catalog source number.
- (2)–(4) Net source counts in the full 0.5–10 keV band and corresponding 1σ errors, calculated as described in Section 2.2. For cases in which the estimated background counts in a source aperture region were determined to be greater than or equal to the total number of counts in the source region, then the catalog presents the 90% upper confidence limit to the net source counts based on the method described in Kraft et al. (1991); in such cases, the error columns are left blank. For sources detected in

multiple observations, net counts from different observations were added together and errors combined in quadrature.

(5)–(7) Net source counts in soft 0.5–2 keV band. Same details as discussed for Columns 2–4 apply.

(8)–(10) Net source counts in hard 2–10 keV band. Same details as discussed for Columns 2–4 apply.

(11)–(13) Photon flux in the full 0.5–10 keV band and corresponding 1σ errors. The photon flux was calculated by dividing the net counts by the exposure time and the mean effective area within the source region. For sources with zero or negative net counts, the catalog provides the 90% upper limit on the photon flux and leaves the error columns blank. For sources detected in multiple observations, the average photon fluxes are reported; if a source was found to be variable between observations (flagged as “vl”) then its photon fluxes from individual observations were simply averaged, but otherwise its photon fluxes were weight-averaged.

(14)–(16) Photon flux in the soft 0.5–10 keV band. Same details as discussed for Columns 11–13 apply.

(17)–(19) Photon flux in the hard 2–10 keV band. Same details as discussed for Columns 11–13 apply.

(20)–(21) The median energy of the source and corresponding 1σ error. It is determined from the total counts (not background corrected) in the source region. For sources detected in multiple observations, the simple average of the energies from individual observations is reported if a source is found to be variable between observations or the weighted-average is reported otherwise.

(22)–(23) The energy below which 25% of the total source counts reside and corresponding 1σ error. Same details as discussed for Columns 20–21 apply.

(24)–(25) The energy below which 75% of the total source counts reside and corresponding 1σ error. Same details as discussed for Columns 20–21 apply.

(26)–(28) The energy flux in the full 0.5–10 keV band and corresponding 1σ errors. This estimate of the energy flux is calculated by multiplying the FB photon flux and the median energy of the source provided in the catalog. In cases where only an upper limit to the photon flux is available, the 90% upper limit to the energy flux is reported and the error columns are left blank.

(29) Photometric flags. If the photometric values provided for a source are 90% upper limits in the full, soft, or hard energy bands, this column displays an F, S, or H, respectively.

(30) The spectral group defined using quantile diagrams to which the source belongs. See Section 3 for details about quantile analysis and the spectral groups defined in this work.

A.3. Table of Infrared Counterparts

- (1) NARCS catalog source number.
- (2) Name of VVV source that is closest to the *Chandra* source position, within 3σ of the position provided in Table 3.
- (3) Right ascension (J2000.0) of the VVV source.
- (4) Declination (J2000.0) of the VVV source.
- (5) Angular separation between the *Chandra* and VVV source.
- (6) Probability that the VVV source is a noise fluctuation, provided in the VVV catalog.
- (7) Reliability of the VVV counterpart calculated according to the method of Sutherland & Saunders (1992). The reliability depends on the distance between the X-ray and IR sources, the positional uncertainties of the X-ray and IR sources, and the spatial density of IR sources. The reliability is expressed as a

fraction between zero and one; VVV sources with a higher reliability are more likely to be true IR counterparts to the *Chandra* sources.

REFERENCES

- Allen, C., Jerius, D. H., & Gaetz, T. J. 2004, *Proc. SPIE*, 5165, 423
- An, H., Kaspi, V. M., Tomsick, J. A., et al. 2012, *ApJ*, 757, 68
- Anders, E., & Grevesse, N. 1989, *GeCoA*, 53, 197
- Binney, J., Gerhard, O., & Spergel, D. 1997, *MNRAS*, 288, 365
- Bird, A. J., Barlow, E. J., Bassani, L., et al. 2004, *ApJL*, 607, L33
- Bodaghee, A., Rahoui, F., Tomsick, J. A., & Rodriguez, J. 2012a, *ApJ*, 751, 113
- Bodaghee, A., Tomsick, J. A., & Rodriguez, J. 2012b, *ApJ*, 753, 3
- Bodaghee, A., Tomsick, J. A., Rodriguez, J., & James, J. B. 2012c, *ApJ*, 744, 108
- Bodaghee, A., Walter, R., Zurita Heras, J. A., et al. 2006, *A&A*, 447, 1027
- Bozzo, E., Falanga, M., & Stella, L. 2008, *ApJ*, 683, 1031
- Bronfman, L., Alvarez, H., Cohen, R. S., & Thaddeus, P. 1989, *ApJS*, 71, 481
- Buccheri, R., Bennett, K., Bignami, G. F., et al. 1983, *A&A*, 128, 245
- Cappelluti, N., Brusa, M., Hasinger, G., et al. 2009, *A&A*, 497, 635
- Cardelli, J. A., Clayton, G. C., & Mathis, J. S. 1989, *ApJ*, 345, 245
- Civano, F., Elvis, M., Brusa, M., et al. 2012, *ApJS*, 201, 30
- Combi, J. A., Benaglia, P., Romero, G. E., & Sugizaki, M. 2005, *A&A*, 431, L9
- Dame, T. M., Hartmann, D., & Thaddeus, P. 2001, *ApJ*, 547, 792
- Ducati, J. R., Bevilacqua, C. M., Rembold, S. B., & Ribeiro, D. 2001, *ApJ*, 558, 309
- Dwek, E., Arendt, R. G., Hauser, M. G., et al. 1995, *ApJ*, 445, 716
- Ebisawa, K., Tsujimoto, M., Paizis, A., et al. 2005, *ApJ*, 635, 214
- Filippova, E. V., Tsygankov, S. S., Lutovinov, A. A., & Sunyaev, R. A. 2005, *AstL*, 31, 729
- Freeman, P. E., Kashyap, V., Rosner, R., & Lamb, D. Q. 2002, *ApJS*, 138, 185
- Freudenreich, H. T. 1998, *ApJ*, 492, 495
- Funk, S., Hinton, J. A., Pühlhofer, G., et al. 2007, *ApJ*, 662, 517
- Gagné, M., Fehon, G., Savoy, M. R., et al. 2011, *ApJS*, 194, 5
- Garmire, G. P., Bautz, M. W., Ford, P. G., Nousek, J. A., & Ricker, G. R., Jr. 2003, *Proc. SPIE*, 4851, 28
- Gehrels, N. 1986, *ApJ*, 303, 336
- Georgakakis, A., Nandra, K., Laird, E. S., Aird, J., & Trichas, M. 2008, *MNRAS*, 388, 1205
- Georgelin, Y. M., Russeil, D., Marcelin, M., et al. 1996, *A&AS*, 120, 41
- Grebenev, S. A., & Sunyaev, R. A. 2007, *AstL*, 33, 149
- Green, D. A. 2004, *BASI*, 32, 335
- Green, D. A. 2009, *BASI*, 37, 45
- Grimm, H.-J., Gilfanov, M., & Sunyaev, R. 2002, *A&A*, 391, 923
- Grosso, N., Feigelson, E. D., Getman, K. V., et al. 2005, *ApJS*, 160, 530
- Güdel, M., Briggs, K. R., Arzner, K., et al. 2007, *A&A*, 468, 353
- Güver, T., & Özel, F. 2009, *MNRAS*, 400, 2050
- Hammersley, P. L., Cohen, M., Garzón, F., Mahoney, T., & López-Corrodoira, M. 1999, *MNRAS*, 308, 333
- Harrison, F. A., Craig, W. W., Christensen, F. E., et al. 2013, *ApJ*, 770, 103
- Hoard, D. W., Wachter, S., Clark, L. L., & Bowers, T. P. 2002, *ApJ*, 565, 511
- Hong, J., Schlegel, E. M., & Grindlay, J. E. 2004, *ApJ*, 614, 508
- Hong, J. S., van den Berg, M., Grindlay, J. E., & Laycock, S. 2009, *ApJ*, 706, 223
- Hong, J., van den Berg, M., Schlegel, E. M., et al. 2005, *ApJ*, 635, 907
- Illarionov, A. F., & Sunyaev, R. A. 1975, *A&A*, 39, 185
- Jakobsen, S. J. 2013, Master's thesis, Copenhagen University
- Jakobsen, S. J., Tomsick, J. A., Watson, D., Gotthelf, E. V., & Kaspi, V. M. 2014, *ApJ*, 787, 129
- Kalberla, P. M. W., Burton, W. B., Hartmann, D., et al. 2005, *A&A*, 440, 775
- Kraft, R. P., Burrows, D. N., & Nousek, J. A. 1991, *ApJ*, 374, 344
- Krivonos, R., Revnivtsev, M., Churazov, E., et al. 2007, *A&A*, 463, 957
- Kuulkers, E., Norton, A., Schwobe, A., & Warner, B. 2006, in *Compact Stellar X-ray Sources*, ed. W. H. G. Lewin & M. van der Klis (Cambridge: Cambridge Univ. Press), 421
- Lehmer, B. D., Xue, Y. Q., Brandt, W. N., et al. 2012, *ApJ*, 752, 46
- Luna, G. J. M., Sokoloski, J. L., Mukai, K., & Nelson, T. 2013, *A&A*, 559, A6
- Lutovinov, A. A., Revnivtsev, M. G., Tsygankov, S. S., & Krivonos, R. A. 2013, *MNRAS*, 431, 327
- Matthews, O. M., Wheatley, P. J., Wynn, G. A., & Truss, M. R. 2006, *MNRAS*, 372, 1593
- Mauerhan, J. C., Muno, M. P., Morris, M. R., Stolovy, S. R., & Cotera, A. 2010, *ApJ*, 710, 706
- Minniti, D., Lucas, P. W., Emerson, J. P., et al. 2010, *NewA*, 15, 433
- Molina, M., Bassani, L., Malizia, A., et al. 2009, *MNRAS*, 399, 1293
- Muerset, U., Wolff, B., & Jordan, S. 1997, *A&A*, 319, 201

- Muno, M. P., Arabadjis, J. S., Baganoff, F. K., et al. 2004, *ApJ*, **613**, 1179
- Muno, M. P., Bauer, F. E., Baganoff, F. K., et al. 2009, *ApJS*, **181**, 110
- Rahoui, F., Tomsick, J. A., Fornasini, F. M., Bodaghee, A., & Bauer, F. E. 2014, *A&A*, **568**, A54
- Ransom, S. M., Eikenberry, S. S., & Middleditch, J. 2002, *AJ*, **124**, 1788
- Revnivtsev, M., & Sazonov, S. 2007, *A&A*, **471**, 159
- Revnivtsev, M., Sazonov, S., Gilfanov, M., Churazov, E., & Sunyaev, R. 2006, *A&A*, **452**, 169
- Revnivtsev, M., Sazonov, S., Krivonos, R., Ritter, H., & Sunyaev, R. 2008, *A&A*, **489**, 1121
- Russeil, D. 2003, *A&A*, **397**, 133
- Sazonov, S., Revnivtsev, M., Gilfanov, M., Churazov, E., & Sunyaev, R. 2006, *A&A*, **450**, 117
- Scaringi, S., Bird, A. J., Norton, A. J., et al. 2010, *MNRAS*, **401**, 2207
- Shtykovskiy, P., & Gilfanov, M. 2005, *A&A*, **431**, 597
- Smith, N., & Brooks, K. J. 2007, *MNRAS*, **379**, 1279
- Smith, R. K., Brickhouse, N. S., Liedahl, D. A., & Raymond, J. C. 2001, *ApJL*, **556**, L91
- Sugizaki, M., Mitsuda, K., Kaneda, H., et al. 2001, *ApJS*, **134**, 77
- Sutherland, W., & Saunders, W. 1992, *MNRAS*, **259**, 413
- Townsley, L. K., Broos, P. S., Corcoran, M. F., et al. 2011, *ApJS*, **194**, 1
- Verner, D. A., Ferland, G. J., Korista, K. T., & Yakovlev, D. G. 1996, *ApJ*, **465**, 487
- Wang, Q. D., Gotthelf, E. V., & Lang, C. C. 2002, *Natur*, **415**, 148
- Wegner, W. 2007, *MNRAS*, **374**, 1549
- Weisskopf, M. C., Wu, K., Trimble, V., et al. 2007, *ApJ*, **657**, 1026
- White, N. E., Swank, J. H., & Holt, S. S. 1983, *ApJ*, **270**, 711
- Wilms, J., Allen, A., & McCray, R. 2000, *ApJ*, **542**, 914
- Winkler, C., Courvoisier, T. J.-L., Di Cocco, G., et al. 2003, *A&A*, **411**, L1
- Zhang, S. N., Yu, W., & Zhang, W. 1998, *ApJL*, **494**, L71

DISCOVERY OF X-RAY PULSATIONS FROM THE *INTEGRAL* SOURCE IGR J11014–6103

J. P. HALPERN¹, J. A. TOMSICK², E. V. GOTTHELF¹, F. CAMILO¹, C.-Y. NG³,
A. BODAGHEE⁴, J. RODRIGUEZ⁵, S. CHATY^{5,6}, AND F. RAHOUI⁷

¹ Columbia Astrophysics Laboratory, Columbia University, 550 West 120th Street, New York, NY 10027, USA; jules@astro.columbia.edu

² Space Sciences Laboratory, 7 Gauss Way, University of California, Berkeley, CA 94720-7450, USA

³ Department of Physics, The University of Hong Kong, Pokfulam Road, Hong Kong, China

⁴ Georgia College & State University, CBX 82, Milledgeville, GA 31061, USA

⁵ Laboratoire AIM (UMR-E 9005 CEA/DSM-CNRS-Université Paris Diderot), Irfu/Service d'Astrophysique, CEA-Saclay, F-91191 Gif-sur-Yvette Cedex, France

⁶ Institut Universitaire de France, 103 boulevard Saint-Michel, F-75005 Paris, France

⁷ European Southern Observatory, Karl Schwarzschild-Strasse 2, D-85748 Garching bei München, Germany

Received 2014 August 24; accepted 2014 October 7; published 2014 October 21

ABSTRACT

We report the discovery of PSR J1101–6101, a 62.8 ms pulsar in IGR J11014–6103, a hard X-ray source with a jet and a cometary tail that strongly suggests it is moving away from the center of the supernova remnant (SNR) MSH 11–61A at $v > 1000 \text{ km s}^{-1}$. Two *XMM-Newton* observations were obtained with the EPIC pn in small window mode, resulting in the measurement of its spin-down luminosity $\dot{E} = 1.36 \times 10^{36} \text{ erg s}^{-1}$, characteristic age $\tau_c = 116 \text{ kyr}$, and surface magnetic field strength $B_s = 7.4 \times 10^{11} \text{ G}$. In comparison to τ_c , the 10–30 kyr age estimated for MSH 11–61A suggests that the pulsar was born in the SNR with initial period in the range $54 \leq P_0 \leq 60 \text{ ms}$. PSR J1101–6101 is the least energetic of the 15 rotation-powered pulsars detected by *INTEGRAL*, and has a high efficiency of hard X-ray radiation and jet power. We examine the shape of the cometary nebula in a *Chandra* image, which is roughly consistent with a bow shock at the velocity inferred from the SNR age and the pulsar's \dot{E} . However, its structure differs in detail from the classic bow shock, and we explore possible reasons for this.

Key words: ISM: individual objects (MSH 11–61A, G290.1–0.8) – pulsars: individual (PSR J1101–6101, PSR J1105–6107) – stars: neutron – X-rays: individual (IGR J11014–6103)

1. INTRODUCTION

IGR J11014–6103 was discovered as a hard X-ray (20–100 keV) source in *INTEGRAL* observations of the Galactic plane (Bird et al. 2010). *Chandra* and *XMM-Newton* images show that it has a complex X-ray morphology (Pavan et al. 2011; Tomsick et al. 2012; Pavan et al. 2014), consisting of a point source, a cometary pulsar wind nebula (PWN) extending 1/2 northeast of the point source, an apparent ≈ 5.5 long jet that is oriented perpendicular to the PWN, and a faint counterjet. The PWN points back to the center of the supernova remnant (SNR) MSH 11–61A (=G290.1–0.8), and its shape and distance from the SNR suggest that the pulsar was born there and kicked with high velocity (Tomsick et al. 2012). The X-ray PWN is associated with the radio source MGPS-2 J110149–610104 detected at 843 MHz (Pavan et al. 2011). Further mapping with the Australia Telescope Compact Array at 2 GHz revealed that the radio source has a bow-shock morphology similar to that of the X-rays (Pavan et al. 2014).

The highly collimated, ≈ 5.5 long X-ray jet most likely parallels the rotation axis of the pulsar, which is therefore oriented nearly perpendicular to the velocity vector. With these properties, IGR J11014–6103 resembles the Guitar Nebula associated with the high velocity pulsar PSR B2224+65 (Hui & Becker 2007; Hui et al. 2012; Johnson & Wang 2010). The twisted jet (and faint counterjet) of IGR J11014–6103 were modeled by Pavan et al. (2014) as a precessing, ballistic outflow emitting synchrotron radiation.

MSH 11–61A is a mixed-morphology SNR whose centrally bright, thermal X-ray emission observed by the *Advanced Satellite for Cosmology and Astrophysics* (*ASCA*) was analyzed by Slane et al. (2002) using two evolutionary models: thermal

conduction and cloudy ISM. The results are that the SNR is 10–20 kyr old and is at a distance of 8–11 kpc. Since PSR J1101–6101 is 11'9 from the center of MSH 11–61A, the evolutionary model constraints imply a tangential velocity of $v_{\perp} = 2400 \text{ km s}^{-1}$ and 2900 km s^{-1} for the thermal conduction and cloudy ISM models, respectively. (Age and distance are correlated in these models.) If this scenario is correct, PSR J1101–6101 would be the highest velocity pulsar known. However, Reynoso et al. (2006) measured a smaller distance of $7 \pm 1 \text{ kpc}$ to MSH 11–61A from H I 21 cm absorption. Using *XMM-Newton* and *Chandra* data, Garcia et al. (2012) derived an age range for MSH 11–61A of 10–30 kyr. With these revisions, the pulsar's kick velocity is still $> 800 \text{ km s}^{-1}$, an exceptional value compared, e.g., to the mean two-dimensional velocity of $307 \pm 47 \text{ km s}^{-1}$ for young pulsars (Hobbs et al. 2005).

2. OBSERVATIONS AND RESULTS

2.1. Pulsar Discovery and Timing

We made two *XMM-Newton* timing observations of IGR J11014–6103 separated by 322 days. The EPIC pn CCD was operated in small window mode, which has a 5.7 ms sampling time. The two EPIC MOS detectors were used in full frame mode to image the entire PWN and jet. This Letter reports only the timing results from the pn CCD. Table 1 is a log of the pn observations, indicating the net useable exposure time (elapsed, i.e., not reduced for dead-time), and the measured signal. The first observation was 44 ks long, but its final 6 ks were contaminated by high radiation background near perigee; thus, we use only the first 38 ks. The second observation was a clean 36.5 ks, and required no filtering.

Table 1
XMM-Newton Timing Observations of PSR J1101–6101

Instr/Mode	ObsID	Date (UT)	Date (MJD)	Exp (s)	Counts ^a	Frequency ^b (Hz)	Z_1^2
EPIC-pn/SW	0722600101	2013 Jul 21	56494.033	38000	2110	15.9235473(14)	123.5
EPIC-pn/SW	0740880201	2014 Jun 8	56816.645	36476	1997	15.9234868(19)	68.5

Notes.

^a Background subtracted source counts in the 0.5–10 keV band from a 15'' radius aperture.

^b 1σ uncertainty in parentheses.

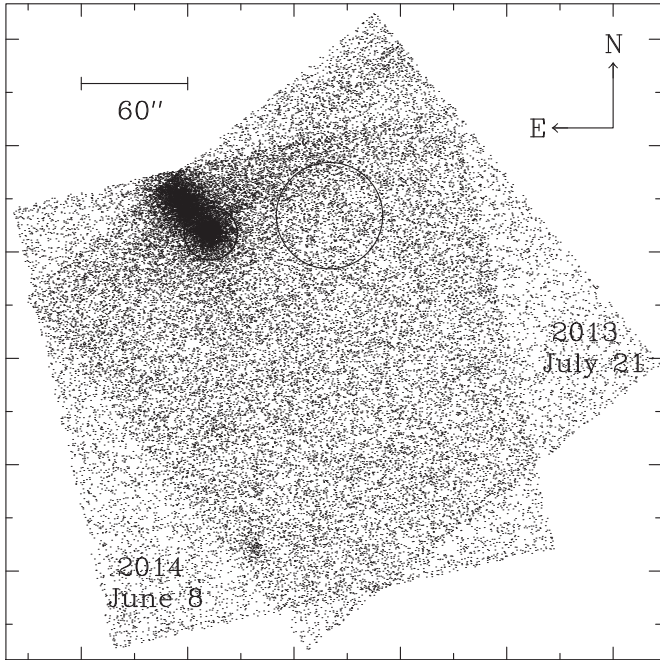


Figure 1. Two EPIC pn small window (4.3×4.3) images of IGR J11014–6103 listed in Table 1. Extraction regions are the small circle (15'' radius) for PSR J1101–6101 and the large circle (30'' radius) for background.

Events in the 0.5–10 keV band were selected from a circle of radius 15'' around the point source. This choice was a compromise between maximizing the counts extracted from the pulsar and minimizing contamination from the adjacent bow-shock nebula and jet. Figure 1 shows the two images superposed, with the extraction circle for the pulsar and another circle used for background estimation. The photon arrival times were transformed to barycentric dynamical time using the *Chandra* measured position of the point source (Tomsick et al. 2012). The Z_1^2 test (Rayleigh test; Strutt 1880; Buccheri et al. 1983) was used to search for pulsations, and a single, highly significant peak was found in each observation at a period of 62.8 ms. The Z_1^2 periodograms are shown in Figure 2, where the peak values are 123.5 and 68.5. Noise power S is distributed as $0.5 e^{-S/2}$, and the number of independent trials in a search to the Nyquist frequency is $\approx 3 \times 10^6$. This leads to negligible probabilities of 5×10^{-21} and 4×10^{-9} , respectively, that the two detections are false. One-sigma uncertainties in the peak frequencies were estimated from the range corresponding to $Z_1^2(\max) - 1$ around the peak. The significant change in frequency results in a measurement of its derivative with 6% precision. Further examination of the radio timing data reported by Tomsick et al. (2012) does not reveal a signal; thus, PSR J1101–6101 remains radio quiet to the same limit derived in Tomsick et al. (2012).

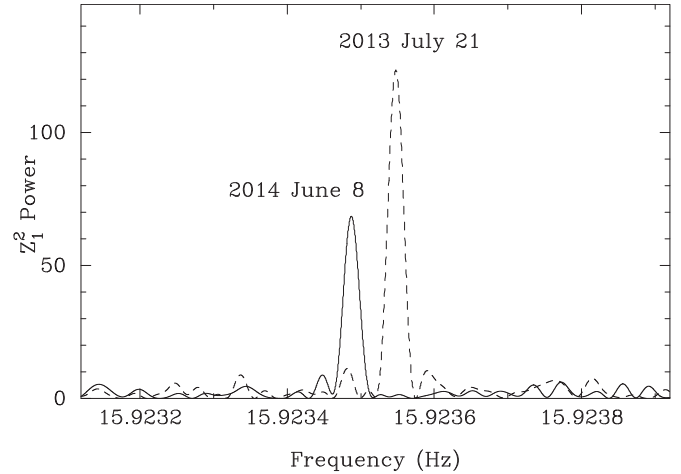


Figure 2. Z_1^2 periodograms from the two XMM-Newton timing observations listed in Table 1. The change in frequency corresponds to $\dot{f} = (-2.17 \pm 0.13) \times 10^{-12} \text{ s}^{-2}$.

Table 2
Timing Parameters for PSR J1101–6101

Parameter	Value
R.A. (J2000.0) ^a	11 ^h 01 ^m 44 ^s .96
Decl. (J2000.0) ^a	−61°01′39″.6
Epoch (MJD TDB) ^b	56494.00000012
Frequency ^c , f	$15.9235474(14) \text{ s}^{-1}$
Frequency derivative ^c , \dot{f}	$(-2.17 \pm 0.13) \times 10^{-12} \text{ s}^{-2}$
Period ^c , P	$0.062800077(6) \text{ s}$
Period derivative ^c , \dot{P}	$(8.56 \pm 0.51) \times 10^{-15}$
Range of dates (MJD)	56494–56817
Spin-down luminosity, \dot{E}	$1.36 \times 10^{36} \text{ erg s}^{-1}$
Characteristic age, τ_c	116 kyr
Surface dipole magnetic field, B_s	$7.4 \times 10^{11} \text{ G}$

Notes.

^a *Chandra* position from Tomsick et al. (2012).

^b Epoch of phase zero in Figure 3.

^c 1σ uncertainty in parentheses.

Table 2 lists the derived dipole spin-down parameters of PSR J1101–6101, including the spin-down luminosity $\dot{E} = -4\pi^2 I f \dot{f} = 1.36 \times 10^{36} \text{ erg s}^{-1}$, the characteristic age $\tau_c \equiv |f/2\dot{f}| = 116 \text{ kyr}$, and the surface dipole magnetic field strength $B_s = 3.2 \times 10^{19} (P\dot{P})^{1/2} \text{ G} = 7.4 \times 10^{11} \text{ G}$. An important caveat is the possibility that an intervening glitch may have biased the measurement of \dot{f} . The fractional change in frequency over 322 days is $\Delta f/f = -3.8 \times 10^{-6}$. This can be compared to the largest glitches in the Vela pulsar, which have $\Delta f/f \sim 2 \times 10^{-6}$ and a mean recurrence time of $\approx 3 \text{ yr}$ (Espinoza et al. 2011). If PSR J1101–6101 glitched between the epochs of our observations, it is possible that its spin-down

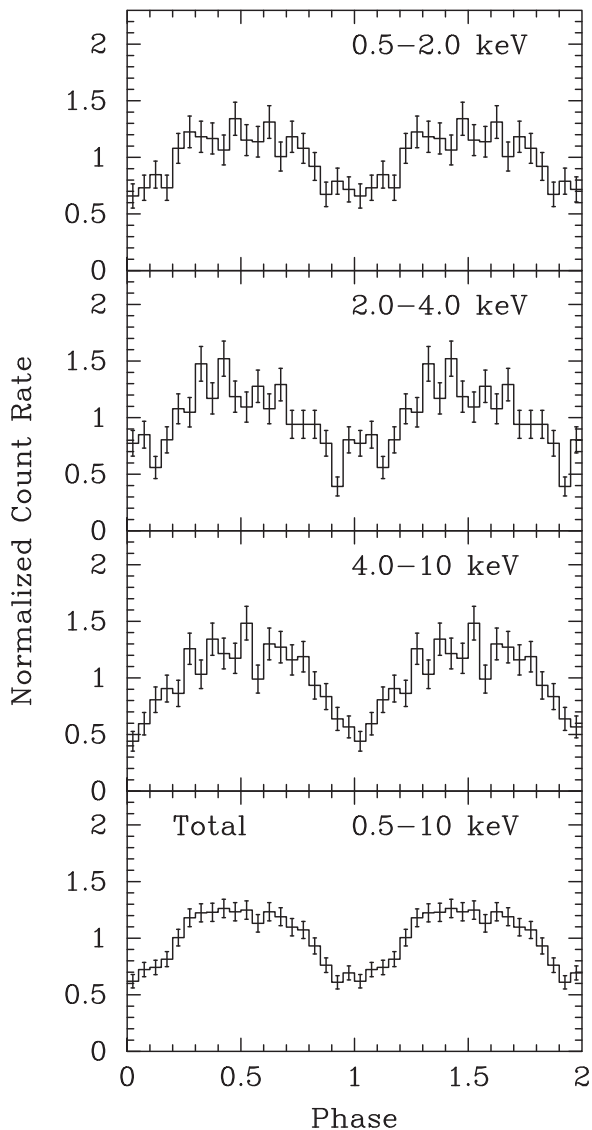


Figure 3. Energy-dependent pulse profiles of PSR J1101–6101 from the two *XMM-Newton* timing observations combined. They are background subtracted and normalized to 1. The phase between the two observations was adjusted to align them.

rate has been underestimated by as much as $\sim 50\%$. However, PSR J1101–6101 is not likely to be as active as the Vela pulsar, which is a uniquely strong and frequent glitcher. In any case, our main conclusions would not be changed by a $\sim 50\%$ revision in age or spin-down power.

The difference in peak Z_1^2 values of the two observations, after scaling for exposure time, is not great enough to claim that the pulsed fraction has changed. The variance in measured power as a function of intrinsic power was treated by Groth (1975), and is summarized in Figure 1 of that paper (with the difference that Groth’s power is actually our $Z_1^2/2$). The figure shows, for example, that if the true power is $Z_1^2 = 100$, then there is a 16% chance that the measured power will be >120 , and a 5% chance that it will be <68 .

We used the timing parameters to combine the pulse profiles of the two observations, adjusting their relative phase to maximize Z_1^2 in the combined data. The folded light curves in a range of energies between 0.5 and 10 keV are shown in Figure 3, where they are background-subtracted and normalized to 1 in each energy band. The single-peaked pulse shape

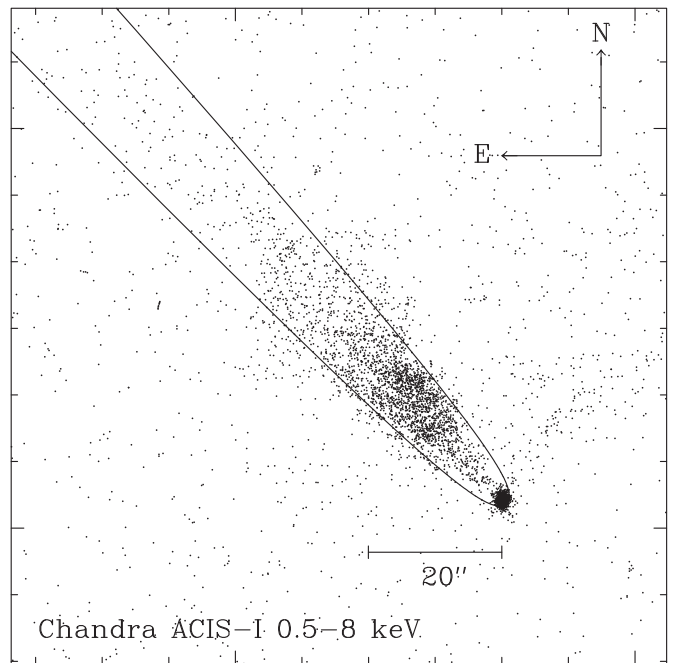


Figure 4. *Chandra* image of PSR J1101–6101 and its PWN from the 49.4 ks observation of Pavan et al. (2014). Superposed is the Wilkin (1996) equation of the contact discontinuity between the shocked pulsar wind and the shocked ISM, fitted by eye. The parameters are the position angle of motion, 223° , and the radius of the apex, or stagnation point, which is $r_0 = 7.9 \times 10^{16} d_7$ cm ($0''.75$) from the pulsar. The inclination angle i of the velocity vector with respect to the plane of the sky is assumed to be 0° .

and its phasing appears to be independent of energy, while the pulsed fraction increases from $\approx 35\%$ at the lowest energy to $\approx 50\%$ at the highest. However, the pulsed fractions shown in Figure 3 are definitely lower limits, as the source extraction circle includes an unknown number of counts from the PWN to the northeast and, to a lesser extent, from the jet, while the circle used for background subtraction (Figure 1) does not correct for this contamination. Although the effect is difficult to quantify, it probably accounts for the apparent increase in pulsed fraction with energy in Figure 3, as the PWN has a softer spectrum than the pulsar ($\Gamma_{\text{PWN}} = 1.9 \pm 0.1$, $\Gamma_{\text{PSR}} = 1.1 \pm 0.2$; Pavan et al. 2014). The intrinsic pulsed fraction is therefore likely to be $\geq 50\%$ at all energies. In support of this interpretation, we find that when we decrease the radius of the extraction aperture from $15''$ to $10''$, the pulsed fraction becomes $\approx 50\%$ at all energies.

2.2. Bow-Shock Fitting

Knowing the spin-down power of PSR J1101–6101, we reexamine the structure of its apparent bow-shock nebula to obtain an independent estimate of the space velocity of the pulsar. For this purpose, the higher resolution of *Chandra* is more useful than *XMM-Newton*. Our analysis here follows and extends that of Tomsick et al. (2012), who used a 5 ks *Chandra* observation (ObsID 12420) with the Advanced CCD Imaging Spectrometer. Here, we revisit the 49.4 ks *Chandra* ACIS-I observation (ObsID 13787) that was presented by Pavan et al. (2014). Figure 4 shows the region of this image containing the pulsar and PWN, with each photon in the 0.5–8 keV band indicated by a dot. Because the pulsar was located only $0''.8$ from the optical axis, the spatial resolution for the pulsar and its immediate surroundings is nearly optimal.

For the case of an isotropic wind from a star moving supersonically through a uniform ISM, Wilkin (1996) derived

an analytic expression for the surface of contact discontinuity between the shocked pulsar wind and the shocked ISM using momentum conservation, $r(\theta) = r_0 \csc \theta [3(1 - \theta \cot \theta)]^{1/2}$, where θ is the polar angle with respect to direction of motion, $r(\theta)$ is the distance of the surface from the star, and r_0 is the stagnation radius, the distance of the apex of the surface from the pulsar. The shape of the contact discontinuity is thus parameterized entirely in terms of r_0 , which in turn is determined in this case by the pulsar wind power, assumed to be $\approx \dot{E}$, the velocity v of the pulsar, and the ambient density ρ of the ISM, using momentum balance:

$$r_0 = \left(\frac{\dot{E}}{4\pi \rho v^2 c} \right)^{1/2}. \quad (1)$$

The assumption we make in graphing the model curve in Figure 4 is that the X-ray emission comes from the shocked pulsar wind, which is bounded by the contact discontinuity and the termination shock interior to it. Therefore, r_0 was chosen by eye so that the curve surrounds the bulk of the emission trailing the pulsar. It was assumed that the pulsar is moving nearly in the plane of the sky ($i = 0^\circ$), both because of the narrow opening angle of the nebula, and the evidently large tangential velocity. The parameters of the curve are $r_0 = 7.9 \times 10^{16} d_7 \text{ cm}$ ($0''.75$), where d_7 is the distance in units of 7 kpc, and the position angle of the motion, 223° . Similar results were obtained by Tomsick et al. (2012). Now substituting the values of r_0 and \dot{E} , Equation (1) is reduced to $v_\perp = 500 d_7^{-1} n_{0.1}^{-1/2} \text{ km s}^{-1}$, where $n_{0.1}$ is the ISM hydrogen density in units of 0.1 cm^{-3} . This velocity is ~ 2 – 4 times less than the estimates from the SNR age, but they can be reconciled if the local density is $\sim 0.01 \text{ cm}^{-3}$. The result is largely unaffected by the unknown angle i , because any inclination of the model would broaden the apparent opening angle of the bow shock, which would then have to be reduced by decreasing r_0 , thus increasing v .

However, before giving this analysis too much credence, note that there are at least two discrepancies between the simple model and the detailed properties of the data. First, there is no evidence of emission from the apex of the shocked wind, which theoretically should be the brightest part of the nebula. In fact, there is no excess emission within $\approx 3''$ of the pulsar, a zone that is entirely consistent with a single point source (Tomsick et al. 2012; Pavan et al. 2014). Second, the faint X-ray emission just behind the pulsar does not in fact follow the model curve, but is confined to a narrower cone, while the brightest regions filling the curve are $13''$ – $26''$ behind the pulsar. The appearance is of a diverging flow getting brighter with distance from the pulsar, rather than a collimated one that is fading. Similar phenomena have been noted in the X-ray images of other pulsar tails; the possible implications will be discussed in Section 3.3.

3. DISCUSSION

3.1. Distance and Associations

Various estimates of the distance to MSH 11–61A were reviewed by Filipović et al. (2005), who concluded from their own CO maps that $d = 7$ – 8 kpc, in agreement with 6.9 kpc from optical emission-line velocities (Rosado et al. 1996), and 7 ± 1 kpc from H I 21 cm absorption (Reynoso et al. 2006). These are all kinematic distances, unlike the X-ray modelling of Slane et al. (2002), who derived $d = 8$ – 11 kpc. We have adopted 7 kpc as the most likely distance.

Since the characteristic age of PSR J1101–6101 is greater than all estimates of the age of MSH 11–61A, we can assume that it was born in the SNR and estimate its birth period P_0 from the relation

$$T = \frac{P}{(n-1)\dot{P}} \left[1 - \left(\frac{P_0}{P} \right)^{n-1} \right],$$

where $n \equiv f\ddot{f}/\dot{f}^2$ is the braking index. Most pulsars have $2 < n < 3$ (Livingstone et al. 2007). For this range, and letting T be the 10–30 kyr age of the SNR, we find $54 \leq P_0 \leq 60$ ms.

PSR J1101–6101 should not be confused with PSR J1105–6107, a 63.2 ms pulsar with $\dot{E} = 2.5 \times 10^{36} \text{ erg s}^{-1}$ and $\tau_c = 63$ kyr that is $23'$ southeast of MSH 11–61A. Kaspi et al. (1997) considered the possibility that PSR J1105–6107 was born in MSH 11–61A, although PSR J1101–6101 is now a more compelling association. The dispersion measure of 271 pc cm^{-3} to PSR J1105–6107 converts to a distance of 5.0 kpc according to the Galactic electron density model of Cordes & Lazio (2002). The corresponding free-electron column of $N_e = 8.4 \times 10^{20} \text{ cm}^{-2}$, assuming a typical ionized fraction of 0.1 (He et al. 2013), is accompanied by a neutral column of $N_H \approx 8.4 \times 10^{21} \text{ cm}^{-2}$, which is consistent with the X-ray measured $N_H = 8 \times 10^{21} \text{ cm}^{-2}$ to IGR J11014–6103 (Tomsick et al. 2012; Pavan et al. 2014). X-ray measurements of N_H to MSH 11–61A are somewhat contradictory, ranging from $(4.3$ – $6.2) \times 10^{21} \text{ cm}^{-2}$ (Garcia et al. 2012) to $(1.3 \pm 0.1) \times 10^{22} \text{ cm}^{-2}$ (Slane et al. 2002). Allowing for this ambiguity, all three objects are probably consistent with being at the same distance.

PSR J1105–6107 is not detected in X-rays. Using archival *Chandra* observations totaling 23.7 ks (ObsIDs 2780 and 4380), we set a 3σ upper limit of $8 \times 10^{-15} \text{ erg cm}^{-2} \text{ s}^{-1}$ on its 2–10 keV flux, corresponding to $L_X/\dot{E} < 2 \times 10^{-5} d_7^2$. This is close to the minimum of the distribution of similarly aged pulsars (Kargaltsev & Pavlov 2008). A previously claimed detection of this pulsar using *ASCA* (Gotthelf & Kaspi 1998) may have instead detected a neighboring star that is present in the *Chandra* images.

3.2. Energetics

With $\dot{E} = 1.36 \times 10^{36} \text{ erg s}^{-1}$, PSR J1101–6101 is the least energetic of the 15 rotation-powered pulsars detected by *INTEGRAL* (for the full set see Mattana et al. 2009; Renaud et al. 2010; Gotthelf et al. 2011; Halpern et al. 2012). These are among the most energetic pulsars, comprising half of all those known with $\dot{E} \geq 3.7 \times 10^{36} \text{ erg s}^{-1}$, the latter value belonging to PSR B1951+32, which has a characteristic age of 107 kyr and was previously the least energetic of the *INTEGRAL* pulsars.

The 20–100 keV flux of IGR J11014–6103 is $8.7 \times 10^{-12} \text{ erg cm}^{-2} \text{ s}^{-1}$ (Bird et al. 2010), corresponding to a luminosity of $5.1 \times 10^{34} d_7^2 \text{ erg s}^{-1}$ that is 4% of the spin-down luminosity of PSR J1101–6101. This exceeds the combined 2–10 keV flux of the pulsar, the PWN, and the jet as measured by *Chandra*, which total $1.8 \times 10^{-12} \text{ erg cm}^{-2} \text{ s}^{-1}$ (Pavan et al. 2014), or 0.8% of the spin-down flux. The flat spectrum of the pulsar must extend into the hard X-rays, where it is responsible for most of the 20–100 keV flux. Using equipartition arguments, Pavan et al. (2014) estimated that a minimum power of $2 \times 10^{35} \text{ erg s}^{-1}$ is needed for the jet, which is 14% of the spin-down luminosity. This is important evidence that a large part of a pulsar's spin-down power can be focused into a narrow polar jet, a fraction therefore not available to power a bow shock.

3.3. Structure of the PWN

The absence of X-rays from the head of the putative bow shock is the principal challenge to the model in which the termination shock of the pulsar is the cause of the PWN emission. A dark region between the termination shock and the contact discontinuity is difficult to understand in the context of shock acceleration. For reasonable values of the magnetic field strength ($B \sim 10^{-4}$ G) and X-ray emitting electron energy ($E \sim 10^{13}$ eV), the gyroradius, $r_g = 3 \times 10^{14} E_{13} B_{-4}^{-1}$ cm, is much smaller than the stagnation radius, $r_0 = 7.9 \times 10^{16} d_7$ cm. So the particles should be easily confined and accelerated.

The cavity *interior* to the termination shock should be dark, so that any emission from around it should be limb brightened. The termination shock will close behind the pulsar at a distance r_1 , which is larger than its forward radius, $\approx r_0$. In analytic and numerical models at low Mach number \mathcal{M} , the relation between these radii is $r_1/r_0 \approx \gamma^{1/2} \mathcal{M}$, where γ is the adiabatic index of the ambient medium, is usually 5/3 (Bucciantini 2002). However, numerical models at high \mathcal{M} show that this ratio saturates at about 5 (Gaensler et al. 2004). While an area $\approx 12''$ long behind PSR J1101–6101 is relatively dim in X-rays, the emission there looks like a narrow cone rather than the expected limb-brightened bow shock. Nevertheless, if we ignore this detail and assume that this is the region bounded by the termination shock, then $r_1/r_0 \approx 12''/0.75$ and $\mathcal{M} \approx 12.4$. The sound speed in the warm (8000 K) phase of the ISM is ≈ 13 km s $^{-1}$, which then implies a pulsar velocity of only ≈ 165 km s $^{-1}$, at odds with the other estimates. Only if the ISM is hot ($\sim 10^6$ K) do we get $v \approx 1900$ km s $^{-1}$. But this would require reducing the ambient density drastically to have a reasonable pressure, which would be inconsistent with the results from Equation (1).

Gaensler et al. (2004) suggested that the “tongue” of emission just behind PSR J1747–2958 (the Mouse) and others represents the surface of the termination shock. But these are bright regions, which contradicts the theory that there should be no emission interior to the termination shock. In the case of PSR J1101–6101, this region is at least underluminous, although not limb-brightened. Another system like PSR J1101–6101 in which trailing emission brightens with distance from the pulsar is PSR J0357+3205 (De Luca et al. 2011, 2013; Marelli et al. 2013). The difficulties in modeling that tail as a synchrotron emitting bow shock led the authors to propose shocked-heated bremsstrahlung emission instead. But that model requires a hot ISM phase with an extraordinarily large pressure.

In several pulsar tails, radio and X-ray brightness are anticorrelated, with the radio increasing with distance from the pulsar (Ng et al. 2010). This is the case for PSR J1101–6101 as well (Pavan et al. 2014). However, it is not clear if this phenomenon relates to why the region closest to PSR J1101–6101 is underluminous in both radio and X-ray.

Considering that the spin axis of PSR J1101–6101 may be orthogonal to its velocity vector, with a large fraction of the spin-down power going into the jet, one may ask if the remaining wind is primarily polar or equatorial, and how that would affect the structure of the PWN. However, numerical models with anisotropic pulsar winds, including an equatorial one, do not significantly change the shape of the termination shock (Vigelius et al. 2007). So far, no model within the framework of ideal MHD appears to explain the features of our data and others.

An alternative model (Romanova et al. 2005) in which particles are accelerated by magnetic reconnection outside the

speed-of-light cylinder results in a fast “magnetotail” behind the pulsar, which may contain a large fraction of the energy of the pulsar wind and extend to large distances. An interesting feature of this model is the flared “trumpet” shape of the magnetotail (Figure 4 of Romanova et al. 2005), which does in fact resemble the PWN of PSR J1101–6101. An approximation for the radiation length of the magnetotail is

$$r \approx 15 P^2 \left(\frac{B_s}{10^{12} \text{ G}} \right)^{-1} \left(\frac{n}{\text{cm}^{-3}} \right)^{-1} \left(\frac{v}{1000 \text{ km s}^{-1}} \right)^{-2} \text{ pc}.$$

Assuming $n = 0.03$ cm $^{-3}$ and $v = 1000$ km s $^{-1}$, this reduces to $r \approx 2.7$ pc (1/3), the actual length of the PWN. However, the authors only investigated the case in which the magnetic axis, the rotation axis, and the velocity are all parallel, while there is good reason to believe that the rotation axis of PSR J1101–6101 is nearly orthogonal to its velocity because of the orientation of the jet. It is not clear if a more realistic geometry would generate undesirable, nonaxisymmetric features.

4. CONCLUSIONS

We discovered the 62.8 ms pulsar PSR J1101–6101 in IGR J11014–6103. Its spin-down luminosity of 1.36×10^{36} erg s $^{-1}$ is the lowest among the 15 rotation-powered pulsars detected by *INTEGRAL*, and an order-of-magnitude less than what was anticipated from the X-ray luminosity of PSR J1101–6101 (Pavan et al. 2014). However, there is a large scatter among pulsars in efficiency of X-ray emission. Its 116 kyr characteristic age is consistent with an origin in MSH 11–61A for any reasonable value of the braking index or SNR age, with its birth period close to its present period.

The velocity of the pulsar inferred from fitting the shape of its cometary nebula is compatible with estimates of 800–2400 km s $^{-1}$ from the SNR age and distance, if the density of the ambient ISM is < 0.1 cm $^{-3}$. The density should be this low if PSR J1101–6101 is within a cavity blown by previous stellar winds or supernovae. Because the structure of the nebula differs in important details from a basic bow-shock geometry, we are not secure in making quantitative estimates of velocity and density from such a simple model. Interestingly, however, an alternative magnetotail theory would require similar velocity and density.

REFERENCES

- Bird, A. J., Bazzano, A., Bassani, L., et al. 2010, *ApJS*, **186**, 1
 Bucciantini, N. 2002, *A&A*, **387**, 1066
 Bucccheri, R., Bennett, K., Bignami, G. F., et al. 1983, *A&A*, **128**, 245
 Cordes, J. M., & Lazio, T. J. W. 2002, arXiv:astro-ph/0207156
 De Luca, A., Marelli, M., Mignani, R. P., et al. 2011, *ApJ*, **733**, 104
 De Luca, A., Mignani, R. P., Marelli, M., et al. 2013, *ApJL*, **765**, L19
 Espinoza, C. M., Lyne, A., Stappers, B. W., & Kramer, M. 2011, *MNRAS*, **414**, 1679
 Filipović, M. D., Payne, J. L., & Jones, P. A. 2005, *SerAJ*, **170**, 47
 Gaensler, B. M., van der Swaluw, E., Camilo, F., et al. 2004, *ApJ*, **616**, 383
 Garcia, F., Combi, J. A., Albacete-Colombo, J. F., et al. 2012, *A&A*, **546**, A91
 Gotthelf, E. V., Halpern, J. P., Terrier, R., & Mattana, F. 2011, *ApJL*, **729**, L16
 Gotthelf, E. V., & Kaspi, V. M. 1998, *ApJL*, **497**, L29
 Groth, E. J. 1975, *ApJS*, **29**, 285
 Halpern, J. P., Gotthelf, E. V., & Camilo, F. 2012, *ApJL*, **753**, L14
 He, C., Ng, C.-Y., & Kaspi, V. M. 2013, *ApJ*, **768**, 64
 Hobbs, G., Lorimer, D. R., Lyne, A. G., & Kramer, M. 2005, *MNRAS*, **360**, 974
 Hui, C. Y., & Becker, W. 2007, *A&A*, **467**, 1209
 Hui, C. Y., Huang, R. H. H., Trepl, L., et al. 2012, *ApJ*, **747**, 74
 Johnson, S. P., & Wang, Q. D. 2010, *MNRAS*, **408**, 1216

- Kargaltsev, O., & Pavlov, G. G. 2008, in AIP Conf. Proc. 983, 40 Years of Pulsars: Millisecond Pulsars, Magnetars and More, ed. C. Bassa, Z. Wang, A. Cumming, & V. M. Kaspi (Melville, NY: AIP), 171
- Kaspi, V., Bailes, M., Manchester, R. N., et al. 1997, *ApJ*, 485, 820
- Livingstone, M. A., Kaspi, V. M., Gavriil, F. P., et al. 2007, *Ap&SS*, 308, 317
- Marelli, M., De Luca, A., Salvetti, D., et al. 2013, *ApJ*, 765, 36
- Mattana, F., Götz, D., Terrier, R., Renaud, M., & Falanga, M. 2009, in AIP Conf. Proc. 1126, Simbol-X: Focusing on the Hard X-ray Universe, ed. J. Rodriguez & P. Forrando (Melville, NY: AIP), 259
- Ng, C.-Y., Gaensler, B. M., Chatterjee, S., & Johnston, S. 2010, *ApJ*, 712, 596
- Pavan, L., Bordas, P., Pühlhofer, G., et al. 2014, *A&A*, 562, A122
- Pavan, L., Bozzo, E., Pühlhofer, G., et al. 2011, *A&A*, 533, A74
- Renaud, M., Marandon, V., Gotthelf, E. V., et al. 2010, *ApJ*, 716, 663
- Reynoso, E. M., Johnston, S., Green, A. J., et al. 2006, *MNRAS*, 369, 416
- Romanova, M. M., Chulsky, G. A., & Lovelace, R. V. E. 2005, *ApJ*, 630, 1020
- Rosado, M., Ambrocio-Cruz, P., Le Coarer, E., & Marcelin, M. 1996, *A&A*, 315, 243
- Slane, P., Smith, R. K., Hughes, J. P., & Petre, R. 2002, *ApJ*, 564, 284
- Strutt, J. W. 1880, *PMag*, 10, 73
- Tomsick, J. A., Bodaghee, A., Rodriguez, J., et al. 2012, *ApJL*, 750, L39
- Vigelius, M., Melatos, A., Chatterjee, S., Gaensler, B. M., & Ghavamian, P. 2007, *MNRAS*, 374, 793
- Wilkin, F. P. 1996, *ApJL*, 459, L31

INITIAL RESULTS FROM *NuSTAR* OBSERVATIONS OF THE NORMA ARM

ARASH BODAGHEE^{1,2}, JOHN A. TOMSICK¹, ROMAN KRIVONOS¹, DANIEL STERN³, FRANZ E. BAUER^{4,5,6},
FRANCESCA M. FORNASINI⁷, NICOLAS BARRIÈRE¹, STEVEN E. BOGGS¹, FINN E. CHRISTENSEN⁸,
WILLIAM W. CRAIG^{1,9}, ERIC V. GOTTHELF¹⁰, CHARLES J. HAILEY¹⁰, FIONA A. HARRISON¹¹, JAESUB HONG¹²,
KAYA MORI¹⁰, AND WILLIAM W. ZHANG¹³

¹ Space Sciences Laboratory, 7 Gauss Way, University of California, Berkeley, CA 94720, USA

² Georgia College and State University, CBX 082, Milledgeville, GA 31061, USA

³ Jet Propulsion Laboratory, California Institute of Technology, Pasadena, CA 91109, USA

⁴ Instituto de Astrofísica, Facultad de Física, Pontificia Universidad Católica de Chile, 306, Santiago 22, Chile

⁵ Millennium Institute of Astrophysics, Vicuña Mackenna 4860, 7820436 Macul, Santiago, Chile

⁶ Space Science Institute, 4750 Walnut Street, Suite 205, Boulder, CO 80301, USA

⁷ Astronomy Department, University of California, Berkeley, CA 94720, USA

⁸ DTU Space, National Space Institute, Technical University of Denmark, Elektrovej 327, DK-2800 Lyngby, Denmark

⁹ Lawrence Livermore National Laboratory, Livermore, CA 94550, USA

¹⁰ Columbia Astrophysics Laboratory, Columbia University, New York, NY 10027, USA

¹¹ Cahill Center for Astronomy and Astrophysics, California Institute of Technology, Pasadena, CA 91125, USA

¹² Department of Astronomy, Harvard University, 60 Garden Street, Cambridge, MA 02138, USA

¹³ NASA Goddard Space Flight Center, Greenbelt, MD 20771, USA

Received 2014 February 12; accepted 2014 June 30; published 2014 July 28

ABSTRACT

Results are presented for an initial survey of the Norma Arm gathered with the focusing hard X-Ray Telescope *NuSTAR*. The survey covers 0.2 deg² of sky area in the 3–79 keV range with a minimum and maximum raw depth of 15 ks and 135 ks, respectively. Besides a bright black-hole X-ray binary in outburst (4U 1630–47) and a new X-ray transient (*NuSTAR* J163433–473841), *NuSTAR* locates three sources from the *Chandra* survey of this region whose spectra are extended above 10 keV for the first time: CXOU J163329.5–473332, CXOU J163350.9–474638, and CXOU J163355.1–473804. Imaging, timing, and spectral data from a broad X-ray range (0.3–79 keV) are analyzed and interpreted with the aim of classifying these objects. CXOU J163329.5–473332 is either a cataclysmic variable or a faint low-mass X-ray binary. CXOU J163350.9–474638 varies in intensity on year-long timescales, and with no multi-wavelength counterpart, it could be a distant X-ray binary or possibly a magnetar. CXOU J163355.1–473804 features a helium-like iron line at 6.7 keV and is classified as a nearby cataclysmic variable. Additional surveys are planned for the Norma Arm and Galactic Center, and those *NuSTAR* observations will benefit from the lessons learned during this pilot study.

Key words: binaries: general – novae, cataclysmic variables – stars: neutron – X-rays: binaries

Online-only material: color figures

1. INTRODUCTION

The Norma Arm is among the most active regions of massive star formation in the Milky Way (Bronfman et al. 2000). It is not surprising that this region is also densely populated with the evolutionary byproducts of massive stars, neutron stars (NSs) and black holes (BHs). Many of these compact objects belong to binary systems and accrete matter from a normal stellar companion. These systems are called X-ray binaries (XRBs) and they represent laboratories for studying the physics of matter subjected to extreme gravitational and electromagnetic potentials. Their numbers can be used to constrain rates of massive star formation (e.g., Antoniou et al. 2010), while their spatial distributions are important for studies of stellar evolution (e.g., Bodaghee et al. 2012b).

One advantage of surveying the Norma Arm is that it represents an intersection of molecular clouds, star-forming regions, and accreting compact objects, thereby providing X-ray source populations at various stages of evolution. These populations can then be compared with large populations residing in other active regions of the Galaxy such as the Galactic Center (Muno et al. 2009) and Carina Arm (Townsend et al. 2011).

Thus, the Norma Arm has been the subject of recent observing campaigns seeking to uncover its X-ray populations. In the soft X-rays ($\lesssim 10$ keV), the *Chandra* telescope discovered ~ 1100 sources in a 1.3 deg² section of this field. The largest source groups are cataclysmic variables (CVs), background active galactic nuclei (AGNs), and stars (flaring, foreground, or massive), with other source types represented in smaller numbers (e.g., XRBs, young massive clusters, and supernova remnants: Fornasini et al. 2014, submitted). In the hard X-rays, *International Gamma-Ray Astrophysics Laboratory (INTEGRAL)*; e.g., Bird et al. 2010; Krivonos et al. 2012) discovered a few dozen sources in the Norma Arm, almost all of which are XRBs.

With the advent of the hard X-ray focusing telescope *NuSTAR* (Harrison et al. 2013), it is now possible to map this region with unprecedented angular (18'' full-width-half-maximum, 58'' half-power diameter) and spectral resolution (400 eV) around 10 keV. This paper presents results from a *NuSTAR* survey of a small section of the Norma Arm that took place in 2013 February. Section 2 describes the analysis procedures employed on the *NuSTAR* data and on selected data from *Chandra*, as well as some of the challenges inherent in X-ray observations of this field. In Section 3, results from imaging, spectral, and timing analyses are presented for X-ray sources detected in the survey.

Table 1
Journal of *NuSTAR* Observations of the Norma Arm

Observation ID	Shorthand	Pointing R.A. (J2000)	Pointing Decl. (J2000)	Position Angle (deg)	Start Date (UTC)	Exposure Time (s)
40014001001	1	248.4829	−47.7204	160.15	2013-02-24 01:46:07	18407
40014002001	2	248.3623	−47.6444	160.15	2013-02-24 11:31:07	19497
40014003001	3	248.2407	−47.5669	160.13	2013-02-21 20:31:07	20846
40014004001	4	248.5977	−47.6374	160.12	2013-02-22 07:46:07	19440
40014005001	5	248.4775	−47.5622	160.13	2013-02-22 17:31:07	21241
40014006001	6	248.3529	−47.4868	160.14	2013-02-23 04:46:07	18959
40014007001	7	248.7099	−47.5554	160.14	2013-02-23 14:31:07	22640
40014008002	8	248.5845	−47.4826	160.12	2013-02-20 23:31:07	16573
40014009001	9	248.4670	−47.4038	160.12	2013-02-21 10:46:07	14653

Their implications on source classifications for these objects are discussed in Section 4.

2. OBSERVATIONS AND DATA ANALYSIS

2.1. *NuSTAR* Data

The *NuSTAR* data consist of nine pointings whose details are summarized in Table 1. These nine pointings are comprised of two focal plane modules A and B (FPMA and FPMB) each having a field-of-view (FOV) of $13' \times 13'$. To increase sensitivity, adjacent pointings were tiled with significant overlap ($\sim 50\%$) resulting in sky region covered by the survey of around 0.2 deg^2 ($0^\circ.4 \times 0^\circ.4$), centered at (J2000.0) R.A. = $16^{\text{h}}33^{\text{m}}47^{\text{s}}$ and decl. = $-47^\circ32'14''$. In Galactic coordinates, this is $l = 336^\circ7776$ and $b = 0^\circ1825$.

Data analysis relied on HEASoft 6.14 and the *NuSTAR* Data Analysis Software (NuSTARDAS 1.2.0¹⁴) with the latest calibration database files (CALDB: 2013 August 30). Raw event lists from FPMA and FPMB were reprocessed using nupipeline¹⁵ in five energy bands: 3–10 keV, 3–79 keV, 10–40 keV, 10–79 keV, and 40–79 keV.

2.1.1. Image Cleaning

Given the density of bright sources and the high level of diffuse background, the Norma Arm presents a number of unique challenges for *NuSTAR*. The first challenge is from the telescope mast, which allows photons to land on the detector without having passed through the focusing optics. These are known as stray-light photons (a.k.a. 0-bounce photons), which originate from bright sources situated a few degrees outside the FOV of each module. Fortunately, these pixels are easily modeled and excluded by creating polygonal region files in ds9 that correspond to the geometric patterns expected from stray light of known bright sources near the FOV. The main source of stray light for these Norma survey observations is IGR J16320–4751 (Tomsick et al. 2003; Rodriguez et al. 2006), a variable but persistent supergiant XRB located between $0^\circ.2$ and $0^\circ.5$ outside the FOV.

The second, and more daunting, challenge was that 4U 1630–47, a BH XRB, was undergoing an outburst, which means it was especially bright during our observations of this field (~ 0.3 Crab in 3–10 keV: Bodaghee et al. 2012a, see also King et al. 2014). When the source is outside the FOV, photons can still arrive on the detector modules without being properly focused. Such photons are called ghost-rays (a.k.a. 1-bounce

photons), and their pattern is not completely understood (Koglin et al. 2011; Harrison et al. 2013).

In order to generate a mosaic image of the entire field where such effects could be minimized, we created new event lists (and exposure maps) in which we excluded regions with pixels contaminated by either stray light or ghost rays. This was done by visually examining the event lists of each observation (showing only those pixels, binned in blocks of 4, with more than 20 counts) and creating a polygonal region file in ds9 that encompasses clusters of pixels (from both modules) on which ghost rays had fallen. By design, the regions were a few pixels wider than necessary to account for both the slightly different sky fields seen by each detector module and to account for the slight jitter due to the motion of the telescope mast. These cleaned event lists were used to generate an exposure-corrected mosaic image in the five energy bands listed above. Vignetting corrections were not applied to these mosaic images.

2.1.2. Systematic Offset of Detected Sources

We ran wavdetect on individual event lists, and on the mosaic images, in order to create lists of detected sources in each energy band. In all cases, we assumed: a point-spread function (PSF) with a constant full-width at half-maximum (FWHM) of $18''$ (Harrison et al. 2013); scale sizes of 1, 2, 4, and 8 pixels; and a threshold of 10^{-5} . This threshold implies around 1 spurious source per observation. For the mosaics, we used the cleaned (non-ghost-ray removed) images assuming a background map that mimics the observed low-frequency (i.e., large scale) ghost ray patterns with wavelet scales with characteristic sizes of 8–32 pixels (Slezak et al. 1994; Starck & Murtagh 1994; Vikhlinin et al. 1997). Each pixel is $2''$ wide, so the wavelet scales are $16''$ – $64''$, i.e., larger than the high-frequency scales expected for point sources. The lack of high-frequency scales in the background map leads to a poor modeling of the sharp edges and dark dips of the ghost ray pattern. This results in a large number of source detections that align with artifacts in the image, and we conclude that they are likely spurious.

We visually inspected the event lists and the mosaic images (in each band) searching for *NuSTAR*-detected sources that were coincident with *Chandra* sources (see Section 2.2). There are three *NuSTAR*-detected sources that have probable *Chandra* counterparts. The *NuSTAR*-derived positions show a systematic offset (i.e., with a similar direction and magnitude) with respect to the *Chandra* positions. In physical coordinates, this offset is $+1.98$ pixels ($3'.9$) and $+4.75$ pixels ($9'.5$) in the x and y directions, respectively, found by averaging the offsets of the *Chandra* sources. This is consistent with the expected performance from *NuSTAR* (Harrison et al. 2013). Therefore, we registered the mosaic images to the *Chandra*

¹⁴ http://heasarc.gsfc.nasa.gov/docs/nustar/analysis/nustardas_swguide_v1.5.pdf

¹⁵ <http://heasarc.gsfc.nasa.gov/docs/nustar/analysis>

Table 2
NuSTAR-detected Sources and Their Angular Separation from Likely *Chandra* Counterparts

Name	R.A. (deg)	Decl. (deg)	90% Confidence Radius	Detection Significance (σ)	Offset
CXOU J163329.5–473332	248.37254	–47.55894	7"9	8.3	1"9
CXOU J163350.9–474638	248.46158	–47.77642	13"0	15.0	4"1
CXOU J163355.1–473804	248.48046	–47.63520	7"0	8.7	2"7

Notes. Results for two other sources detected by *NuSTAR*, 4U 1630–47 and NuSTAR J163433–473841, are presented in separate papers (King et al. 2014; Tomsick et al. 2014).

sources by subtracting these offset values from the reference pixel. We reran `wavdetect` to determine a final source position, positional uncertainty (quoted at 90% confidence), and detection significance in the 3–79 keV band. These values are reported in Table 2.

2.1.3. Spectral and Timing Analyses

Source spectra and light curves were extracted from the cleaned event lists of each module using a 30"–radius circle centered on the *Chandra* position while the background count rates were taken from a 90"–radius circle on the same detector chip: away from the source extraction region, but with a similar background pattern. The effects of vignetting on exposure were accounted for in the response matrices and spectra. The spectra were fit in `Xspec` (Arnaud 1996) assuming Wilms et al. (2000) abundances and photo-ionization cross-sections of Verner et al. (1996).

While this extraction radius covers roughly 40% of the enclosed energy, the *NuSTAR* PSF has a relatively narrow peak (18" FWHM) superimposed on broad wings, which means source extraction radii wider than this (at the off-axis angles considered here) have the undesired result of adding more background relative to the gain in source counts. Results of the spectral analysis showed that the sources emitted few counts above $\gtrsim 20$ keV, and so the energy band used for *NuSTAR* timing and spectral analyses was restricted to 3–24 keV. All *NuSTAR* source spectra were binned to contain at least 20 net (i.e., background-subtracted) source counts and a minimum significance of 2σ .

2.2. Chandra Data

In 2011, *Chandra* observed a $\sim 2^\circ 0' \times 0^\circ 8'$ section of the Norma Arm, a subset of which is the $\sim 0^\circ 4' \times 0^\circ 4'$ *NuSTAR* survey region described in this paper. Of the ~ 1100 X-ray sources detected by Fornasini et al. (2014, submitted), we excluded all objects outside the 0.2 deg^2 *NuSTAR* survey region, and then rejected those whose ratio between net source counts in the 2–10 keV and 0.5–2 keV energy bands was less than 0.8. This yields a catalog of 22 relatively hard sources that are suitable low-energy X-ray counterpart candidates to sources detected at higher energies with *NuSTAR*.

Observations used in this study are ObsID 12532 and ObsID 12533. Reprocessing and reduction of this data relied on CIAO version 4.5. Spectra were extracted from each event list in the 0.3–10 keV band for a source region centered on the *Chandra* position (a circle of radius = 10"), and for a source-free background region (a rectangle with dimensions: $200'' \times 100''$) on the same detector chip. Spectral data were grouped to contain a minimum of 20 source + background counts per bin.

3. RESULTS

The flux map (counts map divided by the exposure map) of the broad-band energy range (3–79 keV) is presented in Figure 1. The surveying strategy, which tiled the pointings so that they contained significant overlap in their observed fields, as well as the redundancy of having two detector modules whose FOVs are slightly shifted, leads to a mosaic image that is practically free of gaps, despite the exclusion of a large fraction of pixels with stray light and ghost rays ($\sim 10\%$ – 50% of the pixels in each module). The photon-free region (black wedge) at the upper-left or northeast of 4U 1630–47 is due to the exclusion of pixels with ghost rays with no redundant observations that can compensate for the lack of exposure. The median exposure time is 24 ks with the deepest regions having 96 ks of exposure.

Although the effects of stray light and ghost rays have been minimized, the background level remains high and inhomogeneous throughout the image. The exclusion of contaminated pixels leads to artifacts that are visible as bright arcs concentric around 4U 1630–47. Increasing the size of the exclusion region leads to exposure gaps in the mosaic. Bright fringes that appear along the right edge of the mosaic image are due to secondary ghost rays from 4U 1630–47. The contaminated pixels are situated in a “halo” whose inner radius is $\gtrsim 0.3$ from 4U 1630–47. We did not attempt to correct for this a posteriori due to insufficient exposure redundancy in the affected regions.

The objects in the survey region that are most easily perceptible are 4U 1630–47 and NuSTAR J163433–473841. Their properties are discussed in separate papers, but highlights include: the discovery of reflection from the inner accretion disk of 4U 1630–47 yielding a BH spin of $a = 0.985(3)$, and an iron absorption feature at 7.03(3) keV suggesting a magnetically driven disk wind (King et al. 2014); and the discovery of a hard X-ray source (NuSTAR J163433–473841) that underwent a 1 day long X-ray flare serendipitously during our *NuSTAR* survey, but was never seen in any wavelength before or since those observations. This suggests that NuSTAR J163433–473841 is a new fast X-ray transient that could be a magnetar or an active stellar binary (Tomsick et al. 2014).

In addition to these objects, there are three significantly detected hard X-ray sources whose positions are compatible with sources seen at lower energies by *Chandra*: CXOU J163329.5–473332, CXOU J163350.9–474638, and CXOU J163355.1–473804 (Figure 1). Their basic properties are listed in Table 2. Uncertainties are quoted at 90% confidence, unless noted otherwise.

3.1. CXOU J163329.5–473332

NuSTAR detects a source at the 8.3σ level whose position (Table 2) is 1"9 away from, and compatible with, that of CXOU J163329.5–473332. The source appears in *NuSTAR* ObsID 5 and ObsID 6. However, it falls in the chip gap and among the

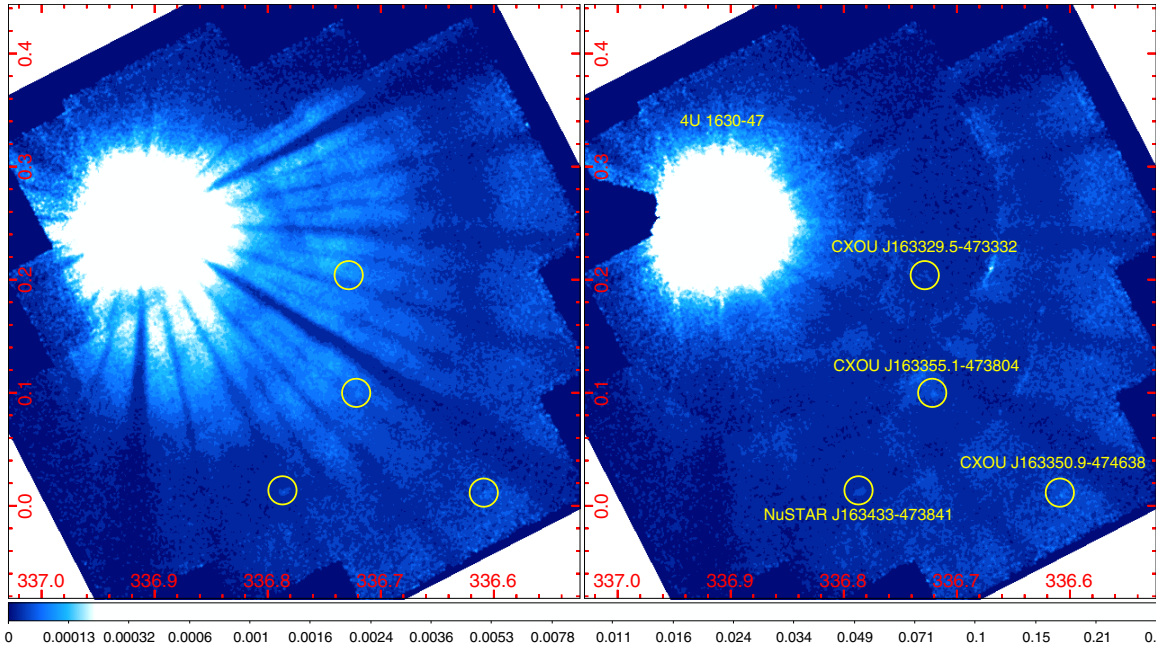


Figure 1. Mosaic images (3–79 keV) from the initial *NuSTAR* survey of the Norma Arm before (left) and after (right) the exclusion of pixels corresponding to stray light and ghost rays. Presented in Galactic coordinates, these exposure-normalized images (flux maps) combine nine pointings with two focal-plane modules. The images are smoothed with a Gaussian kernel of $\sigma = 6''$ (each pixel is $2''$ wide), and they are scaled logarithmically with an exaggerated contrast to aid visual identification of the detected sources (indicated with circles of radius = $45''$).

(A color version of this figure is available in the online journal.)

ghost rays during ObsID 5, and so only data from ObsID 6 was used for spectral and timing analyses (Figure 2).

Chandra spectral data from ObsID 12533 were fit with an absorbed power law yields $N_{\text{H}} = (12_{-9}^{+14}) \times 10^{22} \text{ cm}^{-2}$ and $\Gamma = 1.2_{-1.8}^{+2.2}$ ($\chi^2_{\nu}/\text{dof} = 0.6/3$). There were 125 ± 12 net source counts in 0.3–10 keV, distributed as 14 ± 4 cts (0.3–3 keV) and 111 ± 11 cts (3–10 keV). Using Cash (1979) statistics and Pearson (1900) χ^2 test statistics on unbinned *Chandra* data give consistent results.

An absorbed power law was then fit to the *NuSTAR* data only. With N_{H} fixed to the best-fit value from *Chandra*, we measure a photon index $\Gamma = 2.6_{-1.3}^{+1.3}$ that is consistent with the one from *Chandra*. The source emitted 120 ± 22 net counts in the *NuSTAR* energy band (3–24 keV), and nearly all of them (105 ± 20) were recorded below 10 keV.

We fit the combined spectra from *Chandra* and *NuSTAR* using a cross-instrumental constant fixed at unity for the *Chandra* data, and allowed to vary for the *NuSTAR* data. The best-fitting model parameters for the power-law model are $N_{\text{H}} = (17_{-7}^{+10}) \times 10^{22} \text{ cm}^{-2}$ and $\Gamma = 2.0_{-1.1}^{+1.2}$ (Figure 3 and Table 3). A fit of equivalent quality ($\chi^2_{\nu}/\text{dof} = 1.3/7$) is obtained with an absorbed blackbody model of temperature $kT = 2.0_{-0.6}^{+1.1} \text{ keV}$, and a lower column density $N_{\text{H}} = (7_{-3}^{+6}) \times 10^{22} \text{ cm}^{-2}$. The instrumental constant ($0.9_{-0.5}^{+0.7}$ for the power law, $0.9_{-0.5}^{+0.6}$ for the blackbody), which is consistent with pre-flight expectations for *NuSTAR* (Harrison et al. 2013) and with joint *Chandra*–*NuSTAR* spectral fits of other Galactic objects (e.g., Gotthelf et al. 2014), indicates little variability in source flux between observations taken nearly 2 yr apart. Fitting the joint spectral data with a bremsstrahlung model leads to an unconstrained plasma temperature ($\approx 12 \text{ keV}$).

Figure 4 presents the light curve (3–24 keV, 100 s resolution) of CXOU J163329.5–473332. We searched for periods in the range of 0.004 s (i.e., twice the time resolution of the light

curve data used in this fine timing analysis) to 18959 s (i.e., the observation duration), and we did not detect a significant pulsation signal in the soft (3–8 keV), hard (8–24 keV), or broad energy band (3–24 keV).

The field of CXOU J163329.5–473332 was observed by *XMM-Newton* and this object was detected as part of the *XMM-Newton* Serendipitous Survey Catalog (Watson et al. 2009), although it appears faint and far off-axis ($\gtrsim 10$ arcmin). We analyzed observation ID 0654190201 (rev. 2051), which was taken in 2011 February, with a total exposure time of 22 ks. The parameters from the *XMM-Newton* spectral fit of this source, i.e., the observed flux, column density, photon index, and blackbody temperature, are consistent with those derived from fits to the *Chandra*, *NuSTAR*, and combined *Chandra*–*NuSTAR* spectra.

We observed the near-infrared counterpart to CXOU J163329.5–473332 with the NEWFIRM telescope and its magnitudes are $J = 15.29 \pm 0.07 \text{ mag}$, $H = 11.92 \pm 0.10 \text{ mag}$, and $K_s = 10.13 \pm 0.06 \text{ mag}$ (Rahoui et al. 2014, in press). The infrared spectrum displays strong CO lines in absorption (at 16198 Å and 22957 Å), a number of weak emission lines, and no Br- γ line. This spectrum is typical of an early MIII-type star feeding a small accretion disk (Rahoui et al. 2014, in press).

3.2. CXOU J163350.9–474638

In ObsID 1 (Figure 2), *NuSTAR* detects a source at a significance of 15.0σ (Table 2) whose position is $4''.1$ from, and compatible with, the *Chandra* position of CXOU J163350.9–474638.

The *Chandra* spectral data (ObsID 12532) were fit with an absorbed power law to give $N_{\text{H}} = (13_{-5}^{+8}) \times 10^{22} \text{ cm}^{-2}$ and $\Gamma = 2.0_{-1.1}^{+1.3}$ ($\chi^2_{\nu}/\text{dof} = 0.8/6$). A thermal blackbody model ($kT = 1.4_{-0.4}^{+0.7} \text{ keV}$) fit to the data yields a similar column ($N_{\text{H}} = (8_{-3}^{+5}) \times 10^{22} \text{ cm}^{-2}$) and fit quality ($\chi^2_{\nu}/\text{dof} = 1.1/6$). There are 190 ± 14 net source counts in the 0.3–10 keV range, with

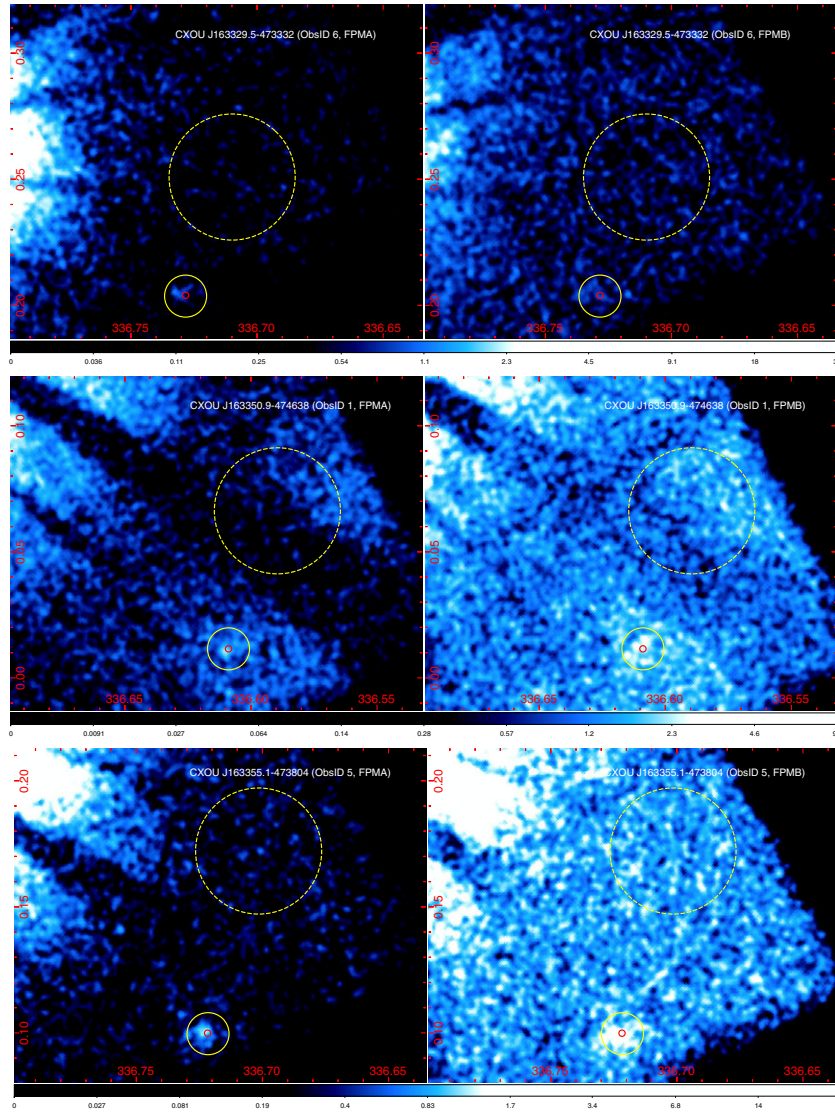


Figure 2. *NuSTAR* images of the sources discussed in this work in Galactic coordinates. The top, middle, and bottom rows present cleaned event lists in the 3–79 keV band from, respectively, CXOU J163329.5–473332 (ObsID 6), CXOU J163350.9–474638 (ObsID 1), and CXOU J163355.1–473804 (ObsID 5). The left panels show FPMA while the right panels show FPMB with the same logarithmic scaling. The images were smoothed with a Gaussian kernel of $\sigma = 6''$. The small circles indicate the *Chandra* positions, the medium circles are the $30''$ source-extraction regions, and the large dashed circles ($90''$ -radius) represent the background regions. (A color version of this figure is available in the online journal.)

30 ± 6 counts having energies below 3 keV, and the rest (159 ± 13) are above 3 keV.

We then fit an absorbed power law to the *NuSTAR* data alone while fixing N_{H} to the best-fit value from *Chandra*. The fit quality is decent ($\chi^2_{\nu}/\text{dof} = 1.2/14$) and the photon index ($\Gamma = 3.3 \pm 0.3$) is consistent with the value measured with *Chandra*. An absorbed blackbody provides an acceptable fit ($\chi^2_{\nu}/\text{dof} = 1.4/22$) with a temperature $kT = 1.1 \pm 0.1$ keV, similar to that measured with *Chandra*. The source emitted 400 ± 30 net counts in 3–24 keV, with most of them (375 ± 28) below 10 keV.

The spectra from *Chandra* and *NuSTAR* were jointly fit with an absorbed power law yielding $N_{\text{H}} = (21^{+6}_{-4}) \times 10^{22} \text{ cm}^{-2}$ and $\Gamma = 3.7 \pm 0.5$ (Figure 3 and Table 3). Although the fit quality is good ($\chi^2_{\nu}/\text{dof} = 1.1/22$), the cross-instrumental constant is $3.8^{+0.9}_{-0.7}$, which indicates significant variability on year-long timescales.

Adding an exponential cutoff constrains the break energy ($E_{\text{cut}} \leq 13$ keV). However, this component is not required

by the data since it returns a similar χ^2_{ν} with 2 less dof. The measured N_{H} is larger in the joint fit than in the *Chandra* data alone, and fixing the column density to the *Chandra* value leads to a poorer fit ($\chi^2_{\nu}/\text{dof} = 1.7/23$).

Thermal models also provide good fits to the data. A blackbody model ($\chi^2_{\nu}/\text{dof} = 1.3/22$) gives a lower column density than for the power law ($N_{\text{H}} = (9^{+3}_{-2}) \times 10^{22} \text{ cm}^{-2}$), and has a temperature of $kT = 1.2^{+0.2}_{-0.1}$ keV. A bremsstrahlung model ($\chi^2_{\nu}/\text{dof} = 1.1/22$) has an absorbing column consistent with the power law model ($N_{\text{H}} = (15^{+4}_{-3}) \times 10^{22} \text{ cm}^{-2}$), and a plasma temperature of $kT = 3.3^{+1.0}_{-0.7}$ keV (a value that is not constrained with the *Chandra* data alone).

The 3–24 keV light curve binned at 100 s is presented in Figure 4, and it shows CXOU J163350.9–474638 to be a relatively soft source that displays low variability on short timescales. The background is mostly due to 4U 1630–47 whose ghost-ray halo covers the extraction regions used to produce the light curves. The apparent decrease in background

Table 3
Parameters from Absorbed Power Law (PL), Blackbody (BB), and Bremsstrahlung (FF) Models Fit to the Joint *Chandra* and *NuSTAR* Spectral Data for Sources in the Norma Arm Survey

Name	Model	C^a	N_H^b	Γ or kT^c	Norm. ^d	χ^2_v/dof^e	S^f	H^g	HR ^h	Obs. Flux ⁱ	Unabs. Flux ^j
CXOU J163329.5–473332	PL	$0.9^{+0.7}_{-0.5}$	17^{+10}_{-7}	$2.0^{+1.1}_{-1.2}$	2.1	1.2/7	105 ± 20	15 ± 8	-0.7 ± 0.3	12.5 ± 5.2	26.2 ± 13.6
	BB	$0.9^{+0.6}_{-0.5}$	7^{+6}_{-3}	$2.0^{+1.1}_{-0.6}$	0.06	1.3/7				10.9 ± 2.7	13.2 ± 3.6
	FF	$0.9^{+0.7}_{-0.5}$	15^{+7}_{-5}	$\approx 12^*$	1.3	1.2/7				$12.0 \pm 2.1^*$	$21.2 \pm 5.9^*$
CXOU J163350.9–474638	PL	$3.8^{+0.9}_{-0.7}$	21^{+6}_{-4}	3.7 ± 0.5	41.3	1.1/22	375 ± 28	25 ± 10	$-0.9^{+0.2}_{-0.1}$	29.1 ± 9.3	362 ± 238
	BB	$3.6^{+0.9}_{-0.7}$	9^{+3}_{-2}	$1.2^{+0.2}_{-0.1}$	0.06	1.3/22				25.8 ± 2.2	39.6 ± 10.9
	FF	$3.7^{+0.9}_{-0.7}$	15^{+4}_{-3}	$3.3^{+1.0}_{-0.7}$	4.0	1.1/22				27.6 ± 5.3	77.2 ± 31.3
CXOU J163355.1–473804 [†]	PL	1.0 ± 0.3	6 ± 1	1.5 ± 0.3	1.5	2.0/35	256 ± 26	52 ± 12	-0.7 ± 0.2	32.8 ± 3.2	43.2 ± 7.1
	BB	1.0 ± 0.2	$1.2^{+0.5}_{-0.4}$	$2.1^{+0.3}_{-0.2}$	0.1	1.3/35				28.1 ± 3.7	29.1 ± 2.8
	FF	1.1 ± 0.3	$5.2^{+1.1}_{-0.9}$	21^{+32}_{-9}	1.9	1.8/35				32.7 ± 10.3	41.0 ± 18.6

Notes.

^a Instrumental constant fixed to 1 for the *Chandra* data and allowed to vary for the *NuSTAR* data.

^b Column density in units of 10^{22} cm^{-2} .

^c Photon index of the power law (PL) model, or plasma temperature (in keV) for the blackbody (BB) and bremsstrahlung (FF) models.

^d Model normalization ($\times 10^{-4}$).

^e Reduced χ^2 over degrees of freedom (dof).

^f Net source counts from both *NuSTAR* modules combined in the soft (*S*) band: 3–10 keV.

^g Net source counts from both *NuSTAR* modules combined in the hard (*H*) band: 10–24 keV.

^h Hardness ratio defined as $(H - S)/(H + S)$.

ⁱ Observed flux (i.e., not corrected for absorption) in units of $10^{-13} \text{ erg cm}^{-2} \text{ s}^{-1}$ in the 0.3–24 keV band.

^j Absorption-corrected flux in units of $10^{-13} \text{ erg cm}^{-2} \text{ s}^{-1}$ in the 0.3–24 keV band.

* The fluxes are derived by fixing the plasma temperature to 12 keV.

[†] The best fitting model for CXOU J163355.1–473804 requires a Gaussian component at 6.7 keV.

counts is not significant. There are no periodicities detected in the range of 0.004 s to 18407 s in any energy range. An upper limit of $\sim 30\%$ (at 90% confidence) is derived for the fractional rms expected for a periodic signal.

3.3. CXOU J163355.1–473804

This source appears in two *Chandra* observations (ObsID 12532 and ObsID 12533); the spectral data from these observations were summed to give 546 ± 24 net source counts (0.3–10 keV), divided into 168 ± 13 and 377 ± 20 net counts in the 0.3–3 keV and 3–10 keV bands, respectively. A power law model fit to the binned spectral data provides an adequate fit ($\chi^2_v/\text{dof} = 1.3/24$) with $N_H = (3 \pm 1) \times 10^{22} \text{ cm}^{-2}$ and a flat photon index: $\Gamma = 0.7^{+0.4}_{-0.3}$. A blackbody of temperature $kT = 1.9^{+0.4}_{-0.3} \text{ keV}$ improves the fit slightly ($\chi^2_v/\text{dof} = 1.2/24$).

The likely hard X-ray counterpart to CXOU J163355.1–473804 is detected at the 8.7σ level (3–79 keV) in the *NuSTAR* mosaic image. Ghost-ray photons contaminate the region around the source in ObsID 4, and so spectral and timing analysis relied only on data from ObsID 5. The 321 ± 28 net source counts (3–24 keV) were distributed as 256 ± 26 net counts in 3–10 keV, and 52 ± 12 in 10–24 keV.

We fit the *NuSTAR* data with power law and blackbody models holding N_H fixed to the best-fit value from *Chandra*, and derived a steeper photon index ($\Gamma = 1.9 \pm 0.3$) or a plasma temperature consistent with that of *Chandra* ($kT = 2.2 \pm 0.3 \text{ keV}$), with both models giving poor fits ($\chi^2_v/\text{dof} = 2.3/9$ and $\chi^2_v/\text{dof} = 1.8/9$, respectively).

Jointly fitting the *Chandra* and *NuSTAR* data gives a poor fit ($\chi^2_v/\text{dof} = 2.0/35$) when using only an absorbed power law: $N_H = (6 \pm 1) \times 10^{22} \text{ cm}^{-2}$ and $\Gamma = 1.5 \pm 0.3$ (Figure 3 and Table 3). The fit quality improves ($\chi^2_v/\text{dof} = 1.3/35$) with a blackbody model having $kT = 2.1^{+0.3}_{-0.2} \text{ keV}$ and a lower column density ($N_H = (1.2^{+0.5}_{-0.4}) \times 10^{22} \text{ cm}^{-2}$), or with a

power law and exponential cutoff ($\chi^2_v/\text{dof} = 1.4/30$) where $N_H = (3 \pm 1) \times 10^{22} \text{ cm}^{-2}$, $\Gamma = 0.6 \pm 0.4$, and the cutoff energy is 5^{+3}_{-1} keV . In both cases, the instrumental constant is 1.1 ± 0.2 suggesting little variability over yearlong timescales.

Residuals remain around 6.7 keV where emission from the fluorescence of ionized iron is expected. Indeed, the best spectral fits are obtained when a Gaussian component ($\sigma = 0$) is added to either the cutoff power law or the blackbody model. In order to analyze this line, we rebinned the *NuSTAR* spectra to have at least 20 source + background counts and a minimum significance of 2σ . For the power law ($\chi^2_v/\text{dof} = 1.1/48$), $N_H = (2 \pm 1) \times 10^{22} \text{ cm}^{-2}$, with $\Gamma = 0.0^{+0.6}_{-1.0}$ and an exponential cutoff at 4^{+3}_{-1} keV . The line centroid is $6.72^{+0.04}_{-0.08} \text{ keV}$ with an equivalent width of $\sim 500 \text{ eV}$ (unconstrained).

For the blackbody model ($\chi^2_v/\text{dof} = 1.2/50$), the line centroid is $6.7^{+0.1}_{-0.2} \text{ keV}$ with an equivalent width of $414^{+370}_{-312} \text{ eV}$. The column density and blackbody temperature are $N_H = (1.2^{+0.6}_{-0.5}) \times 10^{22} \text{ cm}^{-2}$ and $kT = 2.0^{+0.3}_{-0.2} \text{ keV}$, respectively. The radius of the emitting region implied by the blackbody model is very small (0.03–0.16 km assuming source distances of 2–10 kpc). Either the source is very distant ($\geq 20 \text{ kpc}$) or the blackbody is not the right model.

We replaced the blackbody continuum with a bremsstrahlung ($\chi^2_v/\text{dof} = 1.3/50$) and obtained $N_H = (5 \pm 1) \times 10^{22} \text{ cm}^{-2}$, $kT = 16^{+14}_{-5} \text{ keV}$, a line energy of $6.74^{+0.05}_{-0.06} \text{ keV}$, and an equivalent width of $911^{+553}_{-365} \text{ eV}$. We also modeled the continuum with *apec* ($\chi^2_v/\text{dof} = 1.3/51$) and the resulting iron abundance is at least 40% greater than Solar ($N_{\text{Fe}} \geq 1.4$) with a plasma temperature of $kT = 12^{+7}_{-3} \text{ keV}$.

The *NuSTAR* light curve (3–24 keV) for CXOU J163355.1–473804 is presented in Figure 4. No coherent pulsations were detected for search periods ranging from 2 ms to $\sim 21 \text{ ks}$.

The likely infrared counterpart to CXOU J163355.1–473804 was observed with NEWFIRM giving magnitudes of $J = 16.43 \pm 0.07$ mag, $H = 15.45 \pm 0.10$ mag, and $K_s = 14.99 \pm 0.09$ mag (Rahoui et al. 2014, in press). With a weak CO line at 16198 Å, a strong CO line at 22957 Å, and weak Br- γ emission, the infrared spectrum is typical of a late GIII-type star.

4. DISCUSSION

4.1. CXOU J163329.5–473332

The *Chandra* position for CXOU J163329.5–473332 is encompassed by the 2'1 uncertainty radius of an *INTEGRAL*-detected source named IGR J16336–4733 (Krivonos et al. 2010), which was also detected in a short observation by *Swift* (Landi et al. 2011). The flux recorded by *Swift*-XRT (2–10 keV) and by *NuSTAR* (3–10 keV) translate to X-ray luminosities of $1.9 \times 10^{34} [d/10 \text{ kpc}]^2 \text{ erg s}^{-1}$, and $7.9 \times 10^{33} [d/10 \text{ kpc}]^2 \text{ erg s}^{-1}$, respectively. The available X-ray data of CXOU J163329.5–473332 show it to be a faint, absorbed ($N_H \gtrsim 10^{23} \text{ cm}^{-2}$), and relatively hard X-ray source (the bulk of its photons are emitted in 3–10 keV).

Thus, CXOU J163329.5–473332 could be a faint low-mass X-ray binary (LMXB; e.g., Degenaar & Wijnands 2009) or a CV (Kuulkers et al. 2006) of the intermediate polar (e.g., Patterson 1994) variety due to the hard X-ray detection. The detection of CXOU J163329.5–473332 out to ~ 20 keV with a moderately steep photon index ($2.4_{-0.8}^{+0.9}$) and low X-ray luminosity is consistent with both classifications. Another possibility is a binary system in which the compact object is a non-accreting magnetar (e.g., Thompson & Duncan 1996).

4.2. CXOU J163350.9–474638

These *NuSTAR* observations of CXOU J163350.9–474638 extend the source spectrum beyond 10 keV. However, the source demonstrates significant variability in intensity (by at least a factor of four) over the 2 yr separating the *Chandra* and *NuSTAR* observations, which makes it difficult to draw firm conclusions from joint-fitting of the broadband X-ray spectral energy distribution.

Nevertheless, it is possible to compare the spectral parameters derived from single-instrument fits. The photon index is steeper in the *NuSTAR* data (by $\sim 50\%$) compared with the value measured with *Chandra*. This is not uniquely due to the fact that *NuSTAR* covers higher X-ray energies, since $\sim 90\%$ of the photons recorded by *NuSTAR* were below 10 keV, i.e., in an energy range covered by *Chandra*. On the other hand, thermal models also fit the data well, and the blackbody temperature ($kT = 1.2 \pm 0.2$ keV) and column density ($N_H = (9_{-4}^{+5}) \times 10^{22} \text{ cm}^{-2}$) are in agreement for both *Chandra* and *NuSTAR* spectra.

There are no catalogued IR/optical objects from VizieR¹⁶ or in the Vista Variables in the Via Lactae Survey (Minniti et al. 2010) compatible with the *Chandra* position. Thus, CXOU J163350.9–474638 lacks a stellar counterpart that would rule out a CV or XRB located nearby, while the steep power law disfavors an AGN. Given its thermal spectrum, its long-term variability, and the absence of multi-wavelength counterparts, we conclude that CXOU J163350.9–474638 could be a LMXB situated a large distance away, or perhaps an isolated, magnetized NS (i.e., a magnetar).

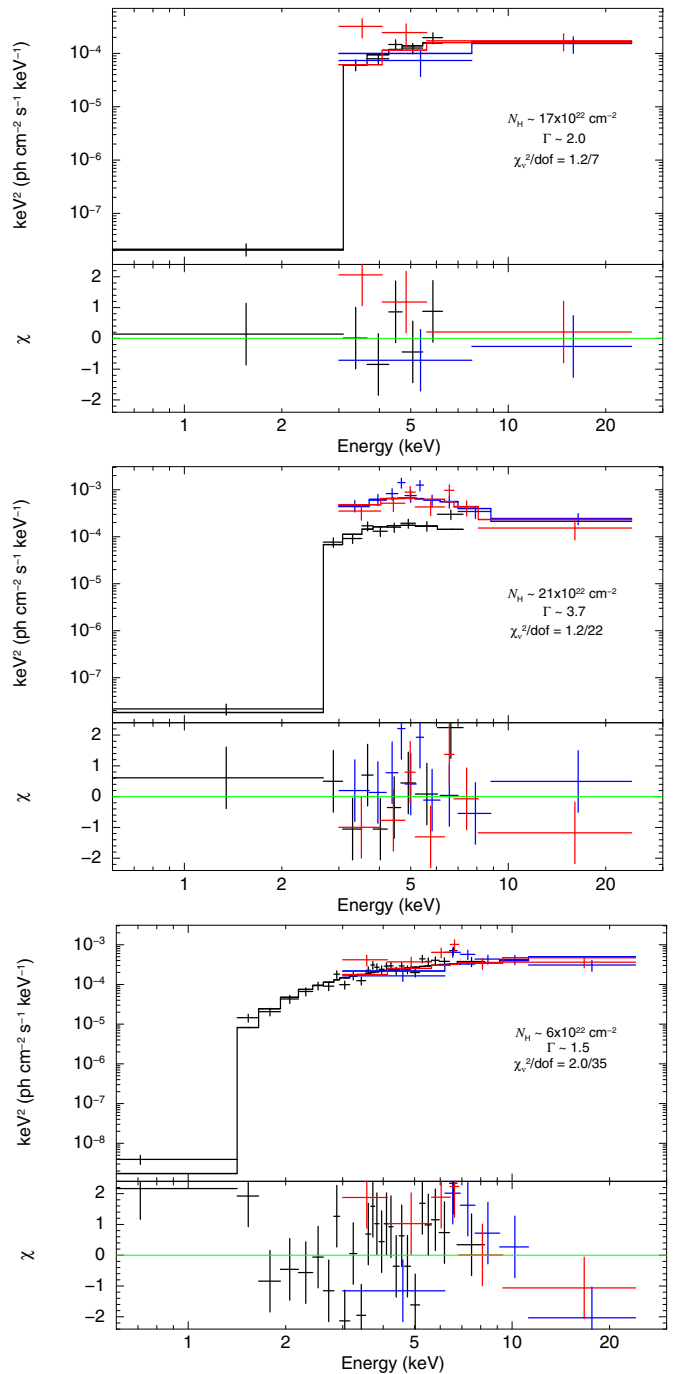


Figure 3. Background-subtracted spectra (νF_ν) collected with *Chandra* (black), *NuSTAR*-FPMA (blue), and *NuSTAR*-FPMB (red) for CXOU J163329.5–473332 (top), CXOU J163350.9–474638 (middle), and CXOU J163355.1–473804 (bottom). Spectral bins for *Chandra* contain a minimum of 20 source + background counts, while those of *NuSTAR* have at least 20 net source counts and a minimum significance of 2σ . Error bars denote 90%-confidence limits. The lower panels show residuals from absorbed power laws fit to the joint *Chandra*–*NuSTAR* data. The derived spectral parameters are listed in Table 3.

(A color version of this figure is available in the online journal.)

4.3. CXOU J163355.1–473804

Prior to the *NuSTAR* survey, *Chandra* found CXOU J163355.1–473804 to be a relatively bright X-ray source with a hard spectral continuum. As the brightest of the three objects in this study, this permitted us to measure the source's

¹⁶ <http://vizier.u-strasbg.fr>

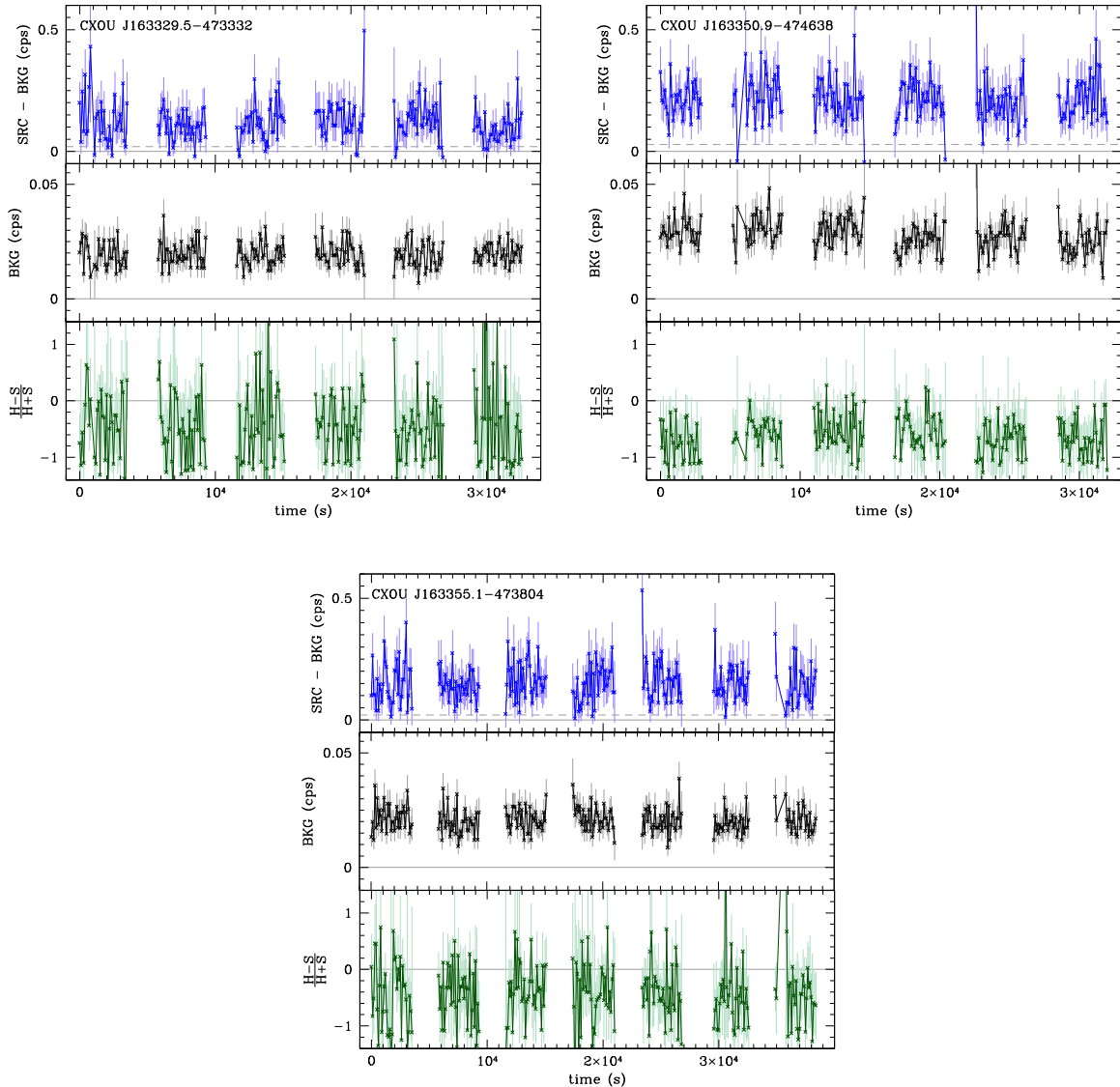


Figure 4. Source and background light curves (3–24 keV) for CXOU J163329.5–473332 (top), CXOU J163350.9–474638 (middle), and CXOU J163355.1–473804 (bottom). The source light curve combines count rates from FPMA and FPMB that are then background-subtracted. The background count rate has been scaled to the size of the source region. The average background rate is shown as a dashed line in the top panel. The hardness ratio is defined as $(H - S)/(H + S)$ where S and H represent count rates in 3–8 keV and 8–24 keV, respectively. Each bin is 100 s.

(A color version of this figure is available in the online journal.)

broadband X-ray spectrum with relatively high precision. The spectrum combining *Chandra* and *NuSTAR* data is consistent with a cutoff power law of $\Gamma = 0.0^{+0.6}_{-1.0}$ and $E_{\text{cut}} = 4^{+3}_{-2}$ keV. Thermal models such as a blackbody with $kT = 2.0^{+0.3}_{-0.2}$ keV or a bremsstrahlung with $kT = 16^{+14}_{-5}$ keV also describe the data well, although the implied size of the emission region is not consistent with the blackbody model. The column density required by the best-fitting models ($N_{\text{H}} \lesssim 3 \times 10^{22} \text{ cm}^{-2}$) is lower than measured for the two other sources in the study, indicating that the source is either less intrinsically absorbed than the others, or more likely, that it is closer to us.

With *NuSTAR*, we are able to confirm the detection of an iron line that is hinted at in the *Chandra* data. The line energy of 6.7 keV suggests thermal $K\alpha$ emission from highly ionized, helium-like iron (Fe xxv) in the optically thin plasma around an accreting white dwarf, i.e., a CV (e.g., Hellier & Mukai 2004; Pandel et al. 2005; Kuulkers et al. 2006). For example, EX Hya and V405 Aur are CVs that show a 6.7 keV line with equivalent

widths $\sim 400\text{--}900$ eV, i.e., consistent with the equivalent width measured in CXOU J163355.1–473804 (Hellier et al. 1998).

The identification of the infrared counterpart as a cool, GIII star supports the CV classification. Another factor favoring a CV nature for CXOU J163355.1–473804 is the apparent lack of change in intensity or spectrum during the 2 yr separating the *Chandra* and *NuSTAR* surveys, with no indication from all-sky X-ray monitors that the system underwent a major outburst ($L_X \gtrsim 10^{36} \text{ erg s}^{-1}$) in that time (or at any time in the past few decades).

Its lower absorbing column compared with the other sources in the survey suggests that CXOU J163355.1–473804 is at a distance of 2 or 3 kpc at most, i.e., in the Crux Arm, or in the nearest arc of the Norma Arm. At an assumed distance of 3 kpc, the absorption-corrected flux (0.3–79 keV) of the bremsstrahlung model translates to an X-ray luminosity of $5 \times 10^{33} \text{ erg s}^{-1}$. This is consistent with the persistent X-ray luminosity expected from a CV (e.g., Muno et al. 2004; Kuulkers et al. 2006).

4.4. Undetected *Chandra* Sources

Of the 22 hard *Chandra* sources in the survey region, 3 were detected by *NuSTAR*, and they ranked first, second, and fourth in order of the number of hard X-ray (≥ 3 keV) counts recorded by *Chandra*. The third brightest source in the hard *Chandra* band is CXOU J163358.9–474214. This source was not detected in the *NuSTAR* event lists and mosaic images, despite the fact that it was located in a relatively ghost-ray free and stray-light free part of the image in ObsID 1. This indicates a variable nature for this object (significant variability was also observed with *Chandra*), and we establish a 3σ upper limit of 7×10^{-13} erg cm $^{-2}$ s $^{-1}$ on the absorbed source flux in the 3–10 keV range, i.e., higher than the average flux registered by *Chandra* in a similar energy band (2–10 keV: Fornasini et al. 2014, submitted). The *Chandra* error circle for this source contains a counterpart candidate seen in the near-IR by Two Micron All Sky Survey, and in the mid-IR by *Spitzer* and *Wide Field Infrared Survey Explorer*. The X-ray variability and the possible association with an IR-emitting source suggest a LMXB or a CV.

All other *Chandra* sources in the *NuSTAR* survey region had less than 35 cts in the hard *Chandra* band, which means they are too faint to be detected by *NuSTAR* given the exposure depth of this survey.

Sections of the Norma field have been observed by *XMM-Newton* and source candidates found therein are listed in the *XMM-Newton* Serendipitous Survey Catalog (Watson et al. 2009). Of the ~ 150 sources in the field, 22 of these are both relatively bright (flux in the 0.2–12 keV band $\geq 5 \times 10^{-13}$ erg cm $^{-2}$ s $^{-1}$) and hard (hardness ratio between the 2–4.5 keV and 4.5–12 keV bands ≥ 0.0). Only one of them coincides spatially with the error circle of a *NuSTAR* source: CXOU J163329.5–473332. It is one of the hardest sources (ranked 6th hardest out of 22), but it is also among the faintest (ranked 19th in flux out of 22).

4.5. Lessons Learned from This Pilot Study

Besides the analysis of X-ray sources, one of the primary goals of this pilot study is to optimize the strategy for future observations. Our experiences with this mini-survey showed us that some of our strategic choices were sound and some can be improved.

Based on the results of the *Chandra* survey, we knew that the mini-survey region contained several sources that *NuSTAR* could detect. As was done here, observers should select regions in such a way that they encompass the largest number of hard *Chandra* sources (or, when available, *XMM-Newton* sources) that are relatively bright, but not so bright that their ghost rays and stray light contaminate adjacent observations. With the exposures available in this survey (10–100 ks), *NuSTAR* was able to detect three out of four X-ray sources that had more than ~ 100 cts in the hard *Chandra* band (≥ 3 keV). The non-detection of the fourth source still gives the useful result that the source is variable. While this *Chandra* hard-band count rate could be used as a rule-of-thumb for a source’s detectability in a typical mini-survey such as this, it is no guarantee since it does not account for X-ray sources that are variable, or that were in the soft state during the *NuSTAR* survey.

Another factor that led to the selection of this region was that we expected it to contain a relatively low level of stray light given the satellite’s roll angle at the time the observations were performed. Even if stray light were to affect one or both of the modules, substitute coverage is available from the overlapping module and/or adjacent observation(s).

The value of exposure redundancy, not only thanks to the two modules but also by tiling observations with significant overlap ($\sim 50\%$ shifts), can not be overstated for eliminating or reducing imaging artifacts. This is an important factor that greatly facilitated the analysis of the faint sources in this study. Further improvements in this direction can be made by dividing up the 25 ks exposures into two or three 10–15 ks exposures tiled with slightly more overlap (roughly 2/3) between adjacent pointings. While data with more overlap will take more time to analyze (i.e., the spectra from separate observations will need to be merged to obtain meaningful statistics) the tradeoff is increased exposure redundancy in case pixels need to be discarded due to ghost rays or stray light.

Observers who wish to use *NuSTAR* for galactic surveys can prevent or reduce the effects of stray light and ghost rays in two ways: (1) by using opportunistic observations gathered only when known transients are off or emitting at low levels according to wide-field X-ray monitors such as *MAXI*, *Swift-BAT*, and *INTEGRAL-ISGRI*; and (2) by increasing the exposure redundancy. While we underestimated its effects during the planning of this survey, we now know more about the brightness and extent of the ghost-ray pattern from objects such as 4U 1630–47, which will help guide the selection of future surveys.

An open question is whether *NuSTAR* should continue to survey “regions” rather than using the observing time to place the most promising targets from these regions on axis. However, it is important to note that a targeted approach might have missed the discovery of the new X-ray transient *NuSTAR* J163433–473841.

While there are technical challenges, there are also tremendous scientific benefits from surveying the Galaxy with *NuSTAR*. Understanding the disk-wind connection in 4U 1630–47, the serendipitous discovery of *NuSTAR* J163433–473841, and insights into the faint members of the galactic X-ray population are primary among these. Surveys allow *NuSTAR* to offer a complete picture of the Inner Milky Way, which will add to our knowledge of the content of our host galaxy and unlock new mysteries.

5. SUMMARY AND CONCLUSIONS

An initial *NuSTAR* survey of the Norma Arm gave insights into the hard X-ray spectral and timing behavior of five sources, three of which are described for the first time in this paper. These three sources have unclassified soft X-ray counterparts from *Chandra*, so the broadband 0.3–79 keV data (including IR follow-up observations) allow us to propose their likely classifications.

As a faint, hard X-ray source with a low-mass companion, CXOU J163329.5–473332 is shown to be either a CV or a faint LMXB. The intensity variations on year-long timescales and the lack of a clear multi-wavelength counterpart indicate that CXOU J163350.9–474638 could be a distant XRB or possibly a magnetar. We discovered a helium-like iron line at 6.7 keV in the *NuSTAR* spectrum of CXOU J163355.1–473804, and so it is classified as a nearby CV given the low mass of its IR counterpart.

With *NuSTAR* we are granted unprecedented views into the hard X-ray populations of our Galaxy. While *NuSTAR* can perform surveys, its observations can be affected by ghost rays and stray light. These effects can be diminished by planning observations to avoid bright sources located just outside the FOV, and by increasing the exposure redundancy. More *NuSTAR* surveys are planned for the Norma Arm and

other crowded fields such as the Galactic Center, and those observations will benefit from the lessons learned during this pilot study.

This work was supported under NASA Contract No. NNG08FD60C, and made use of data from the *NuSTAR* mission, a project led by the California Institute of Technology, managed by the Jet Propulsion Laboratory, and funded by the National Aeronautics and Space Administration. We thank the *NuSTAR* Operations, Software, and Calibration teams for support with the execution and analysis of these observations. This research has made use of the *NuSTAR* Data Analysis Software (NuSTAR-DAS) jointly developed by the ASI Science Data Center (ASDC, Italy) and the California Institute of Technology. This research has made use of: data obtained from the High Energy Astrophysics Science Archive Research Center (HEASARC) provided by NASA's Goddard Space Flight Center; NASA's Astrophysics Data System Bibliographic Services; and the SIMBAD database operated at CDS, Strasbourg, France. F.M.F. acknowledges support from the National Science Foundation Graduate Research Fellowship. F.E.B. acknowledges support from Basal-CATA PFB-06/2007, CONICYT-Chile (FONDECYT 1141218 and "EMBIGEN" Anillo ACT1101), and Project IC120009 "Millennium Institute of Astrophysics (MAS)" of Iniciativa Científica Milenio del Ministerio de Economía, Fomento y Turismo.

REFERENCES

- Antoniou, V., Zezas, A., Hatzidimitriou, D., & Kalogera, V. 2010, *ApJL*, **716**, L140
- Arnaud, K. A. 1996, in ASP Conf. Ser. 101, *Astronomical Data Analysis Software and Systems V*, ed. G. H. Jacoby & J. Barnes (San Francisco, CA: ASP), 17
- Bird, A. J., Bazzano, A., Bassani, L., et al. 2010, *ApJS*, **186**, 1
- Bodaghee, A., Popp, A., Grinberg, V., et al. 2012a, *ATel*, **3945**
- Bodaghee, A., Tomsick, J. A., Rodriguez, J., & James, J. B. 2012b, *ApJ*, **744**, 108
- Bronfman, L., Casassus, S., May, J., & Nyman, L.-Å. 2000, *A&A*, **358**, 521
- Cash, W. 1979, *ApJ*, **228**, 939
- Degenaar, N., & Wijnands, R. 2009, *A&A*, **495**, 547
- Fornasini, F. M., Tomsick, J. A., Bodaghee, A., et al. 2014, *ApJ*, submitted
- Gotthelf, E. V., Tomsick, J. A., Halpern, J. P., et al. 2014, *ApJ*, **788**, 155
- Harrison, F. A., Craig, W. W., Christensen, F. E., et al. 2013, *ApJ*, **770**, 103
- Hellier, C., & Mukai, K. 2004, *MNRAS*, **352**, 1037
- Hellier, C., Mukai, K., & Osborne, J. P. 1998, *MNRAS*, **297**, 526
- King, A. L., Walton, D. J., Miller, J. M., et al. 2014, *ApJL*, **784**, L2
- Koglin, J. E., An, H., Barrière, N., et al. 2011, *Proc. SPIE*, **8147**, 81470J
- Krivonos, R., Tsygankov, S., Lutovinov, A., et al. 2012, *A&A*, **545**, A27
- Krivonos, R., Tsygankov, S., Revnivtsev, M., et al. 2010, *A&A*, **523**, A61
- Kuulkers, E., Norton, A., Schwobe, A., & Warner, B. 2006, in *Compact Stellar X-ray Sources*, ed. W. H. G. Lewin & M. van der Klis (Cambridge, UK: Cambridge Univ. Press), 421
- Landi, R., Bassani, L., Masetti, N., Bazzano, A., & Bird, A. J. 2011, *ATel*, **3272**
- Minniti, D., Lucas, P. W., Emerson, J. P., et al. 2010, *NewA*, **15**, 433
- Muno, M. P., Arabadjis, J. S., Baganoff, F. K., et al. 2004, *ApJ*, **613**, 1179
- Muno, M. P., Bauer, F. E., Baganoff, F. K., et al. 2009, *ApJS*, **181**, 110
- Pandel, D., Córdova, F. A., Mason, K. O., & Priedhorsky, W. C. 2005, *ApJ*, **626**, 396
- Patterson, J. 1994, *PASP*, **106**, 209
- Pearson, K. 1900, *Phil. Mag. Ser. 5*, **50**, 157
- Rahoui, F., Tomsick, J. A., Fornasini, F. M., Bodaghee, A., & Bauer, F. E. 2014, *ApJ*, in press (arXiv:1406.4514)
- Rodriguez, J., Bodaghee, A., Kaaret, P., et al. 2006, *MNRAS*, **366**, 274
- Slezak, E., Durret, F., & Gerbal, D. 1994, *AJ*, **108**, 1996
- Starck, J.-L., & Murtagh, F. 1994, *A&A*, **288**, 342
- Thompson, C., & Duncan, R. C. 1996, *ApJ*, **473**, 322
- Tomsick, J. A., Gotthelf, E. V., Rahoui, F., et al. 2014, *ApJ*, **785**, 4
- Tomsick, J. A., Lingenfelter, R., Walter, R., et al. 2003, *IAUC*, **8076**, 1
- Townsley, L. K., Broos, P. S., Corcoran, M. F., et al. 2011, *ApJS*, **194**, 1
- Verner, D. A., Ferland, G. J., Korista, K. T., & Yakovlev, D. G. 1996, *ApJ*, **465**, 487
- Vikhlinin, A., Forman, W., & Jones, C. 1997, *ApJL*, **474**, L7
- Watson, M. G., Schröder, A. C., Fyfe, D., et al. 2009, *A&A*, **493**, 339
- Wilms, J., Allen, A., & McCray, R. 2000, *ApJ*, **542**, 914

Near-infrared spectroscopy of 20 new *Chandra* sources in the Norma arm

F. Rahoui^{1,2}, J. A. Tomsick³, F. M. Fornasini^{3,4}, A. Bodaghee^{3,5}, and F. E. Bauer^{6,7,8}

¹ European Southern Observatory, Karl-Schwarzschild-Str. 2, 85748 Garching bei München, Germany
e-mail: frahoui@eso.org

² Harvard University, Department of Astronomy, 60 Garden street, Cambridge MA 02138, USA

³ Space Sciences Laboratory, 7 Gauss Way, University of California, Berkeley CA 94720-7450, USA

⁴ Astronomy Department, University of California, 601 Campbell Hall, Berkeley CA 94720, USA

⁵ Department of Chemistry, Physics, and Astronomy, Georgia College & State University CBX 82, Milledgeville GA 31061, USA

⁶ Instituto de Astrofísica, Facultad de Física, Pontificia Universidad Católica de Chile, 306 Santiago 22, Chile

⁷ Millennium Institute of Astrophysics

⁸ Space Science Institute, 4750 Walnut Street, Suite 205, Boulder CO 80301, USA

Received 16 April 2014 / Accepted 4 June 2014

ABSTRACT

We report on CTIO/NEWFIRM and CTIO/OSIRIS photometric and spectroscopic observations of 20 new X-ray (0.5–10 keV) emitters discovered in the Norma arm Region *Chandra* Survey (NARCS). NEWFIRM photometry was obtained to pinpoint the near-infrared counterparts of NARCS sources, while OSIRIS spectroscopy was used to help identify 20 sources with possible high mass X-ray binary properties. We find that (1) two sources are WN8 Wolf-Rayet stars, maybe in colliding wind binaries, part of the massive star cluster Mercer 81; (2) two are emission-line stars, possibly in X-ray binaries, that exhibit near- and mid-infrared excesses either due to free-free emission from the decretion discs of Be stars or warm dust in the stellar winds of peculiar massive stars such as B[e] supergiants or luminous blue variables; (3) one is a B8-A3 IV-V star that could be in a quiescent high mass X-ray binary system; (4) two are cataclysmic variables including one intermediate polar; (5) three may be neutron star symbiotic binaries; (6) five are most likely white dwarf symbiotic binaries; and (7) five exhibit properties more consistent with isolated giant/dwarf stars. The possible detection of one to three high mass X-ray binaries is in good agreement with our predictions. However, our study illustrates the difficulty of clearly differentiating quiescent or intermediate X-ray luminosity systems from isolated massive stars, which may lead to an underestimation of the number of known high mass X-ray binaries.

Key words. X-rays: binaries – stars: massive – stars: low-mass – techniques: spectroscopic – virtual observatory tools – infrared: stars

1. Introduction

The arms of spiral galaxies have long been known to be regions of intense stellar formation, a consequence of the formation of the galaxies themselves. For instance, [Lin & Shu \(1964\)](#) and [Lin et al. \(1969\)](#) proposed, in the framework of the density wave theory, that spiral arms are formed through the propagation of linear discontinuities of the average Galactic gravitational field, which enhances their local density. When fast-rotating clouds of gas and dust encounter a slower density wave, their intrinsic density may therefore increase such that they meet the Jeans criterion and collapse, triggering star formation. Even though this explanation is still controversial, it is at least observationally clear that giant molecular clouds (GMCs) and HII regions are preferentially located in the arms of the Milky Way ([Caswell & Haynes 1987](#); [Dame et al. 2001](#)), where the number of short-lived O/B massive stars is consequently very high. Interestingly, [Sana et al. \(2012\)](#) showed that at least 70% of massive stars interact with a nearby massive companion or, in other words, that most O/B stars are found in binary systems. Even if the authors argue that a third of them will end up in binary mergers, a significant population of high mass X-ray binaries (HMXBs), consisting of a neutron star (NS) or a black hole (BH) accreting from a massive O/B star, must therefore be distributed in the spiral arms

of the Milky Way, a statement supported by two recent studies reported in [Bodaghee et al. \(2012\)](#) and [Coleiro & Chaty \(2013\)](#).

The last decade has seen a renewed scientific interest in HMXBs, following the launch of the International Gamma-Ray Astrophysics Laboratory (INTEGRAL, [Winkler et al. 2003](#)) in October 2002. Indeed, INTEGRAL performed a 20–100 keV survey of the Galactic plane which led to the detection of more than 700 hard X-ray sources ([Bird et al. 2010](#)), including about 400 new or previously poorly studied INTEGRAL gamma-ray (IGR) sources. The subsequent multiwavelength follow-ups (see e.g. [Tomsick et al. 2008](#); [Chaty et al. 2008](#); [Rahoui et al. 2008](#); [Rahoui & Chaty 2008](#); [Tomsick et al. 2012](#); [Coleiro et al. 2013](#)) showed that a significant fraction of these new sources were actually HMXBs in which a NS fed on the stellar winds of a blue supergiant through Bondi-Hoyle processes, known as NS-supergiant X-ray binaries (NS-SGXBs). Not only did these results increase the fraction of NS-SGXBs from 10% of all known HMXBs to about 40% today, but these new NS-SGXBs also appear to exhibit extreme behaviours that were not predicted. Indeed, some are very obscured persistent sources suffering from a huge intrinsic extinction, with N_{H} as high as 10^{24} atoms cm^{-2} (such as IGR J16318–4848, [Matt & Guainazzi 2003](#)), and others are transient sources, completely undetectable in quiescence but randomly exhibiting X-ray flares

that can be as bright as the Crab nebula for time periods as short as a few hours; these are the so-called supergiant fast X-ray transients (SFXTs; [Negueruela et al. 2006](#)).

Although the origins of such properties are still a matter of debate (accretion from clumps of material in the stellar wind or magnetic barrier, see e.g. [Walter & Zurita Heras 2007](#); [Bozzo et al. 2008](#)), these NS-SGXs have opened up a new window on HMXB evolution and, as progenitors of NS-NS and NS-BH binaries, the formation of short gamma-ray bursts. Discovering and studying as many of them as possible is therefore crucial and the Norma arm, as the most active star-forming region in the Milky Way, is the best candidate for this purpose. In 2011, we therefore performed a *Chandra* ACIS survey of a $2^\circ \times 0.8$ area of the Norma arm to detect new 0.5–10 keV sources with hard X-ray spectra, in particular low luminosity HMXBs fainter than the 10^{34} erg s⁻¹ minimum level usually encountered (see [Reig 2011](#), for a recent review). The results of the NARCS survey are comprehensively presented in [Fornasini et al. \(2014\)](#) and we refer to that work for more details. In this paper, we report on the near-infrared (near-IR) photometric and spectroscopic observations which were carried out to pinpoint the near-IR counterparts of the newly discovered hard X-ray sources and identify those we believed to be HMXB candidates. Section 2 describes the data and the reduction process. The results are presented in Sect. 3. We discuss them and conclude in Sect. 4.

2. Observations

To optimize the detection of new HMXBs, our *Chandra* survey of the Norma arm was complemented with a near-IR photometric mapping of the same region, followed by near-IR spectroscopy of the most promising counterparts. The latter were selected and ranked on the basis of their fulfillment of six criteria: (1) X-ray brightness high enough to place good constraints on the source's X-ray spectral parameters; (2) a high column density ($N_{\text{H}} > 10^{22}$ atoms cm⁻²) to exclude foreground sources; (3) a hard X-ray spectrum with a photon index $\Gamma < 2$, which is typical for HMXBs; (4) X-ray variability, which is often seen in HMXBs; (5) a counterpart with $J-K$ colour > 1.5 , indicating that it is also subject to significant absorption; and (6) the reliability of the near-IR counterpart.

Allocating 0, 0.5, or 1 when a criterium was not met, partially met, or fully met, respectively, the number of criteria fulfilled ranged from 1.5 to 6 for the selected sources. The column density and X-ray photon index of the sources were measured through X-ray spectral fitting of the *Chandra* spectra (averaged when a source was present in several pointings) with XSPEC ([Arnaud 1996](#)). We principally made use of the absorbed power-law model TBABS×PEGPWLW although, when a spectrum was found to be very soft ($\Gamma \geq 4$), a thermal plasma model TBABS×VAPEC was also used to obtain a reliable estimate of the flux. Furthermore, to investigate the presence of an intrinsic component of absorption, we also measured the total Galactic column density along the line of sight (LOS) of each source using the relation $N_{\text{H}_{\text{I}+\text{H}_2}}(\text{ISM}) = N_{\text{H}_{\text{I}}}(\text{ISM}) + 2N_{\text{H}_2}(\text{ISM})$. We assessed the neutral hydrogen column density $N_{\text{H}_{\text{I}}}(\text{ISM})$ from the Leiden/Argentine/Bonn Survey ([Kalberla et al. 2005](#)). In addition, the molecular hydrogen column density $N_{\text{H}_2}(\text{ISM})$ was estimated from the MWA CO survey ([Bronfman et al. 1989](#)) using the $N_{\text{H}_2}/I_{\text{CO}}$ factor derived in [Dame et al. \(2001\)](#).

Finally, the reliabilities R of the near-IR counterparts of the *Chandra* sources were estimated following the analytic treatment introduced in [Sutherland & Saunders \(1992\)](#), which is based on the positional uncertainties of the X-ray and near-IR

positions, the distances between the X-ray and near-IR counterparts, and the density of near-IR sources in the vicinity of the X-ray positions. In this framework, R is the probability for a near-IR source of being the real counterpart of an X-ray source. Summing up all the $1 - R$ values, we therefore expect about 0.4 spurious X-ray/near-IR associations in our sample.

2.1. Near-infrared photometry

We performed the observations on 2011 July 19 with the NOAO Extremely Wide Field Infrared Mosaic (NEWFIRM) mounted on the 4 m Blanco telescope at the Cerro Tololo Inter-America Observatory (CTIO). Each NEWFIRM image is divided into four extensions and covers a $28' \times 28'$ field of view with a 0.4 plate scale; this allowed us to observe about 60% of the $2^\circ \times 0.8$ Norma region mapped with *Chandra* in the J , H , and K s bands. For each pointing, the exposure time in each filter was set to 150 s divided into ten dithered four-extension frames for median sky construction. Conditions were clear and the seeing was less than $1''.2$ during the whole night.

We reduced the data with the dedicated IRAF ([Tody 1993](#)) package NFEINTERN. It is composed of several routines that perform the common tasks for near-IR imaging, tailored for wide-field mosaics. The first-pass reduction consisted in bad pixel removal, dark subtraction, linearity correction, flatfielding, and median sky subtraction. The astrometry of each cleaned four-extension frame was calibrated to the world coordinate system (WCS) by deriving the astrometric transformations through comparison with the 2 Micron All Sky Survey catalogue (2MASS, [Skrutskie et al. 2006](#)). The four extensions were then combined into a single image before median stacking. We finally flux-calibrated all the images by deriving the photometric solutions (zero-point magnitudes, atmospheric extinction, and colour terms) through relative photometry using the 2MASS catalogue as a reference. While not as robust as the use of photometric standard stars, we estimate that the measured magnitudes are accurate to about 0.1 mag in each filter, although statistical errors are lower.

As already mentioned, our NEWFIRM observations covered roughly 60% of the *Chandra* field. We completed and complemented the near-IR survey using the Vista Variables in the Via Lactae (VVV, [Minniti et al. 2010](#)), 2MASS ([Skrutskie et al. 2006](#)), and Deep Near Infrared Survey of the Southern Sky (DENIS, [Epchtein et al. 1999](#)) database¹ for the sources we could not observe or which were saturated.

2.2. Near-infrared spectroscopy

Based on the aforementioned criteria, we selected 45 sources and we observed most of them from 2012 June 1 to 4 with the Ohio State Infrared Imager/Spectrometer (OSIRIS) mounted on the 4m SOAR telescope at CTIO. We made use of the cross-dispersed mode with a slit of $1''$ in width, which allowed us to obtain simultaneous J , H , and K -band spectra with an $R \sim 1200$ spectral resolution using the standard ABBA nodding technique for background subtraction. Each night, standard stars were observed in similar conditions for telluric absorption lines removal. We reduced the data with the IRAF routines of the ECHELLE package. The basic steps consisted in bad pixel correction, dark subtraction, linearity correction, flatfielding, sky

¹ <http://irsa.ipac.caltech.edu/applications/BabyGator/> (2MASS and DENIS) and http://horus.roe.ac.uk:8080/vdfs/vregion_form.jsp (VVV)

subtraction, and spectral extraction along the dispersion axis. The spectra were then wavelength-calibrated through comparison with those of an Argon lamp taken before and after each exposure.

Weather and atmospheric conditions were unfortunately not optimal, with thin clouds most of the nights and a seeing higher than $1''.3$. Thus, the signal-to-noise ratio (S/N) of all the spectra are lower than we expected. Consequently, the *J*-band spectra we obtained are too noisy, and we do not use them in this study. Furthermore, the faintest sources in our sample were hard to observe in the *H* and *K* bands. This is the reason why we only report on 20 sources (see Fig. 1 for their *K*s-band counterparts); near-IR spectroscopy of the rest of our sample is on-going and will be presented in another paper.

3. Results and analysis

To strengthen the identification of the X-ray emitters, we made use of the quantile analysis techniques developed in Hong et al. (2004), and we refer to Fornasini et al. (2014) for a complete description. Roughly, it allows the derivation of two energy-binning independent quantities Q_x (which measures the hardness of a spectrum) and Q_y (which depends on how broad or narrow a spectrum is). By placing a source in a Q_x vs. Q_y diagram, it is therefore possible to get a rough measurement of its X-ray spectral characteristics. The quantile diagram for the 20 sources in our sample is displayed in Fig. 2. We divided it into five groups labelled from A to E. Again, comprehensive information can be found in Fornasini et al. (2014), but we can summarize their characteristics as follows:

- *group A*: low column density sources, most likely X-ray active low mass stars and interacting binaries.
- *group B*: similar to group A with a significant population of cataclysmic variables (CVs). Owing to their low column densities, sources in groups A and B are likely foreground objects and their unabsorbed luminosities will thus be estimated for a typical 1 kpc distance, when unknown.
- *group C*: intermediate column density consistent with a 3–5 kpc distance. Likely populated with CVs, LMXBs, and HMXBs. A 5 kpc distance is used for unabsorbed luminosity calculation.
- *group D*: high column density sources, probably located in the Norma arm or beyond. Hard spectra typical of intermediate polars (IPs) or HMXBs. However, some of the sources without near-IR counterparts may be Type II active galactic nuclei (AGN).
- *group E*: highly absorbed sources with softer spectra than group D, likely containing a significant number of isolated high mass stars and colliding wind binaries (CWBs). Sources without near-IR counterparts are likely Type I AGN. The unabsorbed luminosities of sources in Groups D and E are assessed for a 10 kpc distance, typical of the far Norma arm.

Table 1 lists the X-ray characteristics of the 20 sources (X-ray coordinates, quantile groups, X-ray and total ISM column densities N_H and N_{H+H_2} , photon indices Γ or plasma temperatures kT , unabsorbed 0.5–10 keV luminosities) as well as the reliability of the near-IR counterparts. The NEWFIRM and VVV near-IR counterparts are listed in Table 2 and those from 2MASS and DENIS are listed in Table 3. We note that all the magnitudes are given in their original photometric systems. Finally, we also retrieved the GLIMPSE (Benjamin et al. 2003; Churchwell et al. 2009) and WISE (Wright et al. 2010) mid-infrared (mid-IR) counterparts of most of the 20 sources (see Table 4).

We identified the companion stars of the *Chandra* sources from the near-IR spectra, relying on several near-IR spectroscopic atlases to isolate important emission and/or absorption features. We specifically made use of Wallace & Hinkle (1996, 1997), Meyer et al. (1998), Förster Schreiber (2000), Ivanov et al. (2004), and Rayner et al. (2009) for cool stars, as well as Hanson et al. (1996, 1998, 2005), Morris et al. (1996), Blum et al. (1997), Clark & Steele (2000), Steele & Clark (2001), and Repolust et al. (2005) for hot stars.

The 20 sources in our sample are divided into two near-IR spectral groups, six with spectra dominated by hydrogen-like species, in emission for all but one (spectra are displayed in Figs. 3, 5, 7, and 9 and features are listed in Table 5), and 14 with spectra typical of cool stars (spectra are displayed in Figs. 10–14 and the important features are listed Table 6).

3.1. Sources with near-IR spectra dominated by hydrogen-like species

3.1.1. Sources 239 and 1326

Sources 239 and 1326 were detected as relatively bright X-ray point sources with *Chandra*. They both suffer from a high column density $N_H \sim 1.0\text{--}1.5 \times 10^{23}$ atoms cm^{-2} , possibly slightly in excess of the total galactic column density along their LOS N_{H+H_2} (ISM) $\sim (7\text{--}9) \times 10^{22}$ atoms cm^{-2} , but uncertainties are high. Furthermore, both are located at almost the same spot in the quantile diagram (Group D, Fig. 2), a hint that they belong to the same subclass of X-ray emitters. Nonetheless, source 239 is likely constant (30% probability) and source 1326 is likely not (0.02% probability of being constant), while source 1326 may also be harder with $\Gamma = 1.2_{-2.0}^{+2.7}$ compared to $\Gamma = 2.7_{-1.5}^{+2.0}$ for source 239.

In the near-IR domain, both sources are constant. Alternative *J*, *H*, and *K*s magnitudes are 15.65 ± 0.01 , 13.48 ± 0.01 , and 12.16 ± 0.01 for source 239 (from VVV), and 14.55 ± 0.04 , 12.73 ± 0.04 , and 11.60 ± 0.04 for source 1326 (from 2MASS). Their near-IR spectra are also almost identical (see Fig. 3); we detect strong and narrow emission lines (roughly 300–500 km s^{-1} wide) from the whole Brackett series, He I $\lambda 20586$ Å, Fe II $\lambda 15778$, $\lambda 16878$ Å, as well as very faint emission of Na I $\lambda 22090$ Å. Overall, these spectra are consistent with those of early Be III/V stars presented in Clark & Steele (2000) and Steele & Clark (2001). However, we also detect, in both spectra, several emission lines centred at 15 842 Å, 15 964 Å, 17 110 Å, 17 455 Å, and 20 456 Å that could be identified with [Fe II]. As stressed in Morris et al. (1996) and Lamers et al. (1998), the presence of such features would be more consistent with narrow-emission-line massive stars with strongly irradiated outflows, such as B[e] supergiants (sgB[e]) or luminous blue variables (although, by definition, we expect LBVs to be strongly variable). These stars are known to exhibit a mid-IR excess due to a complex circumstellar environment in which warm dust is produced. To investigate the presence of such an excess, we built the spectral energy distributions (SEDs) of sources 239 and 1326 using their near-IR magnitudes (completed with those in *Y* and *Z* bands from VVV) as well as their *Spitzer*/IRAC fluxes at 3.6, 4.5, 5.8, and 8.0 μm . We then fitted these SEDs first with a single absorbed 20 000 K black body mimicking the stellar emission of a blue star, then adding a complementary black body to take into account a possible excess, using Galactic extinction laws from Fitzpatrick (1999) in the optical/near-IR and Chiar & Tielens (2006) in the mid-IR. For both sources, the best fits were obtained with two black bodies, the reduced χ^2 being half

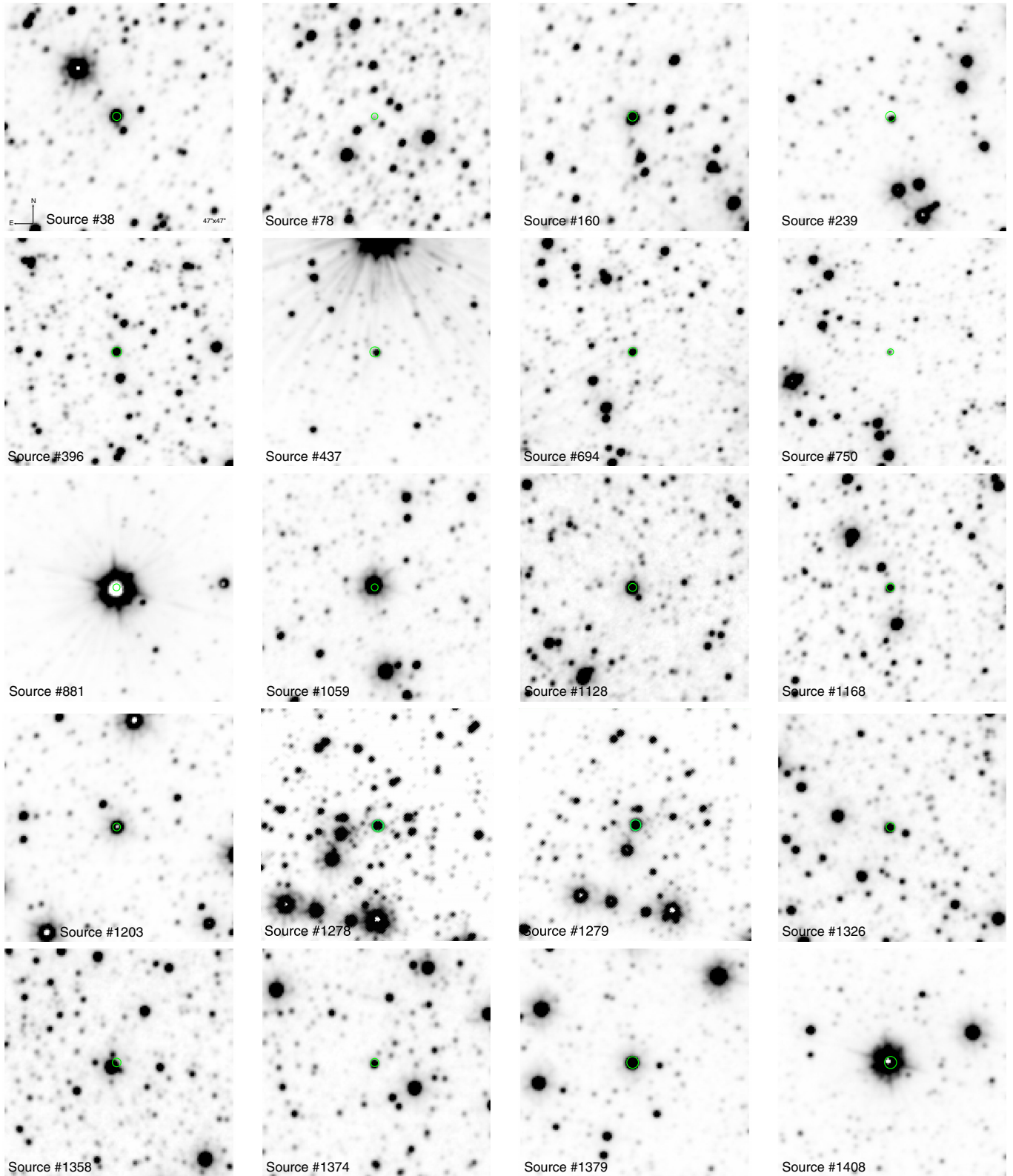


Fig. 1. VVV *Ks*-band counterparts of the newly discovered hard X-ray sources we identified through near-IR spectroscopy with OSIRIS. *Chandra* position error circles (green) are superimposed. Field of view is $47'' \times 47''$ and orientation north (up) and east (left).

the value of the single black body case (see Fig. 4 for plots and best-fit parameters). We stress that the fits were also performed with stellar temperatures as free parameters, and it is then possible to describe the SEDs with single black bodies; however, their best-fit temperatures reach the minimum allowed value of

3000 K, which is not realistic. We also fitted the SEDs fixing the stellar temperatures to lower and higher values (10 000 K, 15 000 K, 25 000 K, 30 000 K, and 35 000 K) and the mid-IR excess is still present. Thus, despite the simplistic use of spherical black bodies (see e.g. [Chaty & Rahoui 2012](#)), we believe

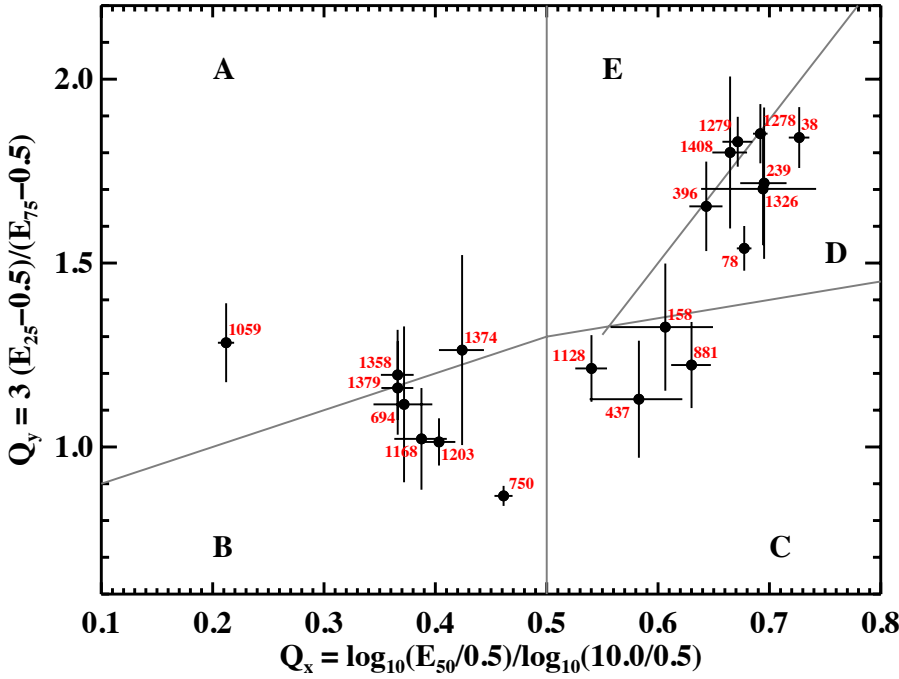


Fig. 2. Q_X vs. Q_Y quantile diagram of the 20 *Chandra* sources we identified through near-IR spectroscopy. E_{25} , E_{50} , and E_{75} are the energies below which the net counts are equal to 25%, 50%, and 75% of the total counts, respectively.

Table 1. List of the 20 new X-ray sources discovered during our survey of the Norma arm with *Chandra*, the companion stars of which we identified through near-IR spectroscopy.

No.	IAU name CXOU J	Quantile group	RA (J2000) (hms)	Dec (J2000) (dms)	$N_{\text{H}+\text{H}_2}$ (ISM) ($\times 10^{22} \text{cm}^{-2}$)	N_{H} (X-ray) ($\times 10^{22} \text{cm}^{-2}$)	Γ	kT (keV)	$F_{0.5-10}$ ($\times 10^{-13} \text{cgs}$)	R
38	163329.5-473332	D	16 33 29.58	-47 33 32.8	5.9	$21.3^{+10.4}_{-9.0}$	$2.6^{+1.4}_{-1.3}$	—	3.05	0.994
78	163355.1-473804	D	16 33 55.11	-47 38 04.9	7.0	$2.4^{+1.1}_{-0.9}$	0.5 ± 0.4	—	10.0	0.994
158	163443.0-472603	C/D	16 34 43.05	-47 26 03.3	7.0	$4.4^{+1.9}_{-2.9}$	$1.5^{+1.2}_{-1.0}$	—	0.71	0.990
239	163515.1-472304	D	16 35 15.19	-47 23 04.0	8.9	$12.7^{+10.5}_{-6.1}$	$2.7^{+2.0}_{-1.5}$	—	0.78	0.989
396	163553.5-470037	D/E	16 35 53.52	-47 00 37.1	4.9	$8.3^{+3.9}_{-3.1}$	$2.8^{+1.1}_{-1.0}$	—	1.26	0.898
437	163607.0-471434	C	16 36 07.03	-47 14 34.8	8.4	$2.8^{+2.4}_{-1.6}$	$1.7^{+1.2}_{-1.0}$	—	0.58	0.984
694	163734.1-464630	A/B	16 37 34.11	-46 46 30.1	7.7	$0.4^{+0.5}_{-0.4}$	$2.4^{+0.9}_{-0.7}$	—	0.50	0.983
750	163750.8-465545	B	16 37 50.82	-46 55 45.3	9.4	$0.11^{+0.1}_{-0.1}$	1.2 ± 0.1	—	10.3	0.989
881	163832.2-470339	C	16 38 32.20	-47 03 39.2	8.5	$1.3^{+0.8}_{-0.6}$	0.8 ± 0.4	—	2.19	0.883
1059	163925.7-465303	A	16 39 25.73	-46 53 03.6	8.0	$0.3^{+0.4}_{-0.2}$	—	0.5 ± 0.2	0.88	0.989
1128	163944.3-465614	C	16 39 44.39	-46 56 14.9	6.4	$2.6^{+1.0}_{-0.9}$	2.2 ± 0.6	—	3.82	0.994
1168	163955.2-463145	B	16 39 55.25	-46 31 45.8	6.2	$0.3^{+0.3}_{-0.2}$	1.8 ± 0.4	—	1.19	0.986
1203	164002.4-463200	B	16 40 02.43	-46 32 00.6	6.2	0.7 ± 0.3	$2.4^{+0.4}_{-0.4}$	—	1.51	0.981
1278	164029.4-462328	D/E	16 40 28.97	-46 23 27.6	7.8	$15.2^{+8.7}_{-5.2}$	—	$2.0^{+2.0}_{-0.8}$	1.18	0.986
1279	164029.5-462329	D/E	16 40 29.68	-46 23 29.2	7.8	$13.2^{+4.4}_{-3.4}$	—	$2.6^{+2.1}_{-0.8}$	2.89	0.986
1326	164045.5-464607	D	16 40 45.54	-46 46 07.1	7.3	$13.8^{+20.3}_{-11.2}$	$1.2^{+2.7}_{-2.0}$	—	0.79	0.991
1358	164105.5-465108	A/B	16 41 05.54	-46 51 08.4	6.0	$0.5^{+0.4}_{-0.3}$	$2.5^{+0.6}_{-0.5}$	—	1.28	0.993
1374	164122.8-464529	A/B	16 41 22.87	-46 45 29.4	6.8	0.4 ± 0.3	$1.5^{+0.5}_{-0.3}$	—	2.45	0.991
1379	164130.8-463048	A/B	16 41 30.88	-46 30 48.8	7.0	$0.01^{+0.24}_{-0.01}$	$2.3^{+0.4}_{-0.2}$	—	4.10	0.982
1408	164204.5-464341	D/E	16 42 04.59	-46 43 41.3	6.3	$7.8^{+7.7}_{-4.2}$	$2.1^{+1.6}_{-1.2}$	—	1.71	0.983

Notes. Column 1: source number in our catalogue. Column 2: *Chandra* name. Column 3: quantile group. Columns 4 and 5: *Chandra* equatorial coordinates. Column 6: total interstellar column density of the source along its line of sight. Column 7: X-ray column density of the source N_{H} . Column 8: Power-law photon index Γ when a power-law model better describes the *Chandra* spectrum. Column 9: Plasma temperature kT in keV when a thermal plasma model better describes the *Chandra* spectrum. Column 10: 0.5–10 keV unabsorbed flux $F_{0.5-10}$. Column 11: Reliability R of the near-infrared counterpart.

that sources 239 and 1326 do exhibit near- and mid-IR excesses. Whether the latter are due to warm dust in sgB[e]/LBV stellar winds or free-free emission from the decretion disc of Be stars is a matter of debate. We note that the derived A_V values are consistent with a minimum 10 kpc distance for the two sources (using the three-dimensional extinction law from Marshall et al. 2006). If the stars do reside at this distance, they must have radii

larger than $20 R_{\odot}$ – whatever the stellar temperature we consider in the fits – which are more consistent with early-B supergiants than giant or main-sequence stars (Vacca et al. 1996; Searle et al. 2008). Furthermore, the unabsorbed 0.5–10 keV luminosities at 10 kpc are about $10^{33} \text{erg s}^{-1}$ for the two sources, which is possible for isolated O/B supergiants but at least 1 or 2 orders of magnitude larger than what is expected from isolated Be III/V stars

Table 2. NEWFIRM and VVV counterparts of the 20 *Chandra* sources identified through near-IR spectroscopy in this study.

No.	NEWFIRM			VVV						
	<i>J</i> (mag)	<i>H</i> (mag)	<i>Ks</i> (mag)	VVV ID.	Dist. ($''$)	<i>Z</i> (mag)	<i>Y</i> (mag)	<i>J</i> (mag)	<i>H</i> (mag)	<i>Ks</i> (mag)
38	15.29 ± 0.07	11.92 ± 0.10	10.13 ± 0.06	515727245968	0.12	–	19.33 ± 0.15	15.21 ± 0.01	11.99 ± 0.01	Sat.
78	16.43 ± 0.07	15.45 ± 0.10	14.99 ± 0.09	515726911773	0.06	17.02 ± 0.01	16.74 ± 0.02	16.46 ± 0.01	15.77 ± 0.04	15.38 ± 0.02
158	12.96 ± 0.03	11.39 ± 0.05	10.58 ± 0.05	515727009565	0.06	16.44 ± 0.01	14.88 ± 0.01	12.96 ± 0.01	11.30 ± 0.01	10.58 ± 0.01
239	15.74 ± 0.07	13.60 ± 0.08	12.12 ± 0.06	515720865399	0.13	–	18.42 ± 0.08	15.65 ± 0.01	13.48 ± 0.01	12.16 ± 0.01
396	15.48 ± 0.05	13.18 ± 0.10	11.99 ± 0.07	515720906266	0.96	–	18.16 ± 0.06	15.49 ± 0.01	13.19 ± 0.01	12.19 ± 0.01
437	14.51 ± 0.04	12.85 ± 0.06	12.01 ± 0.08	515720093751	0.42	17.53 ± 0.02	15.97 ± 0.01	14.31 ± 0.01	12.82 ± 0.01	12.00 ± 0.01
694	12.53 ± 0.05	11.75 ± 0.07	10.26 ± 0.06	515720390344	0.44	13.56 ± 0.01	13.17 ± 0.01	13.29 ± 0.01	12.70 ± 0.01	12.26 ± 0.01
750	No Cov.	No Cov.	No Cov.	515720338856	0.22	15.08 ± 0.01	15.06 ± 0.01	14.91 ± 0.01	14.64 ± 0.01	14.27 ± 0.01
881	No Cov.	No Cov.	No Cov.	515725172945	0.66	Sat.	Sat.	Sat.	Sat.	Sat.
1059	No Cov.	No Cov.	No Cov.	515725290815	0.30	Sat.	Sat.	Sat.	Sat.	Sat.
1128	No Cov.	No Cov.	No Cov.	515725286315	0.08	14.71 ± 0.01	13.63 ± 0.01	12.53 ± 0.01	11.48 ± 0.01	10.76 ± 0.01
1168	No Cov.	No Cov.	No Cov.	515720689720	0.26	12.75 ± 0.01	12.63 ± 0.01	12.23 ± 0.01	12.14 ± 0.01	11.83 ± 0.01
1203	No Cov.	No Cov.	No Cov.	515720696577	0.38	Sat.	Sat.	Sat.	Sat.	Sat.
1278	No Cov.	No Cov.	No Cov.	515721533405	0.18	–	–	17.72 ± 0.06	13.61 ± 0.01	11.26 ± 0.01
1279	No Cov.	No Cov.	No Cov.	515721039612	0.30	–	–	16.02 ± 0.01	12.19 ± 0.04	Sat.
1326	No Cov.	No Cov.	No Cov.	515725424702	0.20	17.59 ± 0.02	16.28 ± 0.01	14.56 ± 0.01	12.71 ± 0.01	11.48 ± 0.01
1358	No Cov.	No Cov.	No Cov.	515725732674	0.13	Sat.	11.45 ± 0.01	10.96 ± 0.01	10.46 ± 0.01	10.18 ± 0.01
1374	No Cov.	No Cov.	No Cov.	515725467960	0.17	14.27 ± 0.01	13.84 ± 0.01	13.36 ± 0.01	12.56 ± 0.01	12.38 ± 0.01
1379	No Cov.	No Cov.	No Cov.	515725581165	0.38	Sat.	Sat.	Sat.	Sat.	Sat.
1408	No Cov.	No Cov.	No Cov.	515725521664	0.41	Sat.	Sat.	Sat.	Sat.	Sat.

Notes. Column 1: source number in our catalogue. Columns 2 to 4: NEWFIRM *J*, *H*, and *Ks* magnitudes. Column 5: IDs of the VVV counterparts. Column 6: distance ($''$) of the VVV counterparts to the corresponding X-ray sources. Columns 7 to 11: VVV *Z*, *Y*, *J*, *H*, and *Ks* magnitudes. “Sat.” means that the source is detected but saturated, while a “–” means that the source is not detected in the corresponding filter.

Table 3. 2MASS and DENIS counterparts of the 20 *Chandra* sources identified through near-IR spectroscopy in this study.

No.	2MASS					DENIS				
	IAU name 2MASS J	Dist. ($''$)	<i>J</i> (mag)	<i>H</i> (mag)	<i>Ks</i> (mag)	IAU name DENIS J	Dist. ($''$)	<i>I</i> (mag)	<i>J</i> (mag)	<i>Ks</i> (mag)
38	16332956-4733327	0.14	15.26 ± 0.04	11.75 ± 0.03	9.99 ± 0.022	163329.6-473332	0.29	–	15.30 ± 0.15	10.01 ± 0.05
78	–	–	–	–	–	–	–	–	–	–
158	16344306-4726033	0.17	12.63 ± 0.03	11.26 ± 0.02	10.54 ± 0.02	163443.0-472603	0.31	17.38 ± 0.18	12.97 ± 0.07	10.54 ± 0.06
239	16351519-4723042	0.25	>15.97	>13.77	12.27 ± 0.04	–	–	–	–	–
396	16355350-4700381	1.02	>15.69	13.30 ± 0.03	12.20 ± 0.03	–	–	–	–	–
437	–	–	–	–	–	163607.0-471434	0.45	–	14.54 ± 0.11	12.04 ± 0.10
694	16373414-4646299	0.40	12.96 ± 0.04	12.15 ± 0.03	11.89 ± 0.04	163734.1-464630	0.16	14.02 ± 0.11	12.59 ± 0.12	11.50 ± 0.12
750	16375079-4655452	0.26	14.69 ± 0.03	14.57 ± 0.06	>15.19	163750.7-465545	0.54	14.66 ± 0.11	14.30 ± 0.15	–
881	16383217-4703397	0.68	6.89 ± 0.02	5.44 ± 0.04	4.72 ± 0.02	163832.1-470339	0.50	11.07 ± 0.03	6.38 ± 0.09	3.87 ± 0.16
1059	16392581-4653002	3.50	9.30 ± 0.02	8.69 ± 0.03	8.43 ± 0.02	163925.7-465300	3.05	0.65 ± 0.03	9.32 ± 0.07	8.49 ± 0.05
1128	16394439-4656149	0.09	12.42 ± 0.02	11.26 ± 0.02	10.86 ± 0.02	163944.3-465614	0.13	15.40 ± 0.05	12.41 ± 0.07	10.77 ± 0.07
1168	16395525-4631454	0.27	12.22 ± 0.03	11.97 ± 0.06	11.83 ± 0.04	163955.2-463145	0.24	12.91 ± 0.02	12.30 ± 0.08	11.68 ± 0.09
1203	16400244-4632002	0.40	9.60 ± 0.02	8.84 ± 0.02	8.51 ± 0.02	164002.4-463200	0.38	11.19 ± 0.02	9.59 ± 0.06	8.46 ± 0.05
1278	16402896-4623276	0.04	>15.68	13.63 ± 0.12	11.29 ± 0.07	164029.0-462327	1.28	17.83 ± 0.17	–	11.13 ± 0.08
1279	16402966-4623295	0.36	>15.16	>11.48	9.84 ± 0.05	164029.6-462329	0.75	–	15.81 ± 0.23	9.69 ± 0.06
1326	16404554-4646072	0.14	14.55 ± 0.04	12.73 ± 0.04	11.60 ± 0.04	164045.5-464607	0.46	–	14.42 ± 0.11	11.73 ± 0.08
1358	16410554-4651085	0.15	11.04 ± 0.03	10.39 ± 0.02	10.16 ± 0.02	164105.5-465108	0.18	12.22 ± 0.02	11.07 ± 0.07	10.13 ± 0.06
1374	16412285-4645292	0.25	13.34 ± 0.02	12.57 ± 0.02	12.33 ± 0.03	164122.8-464529	0.24	14.77 ± 0.04	13.44 ± 0.10	12.27 ± 0.11
1379	16413093-4630488	0.48	9.76 ± 0.02	9.30 ± 0.02	9.13 ± 0.02	164130.9-463048	0.33	10.55 ± 0.03	9.83 ± 0.06	9.14 ± 0.05
1408	16420462-4643411	0.41	8.24 ± 0.03	6.73 ± 0.04	5.87 ± 0.03	164204.6-464341	0.33	14.13 ± 0.04	8.53 ± 0.08	6.01 ± 0.03

Notes. Column 1: source number in our catalogue. Column 2: IAU names of the 2MASS counterparts. Column 3: distance ($''$) of the 2MASS counterparts to the corresponding X-ray sources. Columns 4 to 6: 2MASS *J*, *H*, and *Ks* magnitudes. Column 7: IAU names of the DENIS counterparts. Column 8: Distance ($''$) of the DENIS counterparts to the corresponding X-ray sources. Columns 9 to 11: DENIS *I*, *J*, and *Ks* magnitudes. A “–” means that the source is not detected in the corresponding filter.

near-IR spectroscopy with ESO/ISAAC and the results of these observations are reported in [Davies et al. \(2012\)](#) and [de la Fuente et al. \(2013\)](#). The authors derived a 11 ± 2 kpc distance and showed that Mercer 81 was mainly populated with nitrogen-rich

Wolf-Rayet and blue supergiant stars; in particular, sources 1278 and 1279 (labelled 8 and 2 in these papers, see Fig. 2 in [Davies et al. 2012](#)) were identified as late WN Wolf-Rayet stars (see Fig. 3 in [de la Fuente et al. 2013](#)). We concur with these results.

Table 4. GLIMPSE and *WISE* counterparts of the 20 *Chandra* sources identified through near-IR spectroscopy in this study.

No.	GLIMPSE						WISE					
	IAU name	Dist. (")	$F_{3.6}$ (mJy)	$F_{4.5}$ (mJy)	$F_{5.8}$ (mJy)	$F_{8.0}$ (mJy)	IAU name WISE J	Dist. (")	$F_{3.4}$ (mJy)	$F_{4.6}$ (mJy)	F_{12} (mJy)	F_{22} (mJy)
38	G336.7280+00.2037	0.28	85.79 ± 5.25	53.95 ± 2.36	54.59 ± 2.46	26.23 ± 2.19	163329.53-473331.8	1.09	80.44 ± 2.07	64.35 ± 1.48	–	–
78	–	–	–	–	–	–	–	–	–	–	–	–
158	G336.9601+00.1363	0.18	27.93 ± 1.17	17.88 ± 0.98	12.76 ± 0.71	7.80 ± 0.42	163443.04-472603.7	0.43	29.56 ± 0.92	16.75 ± 0.86	–	–
239	G337.0580+00.1032	0.14	13.02 ± 0.58	11.95 ± 0.62	10.51 ± 0.50	–	–	–	–	–	–	–
396	G337.4072+00.2754	0.15	8.21 ± 0.20	5.25 ± 0.30	4.86 ± 0.22	–	–	–	–	–	–	–
437	G337.2613+00.0906	0.30	6.47 ± 0.49	4.54 ± 0.46	2.56 ± 0.38	–	–	–	–	–	–	–
694	G337.7742+00.2214	0.10	7.20 ± 0.27	4.59 ± 0.26	3.08 ± 0.25	–	–	–	–	–	–	–
750	–	–	–	–	–	–	–	–	–	–	–	–
881	G337.6719-00.0926	0.21	4486 ± 378	2552 ± 114	2420 ± 40	1348 ± 23	163832.16-470339.7	0.11	5681 ± 493	4213 ± 220	634.6 ± 17.2	299.1 ± 58.4
1059	G337.9058-00.0881	1.31	155.3 ± 3.1	100.8 ± 3.0	72.17 ± 1.34	38.52 ± 0.86	163925.74-465303.2	3.11	154.9 ± 3.2	94.36 ± 2.12	52.03 ± 2.02	115.4 ± 5.4
1128	G338.2265+00.0846	0.15	18.68 ± 0.08	11.15 ± 0.04	8.10 ± 0.03	5.20 ± 0.03	163944.37-465615.0	0.22	12.91 ± 0.02	7.31 ± 0.41	–	–
1168	G337.9008-00.1634	0.20	5.92 ± 0.37	4.11 ± 0.34	2.23 ± 0.27	–	–	–	–	–	–	–
1203	G338.2371+00.0665	0.20	131.4 ± 6.0	73.45 ± 3.65	52.48 ± 1.95	29.84 ± 0.84	164002.45-463159.9	0.31	155.4 ± 3.9	79.45 ± 2.36	20.23 ± 1.48	–
1278	G338.3941+00.1040	0.21	36.24 ± 2.68	47.31 ± 3.37	36.51 ± 2.28	2.03 ± 1.43	–	–	–	–	–	–
1279	G338.3951+00.1022	0.46	146.6 ± 19.3	181.6 ± 7.9	163.9 ± 5.6	103.7 ± 3.6	–	–	–	–	–	–
1326	G338.1427-00.1817	0.15	16.19 ± 0.69	15.67 ± 0.56	13.86 ± 0.70	6.76 ± 0.36	–	–	–	–	–	–
1358	G338.1178-00.2799	0.21	26.30 ± 2.28	17.62 ± 0.64	12.13 ± 0.70	6.57 ± 0.17	164105.56-465108.5	0.13	28.49 ± 0.76	15.15 ± 0.44	–	–
1374	G338.2212-00.2546	0.33	4.25 ± 0.28	2.26 ± 0.31	–	2.51 ± 0.52	–	–	–	–	–	–
1379	G338.4200-00.1104	0.23	60.68 ± 2.85	37.25 ± 1.75	27.72 ± 1.13	16.73 ± 0.64	164130.91-463048.9	0.27	72.89 ± 1.81	39.82 ± 1.02	–	–
1408	G338.3224-00.3244	0.16	3120 ± 78	2353 ± 100	2424 ± 76	1601 ± 43	164204.62-464341.1	0.04	1593 ± 84	2113 ± 73	653.8 ± 1.1	1662 ± 93

Notes. Column 1: source number in our catalogue. Column 2: IAU names of the GLIMPSE counterparts. Column 3: distance (") of the GLIMPSE counterparts to the corresponding X-ray sources. Columns 4 to 7: GLIMPSE 3.6 μ m, 4.5 μ m, 5.8 μ m, and 8.0 μ m flux densities (mJy). Column 8: IAU names of the *WISE* counterparts. Column 9: distance (") of the *WISE* counterparts to the corresponding X-ray sources. Columns 10 to 13: *WISE* $W1$ (3.4 μ m), $W2$ (4.6 μ m), $W3$ (12 μ m), and $W4$ (22 μ m) flux densities (mJy). A “–” means that the source is not detected in the corresponding filter.

Table 5. *H*- and *K*-band spectral features of hydrogen-like lines dominated sources.

	Source 239		Source 750		Source 1168		Source 1278		Source 1279		Source 1326	
	\tilde{W}^a (Å)	$FWHM^b$ (km s ⁻¹)	\tilde{W} (Å)	$FWHM$ (km s ⁻¹)								
H I 15087 Å	–	–	–	–	–	–	–	–	–	–	*	*
H I 15137 Å	–	–	–	–	–	–	–	–	–	–	–4.71 ± 0.59	348 ± 76
H I 15196 Å	*	*	*	*	–	–	–	–	–	–	–4.67 ± 0.46	259 ± 73
H I 15265 Å	*	*	–3.59 ± 0.99	508 ± 216	–	–	–	–	–	–	–3.82 ± 0.51	277 ± 105
H I 15346 Å	–6.21 ± 0.61	369 ± 70	*	*	–	–	–4.65 ± 0.91	370 ± 91	–	–	–6.65 ± 0.57	329 ± 57
Fe II 15403 Å	*	*	–	–	–	–	–4.29 ± 0.53	355 ± 111	–	–	*	*
H I 15443 Å	–10.61 ± 0.99	589 ± 92	*	*	–	–	–	–	–	–	–4.71 ± 0.59	304 ± 84
H I 15561 Å	–8.98 ± 0.48	395 ± 38	–2.60 ± 1.15	374 ± 224	8.37 ± 1.71	1073 ± 202	–	–	–	–	12.28 ± 0.88	371 ± 49
H I 15705 Å	–5.31 ± 0.51	253 ± 61	*	*	–	–	–	–	–	–	–7.91 ± 0.52	344 ± 46
Fe II 15778 Å	–1.69 ± 0.62	258 ± 196	–	–	–	–	–	–	–	–	–2.62 ± 0.98	556 ± 298
[Fe II] 15842 Å	–5.29 ± 0.63	416 ± 86	–	–	–	–	–	–	–	–	–3.57 ± 0.35	524 ± 88
H I 15885 Å	–7.65 ± 0.61	268 ± 45	*	*	2.62 ± 0.42	720 ± 233	–7.73 ± 0.92	975 ± 142	–3.34 ± 0.66	841 ± 211	–9.09 ± 0.53	409 ± 45
[Fe II] 15954 Å	–1.41 ± 0.77	324 ± 75	–	–	–	–	–4.12 ± 0.65	446 ± 111	–	–	–	–
He I 16008 Å	–	–	–	–	–	–	–4.77 ± 0.85	604 ± 140	–	–	–	–
H I 16114 Å	–8.15 ± 0.54	374 ± 48	–4.64 ± 1.94	384 ± 224	4.53 ± 0.96	1184 ± 311	*	*	–3.98 ± 0.94	680 ± 203	–5.01 ± 0.57	313 ± 79
H I 16412 Å	–7.70 ± 0.50	332 ± 33	–2.29 ± 0.60	259 ± 166	4.79 ± 0.82	850 ± 168	–1.88 ± 0.77	500 ± 291	–5.34 ± 0.87	872 ± 169	–9.23 ± 0.71	429 ± 35
H I 16811 Å	–11.1 ± 0.79	507 ± 40	–5.04 ± 0.65	489 ± 95	4.31 ± 0.70	762 ± 257	*	*	–6.11 ± 1.29	1077 ± 251	–9.03 ± 0.62	379 ± 36
Fe II 16878 Å	–6.00 ± 0.65	540 ± 80	–	–	–	–	–	–	–	–	–5.01 ± 0.96	590 ± 170
He I 16919 Å	–	–	–	–	–	–	*	*	–	–	*	*
He I+[Fe II] 17007 Å	–	–	–1.71 ± 0.35	183 ± 64	–	–	–3.32 ± 0.52	297 ± 87	–11.0 ± 1.12	1458 ± 217	–1.94 ± 1.19	504 ± 362
[Fe II] 17110 Å	*	*	–	–	–	–	–	–	–	–	*	*
H I 17367 Å	–7.56 ± 0.52	432 ± 56	–9.26 ± 0.89	799 ± 92	6.89 ± 1.00	1233 ± 201	–5.72 ± 1.31	726 ± 189	–12.0 ± 1.11	1209 ± 135	–8.22 ± 0.75	540 ± 60
[Fe II] 17455 Å	*	*	–	–	–	–	–	–	–	–	–	–
[Fe II] 20456 Å	*	*	–	–	–	–	–	–	–	–	–	–
He I 20586 Å	–6.50 ± 0.93	514 ± 105	–17.8 ± 0.80	532 ± 37	–	–	–10.1 ± 1.57	1105 ± 171	*	*	–7.68 ± 0.69	304 ± 57
He I 21127 Å	–	–	–	–	–	–	–7.71 ± 0.91	593 ± 98	–11.4 ± 1.36	761 ± 86	–	–
Mg II 21376 Å	–	–	–	–	2.97 ± 0.53	410 ± 188	–	–	–	–	–	–
H I 21661 Å	–10.1 ± 0.65	159 ± 53	–42.6 ± 1.14	750 ± 19	12.4 ± 1.19	1199 ± 130	–29.4 ± 1.33	1175 ± 52	–45.1 ± 1.34	1318 ± 56	–10.9 ± 0.72	220 ± 41
He II 21891 Å	–	–	–	–	–	–	–6.90 ± 1.27	570 ± 113	–8.57 ± 1.01	533 ± 73	–	–
Na I 22090 Å	*	*	–	–	–	–	–	–	–	–	*	*

Notes. A “*” means that the line is detected but difficult to properly measure, while a “–” means that the line is not detected. ^(a) Equivalent width (Å). ^(b) Full-width at half-maximum (km s⁻¹).

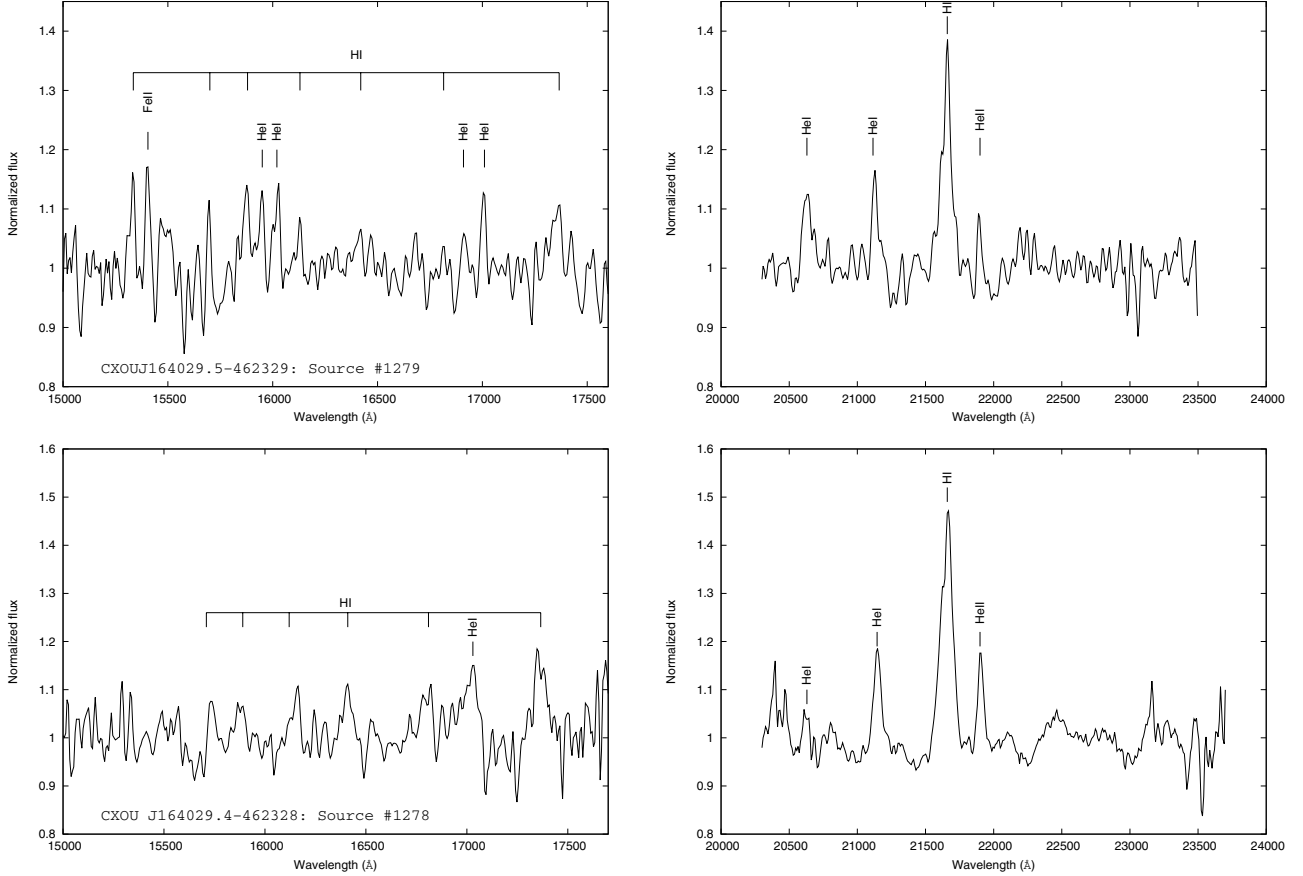


Fig. 5. Near-IR *H*-band (*left*) and *K*-band (*right*) spectra of Source 1278 (*top*) and Source 1279 (*bottom*).

Table 6. Equivalent widths (\AA) of the main absorption lines for cool stars detected in the *H* and *K*-band spectra of 14 sources in our sample.

No.	Fe I 15 830 \AA	Si I 15 890 \AA	CO 16 198 \AA	Mg I 17 115 \AA	H I 21 663 \AA	Na I 22 075 \AA	Ca I 22 637 \AA	CO 22 957 \AA	CO 23 245 \AA	CO 23 464 \AA	CO 23 550 \AA
38	2.88 ± 0.51	1.28 ± 0.40	7.35 ± 0.77	1.73 ± 0.45	2.43 ± 0.95	1.57 ± 0.55	5.25 ± 1.00	43.45 ± 1.50	10.88 ± 0.55	–	12.06 ± 0.40
78	–	2.44 ± 0.51	2.57 ± 1.12	–	3.37 ± 0.85	1.12 ± 0.40	–	9.13 ± 0.72	3.09 ± 0.35	3.24 ± 0.61	–
158	1.56 ± 0.73	1.74 ± 0.48	5.19 ± 1.94	1.31 ± 0.75	4.72 ± 0.61	3.17 ± 0.66	–	10.51 ± 0.75	4.05 ± 0.50	–	–
396	–	2.71 ± 0.46	3.28 ± 0.63	3.43 ± 0.86	1.81 ± 0.85	1.83 ± 0.76	–	8.41 ± 0.70	5.49 ± 0.73	–	–
437	–	1.75 ± 0.62	1.58 ± 0.68	1.84 ± 0.56	3.99 ± 0.69	–	–	6.50 ± 0.49	6.95 ± 0.73	–	–
694	–	1.71 ± 0.48	3.20 ± 1.04	2.01 ± 0.57	4.11 ± 0.75	–	–	6.10 ± 1.01	–	3.48 ± 0.81	–
881	–	2.11 ± 0.57	7.16 ± 0.70	–	2.50 ± 0.68	2.79 ± 0.57	0.80 ± 0.40	27.91 ± 2.01	16.29 ± 0.94	2.48 ± 0.52	12.28 ± 0.88
1059	–	–	–	–	0.96 ± 0.40	–	4.26 ± 0.82	5.79 ± 1.07	4.95 ± 0.75	–	–
1128	2.21 ± 0.56	2.31 ± 0.77	1.46 ± 0.68	–	5.44 ± 1.05	–	2.18 ± 0.86	4.37 ± 0.98	2.27 ± 0.68	–	–
1203	–	2.64 ± 0.65	2.49 ± 0.70	–	–	1.66 ± 0.50	2.13 ± 0.90	13.12 ± 1.02	5.90 ± 0.65	–	–
1358	–	2.24 ± 0.50	2.50 ± 0.81	1.90 ± 1.05	1.49 ± 0.75	1.41 ± 0.51	–	5.29 ± 1.04	–	–	5.73 ± 0.71
1374	–	1.88 ± 0.41	2.87 ± 1.32	2.28 ± 0.52	3.60 ± 0.70	2.22 ± 0.57	1.24 ± 0.61	4.05 ± 0.57	8.86 ± 0.72	–	–
1379	–	1.51 ± 0.57	–	1.62 ± 0.50	4.96 ± 0.72	–	–	3.41 ± 0.97	–	–	–
1408	–	–	4.43 ± 0.61	–	–	–	1.42 ± 0.41	13.95 ± 0.87	5.11 ± 0.48	–	8.94 ± 0.45

Notes. A “–” means that the line is not detected.

Our OSIRIS spectra, displayed in Fig. 5, are similar to theirs, and our derived He II $\lambda 21891 \text{ \AA}$ /H I $\lambda 21661 \text{ \AA}$ ratios – i.e. about 0.23 and 0.19 for sources 1278 and 1279, respectively – are consistent with a WN8 classification (expected values between 0.1 and 0.4, see Table 5 in Crowther et al. 2006). Moreover, Fig. 6 displays a 0.5–10 keV *Chandra* image of Mercer 81 on which we superimposed the near-IR positions of sources 1278 and 1279 (green circles) as well as those of the remaining eight sources identified as Wolf-Rayet or supergiant stars (yellow circles). It is clear that only sources 1278 and 1279 are detected with *Chandra*, although all sources suffer from the same extinction; this indicates

that sources 1278 and 1279 are more effective X-ray emitters than other Wolf-Rayet stars in Mercer 81. To check this hypothesis, we can follow Mauerhan et al. (2010) to estimate the X-ray to bolometric luminosity ratios L_X/L_{Bol} for the two sources and compare them to the expected 10^{-7} value for isolated Wolf-Rayet stars. Using the observed ($J - K_s$) and ($H - K_s$) colours, the intrinsic ($J - K_s$)₀ and ($H - K_s$)₀ colours for WN8 stars given in Crowther et al. (2006), i.e. 0.13 and 0.11, respectively, as well as the relations $A_{K_s} = (1.44 \pm 0.01) \times E(H - K_s)$ and $A_{K_s} = (0.494 \pm 0.006) \times E(J - K_s)$ from Nishiyama et al. (2006), we derive an average K_s -band extinction $A_{K_s} = 3.11 \pm 0.03$

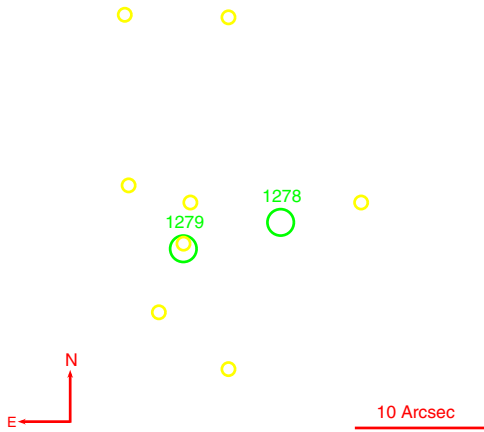


Fig. 6. *Chandra* 0.5–10 keV image of Mercer 81, ObsID 11008. Sources 1278 and 1279 are clearly detected as bright X-ray sources (green circles), but the remaining eight listed as WN Wolf-Rayet or supergiant stars in Davies et al. (2012) and de la Fuente et al. (2013) (yellow circles) are not. The detected northern source does not belong to Mercer 81 and is likely foreground.

for each source. For a 10 kpc distance, this results in the absolute *Ks*-band magnitudes -6.85 ± 0.04 and -8.27 ± 0.06 for source 1278 and 1279, respectively. Using the *Ks*-band bolometric correction for WN8 stars given in Crowther et al. (2006), i.e. -3.4 , we thus find that the total bolometric luminosities are $L_{\text{Bol}} \approx 10^6 L_{\odot} \approx 3.9 \times 10^{39} \text{ erg s}^{-1}$ and $L_{\text{Bol}} \approx 3.8 \times 10^6 L_{\odot} \approx 1.5 \times 10^{40} \text{ erg s}^{-1}$, for sources 1278 and 1279, respectively. This yields $L_{\text{X}}/L_{\text{Bol}}$ ratios of about 3.6×10^{-7} and 2.5×10^{-7} for sources 1278 and 1279, respectively. These values are slightly in excess of the canonical 10^{-7} , and this may indicate that the two sources are CWBs, producing X-rays in the shocks of their colliding winds. Another explanation is that both sources are HMXBs in which the compact object accretes material from the strong stellar winds of Wolf-Rayet stars, but as already mentioned, the fact that their X-ray spectra are better described by thermal plasma models disfavors this possibility.

3.1.3. Source 1168

We detected source 1168 with *Chandra* as a bright and variable hard X-ray point source ($\Gamma = 1.8^{+0.4}_{-0.4}$) with a column density much lower than that of ISM along its entire LOS ($N_{\text{H}} \sim 2.9 \times 10^{21} \text{ atoms cm}^{-2}$ vs. $N_{\text{H}+\text{H}_2}(\text{ISM}) \sim 6.2 \times 10^{22} \text{ atoms cm}^{-2}$). The near-IR spectrum displayed in Fig. 7 is typical of massive stars. In the *H* band, we clearly detect absorption features of the Brackett series centred at 15 561 Å, 15 885 Å, 16 114 Å, 16 412 Å, 16 811 Å, and 17 367 Å. The absence of Brackett lines below 15 500 Å is also consistent with a IV/V luminosity class (Meyer et al. 1998), while the strength of the detected H I lines and the lack of He I are characteristic of late-B/early-A stars (Blum et al. 1997). In the *K* band, Br γ and Mg II 21376 Å, signatures of stellar winds, are present but the strength of Br γ and the absence of He I features point towards a IV/V class with a spectral type later than B8 (Hanson et al. 1996); we therefore conclude that source 1168 is a nearby B8-A3IV/V star. Figure 8 displays its optical to mid-IR SED built using archival fluxes from the VVV and GLIMPSE surveys and fitted with a

11 000 K temperature black body. Using the derived A_{V} value and the three-dimensional law of Marshall et al. (2006), we estimate its distance to be around 3.5 kpc, which results in a stellar radius $R_{*} \approx 4.9 R_{\odot}$, consistent with the typical radii of late-B/early-A subgiant stars listed in Pasinetti Fracassini et al. (2001). Moreover, such a distance gives a 0.5–10 keV unabsorbed luminosity of about $1.8 \times 10^{32} \text{ erg s}^{-1}$, i.e. at least one order of magnitude too high for an isolated B8-A3IV/V star (Berghöfer et al. 1996) and we tentatively classify source 1168 as a quiescent HMXB.

3.1.4. Source 750

Source 750 is one of the brightest X-ray sources that we detected with *Chandra*. It is variable and has a hard spectrum ($\Gamma = 1.2^{+0.1}_{-0.1}$) with a $N_{\text{H}} \sim 1.2 \times 10^{21} \text{ atoms cm}^{-2}$ column density; once corrected from absorption, its 0.5–10 keV luminosity at 1 kpc is about $1.2 \times 10^{32} \text{ erg s}^{-1}$. It is the hardest source of group B and its location in the quantile diagram is clearly separated from the other sources of the group, hinting at a distinct nature. More importantly, its X-ray light curve exhibits a 7150 s period (Fornasini et al. 2014) more likely related to the orbit or the spin period of a white dwarf (WD). Overall, the X-ray behaviour of source 750 is consistent with that of an intermediate polar (IP), in which a WD accretes from a main-sequence star via a truncated accretion disc (see Kuulkers et al. 2006, for a review).

In the near-IR domain, the source is variable, with $K_s = 14.27 \pm 0.01$ from VVV and $K_s > 15.19$ from 2MASS, pointing towards a contribution from an accretion stream. Moreover, its near-IR spectrum, displayed in Fig. 9, is clearly dominated by the whole Brackett series as well as He I $\lambda 17007$ Å and $\lambda 20586$ Å, all in emission. The lines are particularly strong in *K*, with equivalent widths of about 18 Å and 43 Å for He I and Br γ , respectively. Again, this spectrum is consistent with an accretion stream and is actually very similar to those of IPs presented in Dhillon et al. (1997) and Harrison et al. (2007); we therefore believe that source 750 is very likely an IP.

3.2. Sources with typical near-IR spectra of cool stars

In the *H* and *K* bands, cool stars are characterized by the presence of many absorption lines of Fe I, Mg I, Si I, Ca I, and Na I, but the detection of the CO (2,0) and CO (3,1) overtones in absorption beyond 22 900 Å is a clear indicator of their nature. The near-IR counterparts of the 14 sources presented in this section all exhibit at least one of these CO features and this is the reason why we classify them as cool stars. However, deriving a more accurate spectral classification is difficult because (1) the S/N of our spectra are not high enough to perform a quantitative comparison with existing near-IR libraries and (2) a possible veiling by the near-IR continuum of the component responsible for the soft X-ray emission would likely alter the equivalent width measurements. We therefore list tentative spectral types in Table 7 obtained by comparing the relative strength of the CO features at 16 190 Å and 22 957 Å as well as that of Br γ , the last being weak or absent for K/M stars. We nevertheless stress that this classification should be taken with caution due to the aforementioned limitations.

Determining the possible origin of the soft X-ray emission and thus the nature of the X-ray emitters is also not straightforward. On the one hand, the X-ray emission could stem

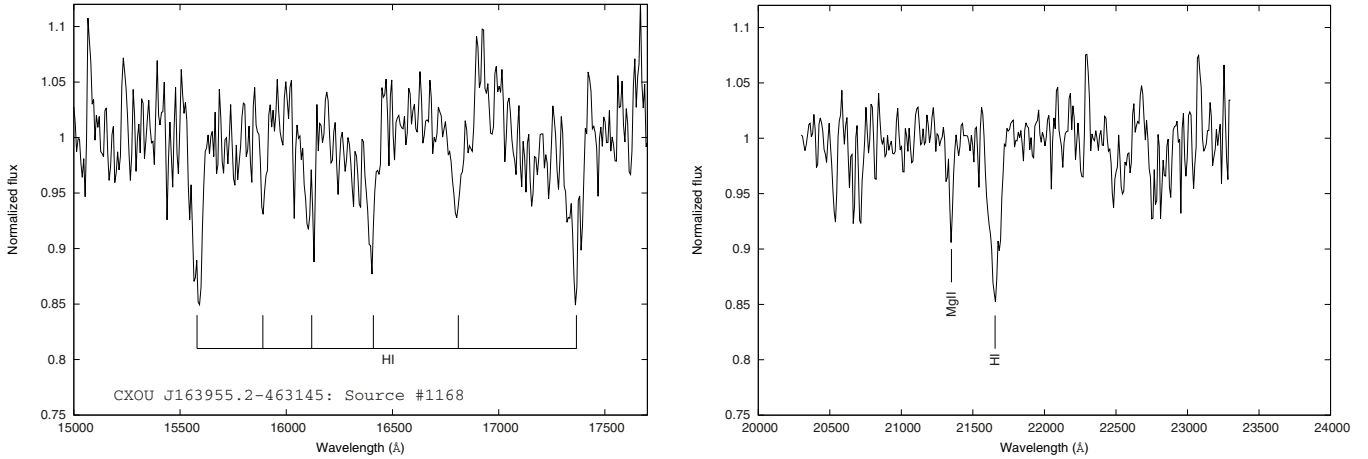


Fig. 7. Near-IR *H*-band (*left*) and *K*-band (*right*) spectra of Source 1168.

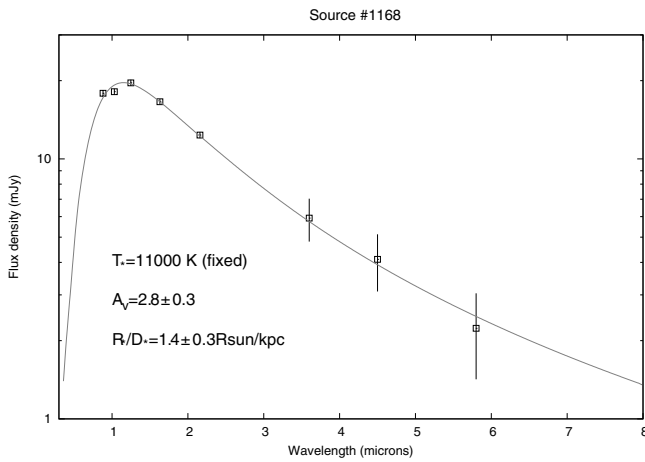


Fig. 8. Optical to mid-IR SED of source 1168. Uncertainties are given at 3σ .

from accreting binaries such as LMXBs, CVs, IPs, or symbiotic binaries (SBs). On the other hand, it could also come from foreground isolated low mass stars (iLMS) or coronally active binaries (ABs). Although discriminating between all these possibilities is difficult, the presence of near-IR emission lines, in particular H I, and/or near-IR variability can be a strong indicator of the presence of an accretion stream. The ISM extinction along the LOS and the X-ray luminosity also provide valuable information; for example iLMS are likely foreground objects and their X-ray luminosity is expected to be lower than 10^{30} erg s^{-1} (see e.g. Güdel & Nazé 2009). Finally, the positions of the sources in the Q_X vs. Q_Y diagram hint at common X-ray spectral properties, and therefore the following sections present the sources grouped by similar location in this diagram.

3.2.1. Groups A/B: sources 694, 1059, 1203, 1358 1374, and 1379

The six sources are weakly extinguished, with $N_H < 10^{22}$ atoms cm^{-2} , indicating that they are foreground objects. However, sources 694, 1203, 1358, 1374, and 1379 exhibit similar photon indices ($\Gamma = 2.4^{+0.9}_{-0.7}$, $\Gamma = 2.4 \pm 0.4$, $\Gamma = 2.5^{+0.6}_{-0.5}$, $\Gamma = 1.5^{+0.5}_{-0.3}$, and $\Gamma = 2.3^{+0.4}_{-0.2}$, respectively), while source 1059 is a much softer and better described by an absorbed thermal plasma model, with $kT = 0.5 \pm 0.2$ keV.

Table 7. Tentative spectral classification of the low mass stars in our sample, based on the relative strength of CO (6, 3) 16198 Å, Br γ , and CO (2, 0) 22957 Å.

No.	Relative strength	Spectral classification
38	Strong CO (6,3); No Br γ ; Strong CO (2,0)	Early MIII
78	Weak CO (6,3); Weak Br γ ; Strong CO (2,0)	Late G III
158	Weak CO (6,3); Strong Br γ ; Strong CO (2,0)	Early/mid GI-III
396	Medium CO (6,3); No Br γ ; Strong CO (2,0)	Mid/Late KI-III
437	Weak CO (6,3); Strong Br γ ; Medium CO (2,0)	Early GI-III
694	Medium CO (6,3); Strong Br γ ; Medium CO (2,0)	Early KI-III
881	Strong CO (6,3); Weak Br γ ; Strong CO (2,0)	Late K/Early MI-III
1059	No CO (6,3); No Br γ ; Medium CO (2,0)	Early MV
1128	No CO (6,3); Strong Br γ ; Medium CO (2,0)	GV
1203	Medium CO (6,3); No Br γ ; Strong CO (2,0)	Mid/Late KI-III
1358	Weak CO (6,3); Weak Br γ ; Medium CO (2,0)	Early KV
1374	Weak CO (6,3); Medium Br γ ; Weak CO (2,0)	Late G/Early KV
1379	No CO (6,3); Strong Br γ ; Weak CO (2,0)	Mid GIII
1408	Strong CO (6,3); No Br γ ; Strong CO (2,0)	KIII

Source 694 is the faintest, with a 0.5–10 keV luminosity at 1 kpc $\sim 6 \times 10^{30}$ erg s^{-1} compared to $\sim (1.1-5) \times 10^{31}$ erg s^{-1} for the other five sources.

These X-ray properties are consistent with those expected from all X-ray emitting low mass systems, including iLMSs and ABs, and do not specifically hint at the presence of accretion discs. However, we note that the near-IR spectrum of source 694 is the only one that convincingly exhibits emission lines. This source is also the only one with variable near-IR emission, with *J*, *H*, and *K*s magnitudes of 12.53 ± 0.05 , 11.75 ± 0.07 , and 10.26 ± 0.06 in NEWFIRM; 13.29 ± 0.01 , 12.70 ± 0.01 , and 12.26 ± 0.01 in VVV; and 12.96 ± 0.04 , 12.15 ± 0.03 , and 11.89 ± 0.04 in 2MASS. We therefore believe that source 694 is a quiescent accreting binary. The other five sources are likely isolated giant or main-sequence stars, although we stress that sources 1203 and 1379 may exhibit a variable emission at $3.5 \mu m$ with GLIMPSE and *WISE* fluxes of about 131.4 ± 6.0 mJy vs. 155.4 ± 3.9 mJy and 60.68 ± 2.85 mJy vs. 72.89 ± 1.81 mJy, respectively. We also note that the optical/near-IR counterpart of source 1059 is classified as an M4V star in Lépine & Gaidos (2011), in agreement with our own classification as an early main-sequence M star.

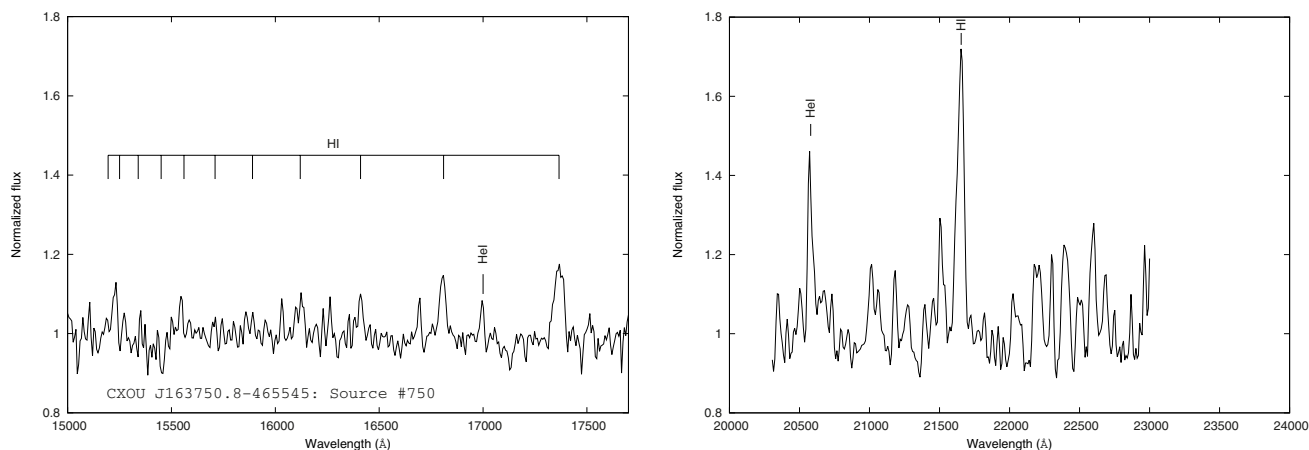


Fig. 9. Near-IR *H*-band (*left*) and *K*-band (*right*) spectra of Source 750.

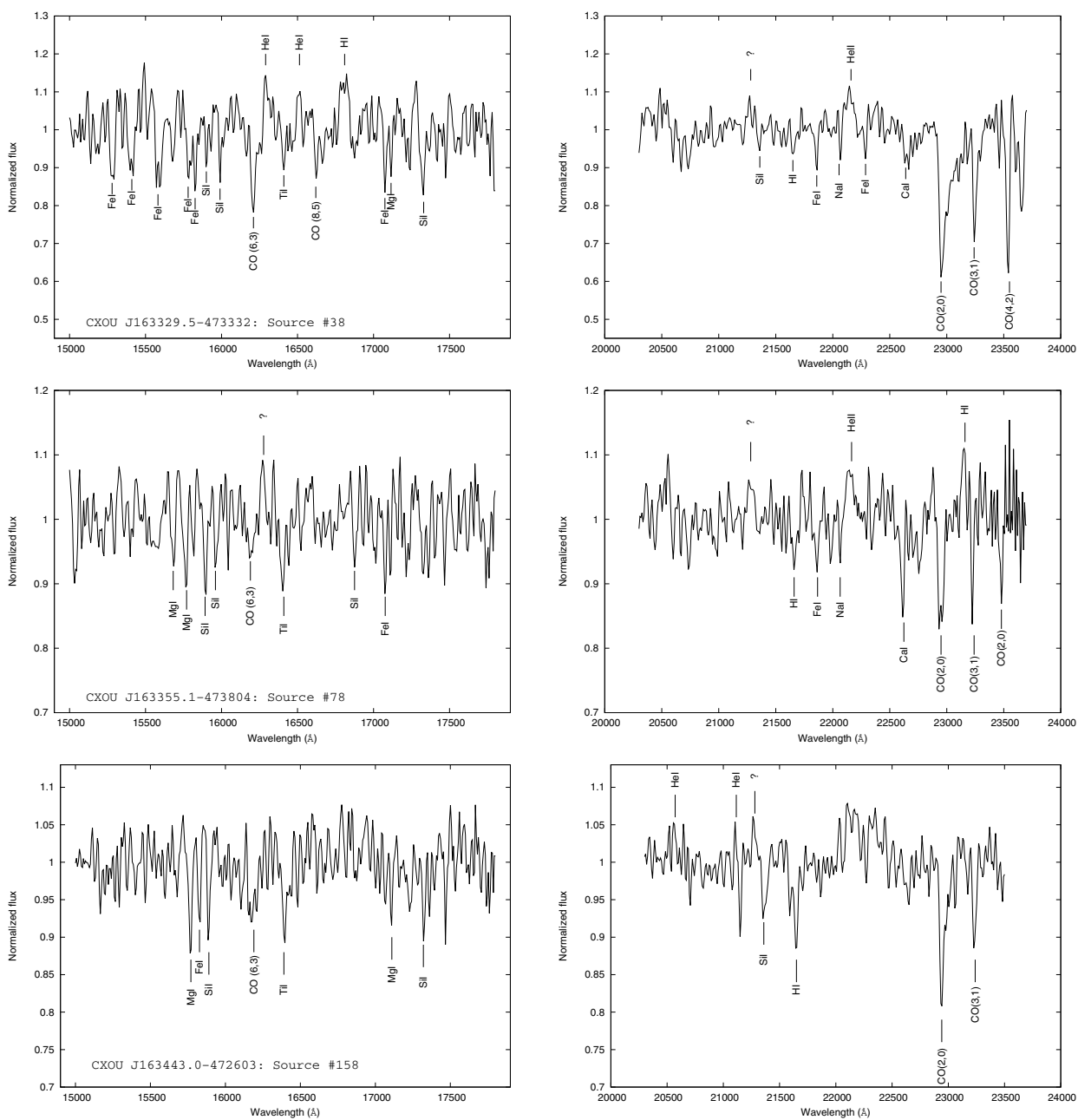


Fig. 10. Near-IR *H*-band (*left*) and *K*-band (*right*) spectra of Source 38 (*top*), Source 78 (*middle*), and Source 158 (*bottom*).

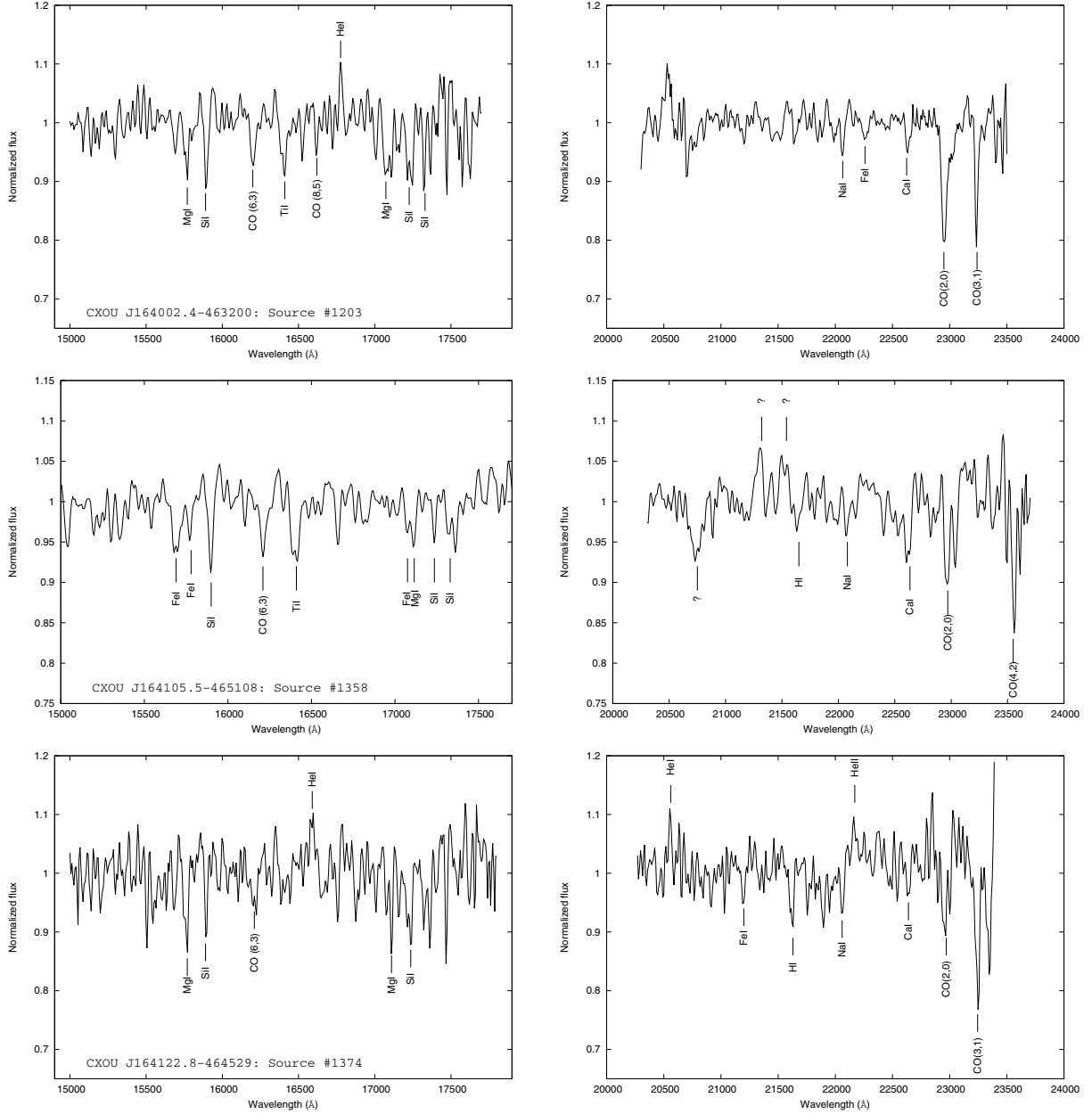


Fig. 11. Near-IR *H*-band (left) and *K*-band (right) spectra of Source 396 (top), Source 437 (middle), and Source 694 (bottom).

3.2.2. Group C: sources 158, 437, 881, and 1128

The four sources are more extinguished than the previous group of sources, with N_{H} values clustered in the range $(1-4.5) \times 10^{22}$ atoms cm^{-2} , lower than the total ISM extinction along their LOS; this extinction indicates that these sources are located in the near Norma arm. They also have harder spectra than the sources discussed in Sect. 3.2.1; sources 158, 437, and 1128 have a similar spectral index ($\Gamma = 1.5^{+1.2}_{-1.0}$, $\Gamma = 1.7^{+1.2}_{-1.0}$ and $\Gamma = 2.2 \pm 0.6$, respectively) while the spectrum of source 881 is even flatter, with $\Gamma = 0.8 \pm 0.4$. Their 0.5–10 keV unabsorbed luminosities at 5 kpc (2.1×10^{32} erg s^{-1} , 1.7×10^{32} erg s^{-1} , 1.1×10^{33} erg s^{-1} , and 5.1×10^{32} erg s^{-1} , respectively) are inconsistent with iLMSs or ABs and thus the four sources are likely accreting binaries. However, the presence of emission lines in their near-IR spectra is scarce, maybe because the accretion stream is less active. Furthermore, source 881 – the brightest X-ray emitter of the four – is convincingly variable in the

near-IR, with 2MASS magnitudes significantly fainter than the DENIS ones (J : 6.89 ± 0.02 vs. 6.38 ± 0.09 ; K_s : 4.72 ± 0.02 vs. 3.87 ± 0.16), as well as in the mid-IR, the GLIMPSE fluxes at $3.5 \mu\text{m}$ and $4.5 \mu\text{m}$ being lower than those from *WISE* at the same wavelengths ($3.5 \mu\text{m}$: 4486 ± 378 mJy vs. 5681 ± 493 mJy; $4.5 \mu\text{m}$: 2552 ± 114 mJy vs. 4213 ± 220 mJy). The lack of significant near-IR variability for the remaining sources may indicate that if accretion is occurring, it is weak. However, we note that source 1128 likely has variable mid-IR emission, with higher GLIMPSE fluxes at $3.5 \mu\text{m}$ and $4.5 \mu\text{m}$ with respect to *WISE* ($3.5 \mu\text{m}$: 18.68 ± 0.08 mJy vs. 12.91 ± 0.02 mJy; $4.5 \mu\text{m}$: 11.15 ± 0.04 mJy vs. 7.31 ± 0.41 mJy).

3.2.3. Groups D and E: sources 38, 78, 396, and 1408

Sources 38, 396, and 1408 suffer from an extinction likely higher than that along their LOS, having $N_{\text{H}} \geq 7.8 \times 10^{22}$ atoms cm^{-2} . They exhibit a similar photon index ($\Gamma = 2.6^{+1.4}_{-1.3}$, $\Gamma = 2.8^{+1.1}_{-1.0}$,

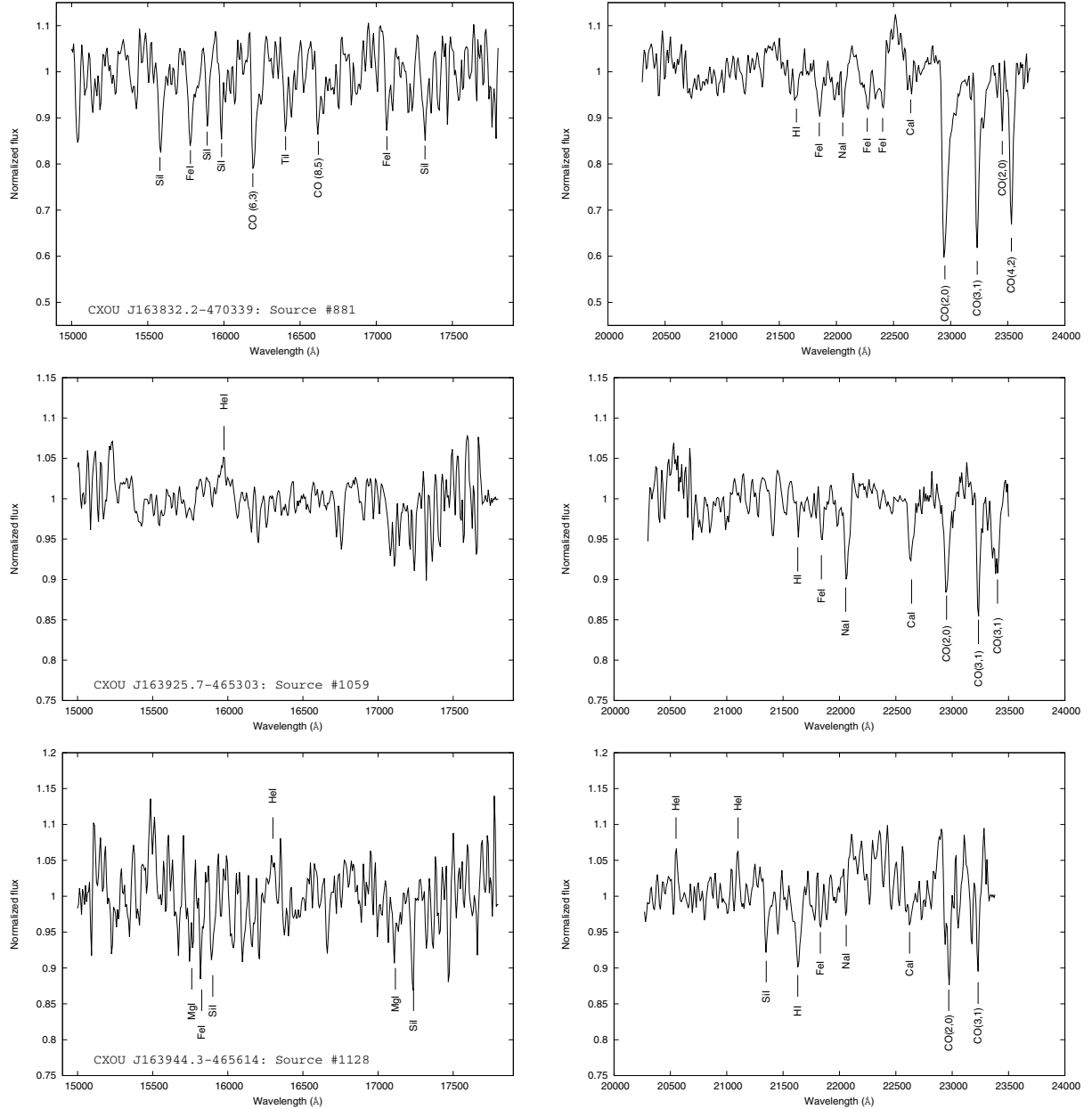


Fig. 12. Near-IR *H*-band (left) and *K*-band (right) spectra of Source 881 (top), Source 1059 (middle), and Source 1128 (bottom).

and $\Gamma = 2.1^{+1.6}_{-1.2}$, respectively) and are relatively bright X-ray emitters, with unabsorbed 0.5–10 keV luminosities assuming a 10 kpc distance of 3.7×10^{33} erg s $^{-1}$, 1.3×10^{33} erg s $^{-1}$, and 1.7×10^{33} erg s $^{-1}$, respectively. The properties of source 78 are slightly different, as it exhibits a lower column density along its LOS of $N_{\text{H}} \sim 2.4 \times 10^{22}$ atoms cm $^{-2}$ and is a lot harder, with $\Gamma = 0.5 \pm 0.4$ and a 0.5–10 keV luminosity at 5 kpc of about 3×10^{33} erg s $^{-1}$. That said, the X-ray properties of the four sources are inconsistent with those expected from iLMSs or ABs, and their X-ray emission likely stems from accretion.

The near-IR properties are in agreement with the latter hypothesis. The four sources exhibit emission lines in their spectra, hinting at an accretion stream presence. In addition, sources 78, 396, and 1408 are variable. Indeed, the near-IR magnitudes of source 78 decreased from VVV to NEWFIRM (*H*: 15.77 ± 0.04 vs. 15.45 ± 0.10 ; *Ks*: 15.38 ± 0.02 vs. 14.99 ± 0.09). Moreover, source 396 is undetected with DENIS and its 2MASS magnitudes are slightly higher than those of NEWFIRM and VVV

(*J* > 15.69, *H* = 13.30 ± 0.03 , and *Ks* = 12.20 ± 0.02 vs. *J* = 15.49 ± 0.01 , *H* = 13.19 ± 0.01 , and *Ks* = 12.0 ± 0.01). Likewise, the 2MASS *J* magnitude of source 1408 is lower than that measured in DENIS (8.24 ± 0.03 vs. 8.53 ± 0.08). Its GLIMPSE fluxes at 3.5 μm is also significantly lower than that from WISE (3120 ± 78 mJy vs. 1593 ± 84 mJy). Based on their X-ray and infrared behaviours and properties, it is therefore reasonable to conclude that all four sources are accreting binaries hosting giant stars.

4. Discussion and conclusion

We have conducted near-IR photometric and spectroscopic observations of 20 soft X-ray sources discovered during a *Chandra* survey of a $2^\circ \times 0.8$ region of the Norma arm. Our main goal was to detect new low-luminosity HMXBs, thought to be principally located in very active star-forming regions. We identify (1) two massive emission-line stars, possibly in HMXBs, exhibiting

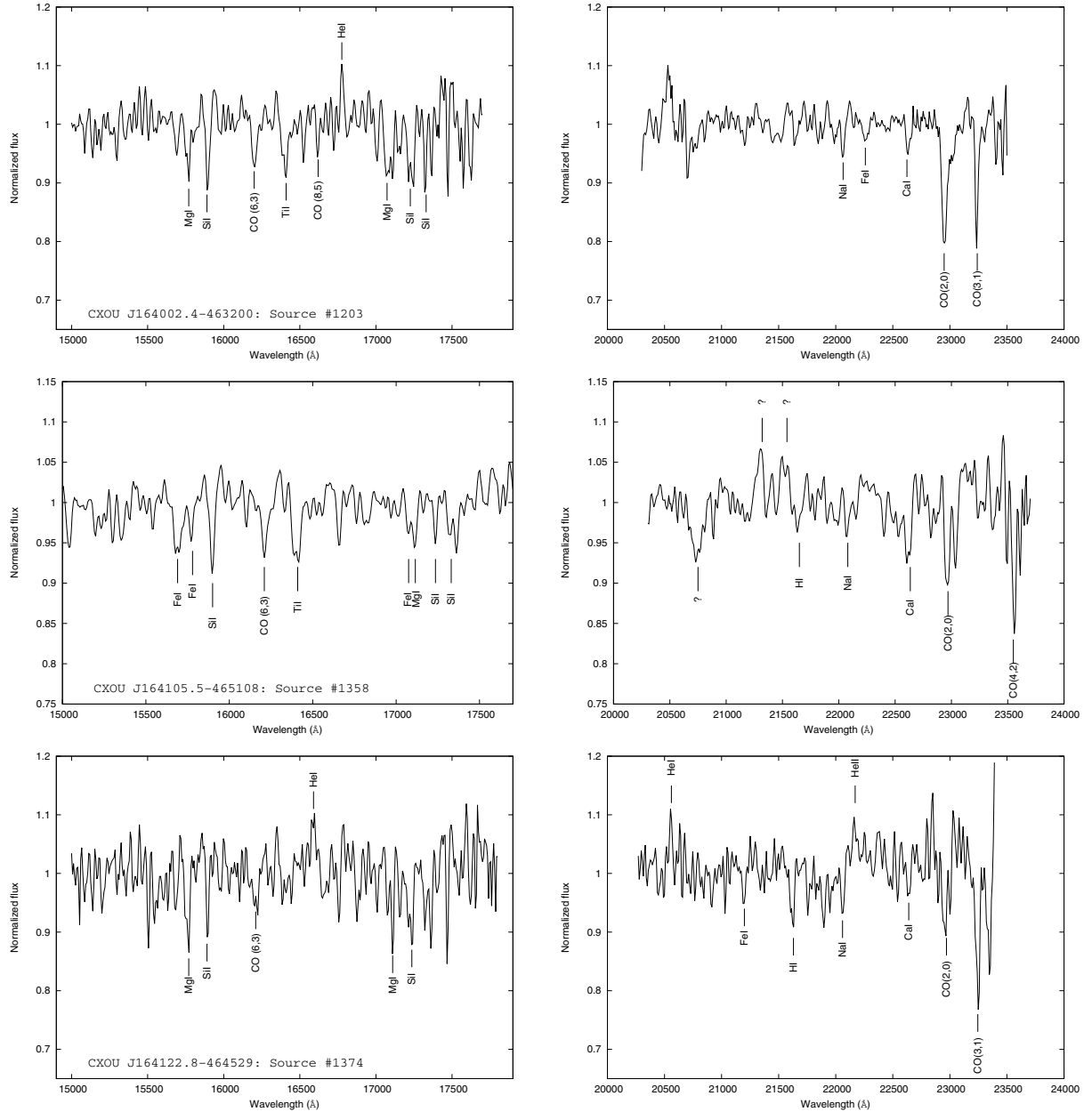


Fig. 13. Near-IR *H*-band (left) and *K*-band (right) spectra of Source 1203 (top), Source 1358 (middle), and Source 1374 (bottom).

near- and mid-IR excesses consistent with either free-free emission from the decretion discs of Be stars or warm dust in the stellar winds of peculiar massive stars such as sgB[e] or LBVs; (2) two WN8 Wolf Rayets, maybe in CWBs and located in the Mercer 81 massive star cluster; (3) a foreground B8-A3 IV/V star, likely in an HMXB; (4) one IP, the near-IR spectrum of which is dominated by the accretion disc; and (5) a foreground isolated M4V dwarf. Among the 13 remaining sources, four are likely isolated late-type giant or main-sequence stars, and nine are low mass accreting binaries.

4.1. The nature of the low mass accreting systems

Even if the outcome of the ongoing near-IR spectroscopy of additional NARCS sources may increase the number of detected massive stars, it is clear that our sample is dominated by low mass accreting binaries. However, it is difficult to be more

specific about the nature of the primaries (WDs, NSs, or BHs) or that of the systems themselves (LMXBs, CVs, or SBs). Based on the presence of many emission lines in their near-IR spectra, their relatively high 0.5–10 keV luminosity and the red giant nature of their companion stars, we can speculate that sources 38, 396, and 1408 are quiescent LMXBs in the outer Norma arm. It is, however, interesting that they all suffer from an intrinsic extinction in excess of the ISM along their LOS (especially source 38) and that they are located at a similar position in the quantile diagram as candidate HMXBs and CWBs. It is therefore possible that sources 38, 396, and 1408 actually are SBs in which the compact objects accrete material from the stellar winds of their late giant companion stars in an eccentric orbit. Whether the compact object is a WD or a NS is a matter of debate, but we stress that their X-ray and near-IR properties (in particular their relative X-ray hardness) could be consistent with the new and rare class of symbiotic X-ray binaries (SyXBs), in which a magnetized NS accretes matter from the wind of a red

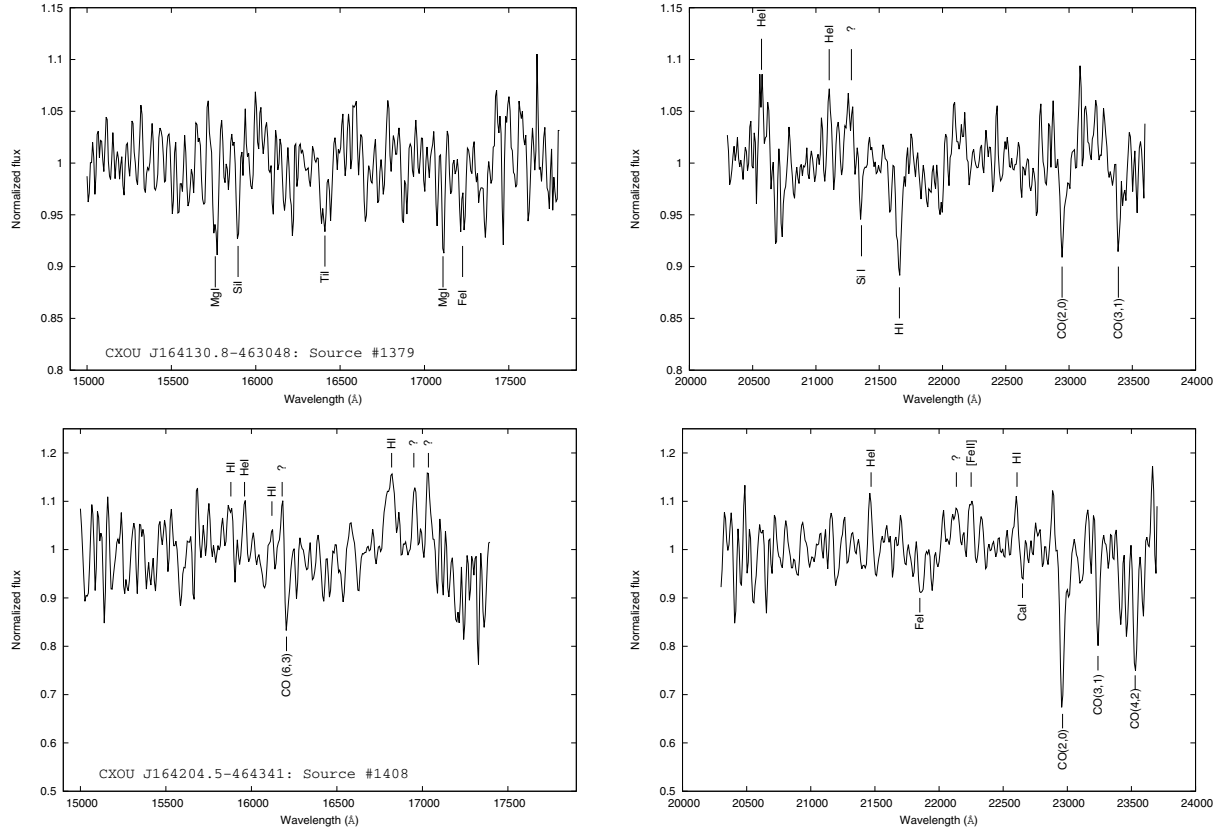


Fig. 14. Near-IR *H*-band (*left*) and *K*-band (*right*) spectra of Source 1379 (*top*) and Source 1408 (*bottom*).

giant (see Masetti et al. 2007; Corbet et al. 2008; DeWitt et al. 2013). Source 694 in groups A/B as well as sources 158, 437, 881, and 78 in groups C/D are also possible SBs but likely belong to two different classes. Indeed, source 694 has all the characteristics of a standard quiescent SB with a WD primary, i.e. a giant companion, weak extinction, and low 0.5–10 keV luminosity. In contrast, sources 78, 158, 437, and 881 exhibit X-ray luminosities of $(1-30) \times 10^{32} \text{ erg s}^{-1}$, are relatively extinguished, and have a hard spectrum. This behaviour may be more consistent with that expected from hard spectrum SBs, in which a WD accretes from a red giant through an accretion disc (dubbed as class δ ; see Luna et al. 2013). Finally, source 1128 has all the properties of a quiescent CV in the inner Norma arm, and likely hosts a WD accreting from a main-sequence companion.

4.2. The nature of the high mass systems

The low number of massive stars in our sample was expected because of their short lifetime. Nonetheless, the possible detection of up to three new HMXBs (sources 239, 1168, and 1326) in a region covering about one square degree is consistent with our prediction of three to four HMXBs per square degree with unabsorbed fluxes larger than $5 \times 10^{-14} \text{ erg cm}^{-2} \text{ s}^{-1}$ (Fornasini et al. 2014). One could argue that none of these sources is an HMXB, in particular because their unabsorbed luminosities are at least one order of magnitude lower than expected. However, these X-ray luminosities also seem too high to be those of isolated stars. A possible way to reconcile these discrepancies is that sources 239, 1326, and 1168 are quiescent HMXBs. We stress that SFXTs, which are transient sources, exhibit luminosities as low as $10^{32} \text{ erg s}^{-1}$ when in quiescence. Furthermore, such low luminosities have been observed in some Be X-ray binaries (see

e.g. V0332+53, Campana et al. 2002) and some γ -Cas analogs which could be – although this explanation is still controversial – WD-Be binaries (Nebot Gómez-Morán et al. 2013); such systems may represent up to 70% of all compact object-Be star associations (Raguzova 2001). More recently, Casares et al. (2014) also confirmed that the Be star MWC 656 was the companion of an X-ray quiescent BH, resulting in the first identification of a BH-BeXB. Population synthesis models point towards the extreme rarity of such systems, which are also thought to be very faint in the X-ray domain due to accretion disc truncation. This illustrates one of the major limitations of soft X-ray surveys in characterizing new low-luminosity HMXBs, as a significant fraction of them appear similar to CWBs or slightly more energetic isolated massive stars. It is therefore reasonable to believe that a significant population of quiescent HMXBs, some with BH primaries, exist in the Galaxy but remain undetected and/or misidentified. A possible way to address this issue is to observe candidate low-luminosity HMXBs through optical and near-IR high-resolution spectroscopy for radial velocity measurements. Alternatively, hard X-ray spectroscopy may allow us to characterize their emission in this spectral domain more accurately, which should be power-law-like and harder than that of isolated massive stars if even weak accretion occurs. In particular, hard X-ray observations of the five X-ray sources with massive stellar counterparts we identified in this study should enable us to verify their HMXB, CWB, or isolated massive star nature.

Acknowledgements. We thank the anonymous referee for her/his comments that helped to improve this work. F.M.F. acknowledges support from a National Science Foundation Graduate Research Fellowship. F.E.B. acknowledges support from Basal-CATA PFB-06/2007, CONICYT-Chile FONDECYT 1141218, “EMBIGGEN” Anillo ACT1101, and Project IC120009 “Millennium Institute of Astrophysics (MAS)” funded by the Iniciativa Científica Milenio del

Ministerio de Economía, Fomento y Turismo. We acknowledge the use of data products from observations made with ESO Telescopes at the La Silla or Paranal Observatories under ESO programme ID 179.B-2002. The VVV Survey is supported by ESO, by BASAL Center for Astrophysics and Associated Technologies PFB-06, by FONDAP Center for Astrophysics 15010003, and by the Iniciativa Científica Milenio del Ministerio de Economía, Fomento y Turismo through grant IC 12009, awarded to the “Millennium Institute of Astrophysics (MAS)”. This publication makes use of data products from the Two Micron All Sky Survey, which is a joint project of the University of Massachusetts and the Infrared Processing and Analysis Center/California Institute of Technology, funded by the National Aeronautics and Space Administration and the National Science Foundation. The DENIS project has been partly funded by the SCIENCE and the HCM plans of the European Commission under grants CT920791 and CT940627. It is supported by INSU, MEN and CNRS in France, by the State of Baden-Württemberg in Germany, by DGICYT in Spain, by CNR in Italy, by FFwFBWF in Austria, by FAPESP in Brazil, by OTKA grants F-4239 and F-013990 in Hungary, and by the ESO C&EE grant A-04-046. This work is partly based on observations made with the *Spitzer* Space Telescope, which is operated by the Jet Propulsion Laboratory, California Institute of Technology under a contract with the National Aeronautics and Space Administration. This publication makes use of data products from the Wide-field Infrared Survey Explorer, which is a joint project of the University of California, Los Angeles, and the Jet Propulsion Laboratory/California Institute of Technology, funded by the National Aeronautics and Space Administration.

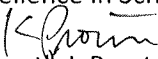
References

- Arnaud, K. A. 1996, in *Astronomical Data Analysis Software and Systems V*, eds. G. H. Jacoby, & J. Barnes, ASP Conf. Ser., 101, 17
- Benjamin, R. A., Churchwell, E., Babler, B. L., et al. 2003, *PASP*, 115, 953
- Berghöfer, T. W., Schmitt, J. H. M. M., & Cassinelli, J. P. 1996, *A&AS*, 118, 481
- Bird, A. J., Bazzano, A., Bassani, L., et al. 2010, *ApJS*, 186, 1
- Blum, R. D., Ramond, T. M., Conti, P. S., Figer, D. F., & Sellgren, K. 1997, *AJ*, 113, 1855
- Bodaghee, A., Tomsick, J. A., Rodriguez, J., & James, J. B. 2012, *ApJ*, 744, 108
- Bozzo, E., Falanga, M., & Stella, L. 2008, *ApJ*, 683, 1031
- Bronfman, L., Alvarez, H., Cohen, R. S., & Thaddeus, P. 1989, *ApJS*, 71, 481
- Campana, S., Stella, L., Israel, G. L., et al. 2002, *ApJ*, 580, 389
- Casares, J., Negueruela, I., Ribó, M., et al. 2014, *Nature*, 505, 378
- Caswell, J. L., & Haynes, R. F. 1987, *A&A*, 171, 261
- Chaty, S., & Rahoui, F. 2012, *ApJ*, 751, 150
- Chaty, S., Rahoui, F., Foellmi, C., et al. 2008, *A&A*, 484, 783
- Chiar, J. E., & Tielens, A. G. G. M. 2006, *ApJ*, 637, 774
- Churchwell, E., Babler, B. L., Meade, M. R., et al. 2009, *PASP*, 121, 213
- Clark, J. S., & Steele, I. A. 2000, *A&AS*, 141, 65
- Cohen, D. H. 2000, in *IAU Colloq. 175: The Be Phenomenon in Early-Type Stars*, eds. M. A. Smith, H. F. Henrichs, & J. Fabregat, ASP Conf. Ser., 214, 156
- Coleiro, A., & Chaty, S. 2013, *ApJ*, 764, 185
- Coleiro, A., Chaty, S., Zurita Heras, J. A., Rahoui, F., & Tomsick, J. A. 2013, *A&A*, 560, A108
- Corbet, R. H. D., Sokoloski, J. L., Mukai, K., Markwardt, C. B., & Tueller, J. 2008, *ApJ*, 675, 1424
- Crowther, P. A., Hadfield, L. J., Clark, J. S., Negueruela, I., & Vacca, W. D. 2006, *MNRAS*, 372, 1407
- Dame, T. M., Hartmann, D., & Thaddeus, P. 2001, *ApJ*, 547, 792
- Davies, B., de La Fuente, D., Najarro, F., et al. 2012, *MNRAS*, 419, 1860
- de la Fuente, D., Najarro, F., Davies, B., & Figer, D. F. 2013, in *Highlights of Spanish Astrophysics VII, Proc. of the X Scientific Meeting of the SEA, held in Valencia*, 534
- DeWitt, C., Bandyopadhyay, R. M., Eikenberry, S. S., et al. 2013, *AJ*, 146, 109
- Dhillon, V. S., Marsh, T. R., Duck, S. R., & Rosen, S. R. 1997, *MNRAS*, 285, 95
- Epchtein, N., Deul, E., Derriere, S., et al. 1999, *A&A*, 349, 236
- Fitzpatrick, E. L. 1999, *PASP*, 111, 63
- Fornasini, F. M., Tomsick, J. A., Bodaghee, A., et al. 2014, *ApJ*, submitted
- Förster Schreiber, N. M. 2000, *AJ*, 120, 2089
- Güdel, M., & Nazé, Y. 2009, *A&ARv*, 17, 309
- Hanson, M. M., Conti, P. S., & Rieke, M. J. 1996, *ApJS*, 107, 281
- Hanson, M. M., Rieke, G. H., & Luhman, K. L. 1998, *AJ*, 116, 1915
- Hanson, M. M., Kudritzki, R.-P., Kenworthy, M. A., Puls, J., & Tokunaga, A. T. 2005, *ApJS*, 161, 154
- Harrison, T. E., Campbell, R. K., Howell, S. B., Cordova, F. A., & Schwope, A. D. 2007, *ApJ*, 656, 444
- Hong, J., Schlegel, E. M., & Grindlay, J. E. 2004, *ApJ*, 614, 508
- Ivanov, V. D., Rieke, M. J., Engelbracht, C. W., et al. 2004, *ApJS*, 151, 387
- Kalberla, P. M. W., Burton, W. B., Hartmann, D., et al. 2005, *A&A*, 440, 775
- Kuulkers, E., Norton, A., Schwope, A., & Warner, B. 2006, in *Compact stellar X-ray sources*, Cambridge Astrophysics Series, 39, 421
- Lamers, H. J. G. L. M., Zickgraf, F.-J., de Winter, D., Houziaux, L., & Zorec, J. 1998, *A&A*, 340, 117
- Lépine, S., & Gaidos, E. 2011, *AJ*, 142, 138
- Lin, C. C., & Shu, F. H. 1964, *ApJ*, 140, 646
- Lin, C. C., Yuan, C., & Shu, F. H. 1969, *ApJ*, 155, 721
- Luna, G. J. M., Sokoloski, J. L., Mukai, K., & Nelson, T. 2013, *A&A*, 559, A6
- Marshall, D. J., Robin, A. C., Reylé, C., Schultheis, M., & Picaud, S. 2006, *A&A*, 453, 635
- Masetti, N., Landi, R., Pretorius, M. L., et al. 2007, *A&A*, 470, 331
- Matt, G., & Guainazzi, M. 2003, *MNRAS*, 341, L13
- Mauerhan, J. C., Munro, M. P., Morris, M. R., Stolovy, S. R., & Cotera, A. 2010, *ApJ*, 710, 706
- Mercer, E. P., Clemens, D. P., Meade, M. R., et al. 2005, *ApJ*, 635, 560
- Meyer, M. R., Edwards, S., Hinkle, K. H., & Strom, S. E. 1998, *ApJ*, 508, 397
- Minniti, D., Lucas, P. W., Emerson, J. P., et al. 2010, *NewA*, 15, 433
- Morris, P. W., Eenens, P. R. J., Hanson, M. M., Conti, P. S., & Blum, R. D. 1996, *ApJ*, 470, 597
- Nebot Gómez-Morán, A., Motch, C., Barcons, X., et al. 2013, *A&A*, 553, A12
- Negueruela, I., Smith, D. M., Reig, P., Chaty, S., & Torrejón, J. M. 2006, in *The X-ray Universe 2005*, ed. A. Wilson, ESA SP, 604, 165
- Nishiyama, S., Nagata, T., Kusakabe, N., et al. 2006, *ApJ*, 638, 839
- Pasinetti Fracassini, L. E., Pastori, L., Covino, S., & Pozzi, A. 2001, *A&A*, 367, 521
- Raguzova, N. V. 2001, *A&A*, 367, 848
- Rahoui, F., & Chaty, S. 2008, *A&A*, 492, 163
- Rahoui, F., Chaty, S., Lagage, P.-O., & Pantin, E. 2008, *A&A*, 484, 801
- Rayner, J. T., Cushing, M. C., & Vacca, W. D. 2009, *ApJS*, 185, 289
- Reig, P. 2011, *Ap&SS*, 332, 1
- Repolust, T., Puls, J., Hanson, M. M., Kudritzki, R.-P., & Mokiem, M. R. 2005, *A&A*, 440, 261
- Sana, H., de Mink, S. E., de Koter, A., et al. 2012, *Science*, 337, 444
- Searle, S. C., Prinja, R. K., Massa, D., & Ryans, R. 2008, *A&A*, 481, 777
- Skrutskie, M. F., Cutri, R. M., Stiening, R., et al. 2006, *AJ*, 131, 1163
- Steele, I. A., & Clark, J. S. 2001, *A&A*, 371, 643
- Sutherland, W., & Saunders, W. 1992, *MNRAS*, 259, 413
- Tody, D. 1993, in *Astronomical Data Analysis Software and Systems II*, eds. R. J. Hanisch, R. J. V. Brissenden, & J. Barnes, ASP Conf. Ser., 52, 173
- Tomsick, J. A., Chaty, S., Rodriguez, J., Walter, R., & Kaaret, P. 2008, *ApJ*, 685, 1143
- Tomsick, J. A., Bodaghee, A., Chaty, S., et al. 2012, *ApJ*, 754, 145
- Vacca, W. D., Garmany, C. D., & Shull, J. M. 1996, *ApJ*, 460, 914
- Wallace, L., & Hinkle, K. 1996, *ApJS*, 107, 312
- Wallace, L., & Hinkle, K. 1997, *ApJS*, 111, 445
- Walter, R., & Zurita Heras, J. 2007, *A&A*, 476, 335
- Winkler, C., Courvoisier, T. J.-L., Di Cocco, G., et al. 2003, *A&A*, 411, L1
- Wright, E. L., Eisenhardt, P. R. M., Mainzer, A. K., et al. 2010, *AJ*, 140, 1868



Office of the Dean
College of Arts and Sciences
Campus Box 48
Milledgeville, Georgia 31061-0490
Phone 478-445-4441
Fax 478-445-0873

March 10, 2016

TO: Excellence in Scholarship & Creative Endeavors Award Committee
FROM: 
Kenneth J. Procter, Dean, College of Arts and Sciences
SUBJECT: Support of Dr. Arash Bodaghee

In his brief time at Georgia College, Dr. Arash Bodaghee has produced a remarkable quantity of scholarship in a groundbreaking domain of astrophysics, and he has included undergraduate students in the process. As Dr. Ken McGill, Chair of Chemistry, Physics, and Astronomy, noted, Dr. Bodaghee has achieved a level of productivity and significance in his scholarship that would be prized at a research institution, yet Dr. Bodaghee has accomplished this work while carrying out the teaching responsibilities that we expect at Georgia College. Dr. Bodaghee's senior colleague, Dr. Domingue, has shared more detail about the groundbreaking nature of Dr. Bodaghee's research. In his nomination letter, Dr. Domingue mentions Dr. Bodaghee's "acceptance of time and grant funds for the Chandra and Hubble space telescopes." It must be understood that research time on these telescopes is costly and limited. To gain access to these telescopes, even for brief periods of time, means competing with astronomers worldwide. That Dr. Bodaghee has been granted research time on not just one, but two of these orbiting telescopes is a remarkable achievement in itself. Even more noteworthy for the Georgia College mission, through Dr. Bodaghee's work, our undergraduate students are able to participate in this exciting cutting-edge research—at a typical research institution this kind of access would be the preserve of graduate students.

Dr. Bodaghee is very deserving of the Excellence in Scholarship and Creative Endeavors Award.